Imaging strong-field induced molecular dynamics

Im Fachbereich Physik der
Freien Universität Berlin
eingereichte

Dissertation

zur Erlangung des akademischen Grades Dr. rer. nat.

von

Katrin Reininger

Berlin 2018

Diese Arbeit wurde am Max-Born-Institut für Nichtlineare Optik und Kurzzeitspektroskopie im Forschungsverbund Berlin e.V. angefertigt.

Erstgutachter:	Prof. Dr. M.J.J. Vrakking
Zweitgutachter:	Priv.-Doz. Dr. A. Dorn

Tag der Disputation: 12.10.2018

Contents

1 Chapter 1. Introduction

One important goal of modern chemical physics consists of following chemical reactions in real-time and with atomic resolution. The development of methodologies to obtain sub-Ångström spatial and femtosecond temporal resolution is of major interest to the goal of recording such a molecular movie [1, 2]. Today much is known about the static structure of molecules, based on experiments with elaborated techniques like electron and x-ray diffraction or the scanning tunneling and atomic force microscopy. Furthermore, high-resolution spectroscopic techniques such as Raman spectroscopy, Fourier-transform infrared spectroscopy, or Doppler-free spectroscopy, brought insight into electronic, vibrational and rotational states and structures of molecules with an up-to-date unique resolution. However, capturing of the nuclear motion in the defining processes of chemistry, the bond-breaking and -forming or the rearrangement of nuclei and electrons in a chemical reaction, remains a challenging task. Especially, far-off equilibrium configurations of moving molecules are difficult to image due to their transient appearance. However, in order to fully understand a movie, it is not enough to watch the first and last scene. One must watch the full film. And in order to fully understand a chemical reaction and to access defined control mechanisms, it is insufficient to only know the reactants and the products. One must follow the complete reaction.

Femtochemistry deals with the investigation of chemical processes on the time-scale of several 10^{-15} s. The field benefited from great advancements by lasers providing ultrashort optical pulses in combination with the development of the pump-probe technique [3]. In pump-probe experiments, a first pulse initiates molecular dynamics, e.g. by exciting or ionizing a molecule (pump step). A wave packet, the coherent superposition of excited states, is created. A second pulse follows after a certain time-delay and probes the temporal evolution of the wave packet (probe step). A flip-book-like movie can be recorded by varying the time delay between the two pulses. One of the first experiments where a chemical process was investigated with femtosecond resolution is shown in Fig. 1.1 (Figures taken from Ref. [4]). Zewail and coworkers studied the dissociation process of ICN, a so-called half-collision reaction. By a defined clocking of the reaction the authors could determine the I-CN bond-breaking time to be (205 ± 30) fs. The time-resolved appearance of the CN fragment was measured by the absorption of the time-delayed probe pulse resulting in laser-induced fluorescence.

With time-resolved experiments, there is not only the goal to investigate unimolecular reactions, like a dissociation. One interest is the investigation of the time-dependent structural change during bimolecular chemical reactions, e.g.:

$$\mathrm{AB} + \mathrm{C} \rightarrow \mathrm{A} + \mathrm{BC}. \tag{1.1}$$

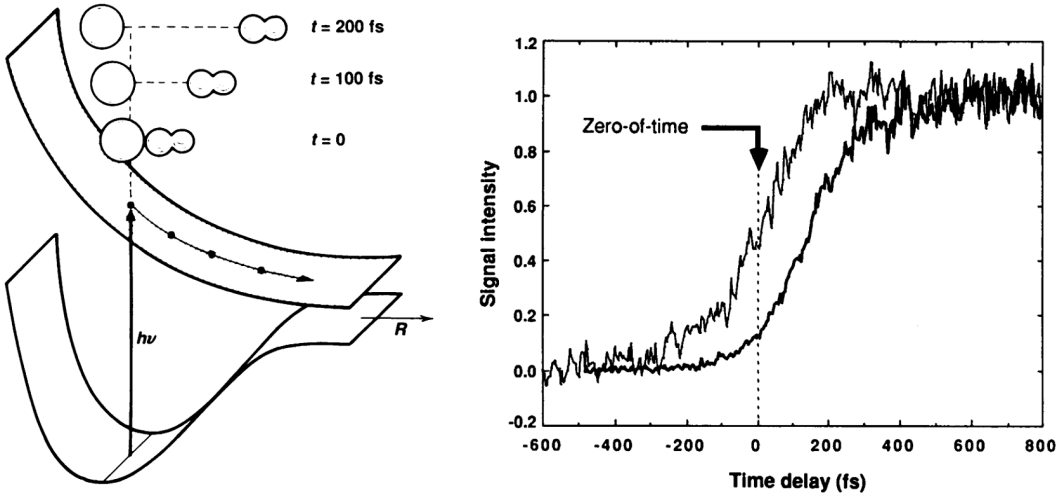

Figure 1.1.: Investigation of the bond-breaking time in the half-collision reaction $ICN \rightarrow I + CN$, taken from Ref. [4]. Left: Schematic view of the induced dynamics. The dissociation is initiated by a pump pulse which excites the parent molecule to a repulsive state. A time-delayed second pulse probes the appearance of the CN fragment via laser-induced fluorescence. Right: The measured absorption signal (bold line) and a measured reference photoionization signal (thin line) to determine the time zero of the experiment.

One wants to explore the structural change during the whole process from reactants to products, including transient intermediate configurations around the transition state. For designing an experiment to investigate time-resolved bimolecular chemical reactions, there are some key points to consider. The two most obvious points are the need for a time-resolved measurement method, able to resolve dynamics from the picosecond to the femtosecond range, and the need for a probe mechanism which gives information about the structure of the molecule. Furthermore, there is the necessity to clock the reaction in a controlled way to draw conclusions on the time-dependent behavior. At the same time a defined relative orientation between the two reactants is required to ensure a defined reaction pathway. The last two points are a conceptual challenge in exploring bimolecular reactions. There is often the lack of a defined start time and a defined start geometry of the reactants. Furthermore, the most chemical reactions happen on the ground state electronic potential surface, while often in pump-probe experiments the reaction is started by exciting the molecule to a higher electronically excited state.

The applied probe mechanisms in pump-probe experiments vary. Tools like transient absorption spectroscopy and time-resolved photoelectron spectroscopy make use of the nowadays available short-pulse laser systems [5, 6]. Also first experiments using diffraction techniques, the classical imaging tool for static structures, have been performed [7–9]. Since the time-resolution in pump-probe spectroscopy is mainly defined by the temporal length of the pulses, the development of short laser pulses with pulse lengths in the temporal range of the fastest nuclear dynamics ($< 10\,\mathrm{fs}$) is a major benefit.

A promising technique to image nuclear structural changes in a pump-probe experiment is laser-induced Coulomb explosion imaging (CEI) [10]. This approach makes use of the classical repelling Coulomb force of charged particles, which strongly depends on the distance between the single charges. The instantaneous removal of the valence electrons of a molecule by strong-field ionization in an ultrashort laser pulse, leads to a system of positively charged cores that repel each other explosion-like on a Coulomb potential. The momenta that the individual ions gain in this explosion contain information about the original position of the nuclei and can hence be used to reconstruct the transient structure of the molecule at the time of the ionization. The ability of CEI as tool to study molecular structure and molecular dynamics, was shown in many experiments, see for example [11–18]. Compared to other approaches, the advantage of CEI is that for CEI experiments in principle no a priori knowledge of the potential energy surfaces of the molecules is required. Furthermore, the technique is independent of the absorption sensitivity of certain states. At the same time, CEI benefits twice from the development of ultrashort laser pulses. The spatial resolution in CEI experiments is not defined by the wavelength of the laser but by the accuracy of a defined ionization time. Hence, with a shorter pulse both the temporal and spatial resolution are increased.

CEI is a single-molecule imaging technique. To receive a complete picture of the molecular structure, all created ionic fragments from the explosion of each single molecule have to be recorded and correlated. Further, the individual data sets must not contain fragments from other molecules ionized by the same laser pulse. A powerful approach to filter single molecule events is the technique of coincidence detection [19, 20]. In a coincidence detection scheme, the recorded data is filtered for events where a certain sequence of processes, e.g. the measurement of all ionic fragments of an exploding molecule, is detected in a specific time-span. With this approach, all detected events of no importance for the experiment are discarded. Hence, even rarely occurring physical processes can be visualized.

Using CEI in a pump-probe experiment opens the potential to map time-dependent structural dynamics in molecules. As a future goal, we want to use the technique to study time-resolved bimolecular chemical reactions. Here, we want to introduce the idea for a new approach, where we plan to combine CEI with established techniques of the reaction precursor preparation of molecular ions and ionic clusters. We propose a table-top experiment, fulfilling the requirements to image the structural dynamics in bimolecular reactions, including intermediate molecular configurations around the transition state of the reaction. The fundamental idea for the new approach of Transition State Coulomb Explosion Imaging (TSCEI) was proposed by Dr. Jochen Mikosch.

Transition State Coulomb Explosion Imaging The first essential point to consider when investigating bimolecular reactions is the need to clock the chemical reaction to receive a specific starting time. With this requirement comes the need for a proper precursor preparation. One promising concept to clock bimolecular reactions is to create small clusters, which hold the precursors in close proximity, but with a certain reaction barrier preventing the uncontrolled start of the reaction. The reaction barrier is then overcome with the help of a pump pulse, depositing enough

energy in the system e.g. by introducing a photodissociation of a chromophore or by photodetachment of a molecular anion. By this, the reaction is started at a controlled time. It has been shown in a few experiments that starting bimolecular reactions from van der Waals clusters and ion-dipole complexes as precursors is possible [21, 22]. These small ionic clusters ion-dipole complexes or molecular ions (all refered to as targets) can be created in a supersonic expansion. Varying the temperature and the pressure during the expansion gives a control mechanism for the cluster formation. For each specific molecular cluster or ion-dipole complex there exists a certain equilibrium geometry. Hence, depending on the temperature the equilibrium geometry ensures a defined start geometry of the reactants. To study ionic targets a mechanism to ionize the targets in the expansion has to be included. Working with ionic targets has the great advantage of controllability via established mass-spectrometric techniques (see e.g. [23]). First, a specific target can be selected via its mass-to-charge ratio with standard mass spectrometric tools before it reaches the interaction zone. All species of no interest are blocked and do not disturb the measurement. Second, there are established tools for trapping and cooling ions. The ionic targets can be captured in a radio-frequency trap to control their temperature with a buffer gas. Furthermore, implementing an additional electrostatic ion beam trap opens the potential to recycle the ion target and to increase the repetition rate of the experiment. After the mass selection of the desired species the prepared ionic targets enter an interaction zone and are overlapped with two femtosecond laser pulses in a pump-probe scheme. Molecular dynamics are triggered by a pump pulse which, for example, photodissociates a chromophore as a start mechanism for the reaction or via the photodetachment of a negative ion. Both mechanisms are described and used before, e.g. photodissociation in Ref. [22] and photodetachment in Ref. [24]. When using photodissociation as trigger, the relative kinetic energy of the reactants can be varied and controlled via tuning the photodissociation wavelength to study energy-dependent reaction pathways. In addition, the clusters can be prepared from the reactants side as well as from the products side, the reaction can be examined in both directions. By clustering several solvent molecules together with the precursors, solvation effects can be simulated.

After launching the reaction dynamics the changing molecular structure, including intermediate states around the transition state, is probed with a time-delayed probe pulse which induces a Coulomb explosion. CEI is anticipated to be specifically sensitive to transition states due to enhanced ionization (EI, see section 2.1) [10]. Hence, an increased ionization probability in this area is expected.

The interaction region is embedded in a second spectrometer. After inducing the Coulomb explosion the created ionic fragments are projected on a time- and position sensitive detector. With measuring the time-of-flight of the fragments and their impact position on the detector information on the full three-dimensional momentum vector of all fragments is gained. The momentum information is finally used to reconstruct the transient structure of the molecules in the reaction.

The overall aim of the approach is, by combining the precursor cluster preparation technique with Coulomb explosion imaging, to get a time-resolved measurement of the evolving structures during a bimolecular chemical reaction on the electronic ground state potential on a single molecule basis.

However, despite the great possibilities coming with CEI, there are also some challenges to consider. The molecular geometry is reconstructed based on a repelling Coulomb potential at the point of ionization. If there are deviations, e.g. because the nuclei are moving during the ionization process or there exist several break-up pathways besides the direct Coulomb explosion, the obtained structural information is distorted. The technique is still developing. Depending on the explored molecule and the specific experimental conditions it has to be explored how well the molecular structure can be reconstructed with CEI and how experiments can potentially be improved. At the same time, with the increasing size of molecules it is more challenging to (i) break all bonds in the molecule and create only ionic fragments and (ii) measure all created ionic fragments in coincidence. However, information about the molecule can already be gained from the momenta of ionic fragments of a partial Coulomb explosion. Hence, partial CEI can be an advantageous tool for large molecules or low laser intensities. A further huge challenge is the requirement to record single-molecule events per laser pulse, while at the same time high intensities are needed to induce the Coulomb explosion. To fulfill the single-molecule coincidence condition per laser pulse and receive at the same time sufficient statistical power for the interpretation of an experiment the experiment has to be repeated many times and large data sets have to be recorded and processed. Therefore, long measurement times or high repetition rates are needed especially in pump-probe experiments.

Within the frame of this thesis we want to make one step further in the direction of recording transient molecular structures in molecular dynamics with strong-field ionization and with coincidence Coulomb explosion imaging. In our three experimental parts we (i) conducted a single-pulse coincident Coulomb explosion imaging experiment to study the different fragmentation pathways of a triply ionized five-atomic molecule, (ii) performed a pump-probe experiment where we recorded the momenta of fragments from a partial molecular break-up following a single-ionization process to study a vibrational motion that was excited in the pump-step via impulsive stimulated Raman scattering, and (iii) constructed and implemented the first parts of a new experimental setup designed for the approach of TSCEI.

The thesis is structured as follows: In chapter 2 the fundamental concepts underlying the following experiments are explained, including the theory of strong-field ionization, the technique of Coulomb explosion imaging and coincidence detection, and the mechanism of impulsive stimulated Raman scattering. In the first experimental part (chapter 3), the Coulomb explosion of CH_2BrI is studied in a reaction microscope. With the example of the measured data, it is described how the approach of a coincidence experiment with an event-by-event based analysis is conducted, including the calculation of the single fragment momenta and the post-measurement alignment of the gained momentum vectors. The experiment was performed in a single pulse scheme, concentrating on the different possible pathways in which the break-up of the molecule can proceed. On the basis of the results, the possibilities and limitations of CEI as a tool to measure the structure of a molecule are discussed. In the second part of the thesis (chapter 4) the N-N stretching vibration of dinitrogen tetroxide is explored in a time-resolved pump-probe experiment. The used ion-ion-coincidence machine [25] and the used detector system [26] are

introduced. Furthermore, the data processing is explained in detail as well as the off-line analysis approach to improve the spatial as well as the temporal resolution of the implemented detector. In the third experimental part of this thesis (chapter 5), the construction and implementation of a new setup designed for the approach of TSCEI, including an ion source, a time-of-flight mass spectrometer, a Coulomb explosion imaging spectrometer, and a neutral molecular beam source, is described. In chapter 6, a summary of the gained results and a future outlook is given.

Chapter 2. Fundamentals

In all experiments carried out and proposed in this thesis we use intense and ultrashort laser pulses to ionize molecules. In this chapter, we give an introduction into the fundamental concepts underling our experiments. First, we introduce the concept of strong-field ionization. We describe how the ionization probability depends on the laser parameters and discuss the topic of enhanced ionization, an effect which influences our Coulomb explosion experiments. Next, we introduce Coulomb explosion imaging, the technique we use in the first experiment of this thesis (see chapter 3) to study the fragmentation dynamics of a polyatomic molecule and that we intend to use in our newly built experiment (see chapter 5) to study the structural change of molecules during chemical reactions. Connected to the technique of Coulomb explosion imaging is the detection of ionic fragments in coincidence, which is explained in the third part of this chapter. As last topic, we introduce the mechanism of impulsive stimulated Raman scattering (ISRS). In the experiment described in chapter 4, we used an ISRS process to excite a vibrational motion in a molecule.

2.1. Strong-field ionization

Strong-field ionization is a widely discussed and explored topic (see for example Ref. [27–29]). The basic concept of strong-field ionization depends on the laser intensity and can be described in two different regimes: the *multiphoton ionization* regime at low intensities and the *tunnel ionization* regime at high intensities. In this section, we first introduce the Keldysh parameter which is a measure to decide which of the two concepts is suitable to treat the problem. Afterwards, we introduce both theories and give several examples of effects described in the two regimes.

The Keldysh parameter The fundamental difference between a description of strong-field ionization as multiphoton ionization (MPI) or tunnel ionization (TI) is that in the TI regime the electron tunnels through a barrier created by the combined Coulomb field of the atom or molecule and the external electric field of the laser while in the MPI regime the needed energy to ionize the atom or molecule is provided by the simultaneous absorption of a number of photons. To decide which regime is valid for a certain intensity range, the Keldysh parameter γ is introduced [30]. It compares the ionization potential IP of an atom or molecule with the ponderomotive potential U_P, the cycle-averaged kinetic energy of an oscillating electron in the external laser field:

$$\gamma = \sqrt{\frac{IP}{2\,U_\mathrm{P}}} \tag{2.1}$$

$$U_\mathrm{P} = \frac{q_e^2\,E_0^2}{4\,m_e\,\omega^2} = \frac{q_e^2}{8\,\pi\,m_e\,\epsilon_0\,c^3} I\,\lambda^2, \tag{2.2}$$

where m_e and q_e are the electron mass and charge, E_0 is the peak electric field, ω is the laser frequency, ϵ_0 is the vacuum permittivity, c is the speed of light, I is the intensity of the laser and λ is the wavelength of the laser. U_P is a property of the external laser field. It is highest for long wavelengths λ and high laser intensities I. A common differentiation is that for $\gamma > 1$ the process can be described as multiphoton ionization (the ionization potential is much higher than the ponderomotive energy). For $\gamma < 1$, on the other hand, the ionization takes place mainly in the tunneling regime. However, a clear separation between both regimes is not possible. There is rather a smooth transition between both regimes.

Multiphoton ionization For a Keldysh parameter $\gamma > 1$ the strong-field ionization can be treated in the MPI regime. An example would be the ionization of an argon atom ($IP = 15.76\,\mathrm{eV}$) using a laser with 400 nm wavelength. At an intensity of the laser field in focus of $10^{13}\,\mathrm{W\,cm^{-2}}$ the Keldysh parameter is $\gamma = 7.3$. In the MPI regime the ionization process can be treated with perturbation theory [31], leading to a probability P_MPI to ionize an atom or molecule which scales with the intensity of the laser field I to the power of the in total needed amount of photons N:

$$P_\mathrm{MPI} \propto I^N. \tag{2.3}$$

Eq. (2.3) describes the case of ionizing an atom. In the case of molecules, the ionization probability depends also strongly on the orientation of the molecule with respect to the laser field and the geometry of the molecular orbitals. A geometrical factor can be induced, to include these properties [32,33]. The number N of needed photons for the ionization process is composed of the number of photons N_{IP} required to overcome the ionization potential, the number N_{U_P} of photons required to provide the ponderomotive energy the electron has after the ionization, and the required number of photons $N_{E_\mathrm{kin,e}}$ to provide the kinetic energy $E_\mathrm{kin,e}$ the electron has after the ionization. The kinetic energy of the electron can be calculated via:

$$E_\mathrm{kin,e} = N \cdot h\nu - (IP + U_\mathrm{P}). \tag{2.4}$$

Hence, six photons are needed to ionize an argon atom using a laser with the above mentioned parameters.

In the MPI regime for example the processes of resonance-enhanced multiphoton ionization (REMPI) and above-threshold ionization (ATI) can be characterized. A REMPI process occurs when the energy sum of a certain number of photons $M < N$ is in resonance with an electronically excited state of the atom/molecule. This resonance leads to a higher ionization probability compared to the non-resonant

case. The case of ATI, first observed by Agostini *et al.* [34], describes the situation where a higher number of photons $K > N$ than the minimum needed amount N for ionization ($E_{\mathrm{kin,e}} = 0$) is absorbed. The absorption of extra photons leads to additional kinetic energy of the freed electron, quantized in steps of the photon energy. This is visible as peaks in the photoelectron spectrum, called ATI peaks. The impact of the ponderomotive potential on the ionization probability can be clearly seen in the structure of ATI peaks. It was found that the lowest order ATI peak can be completely suppressed by increasing the intensity of the laser and hence, the ponderomotive energy [35]. Due to the rise in U_{P} at a certain point more photons are needed to accomplish the ionization process. The increase of the peak electric field of the laser influences the strong-field ionization process and shifts the process to a regime, which can not be treated with perturbation theory anymore.

Tunnel ionization For a Keldysh parameter $\gamma < 1$ the ionization process can be treated in the tunnel ionization regime. An example would be the ionization of an argon atom using a laser with 800 nm wavelength. At an intensity of the laser field in the focus of $10^{15}\,\mathrm{W\,cm^{-2}}$ the Keldysh parameter is $\gamma = 0.36$.

In the focus of pulsed femtosecond lasers large local electric field strengths can be reached, exceeding the Coulomb field which binds the valence electrons to the atoms' cores. Such field strengths are a major perturbation for the atom or molecule itself and influence the binding potential of the electrons. In Fig. 2.1 the potential curve (blue) of an atom in a strong laser field at the point where the oscillating electric field of the laser is at the peak value is shown. The potential $V(r)$ is described by:

$$V(r) = -\frac{Zq_e^2}{4\pi\epsilon_0 r} - q_e E_0 r. \tag{2.5}$$

Here, r is the distance of the electron from the ion center, E_0 is the instantaneous electric field strength and Z is the charge state of the ion. The electron (green) experiences a barrier-like potential due to the influence of the electric field of the laser (red). Tunneling of the electron through the barrier becomes possible. Hence, the process is called tunnel ionization (TI). The electron can reach a non-bound continuum state, leaving a positive ion behind. Since the external field is regarded as quasi-static during the ionization process (in time and space), this regime is often referred to as *quasi-static regime*.

Due to the strong influence of the external field the system cannot be treated anymore as an atom with a perturbing laser field, but rather as a laser field with a present atom [36]. The solution in the well-known strong-field approximation (SFA) is adopted from perturbation theory. Here, the strong field is the main part, treated exactly and the Coulomb potential is seen as the perturbation. The following mathematical description follows the article [27].

The solution of the time-dependent Schrödinger equation $\mathrm{i}\hbar\frac{\partial}{\partial t}|\psi\rangle = \hat{H}(t)|\psi\rangle$ is the state

$$|\psi(t)\rangle = \mathrm{e}^{-\frac{\mathrm{i}}{\hbar}\int_0^t \hat{H}(t)\mathrm{d}t'}|\phi_i\rangle \tag{2.6}$$

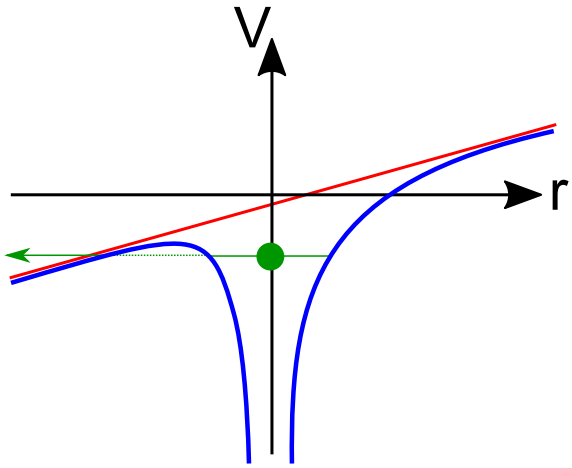

Figure 2.1.: The process of tunnel ionization. The strong laser field (red) modifies the Coulomb potential (blue), binding the electron (green) to the atom. A barrier is created which enables tunneling of the electron to the continuum.

with the propagator $\hat{H}(t)$ and the initial state $|\phi_i\rangle$. There are three major points in the time-evolution regarded. Time $t_0 = 0$ is the start time of the time-evolution, time t' is the time the ionization takes place, and time t is the end point of the time-evolution (e.g. point of measurement). The propagator $\hat{H}(t)$ splits into two parts: $\hat{H}(t) = \hat{H}_0 + \hat{V}_L$, where $\hat{H}_0$ is the field free operator and $\hat{V}_L$ describes the interaction with the laser field. With $\hat{H}(t) = \hat{H}_0 + \hat{V}_L$ the state $|\psi(t)\rangle$ can be written as:

$$\begin{aligned} |\psi(t)\rangle &= -\frac{\mathrm{i}}{\hbar}\int_0^t \mathrm{d}t' \left[\mathrm{e}^{-\frac{\mathrm{i}}{\hbar}\int_{t'}^{t}\hat{H}(t'')\mathrm{d}t''}\right] \hat{V}_L(t') \left[\mathrm{e}^{-\frac{\mathrm{i}}{\hbar}\int_{t_0}^{t'}\hat{H}_0(t'')\mathrm{d}t''}\right] |\phi_i\rangle \\ &= -\frac{\mathrm{i}}{\hbar}\int_0^t \mathrm{d}t' \hat{Q}\,\hat{V}_L(t')\,\hat{O}\,|\phi_i\rangle. \end{aligned} \tag{2.7}$$

There are now three operators processing the time-evolution starting from the initial state $|\phi_i\rangle$. The operators $\hat{O}$ and $\hat{Q}$ describe the propagation during the time intervals $t_0 \to t'$ and $t' \to t$. The operator $\hat{V}_L$ describes the moment of ionization at time t'. Since the exact moment of ionization is unknown, Eq. (2.7) is integrated over all times t'. The system starts in the ground state with the energy $-IP$ and accumulates a phase during the first time period $t_0 \to t'$ according to the operator $\hat{O}$: $\hat{O}\,|\phi_i\rangle = \mathrm{e}^{\frac{\mathrm{i}}{\hbar}IPt'}|\phi_i\rangle$. The operator $\hat{Q}$ of the second time period $t' \to t$ still contains the full Hamiltonian, describing the combined interaction of the laser field and Coulomb potential. In the SFA the electron is mainly influenced by the laser field after the ionization and the interaction with the ion is neglected. Hence, the full Hamiltonian in $\hat{Q}$ can be replaced by the operator $\hat{V}_L$ which does not include the binding potential of the atom. The eigenstates of the operator $\hat{V}_L$, the so-called Volkov states $|\psi^V\rangle$, are plane waves describing a free electron in the laser field. With the vector potential $\vec{A}(t)$ ($\vec{E}(t) = -\frac{\partial \vec{A}(t)}{\partial t}$) and the conserved quantity of the the conical momentum $\vec{p}(t) = m_e\vec{v}(t) - q_e\vec{A}(t)$ the projection of the initial ground state $|\phi_i\rangle$ on the final

state $|\psi^V\rangle$ leads to the wave function amplitude:

$$M(\vec{v},t) = -\frac{\mathrm{i}}{\hbar}\int_0^t \mathrm{d}t' \mathrm{e}^{-\frac{\mathrm{i}m_e}{2\hbar}\int_{t'}^{t}\left[\vec{v}(t)+\frac{q_e}{m_e}\vec{A}(t'')-\frac{q_e}{m_e}\vec{A}(t)\right]\mathrm{d}t''} \langle\psi^V|\hat{V}_L(t')|\phi_i\rangle \mathrm{e}^{\frac{\mathrm{i}}{\hbar}IPt'}, \tag{2.8}$$

where $\vec{v}(t)$ is the velocity of the electron. In Ref. [27] the authors show that for a Keldysh parameter $\gamma > 1$ Eq. (2.8) leads to the above described power law (Eq. (2.3)) for the ionization probability and for $\gamma < 1$ Eq. (2.8) leads to an exponential dependence of the ionization probability on the intensity of the laser:

$$P_{\mathrm{TI}} \propto \exp\left[-\frac{2\,(2I_{\mathrm{P}})^{3/2}}{3\sqrt{I}}\right]. \tag{2.9}$$

Similar to Eq. (2.3), Eq. (2.9) describes the case of the ionization regarding an atomic s-orbital. Following Ref. [32,33] a geometrical factor $R(\theta_L)$ can be introduced (θ_L is the angle between the polarization axis of the electric field and the molecular axis), which includes the dependency of the ionization rate on the geometry of the molecular orbital and the alignment of the molecule with respect to the laser field.

Over-the-barrier ionization Increasing the intensity of the laser field further can lead to another extreme case of ionization. If the laser field deforms the Coulomb potential of the atom-electron system to an extent where the barrier for the electron is below the binding potential, the electron can leave the atom without tunneling. This process is called over-the-barrier ionization. The intensity at which over-the-barrier ionization becomes possible can be estimated from the deformed potential $V(r)$ (Eq. (2.5)). The maximum of $V(r)$ has to match the ionization potential: $V(r_{\max}) = -IP$. From this condition follows the critical intensity

$$I_{\mathrm{c}} = \frac{\pi^2}{2}\frac{c\,\epsilon_0^3}{q_e^6 Z^2}\,IP^4. \tag{2.10}$$

The critical intensity at which the regime of over-the-barrier ionization is reached for the case of the argon atom and a laser with 800 nm wavelength is already $I_{\mathrm{c}} = 2.5 \times 10^{14}\,\mathrm{W\,cm^{-2}}$ (i.e. with a Keldysh parameter of $\gamma = 0.7$).

The different regimes In Fig. 2.2 the different regions, characterized by the Keldysh parameter, are illustrated (Figure adapted from Ref. [37]). The panels on the right and left side of the figure depict different processes in the two regimes. The x-axis represents the photon energy $\hbar\omega$. For higher frequencies the process is located clearer in the MPI regime. The second x-axis represents the number of photons needed (in the MPI regime) to ionize the atom or molecule. If the photon energy is high, less photons are needed for the ionization. And if less photons are needed for the ionization the process takes rather place in the MPI regime. The y-axis represents the peak electric field strength. For higher field strengths (and higher U_{P}) the process takes place in the quasi-static regime. The two regimes are separated by a diagonal line which marks the border value $\gamma = 1$. The figure shows that one has to consider both parameters at the same time, the frequency of the laser

and the peak field strength. Even for large field strengths the ionization process can be located in the MPI regime, if at the same time the frequency of the laser is high and the other way round. Inside the quasi-static regime there is a second separation in the two parts where tunnel ionization or over-the-barrier ionization takes place.

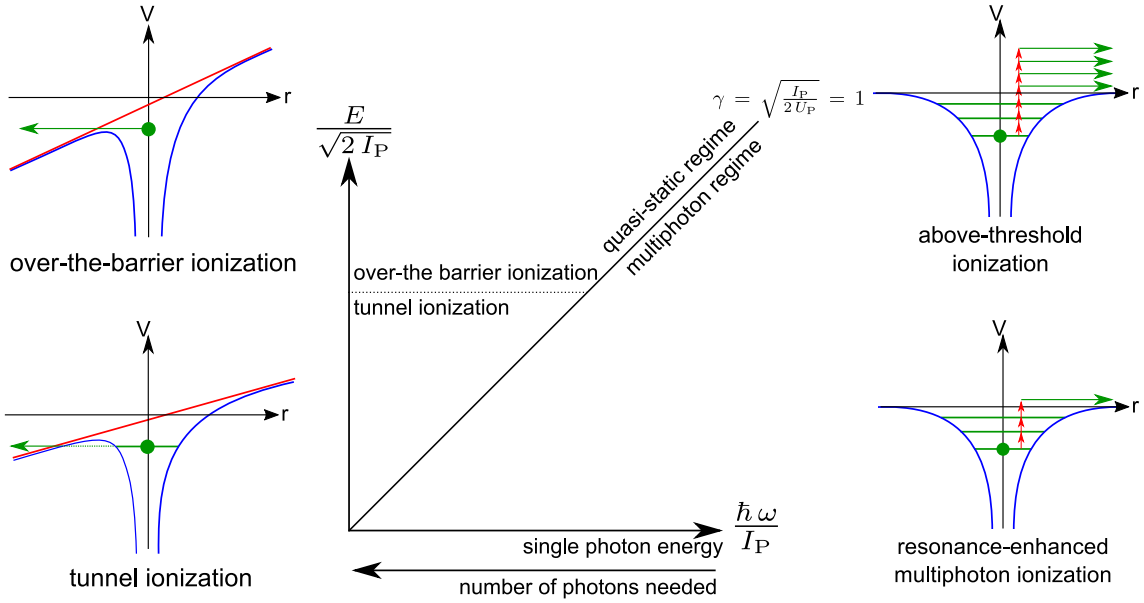

Figure 2.2.: Middle: Different ionization regimes depending on the ionization potential IP, the peak electric field strength E and the laser frequency ω. Left/Right: Illustration of different processes of strong-field ionization. Figure adapted from Ref. [37].

The three-step model The tunneling process induced by a strong laser field is the origin of a variety of physical effects which are described in the three-step model [38, 39]. The three steps take place one after another, in a single optical cycle of the laser pulse ($\approx$ 2.7 fs for 800 nm wavelength) and are illustrated in Fig. 2.3. The first step is the ionization due to the tunneling of the electron. In the second step the electron is accelerated in the laser field. Since the laser field is oscillating the electron is first driven away from the atom/molecular center, reaches a turning point, and can then be accelerated back to its origin. During the second step, the influence of the ionic potential on the electron is neglected in the strong-field approximation and only the external electric field is regarded to describe the trajectory of the electron. The third step describes the interaction of the returning electron with the ion. Due to the acceleration in the laser field, the electron gained kinetic energy in the second step. A reabsorption of the electron can lead to High Harmonic Generation [40], the emission of light with odd multiples of the ionizing laser frequency. Elastic scattering of the electron at the parent molecule can be used to gain information on the molecular structure in a technique called Laser Induced Electron Diffraction (LIED) [41–43] or can lead to high-order above-threshold ionization (HATI) due to a further acceleration of the electrons in the external laser field [44, 45]. And inelastic scattering of the electron can lead to

non-sequential double or higher ionization [46, 47].

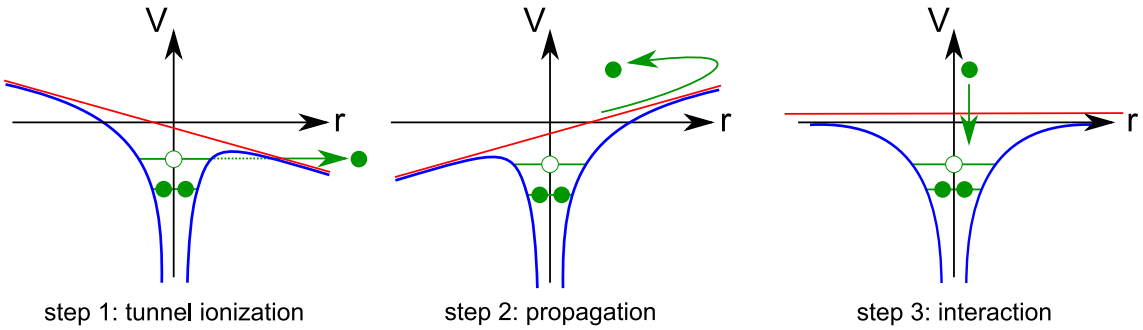

Figure 2.3.: Illustration of the three-step model. In the first step, the electron escapes the atomic or molecular potential via tunneling. In the second step, the electron propagates in the external field. In the third step, the electron returns to the parent ion, where several interactions, e.g. non-sequential double ionization or high harmonic generation, are possible.

The motion of the electron in the laser field contains a drift term and an oscillating term:

$$x(t) = \underbrace{\left[v_0 + \frac{q_e\, E_0}{m_e\, \omega}\cos(\omega t_0)\right](t - t_0)}_{\text{drift term}} - \underbrace{\frac{q_e\, E_0}{m_e\, \omega^2}\left[\sin(\omega t) - \sin(\omega t_0)\right]}_{\text{oscillation term}}. \tag{2.11}$$

Here, v_0 is the initial velocity of the electron after the ionization. The exact trajectory and the kinetic energy of the electron depends on the time t_0 the electron is released from the atom or molecule. The different type of trajectories are illustrated in Fig. 2.4 (adapted from Ref. [48]). The oscillating laser field is shown as black line, the different trajectories are shown in different colors. Electrons which are released before the peak of the electric field leave the vicinity of the ionic core directly and do not return (orange line in Fig. 2.4, ionization without recollision). These direct electrons can reach a maximum kinetic energy of $E_{\text{direct,max}} = 2\,U_\text{P}$. The maximum kinetic energy of returning electrons is $E_{\text{return,max}} = 3.17\,U_\text{P}$ (blue, dashed line in Fig. 2.4). It is reached for a release time $t_{0,\text{max}} = t_p/20$ after the peak of the field, where t_p is the oscillation period of the laser field. For electrons which are released shortly before or after $t_{0,\text{max}}$ always two trajectories are possible which result in different recombination times but with the same kinetic energy of the electron. These are referred to as short and long trajectories (dotted, green and red lines in Fig. 2.4). In addition to the direct ionization without recollision and the recolliding electrons, the electron can elastically scatter at the ion core. After this process the electron is accelerated further in the laser field and can reach a maximum kinetic energy of $E_{\text{max}} = 10\,U_\text{P}$.

Besides singly ionizing an atom or molecule, as discussed so far, also double or multiple ionization can occur. Double ionization can take place in a sequential way, where both electrons undergo the same process in subsequent laser cycles or in a non-sequential way in one single laser-cycle. In a sequential process both electrons tunnel through the barrier after each other, both leave the ion via over-the-barrier

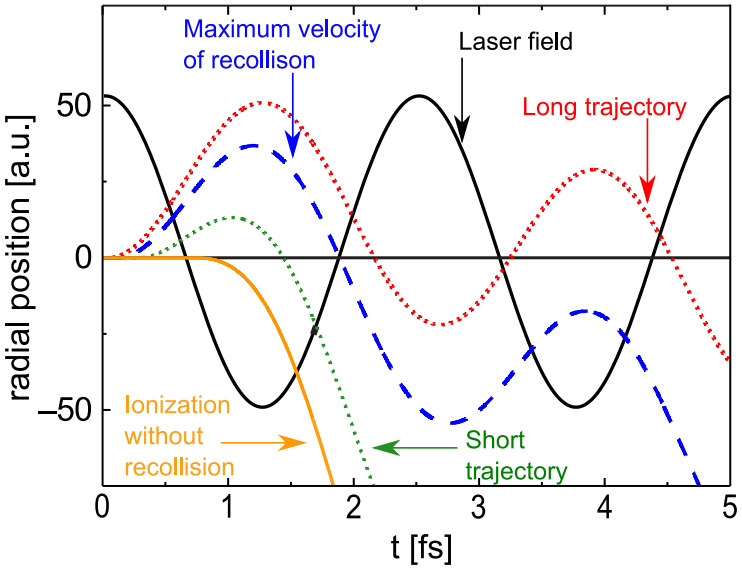

Figure 2.4.: Schematic illustration of different electron trajectories in the oscillating laser field after the tunnel ionization. The oscillating laser field is shown as black line, the different trajectories are shown in different colors. Figure adapted from Ref. [48].

ionization, or both absorb the needed amount of photons and follow the MPI path. On the other hand, non-sequential double ionization, as mentioned before, can be the outcome of an inelastic scattering event following tunnel ionization. If the electron returns to the ion carrying kinetic energy, this energy can be transferred to a second electron in an inelastic scattering process. As a result, the second electron can either be ionized directly [49,50] or be excited to a higher state, which enables tunneling or multiphoton ionization [51]. Another possible mechanism is that the first electron is recaptured by the nucleus and the spare energy is used to generate an intermediate state with two highly excited electrons . In the next laser cycle, the two electrons are liberated at the same time [52].

Enhanced ionization In the descriptions of strong-field ionization processes given above we did mostly not differentiate between the case of an atom or a molecule. Regarding molecules the topic can be more complex. The basic concept is the same: electrons can leave the parent molecule via tunneling or multiphoton absorption, the freed electron follows a certain trajectory, driven by the external field and under certain conditions recollision can occur. But there are some intrinsic differences between the ionization of molecules and atoms. E.g. the orientation of the molecule becomes important and the nuclear degrees of freedom can couple to the electron motion. Here, an effect is mentioned which highlights one special fundamental difference of atoms and molecules regarding strong-field ionization and which influences our Coulomb explosion imaging experiments (see chapter 3). The effect is called *Enhanced Ionization* (EI) (see for example [53–55]). It is illustrated for diatomic molecules that there exists a critical internuclear distance R_c, greater

than the equilibrium distance R_{eq}, at which the strong-field ionization probability of the molecule is highly increased. The critical distance can be reached if the molecule starts to dissociate e.g. following an ionization process. In a diatomic molecule, the binding potential of the outer valence electron along the internuclear axis is a double-well structure (see Fig. 2.5). At small core distances around R_{eq} or at large core distances $R \gg R_{eq}$ the effective Coulomb binding potential appears for the electron atomic-like. In the first case, the inner barrier between the two nuclei is very low, the ground state of the electron is located over the barrier (green, dotted line in Fig. 2.5). In the second case, on the other hand, the two wells are separated to a great extent, leading to nearly two independent atomic-shaped potentials [53] (dark blue, dashed line in Fig. 2.5). The condition for EI is in between. For an increasing internuclear distance R the barrier between the two wells increases and the electron gets localized at one of the two atoms. At the critical distance R_c the inner and the outer barrier reach a similar height (blue line in Fig. 2.5). Due to the Stark shift in the oscillating laser field the localized electronic state can be shifted above both barriers which highly increases the probability for the electron to leave the molecule. EI can be suppressed by controlling the polarization of the ionizing laser pulse with respect to the molecular axis [54]. In the case of a diatomic molecule, the double-well potential shown in Fig. 2.5 is only valid for a laser polarization along the axis connecting the two nuclei. For a linearly polarized laser field, with the polarization axis perpendicular to the molecular axis, the binding potential of the electron can be described as an atomic-like single well.

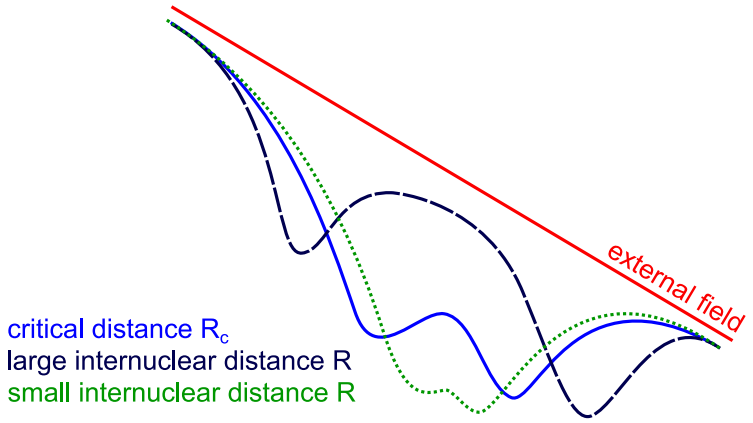

Figure 2.5.: Illustration of the potential energy curves of a diatomic molecule at different internuclear bond distances R under the influence of an external laser field. At a critical distance R_c enhanced ionization can occur. Figure adapted from Ref. [53].

It was proposed that enhanced ionization cannot only occur in a dissociating molecule, but also in the transition state region in a chemical reaction [10]. The transition state is difficult to observe. It is a transient state formed in a chemical reaction on the way from the reactants to the products. The reaction partners have to come in close vicinity for the reaction. The combined action of the laser field and the Coulomb potential of the forthcoming reaction partners leads to a suppression of the binding potential. It was claimed that the transient bond distances between the

reaction partners in the transition state are in the range of the critical distance of EI, an increased ionization probability in this area is expected. Hence, EI could act as a filter for the transition state, e.g. in following a chemical reaction via Coulomb explosion imaging.

2.2. Coulomb explosion imaging

Since valence electrons form the bonds of a molecule, multiple ionization can lead to strong deformations of the molecular electronic structure and geometry. In the extreme case of highly ionized molecules, all bonds can be destroyed. Due to the Coulomb interaction, the remaining isolated positively charged nuclei will repel each other, leading to an explosion of the molecule. The gained momenta of the ions in the explosion, are strongly dependent on the molecular geometry during the time that the electrons are stripped off since the Coulomb potential depends on the charge q of the ions and the distances $R_{i,j}$ between the single fragments. Hence, the gained momenta of the ions reflect the structure of the parent molecule and can be used to study the original geometry.

This technique, named *Coulomb explosion imaging (CEI)*, has its origin in fast ion beam experiments in the 1970s [56–59]. In this technique (singly-charged) ions are accelerated to a high energy of several MeV and sent through a thin foil. Due to the interaction with the foil, the valence electrons of the molecules get stripped off. The resulting highly ionized molecules undergo a Coulomb explosion and the momentum/kinetic energy of the created fragments is measured. The time scale of the stripping-process is in the range of 0.1 fs. The molecular structure can be considered frozen during the time of ionization. For diatomic molecules, the released energy of the two charged fragments mirrors the bond-length of the molecule. The shorter the bond lengths the higher the resulting momenta will be. Hence, measuring the resulting momenta of the Coulomb explosion can be used to study the geometry of the molecules. For example, Jordon-Thaden *et al.* used this technique to determine the extended internuclear separation of the two protons in the metastable H_2^- anion to be 6 a.u., in good agreement with theory [60].

For molecules consisting of more than two atoms, the gained momenta cannot be intuitively assigned to a molecular geometry, as it is possible for diatomic molecules. Instead of a potential curve depending on the distance of the two nuclei, a higher-dimensional potential energy surface describes the dynamics of the fragments. Nonetheless, the fragments carry information on the geometric properties as the two following examples show. Vager *et al.* induced the Coulomb explosion of CH_4^+ and measured the momentum vectors of the created five fragments in coincidence [58]. From the momentum information the authors obtained the structure of CH_4^+. In this way, the group could show that the ion geometry is distorted with respect to the neutral tetrahedral geometry due to a deformation caused by the Jahn-Teller effect[1]. As a second example, the differentiation between

[1] The Jahn-Teller effect [61] predicts a distortion of non-linear molecules with spatially degenerated molecular orbitals. The reduced symmetry leads to a energetically more favorable state of the molecule.

two enantiomers of the seven-atomic $C_2H_2D_2O$ molecule was performed by Herwig *et al.* using foil-induced Coulomb explosion imaging [62].

Besides sending accelerated ions through a foil, other approaches of inducing a Coulomb explosion exist. For example, molecules can be highly ionized with synchrotron radiation (see e.g. [63–65]), or with strong laser fields (see e.g. [10, 11, 14–16, 66]). In this thesis we work with laser-induced Coulomb explosion imaging. In Fig. 2.6 the process is schematically depicted. As introduced in section 2.1, short pulse lasers can create electric field strengths comparable to the valence electron binding energy, and thus multiply ionize a molecule. An important advantage of laser-induced Coulomb explosion is the possibility of conducting pump-probe experiments. With two laser pulses, separated by a time-delay, it is possible to first trigger a dynamic process in the molecule and probe the resulting dynamics with the second pulse via Coulomb explosion imaging. However, there are some important limitations to take into account.

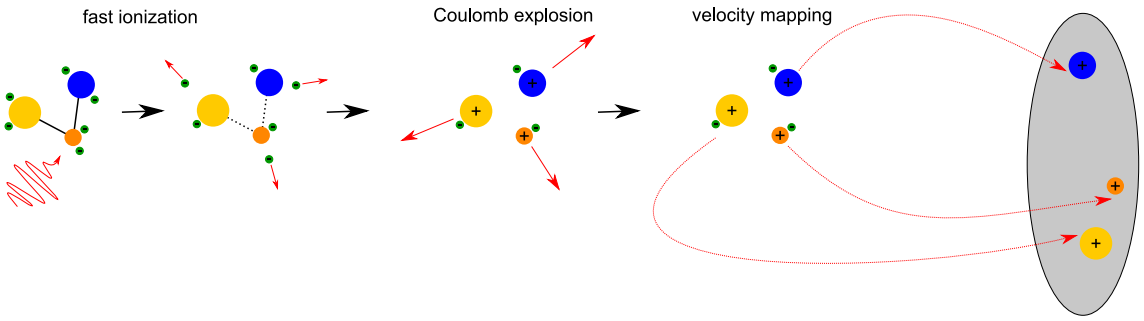

Figure 2.6.: The principle of Coulomb explosion imaging. The molecule is highly ionized in the strong laser field. The ionization is faster than the movement of the nuclei, hence the molecular structure can be regarded as frozen. After the ionization, the positively charged nuclei repel each other on a Coulomb potential. The exploding fragments are guided by electric fields to a time- and position-sensitive detector and are measured in coincidence.

The above described simple model of a pure Coulomb explosion neglects several influences on the fragmentation dynamics. Atoms in molecules are no point charges at frozen positions with no other interaction than the repulsive Coulomb potential. The first aspect to regard is that the nuclei are moving e.g. by excited vibrations or an interaction with the strong field. To avoid that the molecular geometry is changing during the ionization process, the laser pulses used to ionize the molecule should be shorter than the time-scale of the present dynamics. Lighter fragments require shorter pulses due to their faster movement. Légaré *et al.* showed that deviations in measured bond angles and lengths of the D_2O molecule from theoretical values are mainly caused by the movement of the nuclei during the ionization process - even when using ultra-short pulses of 8 fs pulse length [12]. For the heavier fragments of the molecule SO_2, which was also studied in Ref. [12], this effect was much weaker.

With shorter pulses it can also be ensured that enhanced ionization will not distort the measurement results. If the molecule preferentially ionizes at a certain bond

distance which is not the equilibrium distance, the measurement results are strongly biased. Légaré *et al.* detected a great difference in the kinetic energy of the fragments of D_2 in a Coulomb explosion, introduced with (i) 40 fs and (ii) 8 fs duration laser pulses [13]. The measured kinetic energy from ionization with the 8 fs pulses reached 75 % of the theoretically expected value, while for the 40 fs pulses the measurement led only to 33 % of the theoretical energy resulting from a Coulomb explosion of D_2. As the main reason for the dramatic shift in the kinetic energy for the 40 fs pulses, EI was identified. Fortunately, a lot of progress has been made in producing intense laser pulses with pulse lengths shorter than the typical time-scales of the nuclear motion (< 10 fs, see e.g. [67]).

Besides the aspect of time-scales in the ionization process, also the created charge state of the molecule has to be considered. Remaining inner shell electrons and valence electrons can lead to deviations from a pure Coulomb potential in the fragmentation. A change in the bond order due to the ionization process can create potential minima modifying the Coulomb potential. The result are discrepancies in the obtained molecular geometry. Corkum *et al.* investigated how severe the deviations are for a CEI experiment with highly charged iodine ions [68]. The authors calculated the potential curves for I_2^n, with $+2 \leq n \leq +6$, and discussed the molecular bond order and the resulting change in the equilibrium distance for these charge states of molecular iodine. Neutral iodine has a bond order of 1.0 and an equilibrium internuclear distance of 2.67 Å. The highest occupied orbital is an anti-bonding orbital. Hence, by removing two electrons the bond order for I_2^{2+} is changed to 2.0. The increase in the bond order leads to a shifted potential minimum and changed equilibrium distance of 2.5 Å despite the Coulomb repulsion of the two charged ions. By removing more electrons from the iodine molecule the bond order increases, and reaches a maximum for the four times charged molecule I_2^{4+} with the bond order of 3.0. Hence, for I_2^{4+} the greatest bond length contraction and the greatest deviation from the Coulomb potential appears. In Ref. [68] the deviation in the bond distance was determined to be $\Delta R \approx 0.5$ Å. The deviations decrease with an increase in the repelling Coulomb force for higher charge state. Hence, not only short laser pulses, but also high intensities are desirable.

The deviations in CEI experiments due to non-Coulomb potentials and non-stationary molecular structures are a drawback in this method. We will not reach the same precision with CEI as reached with classical spectroscopic methods, e.g. high-resolution rotational-vibrational-resolved Raman spectroscopy. However, CEI is not regarded as an alternative for spectroscopy, but rather as a new tool with a focus on imaging the structural change in molecular dynamics. In CEI experiments, no previous knowledge on the potential curves of the molecule is needed. The momentum calculation and geometry reconstruction relies only on the direct measured data in the experiment. In addition, the method is not state-selective. We do not need to find a specific transition in the probe-step, which is sensitive to a certain molecular change (in a traditional pump-probe experiment the created wave-packet is projected onto a certain final state in the probe step). The strong-field ionization of molecules and the Coulomb repulsion of charged particles are more general concepts. Hence, CEI is a promising and powerful technique to explore structural molecular changes which can not be easily

traced otherwise. This includes the transition state dynamics during a chemical reaction.

There are a variety of elaborate experiments, showing the great potential of laser-induced Coulomb explosion imaging, of which just a few are mentioned here. Matsuda *et al.* were able to follow a hydrogen migration process in deuterated acetylene with sub-10 fs laser pulses in a pump-probe experiment [15]. The pump pulse doubly-ionized C_2D_2 and the migration of one of the deuterium atoms away from the linear start geometry followed. With the strong probe pulse this process, which is on the time-scale of 60 fs, was followed using Coulomb explosion imaging. Pitzer *et al.* explored the five-atomic chiral molecule CHBrClF with CEI in a reaction microscope [16]. The authors were able to distinguish between the two stereoisomers of the molecule by measuring the full three-dimensional momentum vector of all created five ionic fragments in coincidence. Worth mentioning is also the work of Kunitski *et al.* [18], where the trimer $^4He_3$ was triply ionized and the resulting three fragments were measured in coincidence in a reaction microscope. The authors were able to detect the very elusive Efimov state of the molecule and could confirm the predicted bond lengths and structure of this special state.

It was further shown that partial Coulomb explosion can give already insight into the motion of molecules. Hansen *et al.* explored the torsional motion of the large molecule 3,5-difluoro-3',5'-dibromo-4'-cyanobiphenyl [69]. After aligning the molecule in the first step, a torsional motion was induced in the pump step with a so-called kick pulse. The torsion was probed with Coulomb explosion imaging by studying the recoil of only two fragments (F^+ and Br^+) for a varying delay between the kick pulse and the probe pulse. Partial CEI is also a tool to identify molecular alignment [70]. Larsen *et al.* probed the molecular alignment of 3,4-dibromothiophene and iodobenzene by detecting the recoil direction of specific fragments which are characteristic for the molecular axis [71,72]. It is expected that for experiments exploring the structural evolution in a chemical reaction including intermediate configurations around the transition state, insight into the dynamics can be obtained already from partial CEI.

2.3. Coincidence detection

To induce a Coulomb explosion, strong and short laser pulses are needed. At intensities exceeding $10^{15}\,\mathrm{W\,cm^{-2}}$ nearly all molecules or atoms in the focus get ionized. Hence, several types of processes will occur. In a Coulomb explosion imaging experiment, events of a specific molecular break-up with a complete detection of all created ions have to be filtered from the rest of the data set. The measured momenta of all fragments of a single molecule have to be correlated to obtain the structural information. Hence, it is not possible to integrate over many events since then the correlation is lost.

Coincidence detection is a method to filter specific events from a bigger data set. Coincidence in general means the chronological co-occurrence of special events, e.g, the detection of two ionic fragments with masses M_1 and M_2. By selecting only events with a certain outcome of products N ($N \geq 2$) arriving at the detector in a

short time span, even rare processes can be accessed by discarding the majority of processes not fulfilling the coincidence condition. In pulsed laser experiments one event is defined by all detected particles resulting from one single laser pulse.

Today, coincidence techniques are routinely used, e.g. in photoelectron-photoion-coincidence machines (PEPICO) [20], ion-ion-coincidence techniques [25], or in reaction microscopes (REMI) [73, 74]. The latter enables the measurement of the full three-dimensional momentum vector of all created fragments in coincidence. A technical challenge of these experiments is the suppression of false coincidences. A false coincidence would be for example the chronological co-occurrence of two ionic fragments, originating from two different diatomic molecules of the same type, e.g. in the following event:

$$2\,\mathrm{CO}^{2+} \rightarrow (\mathrm{C}^+ + \mathbf{O}^+) + (\mathbf{C}^+ + \mathrm{O}^+). \tag{2.12}$$

If only the two bold marked fragments are detected, the event is counted as true coincidence (Coulomb explosion of the CO molecule), although it is not. One approach to keep the occurrence of false coincidence small, is to lower the ionization rate[2]. To verify this statement, we follow the derivation for coincidence rates in Ref. [75] on the basis of the Poisson statistic.

We want to calculate under which conditions the ratio between true and false coincidences is maximized in a Coulomb explosion experiment of CO into two charged particles. Hence, only events are considered where the two fragments $\mathrm{C}^+ + \mathrm{O}^+$ are detected. The probability $p(n)$ to create n pairs of the two fragments with one laser pulse is described by the Poisson distribution:

$$p(n) \;=\; \frac{m^n}{n!}\mathrm{e}^{-m}, \tag{2.13}$$

where m is the average number of created $\mathrm{C}^+ + \mathrm{O}^+$ ion pairs. For each created single ion there is a certain detection probability $\xi_{\mathrm{O,C}} < 1$. The detection probability is influenced for example by the detection efficiency of the microchannel plate detectors. The probability to detect k ions of one species if n ions of this species are resulting from the laser interaction can be calculated by the binominal distribution:

$$p_{\mathrm{O,C}}(n,k) \;=\; \binom{n}{k} \xi_{\mathrm{O,C}}^k \,(1-\xi_{\mathrm{O,C}})^{n-k}. \tag{2.14}$$

Combining Eq. (2.13) and (2.14) gives the probability to detect exactly one ion of each species:

$$\begin{aligned} P_{\mathrm{O+C}}(n) \;&=\; \sum_{n=0}^{\infty} p_{\mathrm{O}}(n,1)\, p_{\mathrm{C}}(n,1)\, p(n) \\ &=\; \xi_{\mathrm{O}}\xi_{\mathrm{C}} m \times [1 + m(1-\xi_{\mathrm{O}})(1-\xi_{\mathrm{C}})] \times \exp\left[-m + m(1-\xi_{\mathrm{O}})(1-\xi_{\mathrm{C}})\right] \\ &=\; P_{\mathrm{O+C}}^{\mathrm{true}}(n) + P_{\mathrm{O+C}}^{\mathrm{false}}(n). \end{aligned} \tag{2.15}$$

[2]The ionization rate is defined as the number of ionized molecules per laser pulse.

Here, it is summed up over all possible numbers n of produced ion-ion pairs. $P_{\mathrm{O+C}}(n)$ includes all coincidence events, true and false ones. If there are n ion-ion pairs created, the probability to detect two ions from the same molecule is $1/n$. Hence,

$$\begin{aligned} P^{\mathrm{true}}_{\mathrm{O+C}}(n) &= \sum_{n=0}^{\infty} \frac{p_{\mathrm{O}}(n,1)\, p_{\mathrm{C}}(n,1)\, p(n)}{n} \\ &= \xi_{\mathrm{O}}\xi_{\mathrm{C}} m \times \exp\left[-m + m(1-\xi_{\mathrm{O}})(1-\xi_{\mathrm{C}})\right] \end{aligned} \tag{2.16}$$

follows. The number of false coincidences is the difference between all coincidences and true coincidences:

$$\begin{aligned} P^{\mathrm{false}}_{\mathrm{O+C}}(n) &= P_{\mathrm{O+C}}(n) - P^{\mathrm{true}}_{\mathrm{O+C}}(n) \\ &= \xi_{\mathrm{O}}\xi_{\mathrm{C}} m^2 \times (1-\xi_{\mathrm{O}})(1-\xi_{\mathrm{C}}) \times \exp\left[-m + m(1-\xi_{\mathrm{O}})(1-\xi_{\mathrm{C}})\right]. \end{aligned} \tag{2.17}$$

Interesting to notice in Eq. (2.17) is that for a 100 % detection efficiency ξ_{O} or ξ_{C} the number of false coincidences is zero. Due to the coincidence condition all events which do not contain exactly the two wanted ion species are discarded. The left panel in Fig. 2.7 shows the distribution of all coincidences (black), true coincidences (blue), and false coincidences (red) as a function of the average number of created ion pairs per laser pulse. The maximum amount of true and false coincidences is reached for different numbers m. In the right panel of Fig. 2.7 the ratio between the true coincidences and all coincidences is plotted. It decreases with the increase of m. The red dotted line marks the point $m = 1$, with in average one ionized molecule per laser pulse. For this ionization rate the ratio $P^{\mathrm{true}}_{\mathrm{O+C}}/P_{\mathrm{O+C}}$ is around 0.8.

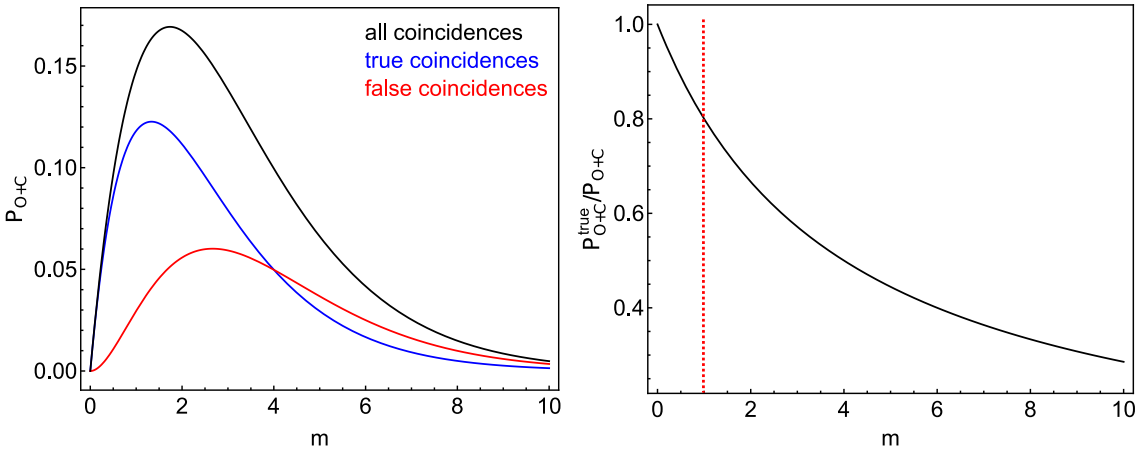

Figure 2.7.: Left: The distribution of all coincidences (black), true coincidences (blue), and false coincidences (red) for the detection of two ions ($C^+ + O^+$) resulting from a break-up of a doubly-charged diatomic molecule (CO^{2+}) as a function of the average number m of created ion pairs per laser pulse. Right: The ratio between true coincidences and all coincidences for the distributions of the right panel. The red, dotted line marks the case, where in average one ion pair is created per laser pulse.

Momentum sum filter In the Coulomb explosion coincidence experiment conducted in this thesis in chapter 3, we do not only record the occurrence of coincidences between ionic fragments, but also the three-dimensional momentum distribution of all ionic fragments. The momentum information gives access to a sophisticated method to discard false coincidences due to the inherent property of momentum conservation. Since the intact neutral parent molecule has a zero momentum in the molecular frame, the three-dimensional momentum sum of all resulting fragments from the laser-molecule interaction has to be zero as well. Applying this condition to the pre-selected (right and false) coincidence events is an additional tool to increase the ratio of single-molecule events over false coincidences. The procedure is explained in detail in chapter 3 on the basis of coincidence data gained in an experiment using a reaction microscope to study the break-up dynamics of CH_2BrI^{3+} into three charged fragments.

Filtering on the momentum sum of all created ionic fragments opens the way to an increase of the ionization rate in the measurement, too. In experiments where on average two or more molecules are ionized within the same laser pulse, the coincidence condition to keep only events with a certain number of detected ions has to be omitted. A post-detection analysis of the momentum sum of all combinations of measured ionic fragments could afterwards provide the right coincidences. However, what has to be considered is that for increasing ionization rates, all possible combinations of fragments have to be tested for their momentum sum. For a number of m ionized molecules per laser pulse with q fragments per molecule, this means m^q combinations. Hence, for an experiment as conducted in chapter 3, where the three-body fragmentation of CH_2BrI^{3+} is studied, this leads to 1000 combinations for an ionization rate of in average $m = 10$ ionized molecules per laser pulse. This brings up the question if the saved time in taking the data due to an increased ionization rate is counterbalanced by an increased time in the data processing. In the Coulomb explosion coincidence experiment in chapter 3 the ionization rate was kept low: at around three ionized molecules per 10 laser pulses.

2.4. Impulsive stimulated Raman scattering

The excitation of vibrational or rotational modes in a molecule due to an inelastic scattering of photons is referred to as *Raman scattering* or *Raman effect*. It was already described in 1923 by Smekal [76] and first detected by Raman and Krishnan in liquids [77]/Landsberg and Mandelstam in crystals [78], both in 1928. Photons can be scattered elastically in their interaction with a molecule, hence no energy is transferred. The outgoing photon has the same wavelength as the incoming which is referred to as Rayleigh scattering. On the other hand, there is the possibility of an inelastic process, both, with energy transferred from the photon to the molecule and from the molecule to the photon. The first case describes a Stokes-scattering process, the second case an Anti-Stokes-scattering process. The scattering of the photon can be described as an absorption process, where the molecule is excited to an intermediate virtual state. By emitting a photon of another wavelength, the molecule ends up in a different final state. If the molecule was in the ground state

before, with the inelastic scattering process vibrations or rotations can be induced (Stokes-scattering). The different scattering mechanisms are schematically depicted in Fig. 2.8.

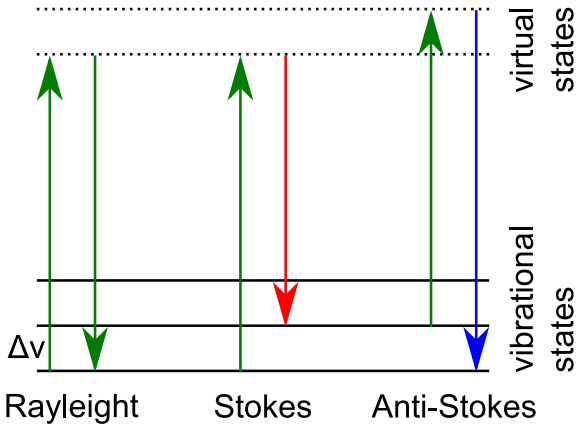

Figure 2.8.: Schematic picture of a Raman scattering process. In the Rayleigh case, the photon is scattered elastically with no energy transferred to the molecule. The Stokes and Anti-Stokes scattering are both inelastic processes. In the first case, energy is transferred from the light field to the molecule. In the second case, the light field gains energy from the molecule.

The main scattering of photons by molecules is Rayleigh scattering, the inelastic processes of Stokes-/Anti-Stokes-scattering take place spontaneously. However, it is possible to convert the spontaneous process into a stimulated process and, by this, increase the inelastic scattering probability. To stimulate the process two narrow-band lasers whose frequency difference matches the frequency difference between two vibrational (rotational) states in the molecule ($\Delta\nu$ in Fig. 2.8) can be used. This mechanism is referred to as stimulated Raman scattering. However, the process can also be stimulated with a single pulse of an ultrahort broad-band laser, which is referred to as impulsive stimulated Raman scattering (ISRS). The condition for a stimulated process is that in the broad-band pulse two photons have to be present at the same time, matching the wavelength of the absorbed and emitted photon in the Raman description. Since the intermediate state is a virtual state, the absolute values of wavelengths are not crucial, but only the difference in the photon energy. This difference has to match the difference $\Delta\nu$ in the molecule. At the same time the pulse length of the laser has to be short compared to the oscillation period of the vibrational or rotational mode.

The mathematical description of a stimulated impulsive Raman scattering process can be formulated based on the concept of a classical harmonic oscillator with an external impulsive force due to the electric field of the short laser pulse. The equation of motion for the normal coordinate Q along the polarization axis of a linear excitation laser pulse:

$$\frac{\partial^2 Q}{\partial t^2} + 2\gamma\frac{\partial Q}{\partial t} + \omega_0^2 Q = F(t) \tag{2.18}$$

contains the damping constant γ, the vibrational frequency ω_0, and the driving force $F(t)$. The latter can be obtained from the gradient of the potential energy of a molecule $E_\mathrm{P} = -1/2\hat{\alpha}\vec{E}\vec{E}$, where $\hat{\alpha}$ is the polarizability tensor and $\vec{E}$ is the electric field. Assuming a linearly polarized laser pulse along the normal coordinate Q of the Raman active molecular vibration and a wavelength of the vibration which is much longer than the wavelength of the laser leads to [79]:

$$\frac{\partial^2 Q}{\partial t^2} + 2\gamma\frac{\partial Q}{\partial t} + \omega_0^2 Q = \frac{1}{2}\frac{\partial \alpha}{\partial Q}E^2(t). \tag{2.19}$$

Here, $\partial\alpha/\partial Q$ is the change of the polarizability along the respective normal coordinate and $E(t)$ the electric field of the laser. The high frequency term in the squared electric field

$$E^2(t) = E_0^2(t) \underbrace{\cos^2\left[\omega_L t + \phi\right]}_{\text{high frequency term}}, \tag{2.20}$$

where ω_L is the central frequency of the laser pulse, leads to a factor 1/2 in the time average and is not responsible for the executed impulsive force. With a gaussian-shaped laser pulse

$$E_0(t) = E_0\,\mathrm{e}^{-2\ln 2\,\frac{t^2}{\tau^2}}, \tag{2.21}$$

where τ is the laser pulse duration and E_0 is the amplitude of the electric field, the combination of Eq. (2.19) and (2.20) leads to:

$$\frac{\partial^2 Q}{\partial t^2} + 2\gamma\frac{\partial Q}{\partial t} + \omega_0^2 Q = \frac{1}{4}\frac{\partial \alpha}{\partial Q}E_0^2(t) = \frac{1}{4}\frac{\partial \alpha}{\partial Q}E_0^2\,\mathrm{e}^{-4\ln 2\,\frac{t^2}{\tau^2}}. \tag{2.22}$$

The differential equation (2.22) can be solved using the Green's function approach [79], which leads to:

$$Q(t) \propto \exp\left[-\frac{\omega_0^2\tau^2}{16\ln 2}\right]\sin\left[\omega_0 t\right]. \tag{2.23}$$

From Eq. (2.23) it can be seen that (i) the force due to the laser pulse excites a vibrational motion with frequency ω_0 and (ii) for a non-vanishing amplitude the pulse duration τ of the laser has to be short compared to the oscillation period of the vibration.

In chapter 4 the ν_3 vibration in N_2O_4 is excited via an ISRS process. The oscillation period is $T = 130\,\mathrm{fs}$ and the oscillation frequency is $f_0 = 7.7\,\mathrm{THz}$. Hence, the pulse length of the excitation laser has to be small compared to 130 fs. The short pulse length can also be motivated by the requirement of having two photons with a difference in frequencies $\Delta f = 7.7\,\mathrm{THz}$ in the laser pulse. The bandwidth of a laser pulse and hence, the possibility of finding two matching photons can be estimated

from the pulse length τ. The relation:

$$\Delta f \, \tau \geq c_B \tag{2.24}$$

describes the Fourier-limited pulse duration τ, depending on the bandwidth of the laser Δf and the scaling factor c_B. For gaussian-shaped pulses the scaling factor becomes $c_B = 0.441$. Hence, to reach a bandwidth of $\Delta f = 7.7\,\mathrm{THz}$, a laser pulse duration of $\tau < 57\,\mathrm{fs}$ is needed.

3 Chapter 3. Sequential and non-sequential pathways in the Coulomb explosion of CH_2BrI^{3+}

3.1. Introduction

Molecules in laser fields with field strengths exceeding the molecular bond strengths undergo a variety of extreme dynamics as discussed in chapter 2. Multiple ionization can occur, where more than one electron is removed from the neutral molecule due to tunnel ionization or multiphoton ionization (see section 2.1). Since electrons are responsible for the molecular bonds this leads to bond breaking and the fragmentation of the parent molecule in several charged particles. Each of the resulting possible break-up channels leads to an individual distribution of the final momenta of the created ionic fragments. Hence, by measuring the momentum distribution of the ions, the channels can be separated and explored individually. A well-suited technique to measure the final momentum distribution is laser-induced Coulomb explosion imaging (CEI) in combination with coincident detection of the time-of-flight of the ions and the impact point on the detector (see sections 2.2 and 2.3). The combination of the temporal and spatial distribution allows the reconstruction of the full three-dimensional momentum vector of the reaction products. From the momentum information, conclusions on the pathway and the fragment-specific kinetic energy distribution are gained.

The fragmentation process of a polyatomic highly charged molecule is known to occur in different ways: (i) in a non-sequential direct Coulomb explosion, or (ii) in a sequential Coulomb explosion. In the first process, all bonds are broken in one step and the final ions are created on a faster time-scale than the motion of the nuclei takes place. Depending on the mass of the atoms in the molecule this time-scale is in a range of a few fs to several tens of fs. Data from molecules fragmenting in the non-sequential pathway is typically used to study the geometry of the neutral molecule or molecular dynamics [10]. A careful selection of the data from the direct Coulomb explosion channel would be the basis for designing an experiment, in which the technique of laser-induced Coulomb explosion is used as probe mechanism to record a movie of molecular dynamics in a pump-probe experiment.

For an exact reconstruction of the molecular structure, the created ionic fragments would have to behave like instantaneously created point charges repelling each other on a pure Coulomb potential. In a molecular break-up, these conditions are typically

not fully met, see for example Ref. [13,15,68]. The ionization process is not instantaneous. The molecules are exposed to the strong field at least for the duration of the laser pulse. It is possible that the molecule is first singly or doubly ionized and the atoms start already moving before all bonds are broken completely. Furthermore, the ionic fragments can often not be regarded as point charges. If the fragments are not atomic ions, but bigger ionic fragments consisting of several atoms, there is a certain charge distribution. And additionally, there can be deviations from a pure repelling Coulomb potential, e.g. due to a change in the bond order caused by the ionization. The mechanisms, which distort a CEI measurement, have been discussed in detail in section 2.2. Nevertheless, it was shown that the momenta gained from a Coulomb explosion channel can give insight into the geometry of the molecule and its chirality [12,14,16,18,80,81] and in dynamical processes, like photodisscociation, isomerization, or torsional motion [13, 15, 69, 82–85].

In a sequential process, contrary to a direct non-sequential Coulomb explosion, one of the final created ions is released first and the other reaction products follow after a certain time delay, clearly distinguishable on the time-scales of the experiment. The process of a sequential fragmentation has been a widely explored topic in the last years [86–107]. The research field benefits greatly from the development of detectors capable of measuring the three-dimensional momentum distribution of ionic fragments, which enables to separate between sequential and non-sequential channels due to the different final momentum distribution of the ionic fragments. The sequence of bond breaking in a sequential process proceeds via an intermediate metastable cation state. Part of the energy is transferred to rotational energy of the intermediate. Hence, the intermediate starts rotating after the first bond cleavage. The lifetimes of these intermediates often exceed one rotational period. The final singly-charged fragments, created from the break-up of the intermediate, are released homogeneously within a solid angle of 4π with respect to the first leaving particle. On the other hand, there exist short-lived intermediate states, as newly discussed in Ref. [86], which start to dissociate directly after the first bond cleavage (i.e. within one rotational period). In this case, there is a transition from a slightly asynchronous cleavage of both bonds to the point of a clear sequential fragmentation.

The most of the here cited works focus on the sequential fragmentation of three-atomic molecules with two indistinguishable bonds (such as CO_2^{3+}). Synchrotron radiation [99], heavy ion [90,96] or electron impact [92,93,108] or femtosecond laser pulses [94, 95, 97, 98, 101, 102, 104] are used to create the multiply charged ions. In addition, asymmetric processes for higher charged three-atomic molecules have been studied e.g. the breakup of CO_2^{q+} ($q = 4, 5$) [96] or CS_2^{4+} [99]. Here, it is possible to distinguish between the different final ionic fragments due to their different charge, although in the parent neutral molecule both bonds are the same. For more complex polyatomic molecules there is often a multitude of possibilities for the molecule to fragment into several charged particles. Examples are the detailed study on the fragmentation dynamics of inner-shell ionized difluoroiodobenzene isomers [64], where the authors detected different fragmentation mechanisms for the tri-cation, the investigation of the three-body-breakup of 1,3-butadiene [105], where three different channels with each four fragmentation pathways exist, and the study on the fragmentation dynamics of the doubly, triply and four times charged OCS molecule

following electron impact ionization with fragmentation via different sequential and non-sequential pathways [93]. However, it is still challenging to reach a full picture of the bond breakage and fragmentation dynamics in polyatomic molecules and the topic is of continuous interest. Depending on the ionization process, the input energy and mostly the molecule itself, the different pathways, their occurrence ratios, and the gained kinetic energy vary.

In this thesis, we studied the three-body fragmentation dynamics of triply-charged bromoiodomethane with laser-induced Coulomb explosion imaging in a reaction microscope. Bromoiodomethane is a molecule of the group of dihalomethanes, where two hydrogen atoms of the methane molecules are replaced by one bromine and one iodine atom. The fundamental properties of bromoiodomethane, like structural parameters, bond strengths, and the ionization potential are given in Tab. 3.1. Bromine occurs in two stable isotopes with nearly the same probability: 51 % ^{79}Br and 49 % ^{81}Br. Hence, bromoiodomethane exists with the masses 220 u and 222 u. All given parameters or calculated results in the thesis are for the case of the lighter bromine isotope ^{79}Br.

Dihalomethanes are of high interest, e.g. in the environmental research, since these natural components in the atmosphere and the ocean are sources for free halogen atoms or radicals, produced by absorbing UV light. Furthermore, CH_2BrI is a prototype system for conducting bond-selective chemistry where the C-I or the C-Br bond can be addressed selectively [85, 110, 112, 113]. In this chapter, we investigate the different fragmentation processes of CH_2BrI^{3+}, where (i) both, the C-I and the C-Br bond, are broken simultaneously, (ii) the C-I bond is broken first and an metastable intermediate CH_2Br^{*2+} is created, (iii) the C-Br bond is broken first and an metastable intermediate CH_2I^{*2+} is created:

$$\begin{aligned} &\text{(i)} \quad CH_2BrI^{3+} \rightarrow CH_2^+ + Br^+ + I^+ \\ &\text{(ii)} \quad CH_2BrI^{3+} \rightarrow CH_2Br^{*2+} + I^+ \\ &\text{(iii)} \quad CH_2BrI^{3+} \rightarrow CH_2I^{*2+} + Br^+. \end{aligned}$$

One fundamental question of our research was, if the measured momenta of the direct fragmentation (i) reflect the geometry of the molecule. Further, we wanted to explore, if both possible sequential break-up sequences (ii) and (iii) of CH_2BrI^{3+} are detectable and distinguishable. Additionally, we wanted to estimate the time-scale of the lifetime of the intermediate fragment and explore how the kinetic energy distribution of the final fragments changes in the different processes. With this

bond length [Å]		angle [°]		energy [eV]	
C-Br	1.9261	αBrCI	113.53	C-Br	2.99
C-I	2.1313	αHCH	107.66	C-I	2.04
C-H	1.0830	αBrCH	107.27	IP	9.62

Table 3.1.: Structure parameters [109], bond energies [110], and ionization potential [111] of CH_2BrI.

perspective, we wanted to develop a full picture of the three-body fragmentation of bromoiodomethane as basis for further studies on bond-selective reaction dynamics of CH_2BrI in a pump-probe experiment with CEI as probe mechanism.

This chapter is organized as follows. First, the experimental details, including a description of the momentum determination are given. Next, a general characterization of the different fragmentation channels, depending on the final ions, is given. Afterwards, the data selection for coincidence conditions is depicted and the three-body break-up process into I^+, Br^+, and CH_2^+ is analyzed in full detail. There are two different key aspects: the direct non-sequential Coulomb explosion and the different sequential fragmentation pathways with the intermediate cations CH_2Br^{*2+} and CH_2I^{*2+} .

3.2. Experimental details

3.2.1. Reaction microscope

The measurement was done with a home-built reaction microscope (REMI) [114]. A good overview of the REMI technique and the perspective of experiments designed for it can be found in Ref. [74]. Here, a short introduction to the technique is given. A schematic depiction of the general design of a reaction microscope is shown in Fig. 3.1 on the right-hand side. On the left-hand side of Fig. 3.1 a CAD drawing of the actual design, taken from Ref. [114] is shown. A neutral supersonic molecular beam is crossed with a projectile beam which ionizes the neutral molecules and induces a reaction. We used a short-pulse laser beam to photo-ionize the molecular target. The interaction region is placed in a stack of electrodes, generating a weak electric field. At the same time a pair of Helmholtz coils, surrounding the reaction microscope, is generating a weak homogeneous magnetic field. Due to the influence of the external electric and magnetic fields, the generated ions and electrons are projected onto two detectors placed on top and bottom of the interaction zone. The ions are mainly influenced by the electric field and guided downstream to the ion detector. Due to their heavy mass, the influence of the magnetic field can be neglected. Electrons are lighter and are generated with a reasonably higher velocity than the ions. The magnetic field which forces the electrons on a helix-shaped trajectory increases the number of electrons reaching the active area of the detector. With the combination of electric and magnetic fields, the REMI detects electrons as well as ions within a solid angle of nearly 4π[1].

The ion and the electron detector are each a combination of an MCP stack with a delay-line readout system (RoentDek [115]). From the detector signal the time-of-flight and the impact position on the detector in the x- and y-direction for every single ion or electron is determined, enabling the calculation of the full three-dimensional momentum vector of the measured fragments. For the following analysis, a coordinate system is used with the negative x-axis parallel to the direction of the molecular beam, the y-axis parallel to the laser beam and the z-axis pointing

[1] There are some limitations, e.g. on the kinetic energy of the particles and the electric field of the spectrometer, which can reduce the solid angle.

towards the ion detector. In this work, only the data collected with the ion detector are considered, since no additional information could be gained from the electron momenta.

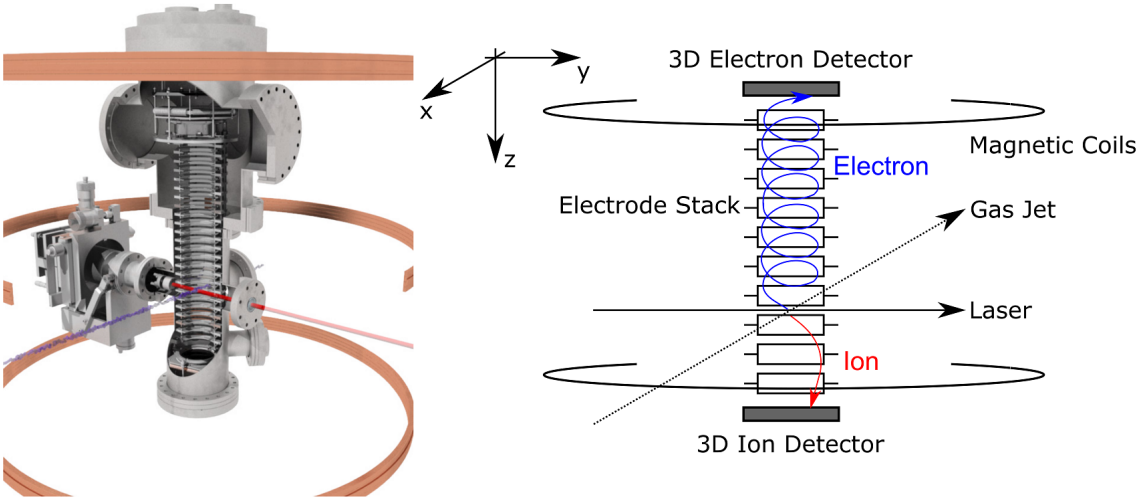

Figure 3.1.: Left: CAD drawing of the actual design of the reaction microscope (taken from Ref. [114]). Right: Schematic drawing of the reaction microscope. The neutral gas jet is overlapped with the laser inside a stack of electrodes creating a homogeneous electrostatic field. Generated positively charged ions are guided downstream to the ion detector. The respective electrons are guided upstream to the electron detector by the electric field of the electrode stack and the magnetic field generated by the coils.

3.2.2. Measurement conditions

In the measurement, a molecular beam of $\approx 0.01\,\%$ CH_2BrI seeded in helium was expanded into the vacuum system through a small nozzle ($d = 10\,\mu m$) in a supersonic expansion (stagnation pressure 1 bar). In the chamber the molecular beam was overlapped in the interaction region with the output of a Titanium:Sapphire chirped-pulse amplified laser system (Amplitude Systems). The central wavelength of the laser was 795 nm with a pulse duration of 25 fs and a pulse energy of 2 mJ. The pulse energy was reduced in the experiment to 11.8 µJ/pulse using an polarizing attenuator. We characterized and optimized the pulse length via the SPIDER technique (Spectral Phase Interferometry for Direct Electric-field Reconstruction). The repetition rate of the laser was 10 kHz. The laser beam was focused at the interaction zone by a spherical mirror ($f = 80\,mm$) placed inside the vacuum chamber and crossed with the molecular beam. At the position of the focus, a peak intensity of around $1 \times 10^{15}\,W\,cm^{-2}$ was reached[2]. After ionization by the laser pulse, the resulting charged particles were accelerated by static electric and magnetic fields to

[2]The intensity was estimated from the beam diameter in front of the focusing mirror ($d = 7.5\,mm$) and the measured average power $P = 118\,mW$ (11.8 µJ/pulse).

either the ion or the electron detector, depending on their charge. We adjusted the measurement conditions (concentration of CH_2BrI in the molecular beam and the intensity of the laser) to receive around three detected ions out of ten laser pulses. From this count rate the probability for ionizing N molecules per laser pulse can be calculated via the Poisson distribution to

$$\begin{aligned} P_{N=1} &= 6.1\,\% \\ P_{N=2} &= 0.6\,\% \\ P_{N=3} &= 0.05\,\%. \end{aligned}$$

Hence, the probability of ionizing more than one molecule is $\approx 10\,\%$ of all ionization events[3]. This fraction of ionization events can lead to false coincidences if fragments from each molecule are detected.

3.2.3. Time-of-flight calibration

The data processing is based on an event-by-event based analysis, meaning that after the measurement each detected ion and each event can be addressed separately in the data analysis. One event refers to all detected ions, resulting from one single laser pulse. With this technique, even rarely occurring processes can be individually selected and investigated.

The first step in the data analysis is the calibration of the time-of-flight spectrum. The real time-of-flight t deviates from the measured time-of-flight t_m by an initially unknown value t_0 ($t = t_m - t_0$). There is a delay in the signal recording due to the cables, connecting the detector with a time-to-digital converter (TDC). Considering a uniform acceleration in the electric field the time-of-flight $\mathrm{t}_{(p=0)}$ for fragments with no initial momentum can be derived by

$$t_{(p=0)}\,(m) = \sqrt{\frac{2dm}{qE}}, \tag{3.1}$$

where E is the electric field strength, d is the distance to the detector, m the mass of the particle, q the particle charge, and $qE/m = a_z$ is the acceleration in the electric field. By inserting $t = t_{(p=0)} = t_m - t_0$ in Eq. (3.1), t_0 can be determined by two well-known mass peaks in the measured time-of-flight spectrum, e.g. the parent molecule (220 u) and the water peak (18 u) via

$$t_0 = \frac{\sqrt{m_1}\,t_2 - \sqrt{m_2}\,t_1}{\sqrt{m_1} - \sqrt{m_2}}, \tag{3.2}$$

and is used to calibrate the spectrum.

[3]This probability is an upper limit. The estimation is made, that one detected ion corresponds to one ionized molecule since single ionization is expected to be the preferential process. However, ionizing one molecule can lead to to several detected ions. Hence, the real number of ionized molecules per laser pulse is lower.

3.2.4. Momentum calculation

For the momentum calculation in the z-direction, the static electric field accelerating the ions to the detector and the calibrated time t have to be taken into account. The magnetic field of the coils points towards the z-direction. Hence, it only influences the x- and y-components of the particle's trajectory since the Lorenz force is the cross product of the particle's velocity vector and the magnetic field vector. Additionally, also in x- and y-direction the force from the magnetic field on the ions is so small, that it can be neglected in all calculations [114]. Including an initial velocity v_0 in the z-direction through the momentum gained in the fragmentation process leads to

$$d = \frac{1}{2}a_z t^2 + v_0 t. \tag{3.3}$$

Hence, the time t can be calculated via

$$t = -\frac{v_0}{a_z} + \sqrt{\left(\frac{v_0}{a_z}\right)^2 + \frac{2d}{a_z}} \tag{3.4}$$

$$t = -\frac{v_0\, m}{qE} + \sqrt{\left(\frac{v_0\, m}{qE}\right)^2 + \frac{2md}{qE}} \tag{3.5}$$

$$t = -\frac{p_z}{qE} + \sqrt{\left(\frac{p_z}{qE}\right)^2 + \frac{2md}{qE}}, \tag{3.6}$$

resulting in

$$0 = -p_z + \sqrt{(p_z)^2 + \left(t_{(p=0)} qE\right)^2} - t\, qE = f(p_z). \tag{3.7}$$

To solve Eq. (3.7) Newton's method was used [116]. The values for $t_{(p=0)}$ are gained from the calibrated time-of-flight spectrum. From Eq. (3.7)

$$p_{z,n+1} = p_{z,n} - \frac{f(p_{z,n})}{f'(p_{z,n})} \tag{3.8}$$

is repetitively calculated until the difference between $p_{z,n}$ and $p_{z,n+1}$ becomes negligible.

The momenta in the x- and y-direction are gained from the impact positions on the detector and the calibrated time-of-flight t. There is no acceleration along the x- and y-direction, hence the momentum can be calculated on basis of a uniform motion:

$$p_x = m\frac{x}{t}, \tag{3.9}$$

where x is calculated from the measured position x_m and the zero position $x_{(p=0)}$

($x = x_m - x_{(p=0)}$) for each mass. The shift $x_{(p=0)}$ is resulting from an initial momentum of the ions due to the initial velocity of the molecular beam. It is determined for each mass from the measured spatial distribution in the x-direction at the flight time $t_{(p=0)}$. The calculation for p_y is identical.

3.3. Overview of different fragmentation pathways

All following data which are shown, are the outcome of an eight hours measurement where approximately 290×10^6 laser pulses led to 50×10^6 events and 65×10^6 detected ions. This corresponds to an event rate of 1.7 kHz. The measurement was performed by my colleagues Friedrich Freyse and Felix Schell, the following data analysis and interpretation was performed by myself.

First, the time-of-flight spectrum of all events, which is shown in Fig. 3.2 in a histogram, is analyzed. The spectrum contains contributions from a lot of different ions which will be explained in detail in the next paragraph. Peaks resulting from the ionization of a complete molecule or an atom from the molecular beam, e.g. the helium peak, have a sharp distribution. Peaks resulting from the background gas or from a break-up process have a broader time-of-flight spread. In the case of an ionization event from the background gas, the time-of-flight spread is due to the isotropic velocity distribution of molecules in the residual gas. In the case of ions from a fragmentation, the time-of-flight spread is due to the kinetic energy release during the fragmentation.

For a first assignment, it is guessed, which contributions are with a high probability in the spectrum. These are lighter ions from the background gas, like H^+, H_2^+ and H_2O^+ since these gases are typically left in the residual gas in a high vacuum system. Additionally, we expect to detect He^+ from the molecular beam and the singly-charged parent ion, since the ionization probability for n times ionizing an atom or molecule decreases with the number n. The lighter ions with masses 1 u, 2 u, 4 u, and 18 u are assigned to the peaks with the smallest time-of-flight in the spectrum. It has to be noticed that on top of the broader peaks from the background gas, a sharp spike is visible (most pronounced for H_2O^+). Since sharp peaks are coming from the defined velocity in the molecular beam, the beam contains impurities. The singly-charged parent ion is assigned to the sharp peak with the double peak structure at the right end of the spectrum. Since bromine occurs in two stable isotopes with nearly the same probability (51 % ^{79}Br, 49 % ^{81}Br) the parent ion as well as fragments including a bromine ion appear as double peak structure in the time-of-flight spectrum.

The conversion from the time-of-flight axis to the mass axis and vice versa is done

via the calculation (see Eq. (3.1))

$$m_i = \left(\frac{t_i - t_0}{k_0}\right)^2 \qquad \text{with} \tag{3.10}$$

$$k_0 = \sqrt{\frac{2d}{qE}}, \tag{3.11}$$

where the index i denotes a certain ion mass. The time shift t_0 was determined via Eq. (3.2) with the assignment of the hydrogen peak, the water peak, the helium peak and one of the parent ion peaks (220 u). t_0 was calculated for all combinations m_i and m_j of these four masses and measured flight times and the average value was used for further calculations. The parameter k_0 was determined with the measured time-of-flight t_{H_2O} of the water peak via Eq. (3.10). With the determined values of $t_0 = 29.0\,\text{ns}$ and $k_0 = 1029.9\,\text{ns}\,\text{u}^{-1/2}$, the flight times of several fragments were calculated. These are listed in Tab. 3.2. The listed numbers are the time-of-flights for the respective fragment with no additional momentum in the z-direction from a fragmentation.

Besides the peaks used for the calculation of the mass axis, several fragments of the parent, as well as the doubly-charged parent itself and further peaks resulting from ions from the background gas are in the spectrum. The doubly-charged parent has a flight time of $\approx$ 10 800 ns and can be identified by the same sharp double peak structure as the singly-charged parent. Fragments resulting from a two-body break-up process like CH_2Br^+ ($+\,I/I^+$) at around 9900 ns and CH_2I^+ ($+\,Br/Br^+$) at around 12 200 ns as well as their doubly-charged equivalent are present. This

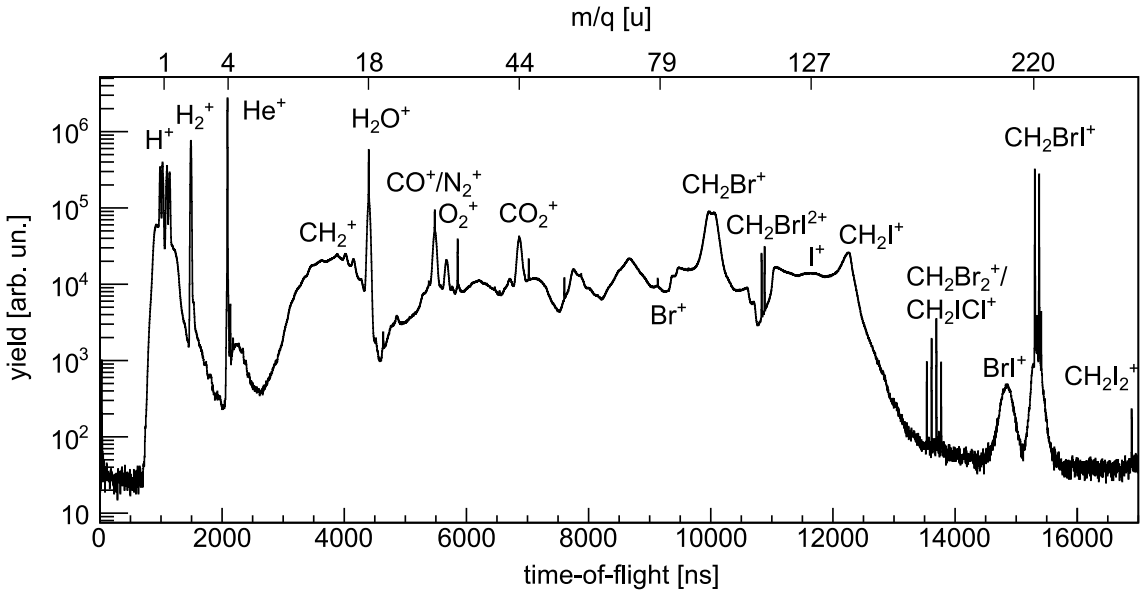

Figure 3.2.: The time-of-flight spectrum of all events in a histogram. Peaks resulting from the fragmentation of the parent molecule show a broad kinetic energy distribution. Non-fragmenting peaks from the molecular beam are sharp.

work focuses on the three-body break-up with the three ions CH_2^+, Br^+, and I^+. The peaks of CH_2^+ and I^+ are located at flight times around 3900 ns and 11 600 ns and clearly detected in the time-of-flight spectrum as broad peaks. The peak of Br^+ around 9200 ns cannot be directly identified in the time-of-flight spectrum of all ions due to the strong background signal, hence a more careful selection has to be done.

Interestingly a small but visible peak fitting to mass 206 u appears in the spectrum. This would be consistent with the fragment BrI^+ which is not directly expected from the geometry of the neutral molecule. As will be shown later in this section, the BrI^+ fragment is correlated with the CH_2^+ fragment, pointing towards the process $CH_2BrI^{2+} \rightarrow BrI^+ + CH_2^+$. Since there exists no Br-I bond in the neutral parent molecule CH_2BrI a bond-forming process has to be involved. A similar effect was detected before in Ref. [117] and Ref. [25] for the formation of O_2^+ from strong-field-ionization of CO_2. Larimian *et al.* observed a slow dissociation of CO_2 in the reaction products $C^+ + O_2^+$ [117]. The authors explain the formation due to an intermediate excited state of CO_2^+ in a bending vibration. Due to the bending motion, the two oxygen atoms come in close proximity, enabling the O-O bond forming. In Ref. [25] on the other hand, an O_2^+ bond forming process taking place on an ultrafast timescale is detected by Long *et al.* However, there is no further analysis done on the occurrence of BrI^+ in the frame of the thesis.

In Fig. 3.3 the measured ion yield as a function of the time-of-flight t and the spatial distribution in the x-direction is shown in a two-dimensional histogram. The molecules are randomly oriented in the molecular beam. Hence, the fragmentation of the molecules leads to a kinetic energy distribution which covers a wide range of angles in a sphere. Measured is the projection of this sphere on the detector, resulting

fragment	m/z [u]	tof [ns]	fragment	m/z [u]	tof [ns]
H^+	1	1058.95	Br^+	79	9183.00
H_2^+	2	1485.55	CH_2Br^+	93	9961.04
He^+	4	2088.85	CH_2BrI^{2+}	110	10830.73
CH_2^+	14	3882.58	I^+	127	11635.43
H_2O^+	18	4398.54	CH_2I^+	141	12258.43
CO^+/N_2^+	28	5478.77	$CH_2Br_2^+$	172	13536.06
O_2^+	32	5855.04	IBr^+	206	14810.89
CO_2^+	44	6860.63	CH_2BrI^+	220	15304.93
CH_2Br^{2+}	46.5	7052.03	$CH_2I_2^+$	268	16889.24
I^{2+}	63.5	8236.00			

Table 3.2.: Mass to charge ratio (m/z) and calculated flight times (tof) from Eq. (3.10) for ions with no initial momentum in the z-direction. Times/masses for fragments including bromine are given for the ^{79}Br isotope.

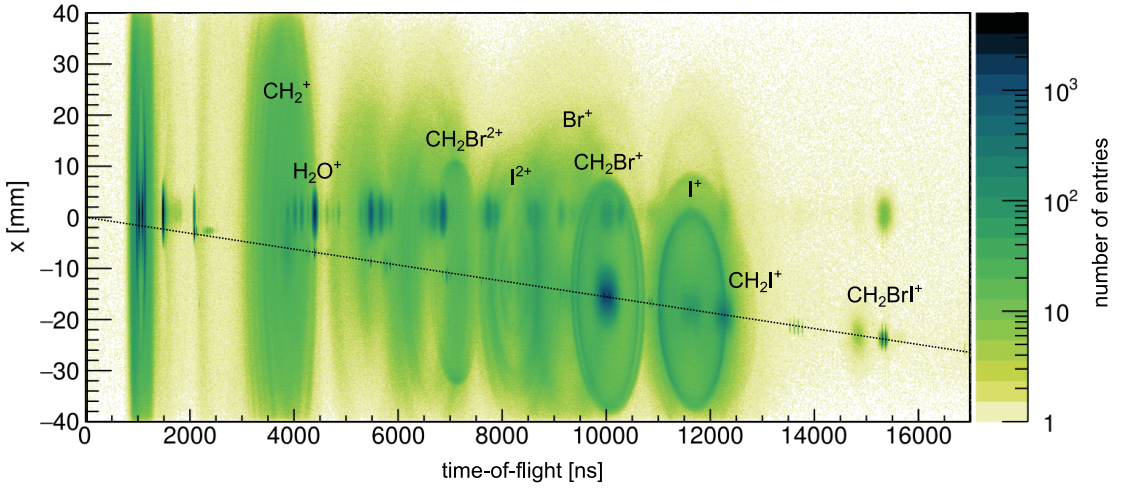

Figure 3.3.: Two-dimensional histogram of the ion yield depending on the spatial distribution in the x-direction and the time-of-flight. Fragments originating from the gas jet appear on a line with slope $\mathrm{m} = -1.53 \times 10^{-3}\,\mathrm{mm\,ns^{-1}}$, as indicated in the figure.

in the ring structures seen in Fig. 3.3. From the x-t distribution, the center-of-mass velocity in the negative x-direction of the molecules before the fragmentation is clearly seen. Ions originating from the background gas appear on a line around $\mathrm{x} = 0$, ions from the gas jet appear on a line with a slope $\mathrm{m} = -1.53 \times 10^{-3}\,\mathrm{mm\,ns^{-1}}$, as indicated in Fig. 3.3. The maximum molecular beam velocity of a supersonic expansion within the used experimental conditions can be calculated to [118]:

$$\begin{aligned} v_{\mathrm{max}} &= \sqrt{2\,\frac{\gamma}{\gamma-1}\,\frac{k_B\,T_0}{m}} \\ &= 1.76 \times 10^{-3}\,\mathrm{mm\,ns^{-1}}. \end{aligned} \tag{3.12}$$

Here, k_B is the Boltzmann constant, γ is the adiabatic index, T_0 is the temperature of the gas before the expansion, and $m = m_1(n_1/(n_1+n_2)) + m_2(n_2/(n_1+n_2))$ is the average mass of the particles in the seeded molecular beam, considering the different number densities $n_{1,2}$ of the two masses $m_{1,2}$ ($m_1 = 220\,\mathrm{u}$, $n_1 = 0.01$, $m_2 = 4\,\mathrm{u}$, $n_2 = 99.99$). The measured beam velocity is slightly lower than the maximum value v_{max}, which is reached for an internal cooling of the beam to $T = 0\,\mathrm{K}$. It has to be taken into account that in the supersonic expansions of seeded molecular beams, which contain two gas species with a great mass difference, an effect termed *velocity slipping* occurs [119]. The heavier molecules in the beam, here CH_2BrI, are accelerated less than the light seed gas molecules. Hence, even for an internal cooling of the beam to $T = 0\,\mathrm{K}$, the theoretical value calculated with Eq. (3.12) is overestimating the velocity.

Two-particle correlations of charged fragments can be seen from a coincidence time-of-flight map, which depicts all events with exactly two detected ions. Such a coincidence map is shown in Fig. 3.4. The time-of-flight of the lighter fragment

is plotted on the x-axis, the time-of-flight of the heavier fragment is plotted on the y-axis. In the coincidence map, indications for two-body break-up processes

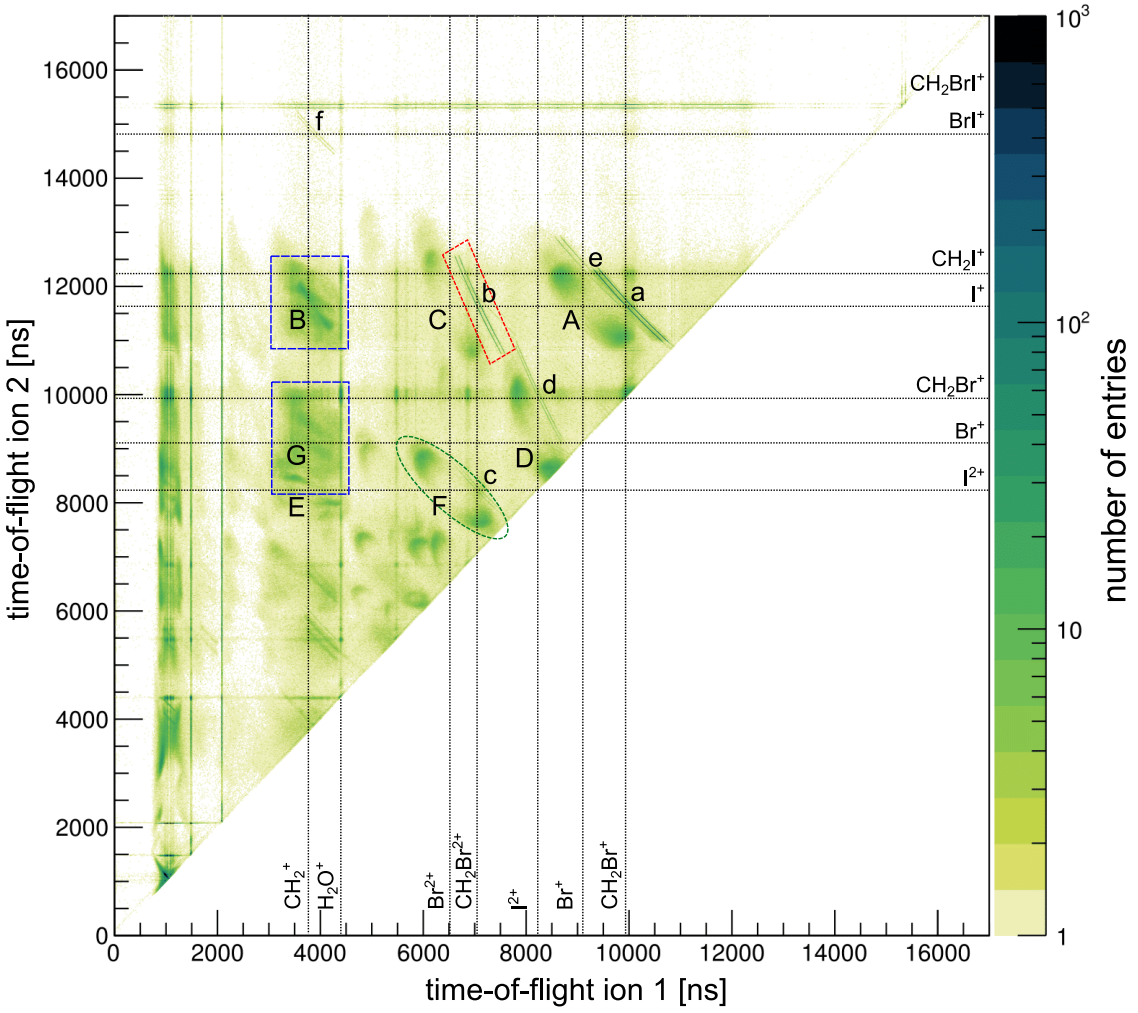

Figure 3.4.: Coincidence map for two-body events. The time-of-flight of the lighter particle is plotted on the x-axis, the time-of-flight of the heavier particle is plotted on the y-axis. The sharp diagonal lines (one marked with the red tilted rectangle) point towards two-body break-up processes where both fragments have been detected. The blue rectangles mark false coincidences from correlations between fragments originating from two different molecules fragmenting in one event. The green tilted oval marks an incompletely detected event, where one fragment (e.g. a neutral fragment) is lost. The characters a-f/A-G mark the different break-up pathways in the figure which are listed in the tables Tab. 3.3 and Tab. 3.4. In the Fig. 3.5 the relative strength of channels a-f is illustrated.

are detected as well as false coincidences and incompletely detected fragmentation

events, e.g. events involving a neutral fragment. The different processes are marked with the characters a-f/A-G in Fig. 3.4 and are listed in Tab. 3.3 and Tab. 3.4. The diagonal sharp lines point towards completely detected break-up processes into exactly two particles (a-f). One example, the break-up into the two fragments I^+ + CH_2Br^{2+} (b), is marked with a red tilted rectangle in Fig. 3.4. In this case, the time-of-flight of the two fragments is clearly correlated. The slope of the lines depends on the charge ratio of the two ions. The double line structure is resulting from the two masses of the bromine isotopes, ^{79}Br and ^{81}Br. Various channels are detected, including singly-charged fragments as well as doubly-charged fragments. In Fig. 3.5 on the right-hand side of Tab. 3.3, a histogram shows the relative contribution of the different completely detected break-up processes into two fragments (100 % corresponds to an integration over the six listed channels). The y-axis is plotted on a logarithmic-scale for better visibility of the smaller bars. The most pronounced feature with a share of 80.0 % is coming from the cleavage of the C-I bond and shows a correlation between the fragments I^+ and CH_2Br^+. The following channel b, with a share of 12.7 %, is originating from the same bond-cleavage after a triple-ionization of the parent molecule, leading to a singly-charged I^+ fragment and a doubly-charged CH_2Br^{2+} fragment. The equivalent channel with doubly-charged I^{2+} fragment and a singly-charged CH_2Br^+ is less pronounced with a share of only 2.3 % (channel d). The probability for this break-up channel is in the same range as channel c (1.8 %), with two doubly-charged fragments and channel e (3.0 %), where the C-Br bond is broken instead of the C-I bond. Consistent with the peak of IBr^+ in the time-of-flight spectrum, channel f shows a correlation between this fragment and the CH_2^+ ion. In this fragmentation channel, originating from a doubly-charged parent molecule, a bond forming process has to be involved since the two atoms I and Br are not connected by a chemical bond in the original molecule. It is the least probable channel with only 0.1 % share. In Fig. 3.6 channels a-e are shown in an enlarged area. Here also uncommon processes become visible, mainly from impurities of the sample like $Br^+ + CH_2Br^+$ or $I^+ + CH_2Cl^+$.

channel	fragment 1	fragment 2
a	I^+	CH_2Br^+
b	I^+	CH_2Br^{2+}
c	I^{2+}	CH_2Br^{2+}
d	I^{2+}	CH_2Br^+
e	Br^+	CH_2I^+
f	CH_2^+	IBr^+

Table 3.3.: Two-body fragmentation channels detected in the coincidence maps in Fig. 3.4 and Fig. 3.6.

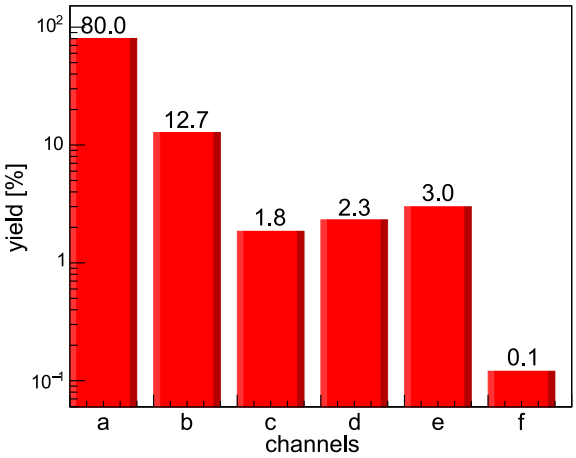

Figure 3.5.: The share of the two-body channels listed in Tab. 3.3.

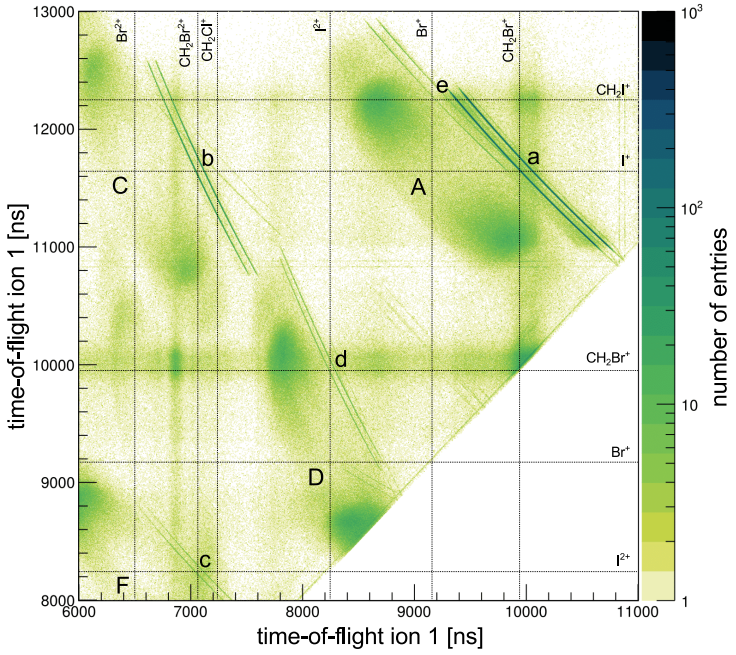

Figure 3.6.: Enlarged coincidence map for two-body events. Here, also uncommon events become visible, e.g from impurities of the sample like $Br^+ + CH_2Br^+$ or $I^+ + CH_2Cl^+$. The broad diffuse parts are originating in an incomplete detection of a fragmentation process.

There are two different features indicating false coincidences[4] in Fig. 3.4 and 3.6. The first ones appear as sharp horizontal or vertical lines. This is clearly seen for the horizontal line at t = 15 305 ns, the time-of-flight of the singly-charged parent molecule or for the vertical line at t = 4399 ns, the time-of-flight of water ions. These false coincidences are most pronounced for strong mass peaks. One frequently appearing fragment (e.g. the singly-charged parent) is detected coincidentally at the same time with some other not specified fragment leading to the straight lines. Another indication of false coincidences are diffuse areas, for example seen for $t_1 \approx$ 3000 ns to 4500 ns, $t_2 \approx$ 8000 ns to 10 200 ns and $t_2 \approx$ 11 000 ns to 12 500 ns, in the areas marked with blue rectangles in Fig. 3.4. These are correlations between fragments originating from two different molecules fragmenting in one event. The whole time-of-flight range of both fragments is covered, but no direct correlation can be detected. In the two above mentioned areas these are the flight times for CH_2^+ (3000 ns to 4500 ns) and Br^+ (8000 ns to 10 200 ns)/CH_2^+ (3000 ns to 4500 ns) and I^+ (11 000 ns to 12 500 ns). Both effects leading to false coincidence occur only if there is more than one molecule in the laser focus, which gets ionized. Although the measurement conditions have been adjusted carefully to decrease the occurrence of false coincidences, it is seen from the coincidence map in Fig. 3.4 that these events are still present.

In addition to false coincidences and the kinematically complete two-body events,

[4]The occurrence of false coincidences is explained in section 2.3.

channel	fragment 1	fragment 2	missing fragment
A	I^+	Br^+	CH_2
B	I^+	CH_2^+	Br
C	I^+	Br^{2+}	CH_2
D	I^{2+}	Br^+	CH_2
E	I^{2+}	CH_2^+	Br
F	I^{2+}	Br^{2+}	CH_2
G	Br^+	CH_2^+	I

Table 3.4.: Incompletely detected fragmentation channels visible in the coincidence maps in Fig. 3.4 and Fig. 3.6. The missing fragment can be either a neutral fragment (as listed in the table) or an ionic fragment which was not detected.

also incompletely detected fragmentation can be seen. These events appear as two blurry peaks along a diagonal line through the crossing point of two central flight times. One example, the break-up into the two fragments $I^{2+} + Br^{2+}$ (F), is marked with the tilted green oval in Fig. 3.4. Since one fragment is missing, either because it was not detected or because a neutral fragment was involved in the process, the correlation is not sharp as for the completely detected processes. The missing fragment is carrying away some unknown momentum. In the enlarged area in Fig. 3.6, the incomplete fragmentation $I^+ + Br^+$ (A), $I^+ + Br^{2+}$ (C), as well as $I^{2+} + Br^+$ (D), are visible beside the sharp lines. They appear as a broad diffuse line, peaking in the endpoints. The momentum of the missing CH_2 or CH_2^+ is not included in this process leading to the broad distribution. The found incompletely detected events are listed in Tab. 3.4.

For first insight into three-body processes in the fragmentation of CH_2BrI^{3+}, in Fig. 3.7 the coincidence map for events with exactly three detected ions is shown. Plotted on the x-axis is the sum of the flight times of the two lightest ions and plotted on the y-axis is the flight time of the heaviest ion. Also in this representation correlations are clearly visible. Completely detected three-body events appear as sharp diagonal lines. As seen from the strengths of the two-body channels, the C-I bond is easiest to break. As a consequence, all of the detected three-body events include I^+ as the heaviest ion. Hence, only an enlarged area in the time-of-flight region of the iodine ion is shown in Fig. 3.7.

In Tab. 3.5 the main correlations with the iodine ion as the heaviest particle are listed. The list includes completely detected events, incompletely detected events, and events where two fragments from a two-body break are detected together with an ion from the contamination of the molecular beam (e.g. H_2^+). For channels which are sharp in Fig. 3.7, the relative strength was evaluated. The result is shown in the histogram on the right-hand side of Tab. 3.5 (100 % corresponds to an integration over the four evaluated channels). Since blurry channels cannot be separated in the data from the background, these are not included in the histogram.

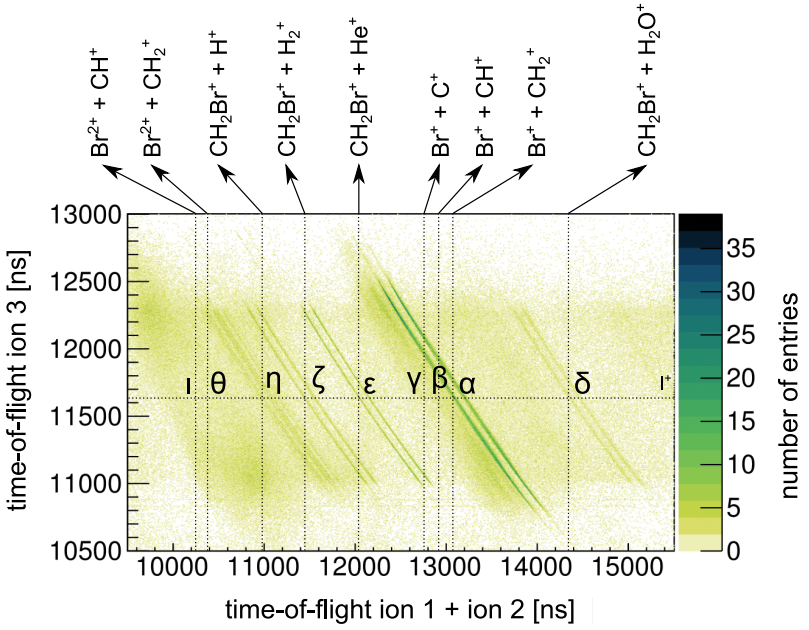

Figure 3.7.: Coincidence map for three-body events. The sum of the time-of-flight of the two lighter particles is plotted on the x-axis, the time-of-flight of the heaviest particle is plotted on the y-axis. The different processes marked with the characters $\alpha - \iota$ are listed in Tab. 3.5. The relative strength of the channels which are sharp is given in Fig. 3.8.

Several three-body correlations are detected. The strongest pronounced features are the lines at flight times of ($Br^+ + CH_2^+$) and I^+ (channel α, with a share of 69.9 %). This break-up process is investigated later in section 3.5. The lines of channel α are directly accompanied by two blurry lines resulting from the fragments ($Br^+ + CH^+$) + I^+ and ($Br^+ + C^+$) + I^+ (channel β and γ). Completely detected two-body processes with an additional detected ion are leading to a sharp line, too (channel δ(7.4 %), ϵ(11.7 %), and ζ (11.0 %)). An example would be the process $CH_2BrI^{2+} + H_2^+ \rightarrow CH_2Br^+ + I^+ + H_2^+$. The additional H_2^+ ion leads to a shift in the time-of-flight sum, however, the correlation between the two particles CH_2Br^+ and I^+ is still conserved in this representation. Since these diagonal lines are sharp, the additional ion is originating from the molecular beam.

3.4. Coincident event selection and data transformation

To gain a deeper insight into the fragmentation processes we have carefully separated and analyzed true three-particle coincidences from the full data-set. A well-established method for selecting true coincidences is to calculate the momenta of the single ions and to apply the condition of momentum conservation (see for example Ref. [14]). In the momentum calculation by Eq. (3.8) and Eq. (3.9) the velocity of the molecular beam was included. Hence, the resulting momenta are in the center-

channel	fragment 1	fragment 2
α	I^+	$(Br^+ + CH_2^+)$
β	I^+	$(Br^+ + CH^+)$
γ	I^+	$(Br^+ + C^+)$
δ	I^+	$(BrCH_2^+ + H_2O^+)$
ϵ	I^+	$(BrCH_2^+ + He^+)$
ζ	I^+	$(BrCH_2^+ + H_2^+)$
η	I^+	$(BrCH^+ + H^+)$
θ	I^+	$(Br^{2+} + CH_2^+)$
ι	I^+	$(Br^{2+} + CH^+)$

Table 3.5.: Completely and incompletely detected three-body correlation channels from the coincidence map in Fig. 3.7.

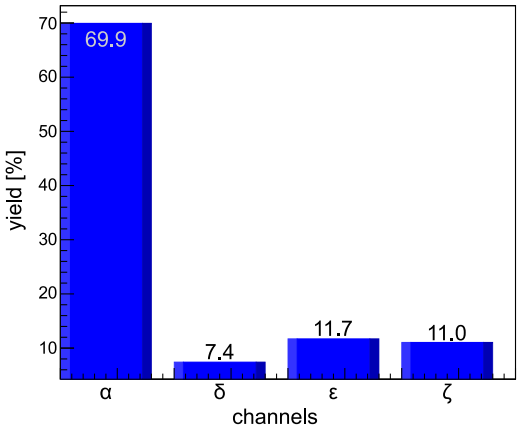

Figure 3.8.: The share of the three-body channels listed in Tab. 3.3 which can be separated in the data.

of-mass-system of the molecule. Since the total momentum of the intact molecule in the center-of-mass system of the molecule is zero, the sum of all momenta from fragments resulting from a break-up of the same parent molecule should be zero as well due to momentum conversation. In our work we focus on break-up dynamics with the three resulting fragments CH_2^+, I^+, and Br^+.

Based on the ring structures in Fig. 3.3, we chose three time-of-flight ranges for which we calculate the momenta. This selection is the first applied filter. The respective time-of-flight ranges are marked in red in Fig. 3.9. There is no additional filter applied at first (e.g. selecting only events with a certain number of detected ions). It can be clearly recognized that other masses than the ones to be investigated are still in the filtered data (see also Fig. 3.2). For example the water peak overlaps with the selection for CH_2^+ due to the broad kinetic energy distribution of the CH_2^+ fragment. Also in the time-of-flight ranges for I^+ and Br^+ other ions contribute to the spectrum. However, to keep every event in the filtering process which include the fragments CH_2^+, I^+, and Br^+ their full range of flight times has to be taken into account to get the entire kinetic energy release distribution.

For each ion signal, with a time-of-flight in one of the three selected ranges, the momenta were calculated, assuming that they originate from fragments CH_2^+, I^+, or Br^+. The two bromine isotopes were considered to have the same time-of-flight range. Hence, for all ions in this range, two momentum values were calculated: first, with mass 79 u and second, with mass 81 u. The momentum calculation is described in section 3.2. We disregard that also other ion masses besides CH_2^+, I^+, and Br^+ are in the selection. The wrong calculated momenta for these additional ions are discarded later with the condition of momentum conversation.

According to the specifications, the spatial resolution of the detectors is below 100 µm [114] and the temporal resolution is below 100 ps [115]. The uncertainty

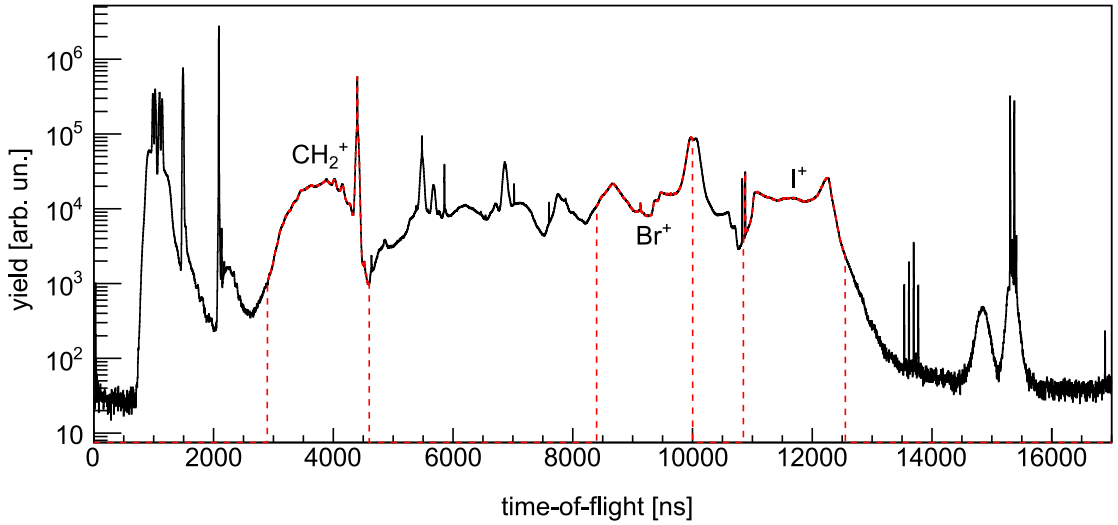

Figure 3.9.: Reproduction from Fig. 3.2. Marked in red are the filters in the time-of-flight that are applied in the first step of the data evaluation. Further steps will remove the contributions from peaks overlapping with the entries from the three fragments CH_2^+, I^+, and Br^+ such as H_2O^+.

in the time-of-flight measurement influences the momentum calculation in the z-direction as well as in the x- and y-direction. The uncertainty in the measurement of the impinging point on the detector influences only the momentum calculation in the x- and y-direction. Hence, the calculation of the ion momentum in the z-direction, based on the time-of-flight information, is the most precise one. Therefore, this direction is chosen for the momentum filter. In Fig. 3.10, panel (a) and (b), the sum of the calculated momenta in the z-direction of the three fragments, $\Sigma p_z = p_{\mathrm{I}_z} + p_{\mathrm{Br}_z} + p_{\mathrm{CH}_{2z}}$, is shown. Here, in addition to the first applied filter on the time-of-flight ranges, a second filter is applied to only keep events with exactly one detected ion in the time-of-flight region of each fragment CH_2^+, I^+, and Br^+. Panel (a) is for the momentum calculation taking into account the bromine isotope with mass 79 u, panel (b) is for the bromine isotope with mass 81 u. The peak centered around $\Sigma p_z = 0$ has a FWHM of 2.5 a.u. In both calculations peaks resulting from the other bromine isotope appear. These are the sharp peaks which are not located at $\Sigma p_z = 0$ (-29 a.u. and 28 a.u. for panel (a) and (b)). Additionally, smaller peaks on the right-hand side of the two sharp maxima are visible at positions 34 a.u. and 72 a.u.(^{79}Br)/63 a.u. and 98 a.u.(^{81}Br). These are coming most likely from the fragments CH^+ or C^+ instead of CH_2^+. For further analysis of the three-body breakup processes into CH_2^+, I^+, and Br^+ the last filter selects only events from both centered peaks. The filtering condition is

$$-5\,\mathrm{a.u.} < \Sigma p_z < 5\,\mathrm{a.u.} \tag{3.13}$$

It is marked in Fig. 3.10 with the red lines and arrows.

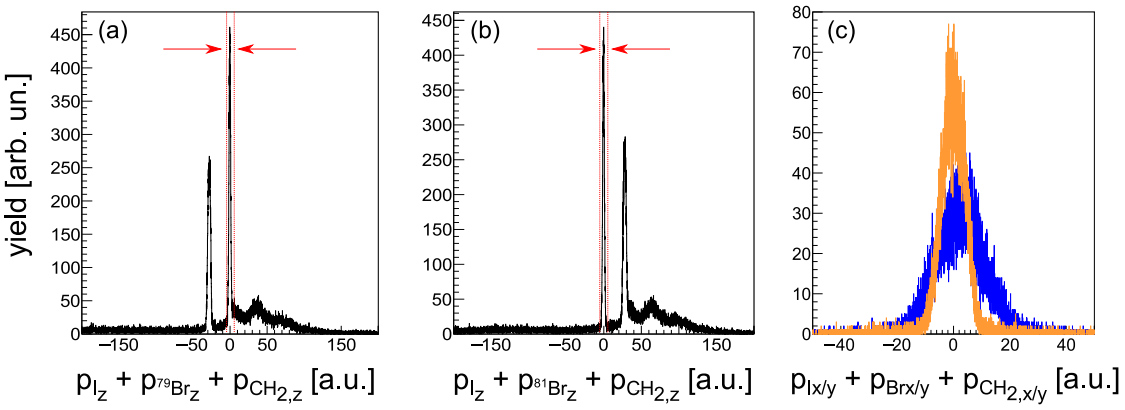

Figure 3.10.: Sum of the calculated momenta in the z-direction of the three fragments p_{I_z}, p_{Br_z}, and $p_{CH_{2z}}$ in atomic units. Panel (a) is for the bromine isotope with mass 79 the, panel (b) is for the bromine isotope with mass 81. Marked in red is the selection of data points for the further analysis. Panel (c) shows the momentum sum in the x- (blue) and y-direction (orange) resulting from the filter on Σp_z. The distributions in panel (c) include the data sets from both bromine isotopes.

For the events fulfilling condition (3.13), we checked the resulting momentum sum in the other two directions to verify that the momentum conservation is fulfilled for Σp_x and Σp_y, too. The resulting distribution for Σp_x and Σp_y is shown in Fig. 3.10 in panel (c) (blue: x, orange: y). The distributions in panel (c) include the data sets from both bromine isotopes. After the selection (3.13), the spread in the x- and y-direction (FWHM) is in the range of ± 10 a.u.(x)/± 5 a.u.(y). Both distributions are centered around zero, due to the velocity of the molecular beam, the FWHM is larger in the x-direction. No further filter on the momentum sum in the x- or y-direction is applied.

Calculating the error in the momentum sum in the different directions, based Eq. (3.6), Eq. (3.9), and the given detector resolutions ($\Delta t = 100$ ps, $\Delta x/y = 100$ µm) via Gaussian error propagation leads to $\Delta\Sigma p_z \approx 0.27$ a.u., $\Delta x/y \approx 1.39$ a.u. These values are by around a factor 5-10 smaller than the measured width of the distributions. However, there are some further uncertainties in the calculation of the momenta besides the spatial and temporal resolution of the detector. The main impact has probably the velocity distribution of the molecular beam which increases the uncertainty of the measurement of the impinging point on the detector. This can be seen e.g. in Fig. 3.3. The impinging parent ion should lead to a sharp spot on the detector since there is no kinetic energy from a fragmentation. However, we observe a line that spreads across a few millimeters. Further, instabilities of the electric field strength and of the focal spot position can lead to uncertainties in the measurement.

Comparing the areas under the curves in panel (a) and (b) of Fig. 3.10 from the main peak centered around $\Sigma p_z = 0$ and the broad background peak in the selected range (3.13), leads to the assumption that still around 10 % of the selected events are false coincidences. However, a smaller filter (3.13) leads to the same qualitative

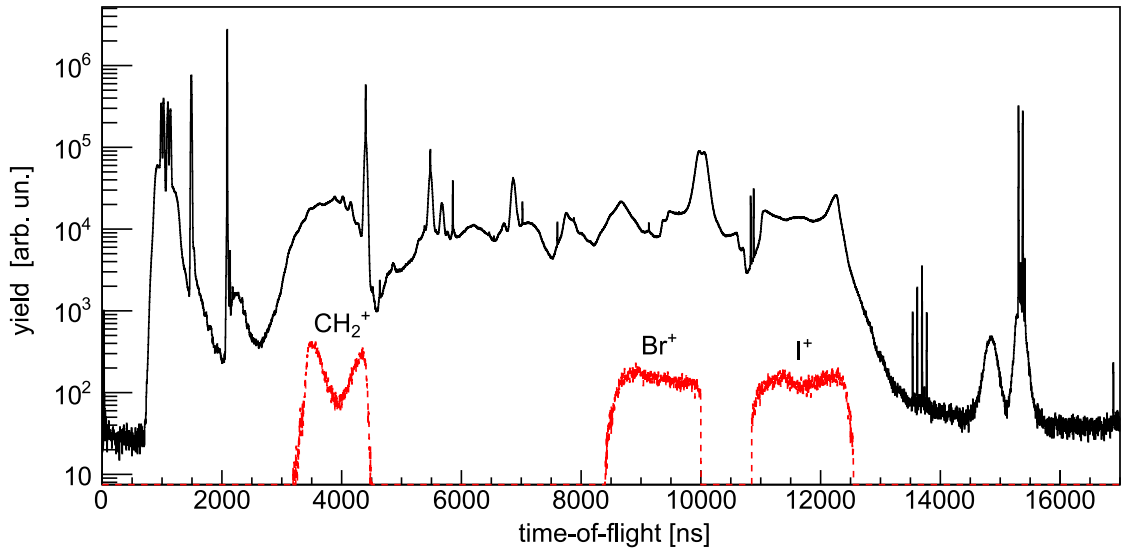

Figure 3.11.: Reproduction from Fig. 3.2. Time-of-flight spectrum of all events (black) and events selected by the momentum conservation condition (red). The red filtered mass spectrum of the fragments I^+, Br^+, and CH_2^+ is resulting from a fragmentation of the same parent molecule.

features, which are discussed in the next section, but a reduced data set. We consider the resulting FWHM in the x- and y-directions, as well as the resulting alignment which is described in the next paragraph, after the filter (3.13) as sufficient. A further analysis of the influence of the false coincidences on the data can be found in the appendix A.

In Fig. 3.11 a time-of-flight spectrum of all events is shown in black and the time-of-flight data for the filtered data set is plotted in red. In this representation, all peaks are appearing as a double peak structure centered around the zero momentum time-of-flight, indicating the kinetic energy release gained during the fragmentation process.

Alignment The molecules are not aligned within the measurement. Hence, the calculated momentum vectors are pointing in random directions mirroring the random orientation of the molecules during the measurement. To get significant information on the fragmentation dynamics from the calculated momenta the coordinate system has to be transformed to the same reference frame for every event. The resulting momentum vectors of a three-body break-up process are always located in a plane. Hence, the three-dimensional problem can be fully described in two dimensions. In Fig. 3.12 the angles of the applied rotation are illustrated in a spherical coordinate system. The system is first rotated by the angle $\varphi_{\vec{p}_\mathrm{I}}$ around the z-axis followed by a rotation by $\theta_{\vec{p}_\mathrm{I}}$ around the y-axis. The index I is indicating that the angles correspond to the vector of the iodine momentum in the laboratory frame. This results in all $\vec{p}_\mathrm{I}$ vectors pointing towards the z-axis. The orientation of the $\vec{p}_\mathrm{Br}$ and $\vec{p}_{\mathrm{CH}_2}$ vectors is still undefined, thus the third rotation by the new angle

$\varphi_{\vec{p}_{\mathrm{Br}}}$ around the z-axis is performed. After the third rotation, all vectors are in the x-z-plane with a small spread of ± 5 a.u.(FWHM) of the p_y component of the CH_2^+ fragment, shown in Fig. 3.13.

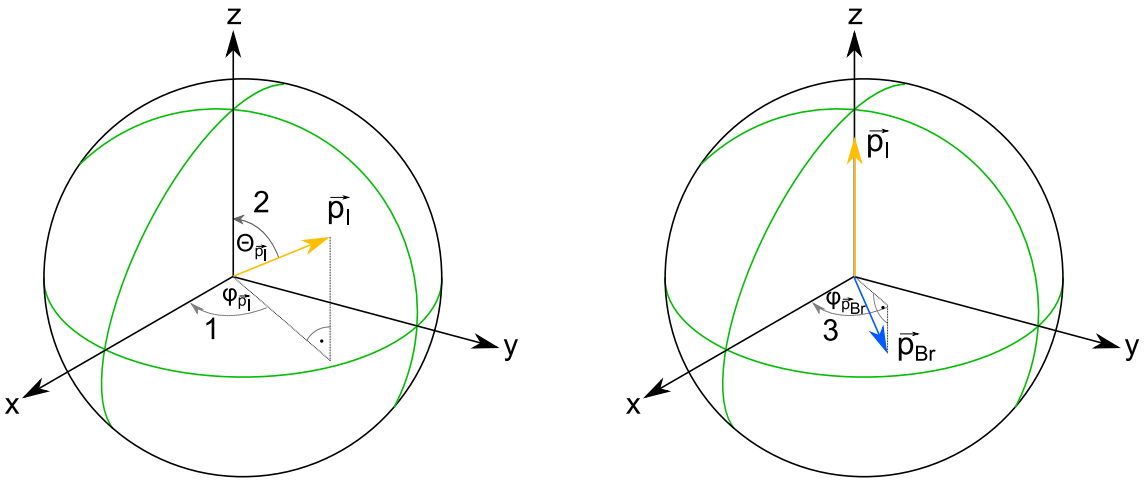

Figure 3.12.: Schematic depiction of the rotation of the coordinate system for each event into a common frame for all events. The three rotation angles $\varphi_{\vec{p}_{\mathrm{I}}}$ (1), $\theta_{\vec{p}_{\mathrm{I}}}$ (2), and $\varphi_{\vec{p}_{\mathrm{Br}}}$ (3) are determined for each event separately. After these rotations, the momentum $\vec{p}_{\mathrm{I}}$ is along the z-axis and all three momenta lie in the xz-plane.

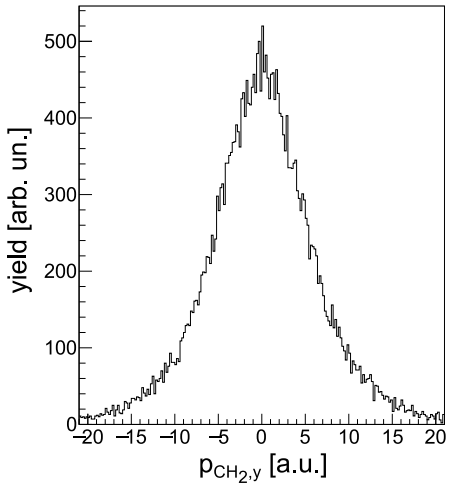

Figure 3.13.: Spread of the p_y momentum component of the CH_2^+ fragment after the rotation. The FWHM of the curve is ± 5 a.u.

3.5. Three-body break-up of CH_2BrI^{3+} in $CH_2^+ + I^+ + Br^+$

To visualize the different fragmentation processes a combination of Newton diagrams and Dalitz plots is chosen. The combined representation of the data gives a deep insight into the different fragmentation processes. The two representation schemes are introduced in the next subsection.

3.5.1. Newton diagrams and Dalitz plots

The Newton diagram representation follows naturally from the transformation of the coordinate system done in section 3.4. One of the three momentum vectors builds the reference for the new coordinate system and is located on a chosen axis. All three momentum vectors are presented in one plane, with the second particle fully depicted in the upper hemisphere and the last particle depicted in the lower hemisphere. The principle of the Newton diagram representation is schematically shown in Fig. 3.14. In a Newton diagram, the relation between the three momentum vector becomes visible in an intuitive way, e.g. a rotating motion leads to a ring-shaped structure in the Newton diagram.

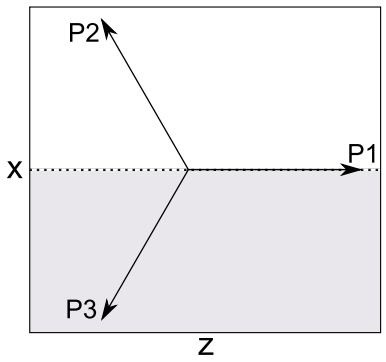

Figure 3.14.: The schematic principle of a Newton diagram. The momentum vector of one fragment (here P1) builds the reference frame and is plotted on one axis (here the z-axis) for all events. The momentum vector of the second particle is plotted in the upper hemisphere, the momentum vector of the third particle is plotted in the lower hemisphere.

An alternative representation of a three-body break-up process is to use a Dalitz plot. It shows the probability density for certain break-up processes in a two dimensional scatter plot. The Dalitz plot representation was originally developed in the area of particle physics [120] and first applied in atomic physics to describe the break-up dynamics of the H_3^+ molecule [121]. The three coordinates for each particle p_x, p_y, and p_z are reduced to two global coordinates x and y, the relative kinetic energies:

$$x = \frac{E_1 - E_2}{\sqrt{3} \cdot E_{\text{tot}}} \tag{3.14}$$

$$y = \frac{E_3}{E_{\text{tot}}} - \frac{1}{3}, \tag{3.15}$$

where E_1 is the kinetic energy of the first fragment, E_2 the kinetic energy of the second fragment, E_3 the kinetic energy of the third fragment, and E_{tot} is the total kinetic energy. Each point in the Dalitz plot represents one final momentum distribution resulting from a molecular break-up. This concept is illustrated in the Dalitz scheme in Fig. 3.15 for a three-body break-up with three identical fragments (e.g. $H_3^{3+} \rightarrow H^+ + H^+ + H^+$). Depending on at which part of the Dalitz plot the highest density of data points accumulates, the probability for a certain process to happen is higher.

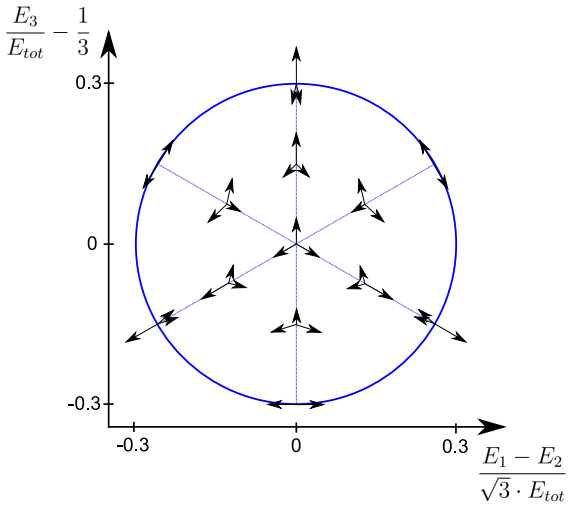

Figure 3.15.: The schematic principle of a Dalitz plot. Each point in the Dalitz scheme represents a certain break-up geometry.

The fully symmetric break-up with a 120° angle between the three vectors is located in the center of the plot. The three axes that run through the origin with a relative angle of 120 degrees between them represent all possibilities for partly symmetric break-ups, where two of the three momentum vectors have the same magnitude, but opposite direction. In between, asymmetric processes are located. For a fragmentation of a molecule in three fragments with the same mass (like for H_3^{3+}), all processes are located within a circle, due to conservation of the momentum and energy. This changes for processes where the fragments are different in their mass. The possible area of all processes in the Dalitz plot becomes an oval and the plot is not anymore centered at the zero position. But, the principle interpretation stays the same. For the interpretation of the Dalitz plot, first, the central point is calculated. This corresponds to the break-up channel in a pure Coulomb explosion[5].

[5]The central point is calculated from the Coulomb repulsion of three point charges with the masses of the three fragments, arranged in the equilibrium geometry of the molecule.

Compared to this central point different processes become visible. A bending of the molecule, for example, appears on a nearly vertical line around the central spot in the Dalitz plot. An asymmetry in bond lengths, e.g. due to a vibration of the molecule, leads to a shift in the x-direction. A last important feature, clearly visible in the Dalitz plot, are sequential break-up processes. If one of the two bonds is broken first, and the second bond-cleavage follows after a certain time-delay (in the time-scale of the molecular dynamics), the final momenta of the two latest reaction products are clearly related, but nearly independent of the momentum of the first leaving fragment. Such a sequential process is visible as a diagonal line in the Dalitz plot.

3.5.2. Three-body break-up process channel assignment

To examine the different three-body break-up processes of $CH_2BrI^{3+} \rightarrow CH_2^+ + I^+ + Br^+$, a first assignment of the detected fragmentation channels is done in this subsection on the basis of a Newton diagram and a Dalitz plot. All assigned processes are afterwards analyzed in detail in the next subsections. The upper panel of Fig. 3.16 shows a Newton diagram of the correlated fragments, filtered from the acquired data as described above. The momenta of the Br^+ fragments are plotted in the upper hemisphere and the momenta of the CH_2^+ fragments are plotted in the lower hemisphere. All momenta are normalized to the respective iodine momentum, resulting in the iodine data appearing as a single point in the Newton diagram. The lower panel of Fig. 3.16 shows a Dalitz plot of the correlated fragments. The normalized kinetic energies of the three fragments are represented by the coordinates (3.14) and (3.15), where E_1 is the kinetic energy of the iodine fragment, E_2 the kinetic energy of the bromine fragment, E_3 the kinetic energy of the methylene fragment, and E_{tot} is the total kinetic energy.

In both plots in Fig. 3.16, different processes can be assigned. In the Newton diagram, all described processes are present in both the upper and in the lower hemisphere (for Br^+ and CH_2^+ fragments, respectively). However, the marks in the plot with Roman numerals are only done in either the upper or underpart for better visibility. The most dominant features in the Newton diagram are lobes (marked with I and the white dashed line), with the highest density of detected events located at around $p_z/p_I = -0.7$ a.u. for the Br^+ fragments and at around $p_z/p_I = -0.3$ a.u. for the CH_2^+ fragments. Weaker features are full and partial ring structures in the momenta of Br^+ and CH_2^+. The full rings are marked with number II (solid red lines) and III (dashed red lines), the partial rings are marked with number IV (solid blue line) and V (dashed blue line). The same features are detected in the Dalitz plot in the lower panel of Fig. 3.16. There is a peak structure at the position (-0.04, 0.30) (marked with I, corresponding to the lobes in the Newton diagram), two long diagonal crossing lines (marked with II/III, corresponding to the full ring structures), and two short, broad diagonal lines starting at the endpoints of the long, sharp diagonal lines and merging into the peak structure (marked with IV/V, corresponding to the partial ring structures)[6].

[6]The intensity in the Dalitz plot which appears in the area $y \gtrsim 0.36$ and which is not assigned to a

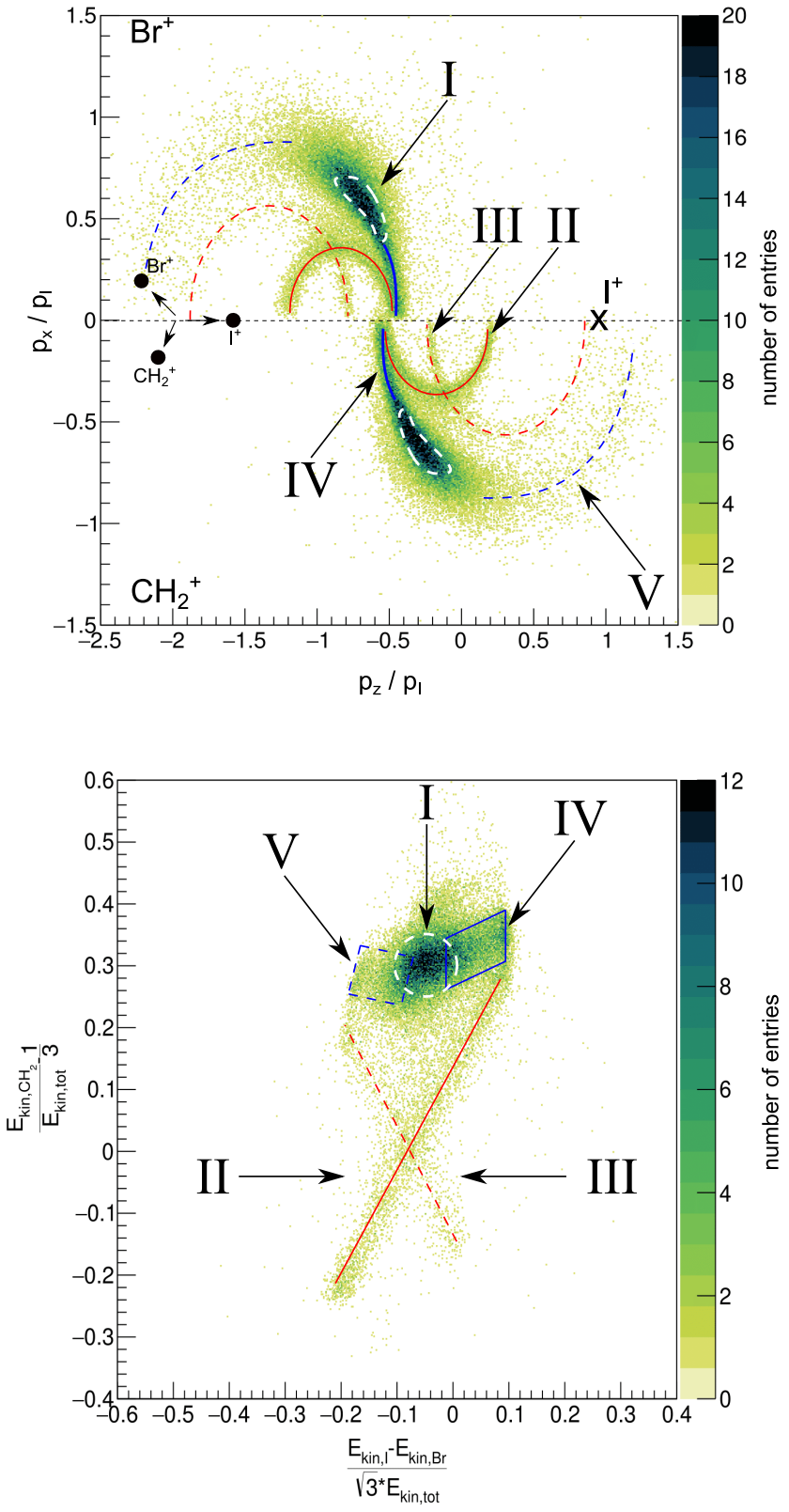

Figure 3.16.: Top: Newton diagram of the momenta of the three fragments CH_2^+, I^+, Br^+ in the molecular frame. All data points are normalized to the iodine momenta. The bromine momenta are plotted in the upper hemisphere and the CH_2^+ momenta are plotted in the lower hemisphere. Bottom: Dalitz plot of the three fragments I^+, Br^+, and CH_2^+. The different marked features are explained in the text.

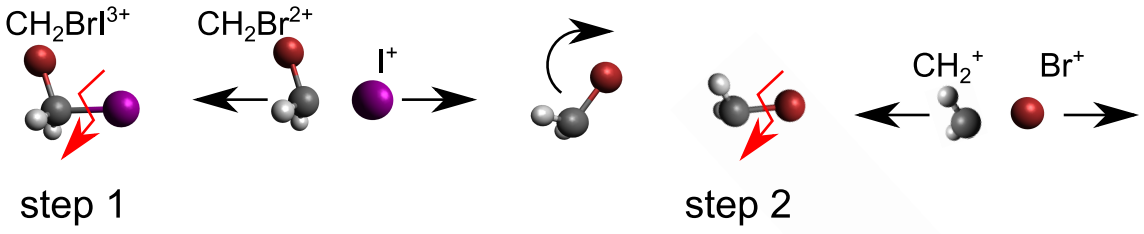

Figure 3.17.: After the C-I bond is broken (step 1), the two created charged fragments repel each other. Since the force of the leaving iodine ion is not acting on the center-of-mass of the CH_2Br^{2+} fragment, the fragment starts to rotate. The C-Br bond is broken in the second step.

These are clear hints to different fragmentation processes: (i) A non-sequential direct Coulomb explosion where both bonds in the parent molecule break simultaneously leading to the peak structures marked with I in both representations, (ii) a sequential fragmentation with a rotating intermediate fragment leading to the ring structures in the Newton diagram and the line structures in the Dalitz plot. A type (ii) process is schematically depicted in Fig. 3.17. In the first step, only the C-I bond is broken and the two created charged fragments repel each other. Since the force of the leaving iodine ion is not acting on the center-of-mass of the CH_2Br^{2+} fragment, the fragment starts to rotate and changes its orientation with respect to the leaving iodine ion. The bond of the rotating doubly-charged intermediate breaks after some time delay in the second step. The rotation of the intermediate is decoupled from the momentum of the leaving ion and hence visible in the Newton diagram as ring structures[7]. Due to the successive bond cleavage, the kinetic energies of the two charged particles created in the second step are clearly related but independent of the first leaving fragment, leading to a diagonal line in the Dalitz plot, as introduced in subsection 3.5.1.

The phenomenon of the ring structures (line structures) visible in the Newton diagram (Dalitz plot) in Fig. 3.16 was detected before (see e.g. [102]) and was assigned to the described effect: a sequential break-up process with an impulsive stimulation of rotational energy. Due to the rotation of the intermediate fragment in the second step, the resulting direction of the final momentum is not definite anymore but distributed up to 360 ° around the axis of rotation, depending on the lifetime of the intermediate fragment. Intermediate fragments with lifetimes longer than the rotational period lead to full ring structures in the Newton diagram, whereas intermediate fragments with shorter lifetimes lead to partial ring-shaped structures. Based on the literature, a first assignment of the ring structures (line structures) to sequential processes is motivated [86–107].

In contrast to experiments with triatomic molecules, such as CO_2, where the two bonds are indistinguishable [90, 92–99, 101, 102, 104, 108], here, at least two full ring

certain channel is resulting from the left false coincidences in our data set. It corresponds to the intensity in the Newton diagram shown in the appendix in Fig. A.1 in panel (a) for a changed filter condition (3.13): 20 a.u. $< \Sigma p_z <$ 50 a.u. (^{79}Br) and 50 a.u. $< \Sigma p_z <$ 80 a.u. (^{81}Br).

[7] A rotation of the complete molecule would not be visible in the Newton diagram, since we transform the coordinate system in the molecular frame.

structures (diagonal lines, II/III) instead of one and two partial ring structures (short diagonal lines, IV/V) are detected. This leads to the assumption that there are contributions from the non-sequential direct Coulomb explosion and additionally from four different sequential fragmentation channels:

$$
\begin{aligned}
\text{I} \quad & \mathrm{CH_2BrI^{3+}} \rightarrow \mathrm{CH_2^+ + Br^+ + I^+} \\
\text{II} \quad & \mathrm{CH_2BrI^{3+}} \rightarrow \mathrm{CH_2Br^{*2+} + I^+} \rightarrow \mathrm{CH_2^+ + Br^+ + I^+} \\
\text{III} \quad & \mathrm{CH_2BrI^{3+}} \rightarrow \mathrm{CH_2I^{*2+} + Br^+} \rightarrow \mathrm{CH_2^+ + I^+ + Br^+} \\
\text{IV} \; &= \text{II}\,(\text{short-lived } \mathrm{CH_2Br^{*2+}}) \\
\text{V} \; &= \text{III}\,(\text{short-lived } \mathrm{CH_2I^{*2+}}).
\end{aligned}
$$

The channel numbers are marked in both plots in Fig. 3.16, in the Newton diagram either in the upper or lower hemisphere. The partial ring structures (short lines, IV/V) mark the connection between the structures II/III and structure I and are evidence for two additional sequential fragmentation processes with short-lived intermediate states. The different processes will be investigated in more detail in the next sections separately.

3.5.3. Non-sequential Coulomb explosion channel

In this section, the direct non-sequential Coulomb channel I is analyzed. The gained three-dimensional momentum data and the gained kinetic energy is compared to the expected values calculated from the known geometry, to see if the momentum vectors reflect the structure of the molecule. The expected momenta of the fragments can be gained in an iterative calculation, assuming single point charges at the positions of the atoms in the molecules. This calculation was done for the break-up $\mathrm{CH_2BrI^{3+}} \rightarrow \mathrm{CH_2^+ + Br^+ + I^+}$.

The start geometry parameters for the positions are taken from Ref. [109] where Bailleux *et al.* determined the structure of CH_2BrI via rotational spectra using a Fourier transform microwave spectroscopy experiment. The start parameters are listed in Tab. 3.6. The bond lengths C-Br and C-I, as well as the angle αICBr, were adjusted to represent a three-particle-molecule with the original positions of the I and Br atom but with the center-of-mass of CH_2 instead of the position of the C atom. In the first step, the force on each fragment resulting from the other two point charges was calculated which led to a uniformly accelerated motion. The calculation was done in a two-dimensional coordinate system since for a three-particle-system the momenta resulting from a direct Coulomb explosion are always in one plane. The momenta, velocities, and positions of the fragments resulting from these forces were calculated for a certain small time step Δt. Next, the forces were calculated again, and the procedure was repeated until the momenta converged to a certain value. We decided to choose the time step for the calculation as an increasing variable $\Delta t = i \cdot \Delta t_0$ with the start value $\Delta t_0 = 1\,\text{as}$ and 5000 loops i. Thereby in the beginning when the variables change a lot the steps are very small and accurate but the converging value is still reached in an appropriate computing time. Figure

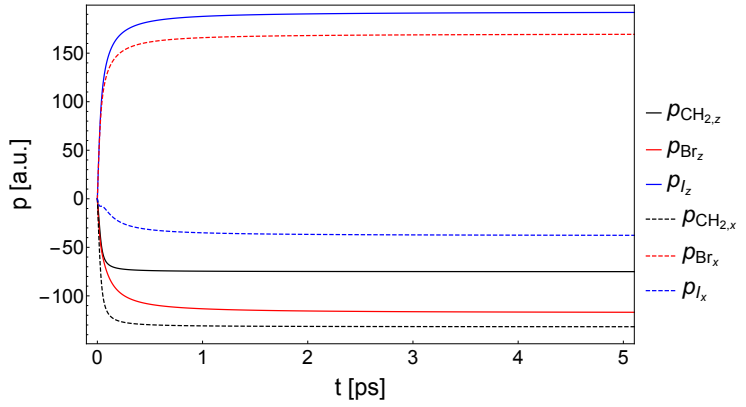

Figure 3.18.: Stepwise calculation of the resulting momenta of a Coulomb explosion of CH_2BrI^{3+}. The time steps for the calculation were chosen as increasing value $\Delta t = i \cdot \Delta t_0$ with the start value $\Delta t_0 = 1\,\text{as}$ and 5000 loops i.

3.18 shows the resulting stepwise calculated momenta in two directions of the three fragments. In the calculation the momentum vectors are not aligned to a specific coordinate system, all three momentum vectors change their direction during the calculation. The transformation to an aligned system follows afterwards in the same way as for the measured momenta, to compare the numerical result with the data. From the calculated momenta the kinetic energy is obtained. The calculated values, in the not aligned and in the aligned case, are listed in Tab. 3.6. The final value is reached after approximately 1 ps.

start parameters		not aligned			aligned	
		fragment	p_z [a.u.]	p_x [a.u.]	E_{kin} [eV]	p_z [a.u.]	p_x [a.u.]
C-I	2.1313 Å	I^+	192.51	-37.98	2.26	196.22	0.00
C-Br	1.9261 Å	Br^+	-117.40	169.88	4.02	-148.06	143.95
αICBr	113.53 °	CH_2^+	-75.11	-131.90	12.27	-48.16	-143.95

Table 3.6.: Left: Start parameters for the momentum calculation. The values are determined via rotational spectra using Fourier transform microwave spectroscopy in Ref. [109]. Right: Resulting momenta and kinetic energies from the calculation. After the calculation the momentum vectors are not aligned to a specific coordinate system. The transformation to an aligned system follows afterwards in the same way as for the measured momenta.

In Fig. 3.19 a Newton diagram, as well as a Dalitz plot is shown, where the aligned calculated positions of the momenta and the kinetic energies are marked with red crosses. For the Newton diagram this is at the positions $\vec{p}_I = (1, 0)\,\text{a.u.}$,

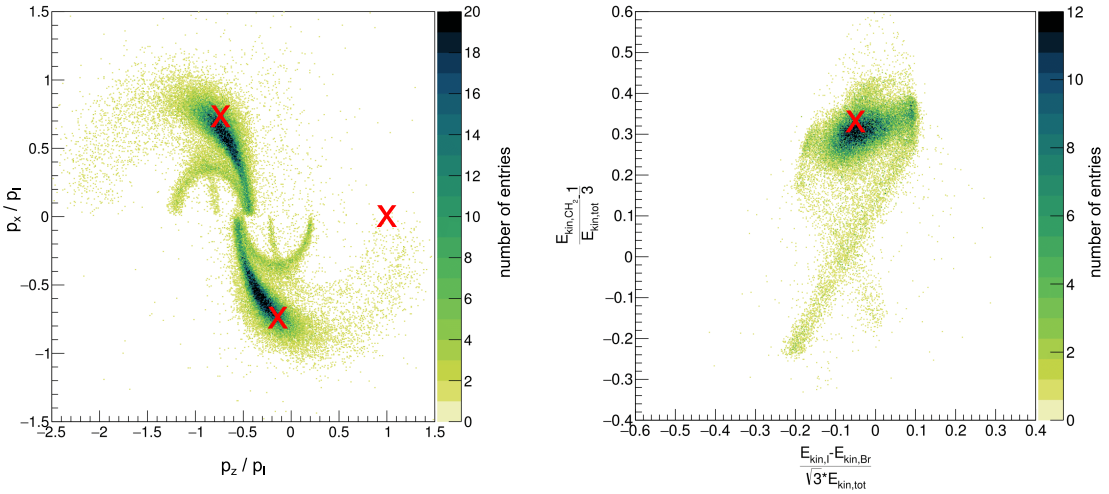

Figure 3.19.: Newton diagram and Dalitz plot for the three fragments CH_2^+, I^+, Br^+. The red crosses show the calculated momenta/KER for a Coulomb explosion of CH_2BrI^{3+}.

$\vec{p}_{Br} = (-0.75, 0.73)$ a.u., and $\vec{p}_{CH_2} = (-0.25, -0.73)$ a.u., the position in the Dalitz plot is at (-0.05, 0.33). The measured peak values do not fit exactly the calculated ones but are close to the theoretical values. In the Dalitz plot, the measured data show a shift in the y-direction, indicating a bending of the molecule. It has to be noted that the angle between the momentum vectors in the Newton diagram are not directly mirroring the angles of the molecule. The two sets of angles are related in a nontrivial way. That is why a recursive calculation is needed.

In Fig. 3.20 the measured total kinetic energy from all fragments is shown. The dashed blue line marks the position of the calculated total kinetic energy $E_{kin,calc} = 18.1$ eV. This value is around 4.4 eV higher than the measured peak value $E_{kin} = 13.7$ eV (indicated with the red dashed line). However, it has to be noted, that the main peak has a small shoulder to the high energy side, centered at the position of the calculated kinetic energy. As mentioned before there are several deviations in the measurement from a pure Coulomb potential. One possible reason for the smaller kinetic energy is the pulse duration of 25 fs. It was shown before that the ionization with longer laser pulses leads to a reduced kinetic energy in the Coulomb explosion [122]. If the molecule is not triply ionized directly in one step, it can already start to dissociate while the laser field is still present. At a critical distance, the ionization rate maximizes due to enhanced ionization (EI) [53, 123] (see sections 2.1 and 2.2). The molecule is ionized to its final triply-charged state and explodes.

The shift in kinetic energy could also originate from a different process. In another experiment, Wales *et al.* studied the Coulomb explosion of OCS for pulse lengths varying from 7 fs to 200 fs [100]. For the final state of $O^+ + C^+ + S^+$, the authors did not detect a dependency of the KER for pulse lengths variations up to 100 fs. The measured value stayed nearly constant at around 64 % of the expected KER from a pure Coulomb explosion. However, in measurements where OCS was ionized with soft x-ray synchrotron radiation [89] and highly-charged ions [106] a higher fraction

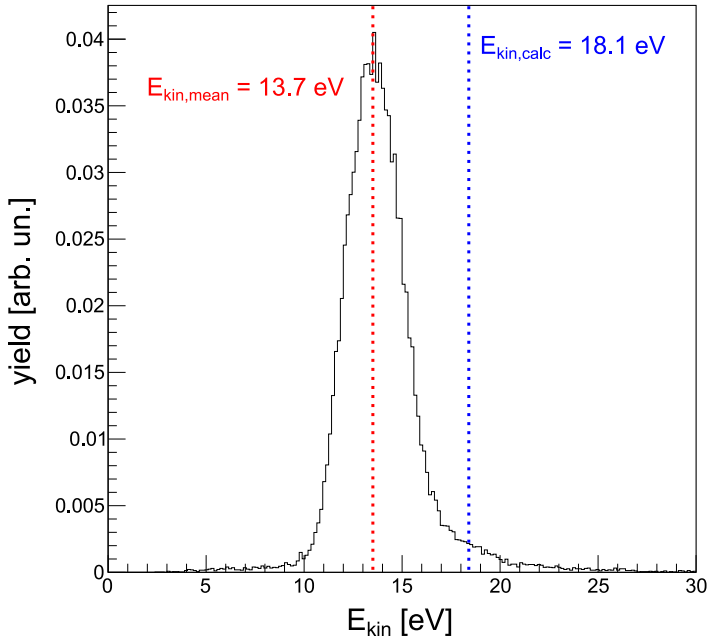

Figure 3.20.: Total kinetic energy release of the three fragments CH_2^+, I^+, Br^+. The blue line shows the calculated KER for a Coulomb explosion of CH_2BrI^{3+}. On the high energy side, the main peak has a tail, centered at the calculated value $E_{kin,calc} = 18.1\,eV$.

of the calculated KER was reached (85 % to 96 %). Ramadhan *et al.* concluded that by femtosecond laser pulses the molecular ion OCS^{3+} is generated in a different state which has a quasi-bound nature [89].

The main peak in the kinetic energy distribution has a small shoulder on the high energy side, visible in Fig. 3.20, centered at the theoretical Coulomb explosion value. To investigate this high energy part further, in Fig. 3.21 a Newton diagram and a Dalitz plot are shown with a filter on the high kinetic energy events with $E_{kin} > 15\,eV$. The red crosses mark, as before, the theoretical values calculated for a pure Coulomb explosion.

For this data selection, the measured data are fitting the calculated values much better[8]. Hence, a fraction of all break-up events takes place on a nearly Coulombic potential, leading to the high kinetic energy and reflecting the geometry of the neutral. This corresponds to around 20 % of all coincidence events. In an experiment with the goal of following a molecular geometry change, e.g. during a chemical reaction, this is the fraction of data to be explored. However, since several other

[8] One has to notice that the momenta resulting from different break-up processes are merging into each other and it is difficult to clearly separate only the events originating from a direct Coulomb explosion. In subsection 3.5.5 sequential processes with a short-lived intermediate state are analyzed. The resulting momenta from such processes show a continuous transition to the momenta of events corresponding to the features labeled I in Fig. 3.16. The still visible tails in the Newton diagram in Fig. 3.21 are most probably coming from a leftover of the sequential channel described in subsection 3.5.5.

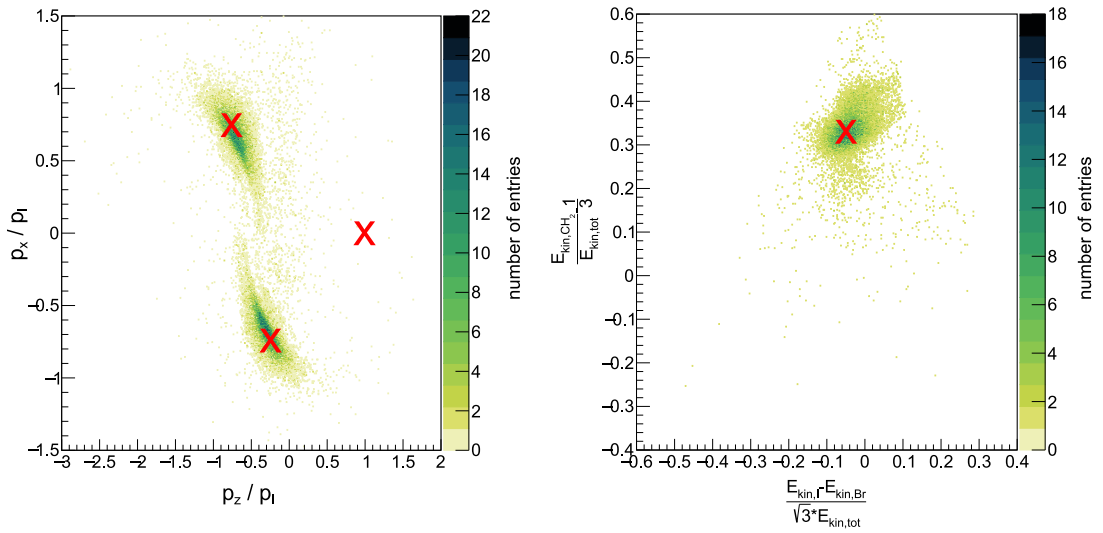

Figure 3.21.: Newton diagram and Dalitz plot for the three fragments CH_2^+, I^+, Br^+. The red crosses show the calculated momenta/KER for a Coulomb explosion of CH_2BrI^{3+}.

processes are affecting the fragmentation dynamics, it is difficult to always ensure the possibility to extract exactly this data. In the experiment done here, the start geometry is known. Hence, it is possible to compare the expected values with the measured values to evaluate which events could be used to reconstruct the geometry. In a pump-probe experiment exploring molecular dynamics, it is not clear that this can always be ensured.

Experiments on the Coulomb explosion of CH_2BrI, which vary the pulse duration and pulse intensity would be an interesting future perspective. On the one hand, if the reason for the KER shift is the laser pulse length, a shorter pulse would be helpful to gain exact information on the geometry or the geometry change of a molecule during a dynamical process. Additionally, it could be explored how the overall fraction of pure channel I events can be increased above the here detected 20 % (high energy part). In the OCS measurement with variable pulse lengths [100], the group could detect a minimum ratio of sequential events to concerted events for around 60 fs. This result speaks against just decreasing the pulse length. Further experiments e.g. on the effect of varying the intensity of the pulse and the wavelength could help to find the best control mechanism of fragmentation dynamics and the best attempt to explore the molecular geometry.

3.5.4. Sequential bond breaking - long-lived states

Besides the direct non-sequential Coulomb explosion channel described in section 3.5.3, a fraction of molecules is fragmenting via sequential pathways. From the Newton diagram and the Dalitz plot in Fig. 3.16 it was already clearly seen, that we detect several sequential channels in CH_2BrI^{3+}, denoted as channels II, III, IV, and V. This subsection focuses on the sequential break-up channels II and III, both

with a long-lived intermediate state. The sequential break-up channels IV and V are investigated later in subsection 3.5.5. The analysis and the physics behind the break-up channels II and III are the same. The difference is the bond which is broken first: the C-I bond for channel II or the C-Br bond for channel III. To distinguish between the sequential channels II and III and assign them more clearly, further transformations have been done. Considering a purely two-body break-up of a rotating molecule, the resulting momentum vectors would be distributed in a full ring-shaped structure, centered at the origin of the center-of-mass system of the two fragments. The second step in channels II and III correspond to such a process (see the reaction pathways in subsection 3.5.2 or Fig. 3.17). Hence, a transformation to the center-of-mass frame of the intermediate fragment was done. For visualizing channel II the coordinate system was transformed in the center-of-mass frame of CH_2Br^{*2+} in the following way:

$$p_{\mathrm{Br}_z,\mathrm{com}} = p_{\mathrm{Br}_z} + p_{\mathrm{I}_z} \cdot \frac{m_{\mathrm{Br}}}{m_{\mathrm{Br}} + m_{\mathrm{CH_2}}} \tag{3.16}$$

$$p_{\mathrm{CH_2}_z,\mathrm{com}} = p_{\mathrm{CH_2}_z} + p_{\mathrm{I}_z} \cdot \frac{m_{\mathrm{CH_2}}}{m_{\mathrm{Br}} + m_{\mathrm{CH_2}}}. \tag{3.17}$$

The iodine momentum is located on the z-axis: $p_I = (0, 0, p_{\mathrm{I}_z})$. Therefore, there is no transformation of the x- and y-components needed. The result of the transformation is shown in Fig. 3.22. In the center-of-mass representation, no normalization is applied. The shown momenta are absolute numbers in atomic units. Part of the momentum vectors of Br^+ and CH_2^+ constitute a symmetric ring structure centered at the origin as expected for a two-body break-up of a rotating molecule (marked in the plot). These are the events corresponding to the features labeled II in Fig. 3.16. The other events that are plotted in Fig. 3.22 are originating either from the Coulomb explosion channel I or from other sequential processes. The momenta constituting the ring structure have a mean value of $p = 85.9$ a.u. This corresponds to a two-body Coulomb explosion of CH_2Br^{*2+} into $CH_2^+ + Br^+$ with a CH_2-Br distance of $l_1 = 1.51\, r_e$. Here, r_e is the C-Br bond length of the neutral parent molecule plus the additional distance to the center-of-mass of CH_2: $r_e = (1.93 + 0.14)$ Å. The CH_2-Br distance of the intermediate fragment increased in comparison to the intact parent molecule. There are mainly two points in the fragmentation process, where the bond-length increase can occur. First, during the ionization process itself. Second, during the time-span between the first and second bond-cleavage, when the intermediate fragment is rotating. It was already seen in the last chapter 3.5.3 for the direct non-sequential Coulomb explosion, that the reached kinetic energy of the final fragments is only 75 % of the expected kinetic energy for a break-up process of a molecule in the geometry of neutral CH_2BrI. Hence, it is highly probable that part of the bond-length increase occurs during the ionization process itself. Comparing the total kinetic energy of the two fragments, calculated from the mean momentum value of the events in the ring structure, with the potential energy calculated via the Coulomb potential of the two fragments CH_2^+ and Br^+ at the distance of the CH_2-Br bond of the neutral molecule, leads to a fraction of $E_{\mathrm{kin}}/E_{\mathrm{pot}}$: 69 %. Since this fraction is even less than in the 75 % reached in the direct non-sequential Coulomb explosion it is concluded, that there is an additional bond-length increase occurring

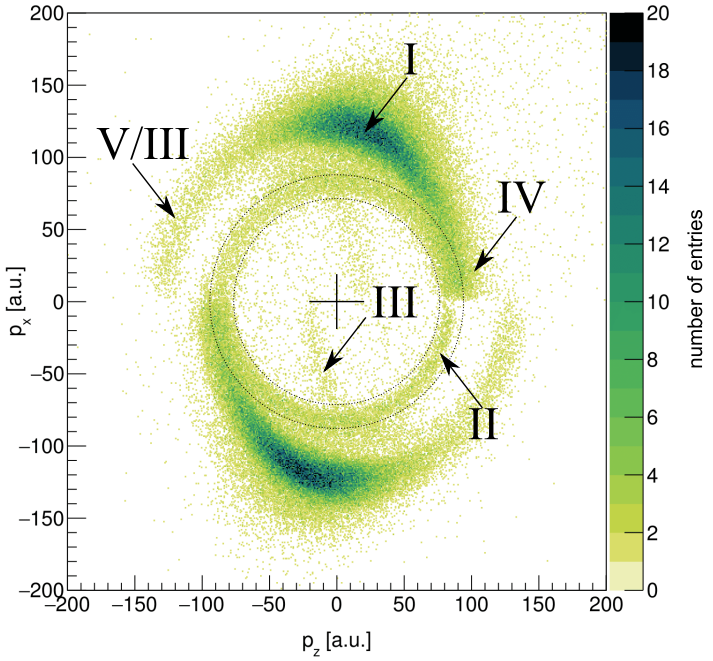

Figure 3.22.: Momenta of the two fragments CH_2^+ and Br^+ in atomic units plotted in the center-of-mass frame of CH_2Br^{*2+}. The symmetric ring, centered at the origin, is resulting from a sequential break-up with the long-lived intermediate state CH_2Br^{*2+} (channel II).

during the rotation of the intermediate fragment.

From the measured bond-length, the moment of inertia I and hence, the rotational constant B of the intermediate can be calculated in the model of the rigid rotor [36]:

$$I = \mu r^2 \tag{3.18}$$

$$B = \frac{\hbar^2}{2\,I\,h\,c}, \tag{3.19}$$

where μ is the reduced mass of the system and r is the internuclear distance. With $r = l_1$ this leads to $B = 0.14\,\mathrm{cm}^{-1}$. The rotational energy of the state is $E_{\mathrm{rot}} = h\,c\,B\,(J+1)\,J$. From the energy, the rotational oscillation period can be calculated to: $T_{\mathrm{rot}} = \frac{1}{\omega} = 1/(E_{\mathrm{rot}}\,c\,2\pi)$. Since the momenta from the channel II break-up are distributed uniformly along the ring structure, it is concluded that the life-time of the intermediate CH_2Br^{*2+} is longer than the rotational period. However, since we do not know the quantum number J of the excited rotation no quantitative statements can be made on the energy E_{rot} and the oscillation period T_{rot} without further information. To calculate the rotational energy of the intermediate from the momentum due to the leaving iodine fragment one would have to consider the relation between the center-of-mass of the CH_2Br^{*2+} fragment and its charge center. The further these two are separated the higher is the excited rotational energy.

In Fig. 3.23 the kinetic energy distribution of all events (black) and for events

constituting in the ring structure (red) is shown. Panel (a) is for iodine fragments, panel (b) for bromine fragments, panel (c) for methylene fragments, and panel (d) shows the total kinetic energy of all fragments. The kinetic energies are calculated from the momenta in the coordinate system of the complete molecule and all histograms are normalized to an area of one. The iodine fragments in the ring selection show a sharp KER distribution centered at a higher value compared to the KER distribution of all events. The KER of the bromine fragments and the methylene fragments in the ring selection is broader distributed and covers the whole range from $\approx 1\,\text{eV} - 8\,\text{eV}$. The two different shaped distributions could be explained in the following way: The iodine ion is released in the first step of the break-up of CH_2BrI^{3+} where still three charges are involved in the Coulomb repulsion. This leads to a high kinetic energy comparable to the direct break-up of channel I. However, in contrast to the direct three-body Coulomb explosion of channel I in the first step of channel II (and III) only one bond needs to be broken which results in some additional energy left for the kinetic energy of the iodine ion. On the other hand part of the energy is transferred into rotational energy of the long-lived intermediate CH_2Br^{*2+}. This leads to the broad kinetic energy distribution of the Br^+ and CH_2^+ fragments. Depending on the time of the second bond cleavage the fragments are released in a certain angle. Hence, the resulting momentum of a single fragment can either sum up to the initial momentum gained in the first bond breaking or nearly cancel out with it. High kinetic energies of a CH_2^+ fragment correspond to low kinetic energies of a Br^+ fragment. Looking at the total kinetic energy for events constituting the ring structure, the value is smaller than for the selection of all data points.

It has to be noted that the selection of the ring structure elements is not clean. In Fig. 3.22 it can be seen, that events resulting from channel II overlap for example with events from channel IV in the outer p_z parts. These events lead e.g. to the peak in the KER distribution in the red curve of Fig. 3.23 at $E_{\text{kin,Br}} = 1.2\,\text{eV}$. Due to the overlap of the data points, a separation of this background is not possible.

To illustrate channel III the first transformation to the molecular frame, described in section 3.4, was done differently from the transformations for channel I and II. The lab frame coordinate system was rotated in a way resulting in the bromine momentum pointing towards the z-axis instead of the iodine momentum. Afterwards, the vectors were transformed to the center-of-mass frame of CH_2I^{*2+} via:

$$p_{\text{CH}_2z,\text{com},2} = p_{\text{CH}_2z} + p_{\text{Br}_z} \cdot \frac{m_{\text{CH}_2}}{m_{\text{I}} + m_{\text{CH}_2}} \tag{3.20}$$

$$p_{\text{I}_z,\text{com},2} = p_{\text{I}_z} + p_{\text{Br}_z} \cdot \frac{m_{\text{I}}}{m_{\text{I}} + m_{\text{CH}_2}}. \tag{3.21}$$

In Fig. 3.24 the resulting Newton diagram is shown. The vectors for the bromine fragment are located on a line at $p_x = 0$ and are not shown in the plot. The analysis follows the same arguments as for channel II. Events originating from a sequential break-up referred to as channel III lead to the ring structure marked in the plot. Since in bromoiodomethane the Br-C bond is stronger (2.99 eV) than the I-C bond (2.04 eV), this channel is less probable, leading to a less pronounced ring

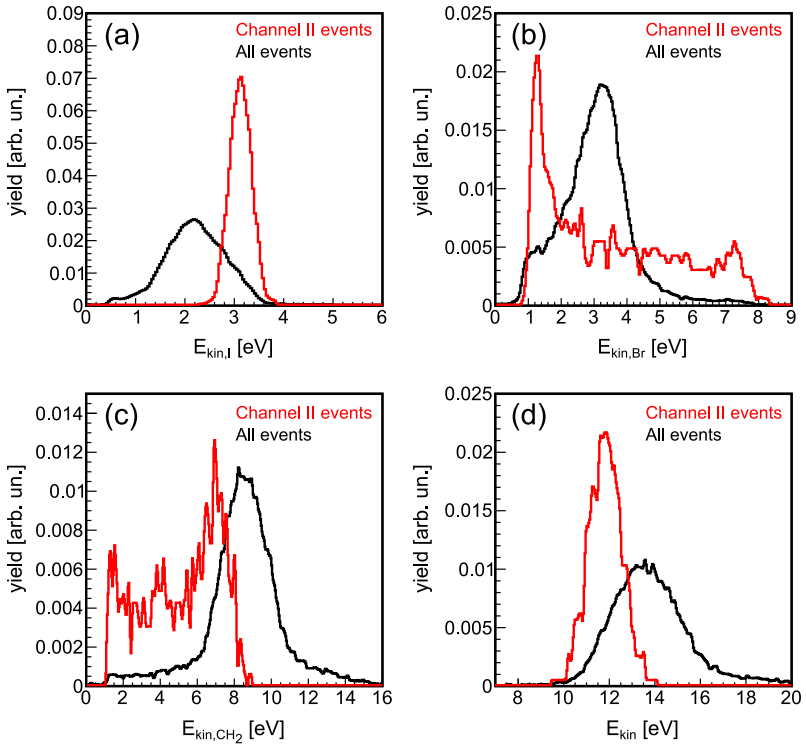

Figure 3.23.: Kinetic energy distribution for all events (black) and events constituting the ring structure in Fig. 3.22 (red). Panel (a) shows the KER of the iodine fragments, panel (b) of the bromine fragments, panel (c) of the methylene fragments, and panel (d) the total kinetic energy of all fragments.

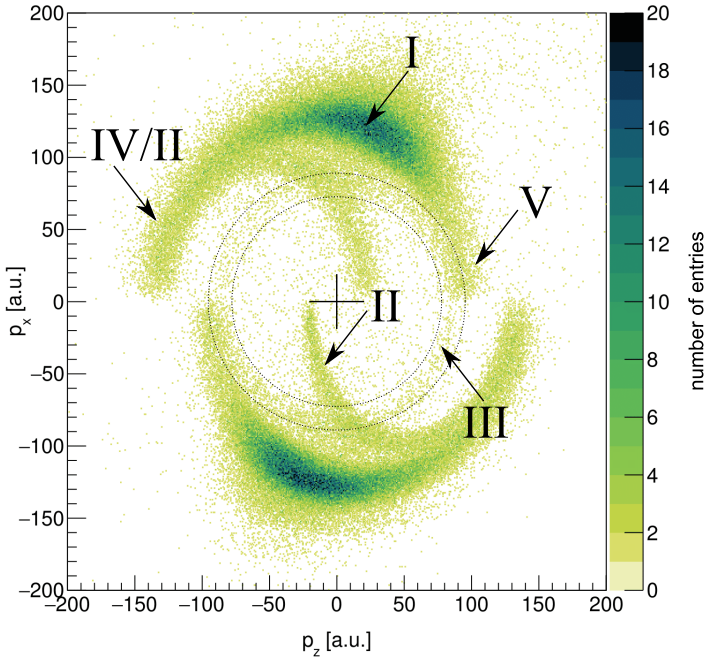

Figure 3.24.: Momenta of the two fragments CH_2^+ and I^+ in atomic units. The momentum vectors are plotted in the center-of-mass frame of CH_2I^{*2+}. Events from channel III are leading to the symmetric ring-shaped structure centered around the origin.

structure [110]. From the mean value of the momentum $p = 87.5\,\text{a.u.}$ the CH_2-I distance can be calculated to $l_2 = 1.40\,r_e$ ($r_e = (2.13 + 0.14)\,\text{Å}$). The share of the measured kinetic energy on the calculated energy from a Coulomb explosion is 69 %. This is in the same percentage than in the sequential channel II break-up. The rotational constant of the intermediate CH_2I^{*2+} can be calculated with the measured distance l_2 to $B = 0.13\,\text{cm}^{-1}$.

In Fig. 3.25 the kinetic energy distribution of all events (black) and for events constituting the ring structure (blue) is shown. Panel (a) is for iodine fragments, panel (b) for bromine fragments, panel (c) for methylene fragments, and panel (d) shows the total kinetic energy of all fragments. Here, the bromine fragments of the selection show a higher kinetic energy release and the ones of the iodine fragments are broader distributed, ranging from 0.5 eV to 5.5 eV. The peaks in the kinetic energy of the iodine fragment located at $E_{\text{kin,I}} = 0.9\,\text{eV}$ and $E_{\text{kin,I}} = 3.1\,\text{eV}$ in Fig. 3.25 are resulting from a not clean data selection. In Fig. 3.24 it can be seen, that events resulting from channel III overlap with events from channel V in the outer p_z parts as well as with events from channel II around $p_z = 0$. This leads to the peaks in the KER at the positions 0.85 eV and 3.10 eV.

Both, channel II and channel III are clearly identified as well in the Dalitz plot in the top panel of Fig. 3.16. In Fig. 3.26 the momenta for two different intensity areas in the Dalitz plot are illustrated (I^+: magenta, Br^+: red, CH_2^+: grey. See also the Dalitz scheme in Fig. 3.15) and two possible break-up mechanisms in channel II are exemplified in small illustrations. Channel II appears as a diagonal line from

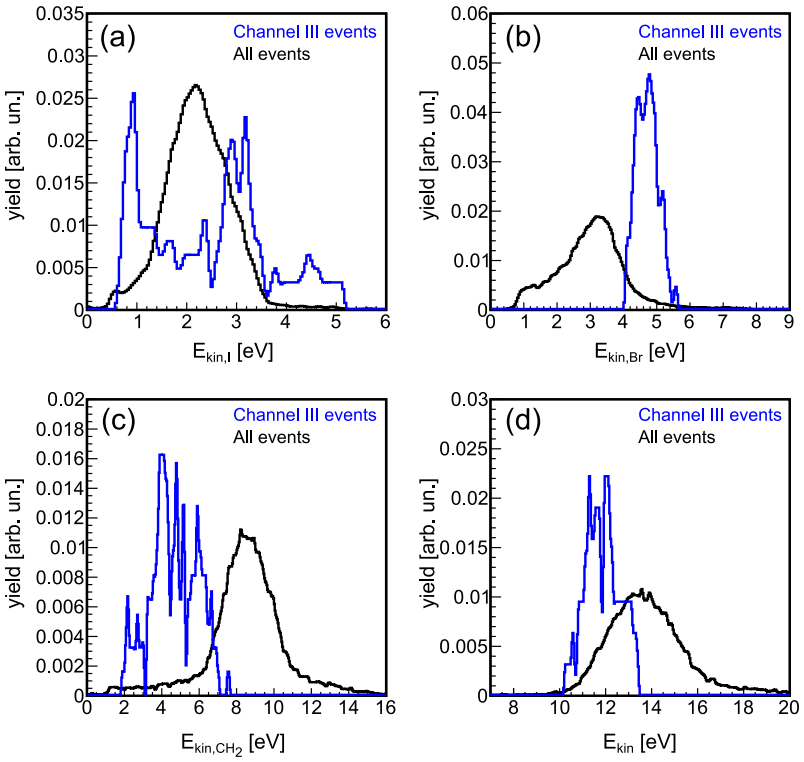

Figure 3.25.: Kinetic energy distribution for all events (black) and events contributing to the ring structure in Fig. 3.24 (blue). Panel (a) shows the KER of the iodine fragments, panel (b) of the bromine fragments, panel (c) of the methylene fragments, and panel (d) the total kinetic energy of all fragments.

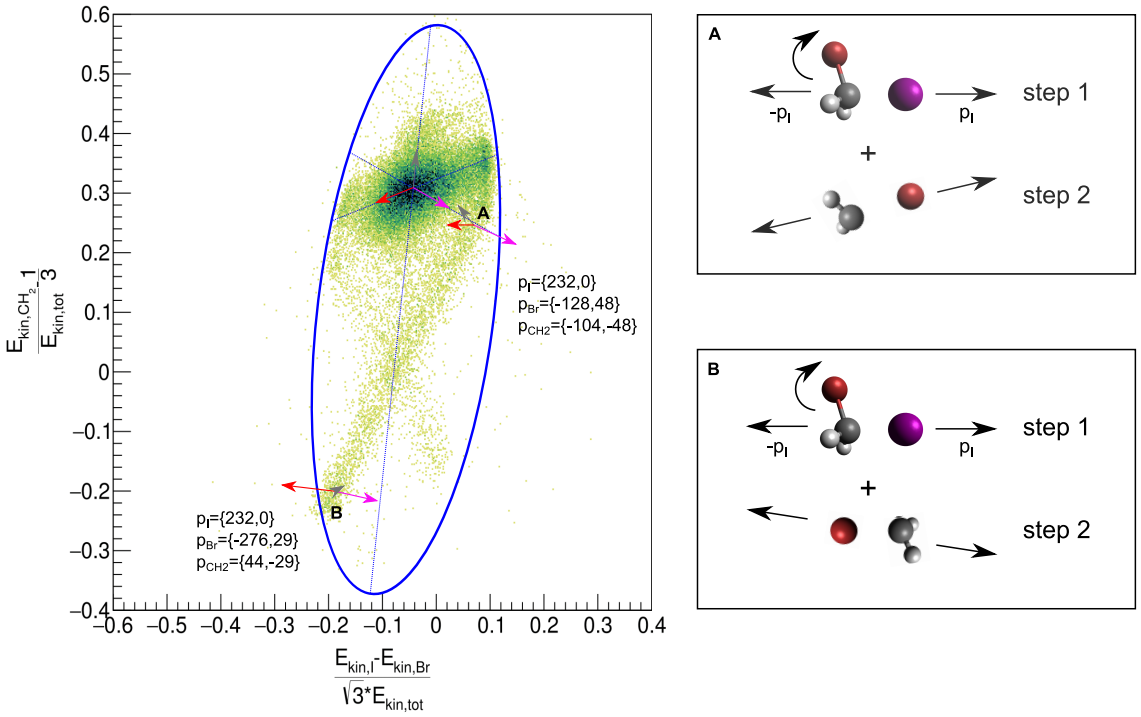

Figure 3.26.: Illustrated are the momenta of the three fragments for different intensity areas in the Dalitz plot (I^+: magenta, Br^+: red, CH_2^+: grey. See also the Dalitz scheme in Fig. 3.15). In channel II the kinetic energy/momentum of the bromine ion is clearly dependent on the kinetic energy/momentum of the methylene ion and at the same time independent on the iodine ion kinetic energy/momentum. On the right-hand side of the Dalitz plot are two possible break-up pathways for two intensity areas of channel II exemplified.

the bottom left to the top right. The kinetic energy/momentum of the bromine ion is clearly dependent on the kinetic energy/momentum of the methylene ion and at the same time independent on the iodine ion kinetic energy/momentum. Channel III is visible as a diagonal line starting from bottom right to the top left. The KER/momentum of the iodine ion is dependent on the KER/momentum of the methylene ion and at the same time independent on the KER/momentum of the bromine ion. This supports the findings from the Newton diagram analysis.

3.5.5. Sequential bond breaking - short-lived states

Besides the two already described sequential channels II and III with long-lived intermediate states, we have evidence for two further sequential channels, denoted as IV and V. In Fig. 3.27 the two features are marked with blue solid lines (IV) and blue dashed lines (V) in the Newton diagram (left) and the Dalitz plot (right). In the following discussion, both representations are used side-by-side to argue that the channels IV and V are sequential fragmentation pathways with short-lived in-

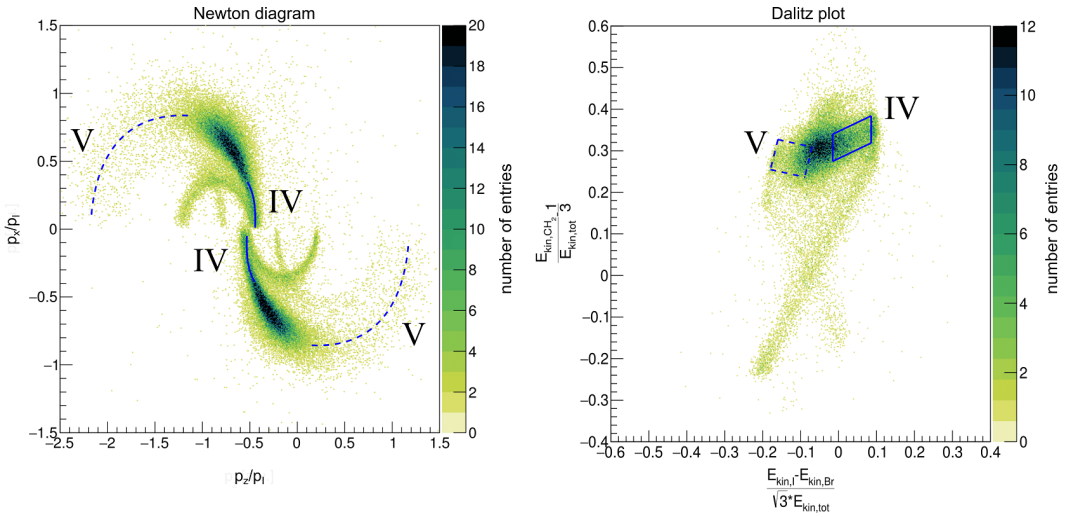

Figure 3.27.: Shown is a Newton diagram (left) and a Dalitz plot (right). In both representations channel IV is marked with blue solid lines and channel V is marked with blue dashed lines.

termediate states. The time-scale regarded here is one rotational period.

In contrast to the previously discussed sequential channels (II/III), events in channel IV and V are not that clearly separated in the two representations. Nevertheless, there are two main properties the following discussion is focusing on:

1. The shape of the respective momenta/energies in channel IV and V in the Newton diagram as well as in the Dalitz plot.
2. The overlap of the respective momenta/energies in channel IV and V with other previously discussed channels (I, II, III).

First, the shape of break-up processes from channel IV, marked with the blue solid lines in Fig. 3.27 is analyzed. In the Newton diagram (left) the resulting momenta of channel IV events form a curved line, starting at position $(-0.45,\ 0)$ for Br and $(-0.55,\ 0)$ for CH_2 and merge into the lobes of the momenta from the non-sequential Coulomb explosion channel I. In the Dalitz plot the energies from the same events form a broad line, starting from $(0.1,\ 0.35)$ and merge into the spot from the channel I data. In the Dalitz plot, it can be clearly recognized that the fundamental shape of channel IV events differs from the shape of channel I events as well as from the shape of channel II events. It is a line-shaped structure, but with a flatter slope, shorter and broader compared with the diagonal lines from the sequential break-up channel II. The channel V break-ups are marked with the dashed blue lines in both plots. In the Newton diagram, they form a curved line, too. The starting positions are $(-2.2, 0)$ for Br and $(1.2, 0)$ for CH_2. The momenta in channel V are not sharp as the momenta in channel IV but widespread. They merge into the lobes of the momenta from the non-sequential Coulomb explosion channel I similar as the channel IV momenta, but from the other side. In the Dalitz plot, channel V events form a wide, line-shaped structure starting from position $(-0.2,\ 0.3)$ and shading off into the events from the non-sequential Coulomb explosion channel I.

The structure marks the transition between the peak structure of channel I and the line structure of channel III, however, the basic shape is different from both of these two features.

Since channels IV and V cannot be separated completely, but overlap with the other channels, the type of overlap with the previously described fragmentation channels I, II and III is investigated in addition to the shape. If momenta/energies from two different channels appear at the same or close positions in the Newton diagram and in the Dalitz plot, most likely the underlying dynamics are the same or similar. In the Newton diagram as well as in Dalitz plot the channel IV events are overlapping with events originating from the non-sequential Coulomb explosion (channel I) at one end and reach the close vicinity of events from the sequential break-up with the long-lived intermediate CH_2Br^{*2+} (channel II) at the other end[9]. The different properties of channel IV and channel V events are listed in Tab. 3.7.

channel	Newton/Dalitz	overlap	dynamic
IV	ring/line	I and II	sequential break-up, short-lived CH_2Br^{*2+}
V	ring/line	I and III	sequential break-up, short-lived CH_2I^{*2+}

Table 3.7.: Properties of the channel IV and channel V events. The discussion is focusing on the basic shape of the structure in the Newton diagram and Dalitz plot representation (column 2) and the overlap with the other, previously discussed, channels I, II, and III (column 3). From these two properties conclusions on the dynamics are drawn (column 4).

Due to the clear similarity between the shape of channels IV/V and channels II/III, it is concluded that there are two additional sequential processes involved. The main difference is that for channel IV/V no complete ring structure is occurring in the Newton diagram, but more two partial rings merging into the lobes of the direct non-sequential Coulomb explosion from two sides (two lines merging into the spot of the direct Coulomb explosion in the Dalitz plot). In addition, the structures of channel II (III) and IV (V) are clearly separated in the Dalitz plot. Hence, we exclude that both, channel II and IV (III and V), are originating from the same break-up process. For channel II (III) it was argued that the intermediate CH_2Br^{*2+} (CH_2I^{*2+}) is created in a long-lived state. The fragment decays on time scales exceeding the rotational period, which is resulting in a homogeneous ring. The ion, which leaves in the first step, has no influence on the final break-up of the intermediate fragment. Channel IV (V) proceeds as well as a sequential process but with a short-lived intermediate state. The CH_2Br^{*2+} (CH_2I^{*2+}) fragment dissociates within one rotational period leading to a partial instead of a full ring structure. The short lifetimes of this intermediate state are close to the concerted bond breaking of the channel I fragmentation when nearly no rotation of the intermediate fragment took place. This results in the transition into the non-sequential Coulomb explosion

[9]In the same way, channel V events are overlapping with events originating from the channel I processes in one end and reach the close vicinity of events from the sequential break-up with the long-lived intermediate CH_2I^{*2+} (channel III) at the other end.

structure. When the second bond breaks, the ion which left in the first step is still in the vicinity of the intermediate and influences the break-up and the final momenta of the created ions. Hence, the line structures in the Dalitz plot are broadened.

The maximum time delay after the bond-cleavage, where the first leaving ion still influences the fragmentation process of the intermediate, can be estimated. First, the final momenta of the two final ions created in the second step, here CH_2^+ and Br^+, are studied under the influence of an I^+ ion in different distances[10]. We determined that the minimum distance of the iodine ion to the intermediate, at which the final momenta of CH_2^+ and Br^+ are independent of the I^+ ion, is reached at around $r_{\min} \approx 40\,\text{Å}$ (20 times the equilibrium distance). Considering a Coulomb repulsion between the two ionic particles after the first bond-cleavage ($CH_2Br^{-2+} + I^+$), the minimum distance $r_{\min}$ is reached within a time $t_{\min} \approx 1\,\text{ps}$. We conclude that the second bond-cleavage in the case of a short-lived intermediate state occurs on a faster time-scale.

In addition to the structure in the Newton diagram and the Dalitz plot, the kinetic energy release of channel IV and channel V break-ups are analyzed. In Fig. 3.28 the kinetic energy release of the fragments I^+ and Br^+ as well as the total KER is shown. The black curve is for all events, the red curve in panel (a) and (c) for events of channel IV and the blue curve in panel (b) and (c) for events of channel V. The kinetic energies are calculated from the momenta in the coordinate system of the complete molecule and all histograms are normalized to one. Events of channel IV show up in the lower part of the bromine KER distribution, as a peak centered at 1.2 eV. Based on this peak, the selection for the KER of the iodine fragment (red curve in panel (a)) and for the total kinetic energy distribution was done (red curve in panel (c)). The selected kinetic energy range is marked in the plot. The iodine KER for this selection is located at higher KER compared with the main peak, centered at a value of 2.9 eV (red curve panel(a)). In the first step of the fragmentation process the C-I bond is broken, similar to channel II. The iodine ion, as well as the CH_2Br^{*2+} ion, gain kinetic energy due to the Coulomb repulsion. The resulting momenta are oriented on the axis connecting the two particles and point in opposite directions. However, compared with channel II the CH_2Br^{*2+} is created in another intermediate state. The KER of the I^+ ion is sharp as for channel II but slightly shifted to a lower value of 2.9 eV (3.2 in channel II). In channel II CH_2Br^{*2+} is created in an intermediate rotating state with a broad kinetic energy distribution in the molecular frame. The cleavage of the second bond after a long lifetime leads to momenta of the particles distributed over an angle of 360°. In contrast to the events discussed here, the bromine ion has a sharper kinetic energy peaking at the lower edge of the spectrum. The intermediate fragment is dissociating before one rotation period is completed.

Events of channel V are leading to a peak in the iodine KER at low values centered at 0.5 eV (broad distribution for channel III). The data selection leading to the blue curves in panels (b) and (c) for channel V is based on this peak and marked in the

[10] We repeated the numerical calculation of the momenta resulting from three charged fragments which repel each other on a Coulomb potential, as performed in subsection 3.5.3. In the calculation we increased the C-I bond distance until the final momenta converge to a certain value.

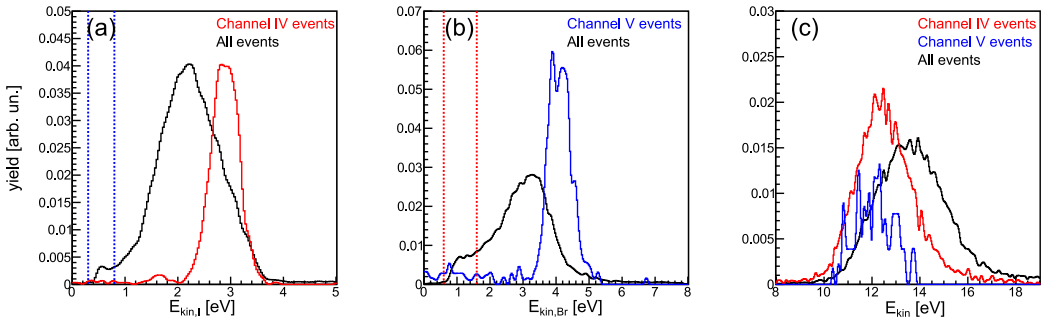

Figure 3.28.: Kinetic energy release of the bromine fragment (a), the iodine fragment (b), and the total kinetic energy release (c). Events of channel IV are drawn in red, events of channel V in blue. The KER of all events is shown in black.

plot. The bromine KER is located at higher KER than the main peak. It is centered at a value of 4.1 eV, (4.8 eV for events of channel III). The explanation follows the same arguments as for channel IV.

In a recent experiment, Ding *et al.* discovered a similar short-lived state in an intermediate doubly-charged fragment [86]. The authors ionized carbon monoxide dimers with ultrashort laser pulses (25 fs) and studied the three-body break-up channel $(CO)_2^{3+} \rightarrow C^+ + O^+ + CO^+$. A fast decaying intermediate state of CO^{2+} was found, which led to ring structures in a Newton diagram and merged into the peak structure of a non-sequential direct Coulomb explosion. Since this short-lived intermediate state of CO^{2+} is not present in direct double ionization of a CO monomer, the authors concluded that due to the sequential process other potential curves can be reached. The leaving CO^+ from the first bond cleavage disturbs the potential energy curves of the left CO^{2+} fragment and creates an avoided crossing. This opens a fast decay pathway for the CO^{2+} into C^+ and O^+ which is not present in the monomer. In analogy to the work of Ref. [86], we conclude that in the sequential processes detected here, the ion created during the first bond-cleavage influences the state of the intermediate doubly-charged fragment.

3.6. Summary

We investigated the fragmentation of CH_2BrI^{3+} following strong field ionization with femtosecond laser pulses in a reaction microscope. In the experiment, five different fragmentation channels have been detected, the direct non-sequential Coulomb explosion channel and four sequential channels. We could show, that both possible sequential pathways, where the C-Br bond or the C-I bond breaks first are present in the data and can be clearly identified. Besides the sequential channels with long-lived intermediate states, we found evidence for two other new sequential break-up processes with a short-lived intermediate state. The two bonds break with a short time-delay on the order of the rotational period of the molecule marking the transition between the direct non-sequential Coulomb explosion and the sequential

break-up pathways with metastable intermediate states. Further, we could show that the momentum vectors of the high energy part of the fragments reflect the geometry of the neutral molecule. This contribution corresponds to around 20 % of the filtered data. In an experiment focusing on the reconstruction of the geometry of the molecule, this high energy part of the data could be used to gain the structural information.

Chapter 4.

4 Time-resolved strong-field ionization of N_2O_4

4.1. Introduction

The strong-field ionization (SFI) of molecules depends strongly on the molecular geometry and hence, on the molecular vibration. An interesting object to study in this context is the dinitrogen tetroxide molecule (N_2O_4), since large amplitude vibrational motions can be induced in a non-resonant Raman process. In contrast to a resonant excitation where specific transitions are excited, a collection of states (rotational states within one vibrational mode) is populated in the excitation scheme in a non-resonant process. SFI is particularly suited to investigate such an ensemble since it probes all states at the same time. In this chapter, we present a detailed time-resolved study on the SFI of N_2O_4 which is vibrationaly excited in an impulsive stimulated Raman scattering (ISRS) process.

The influence of vibrations in N_2O_4 excited via an ISRS process on strong-field processes have been studied before [124–126]. It was shown that the structural change due to the N-N stretching motion in N_2O_4 influences the overall ion and electron yield in the SFI process [125] and the overall high harmonic generation (HHG) yield [124]. Furthermore, it modulates the generation of odd and even harmonics differently depending on the orientation of the molecule with respect to the laser field [126]. To fully understand the SFI/HHG in polyatomic molecules like N_2O_4 it is hence of high importance to explore the dynamics which influence these processes. The amplitude of the vibration, defining the extent of the structural change, is one key factor in these investigations. Spanner *et al.* [125] as well as Ferré *et al.* [126] estimated the vibrational amplitude resulting from an ISRS excitation based on the derivative of the polarizability of N_2O_4. In our experiment we provide the first experimental determination of the vibrational amplitude of the N-N stretching vibration in N_2O_4. Complementary to the mentioned works, we do not only measure the ion/electron yield or high harmonics yield but image the full momentum vector of created fragments in the process of SFI of N_2O_4. We extract information about the specific time-dependent kinetic energy release of the generated fragments. With the help of the known potential curves of the neutral and cationic molecule we are able to extract the information about the amplitude of the vibration from the experiment.

The chapter is structured as follows. After introducing the investigated molecule, a description of the setup, including details on the data processing, the detector, and the measurement conditions of the performed pump-probe experiment are given. Afterwards, the results of the experiment are presented and discussed.

4.2. Dinitrogen tetroxide

The experiment we describe in this chapter was done with the molecule dinitrogen tetroxide (N_2O_4). N_2O_4 exists in a chemical equilibrium with NO_2:

$$2NO_2 \rightleftharpoons N_2O_4. \tag{4.1}$$

By variation of the temperature and pressure the equilibrium can be shifted to the one or the other side (following Le Chatelier's principle [127]), but the single components can not be studied as pure substances. The covalent N-N bond in N_2O_4 is a weak bond with a comparatively large bond length of 1.75 Å [128] (In comparison: N_2H_4 has a N-N bond length of 1.47 Å [129]). N_2O_4 has a planar structure (D_{2h} point group) with nearly the same N-O bond distances (1.19 Å [128]) and O-N-O bond angles (134.46 ° [128]) as NO_2. Twelve vibrational modes of N_2O_4 are identified from spectroscopic studies. The respective symmetries, wavenumbers and whether they are Raman or IR active is listed in Tab. 4.1. In Fig. 4.1 a schematic illustration of the modes can be found.

no.	vibrational symmetry/mode		cm^{-1}	IR/Raman-active	reference
ν_1	a_g	N-O s-stretch in phase	1382.3 ± 3	Raman	[130]
ν_2	a_g	NO_2 bend in phase	807 ± 3	Raman	[130]
ν_3	a_g	N-N stretch	257 ± 3	Raman	[130]
ν_4	a_u	torsion	82	IR	[131]
ν_5	b_{1g}	N-O a-stretch out of phase	1718 ± 3	Raman	[130]
ν_6	b_{1g}	NO_2 rock out of phase	498 ± 3	Raman	[130]
ν_7	b_{1u}	NO_2 wag in phase	425	IR	[131]
ν_8	b_{2g}	NO_2 wag out of phase	657 ± 3	Raman	[130]
ν_9	b_{2u}	N-O a-stretch in phase	1756.76	IR	[131]
ν_{10}	b_{2u}	NO_2 rock in phase	265	IR	[132]
ν_{11}	b_{3u}	N-O s-stretch out of phase	1261.08	IR	[131]
ν_{12}	b_{3u}	NO_2 bend out of phase	755.37	IR	[131]

Table 4.1.: The vibrational modes of N_2O_4 [133]. The terms *in phase/out of phase* refer to the two NO_2 groups in the molecule. A schematic sketch of all listed modes can be found in Fig. 4.1. We excited the lowest Raman-active mode, the symmetric N-N stretching vibration (ν_3).

In our work, we excited the N-N stretching mode of N_2O_4 (ν_3). It is the strongest Raman-active mode with an energy of 257 cm^{-1} [130]. This corresponds to a frequency of $f = 7.7$ THz and an oscillation period of $T = 130$ fs. The potential curve of the neutral molecule and the cation along this vibration-axis is shown in Fig. 4.2 (adapted from Ref. [124]). In former works of other groups it was shown that N_2O_4 experiences an ionization probability which depends on the internuclear N-N distance R [125]. The ionization probability at the outer turning point of the

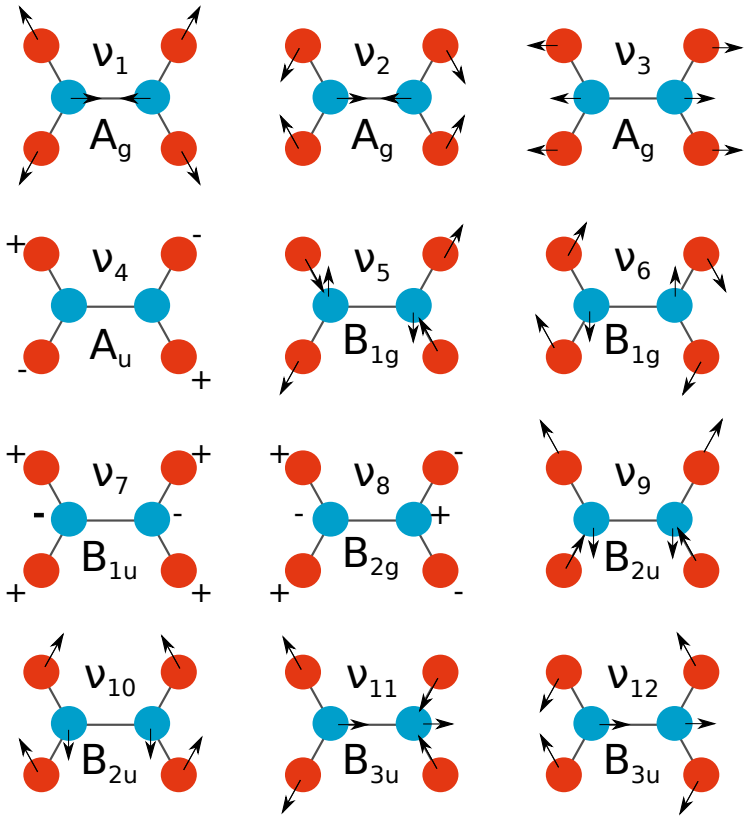

Figure 4.1.: Schematic sketch of the vibrational modes of N_2O_4, listed in Tab. 4.1. Figure adapted from Ref. [131].

N-N vibration is significantly higher as at the inner turning point. Furthermore, Spanner *et al.* showed that the overall probability for an ionization event to the final state A_g is around six times higher than an ionization event to the next higher B_{2g} state for all bond lengths [125]. This effect was assigned by the authors to the symmetry of the Dyson orbitals. The authors state that the Dyson orbitals of the stable B_{2g} state have a node along the dominant symmetry axis of the molecule (for all N-N bond lengths) which leads to a suppressed ionization rate. Since the A_g cationic state is not stable the molecule dissociates directly after the ionization process into the two fragments NO_2 and NO_2^+. Hence, in a pump-probe experiment, similar to the one performed in Ref. [125], where the pump-pulse excites the ν_3 N-N stretching mode in the neutral molecule and the probe-pulse ionizes the molecule, a modulation of the ion yield of NO_2^+ is detected.

We do not only measure the overall ion/electron yield or high harmonic yield but image the complete momentum vector of the created NO_2^+ fragments. We are using a detection system based on an in-vacuum pixel detector (Timepix, developed in the Medipix collaboration at CERN [134]) in combination with a recently developed high-repetition rate Optical Parametric Chirped-Pulse Amplification (OPCPA) laser system delivering 7 fs duration pulses [135]. In our experiment we can extract information about the specific time-dependent kinetic energy release of the fragments. Included in the shown potential curve (Fig. 4.2) is a schematic drawing of the probed dynamics.

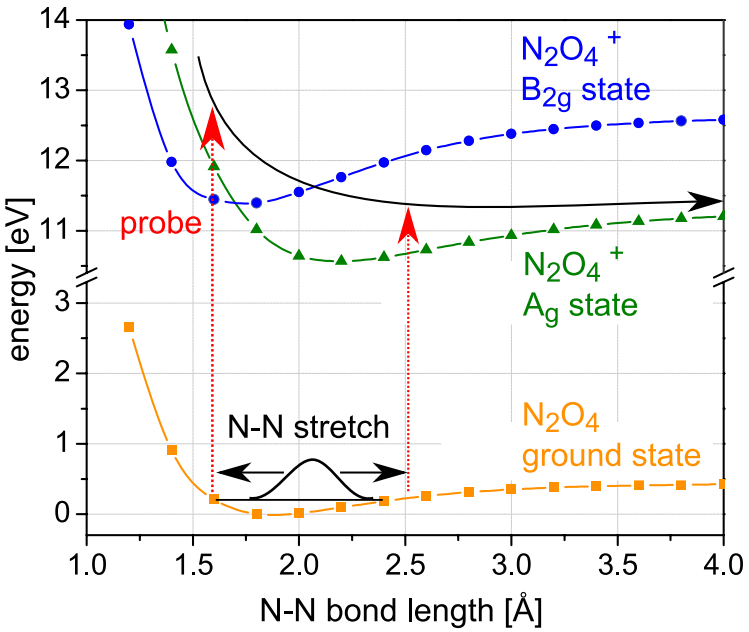

Figure 4.2.: Potential energy curve of N_2O_4 along the ν_3 vibration-axis, adapted from Ref. [124]. Molecules in the ground state are preferably ionized to the A_g cation state, where they start to dissociate to $NO_2^+ + NO_2$. There is a strong N-N bond length dependence of the ionization probability, with a higher chance of ionization at the outer turning point.

4.3. Experimental details

4.3.1. Setup

In the experiment we combine a quad-chip Timepix detector [26], a velocity map imaging (VMI) spectrometer [136], and a high repetition rate (400 kHz) laser system [135]. The description of the setup, the detector and the off-line data processing is based on the work of Long *et al.* [25], a recent publication on the first results on the imaging spectrometer containing all technical details. A schematic view of the setup and the detection system, taken from Ref. [25], is shown in Fig. 4.3.

A neutral gas jet is expanded through a small nozzle (diameter $d_1 = 20\,\mu\text{m}$) inside the source chamber in a supersonic expansion. The gas jet passes two skimmers ($d_2 = 100\,\mu\text{m}$, $d_3 = 1\,\text{mm}$), to maintain a vacuum of $\approx 5 \times 10^{-10}\,\text{mbar}$ in the reaction chamber with the gas inlet in operation. In this chamber, a velocity map imaging spectrometer is located which consists of three electrodes designed after Ref. [136]. The gas jet enters the VMI spectrometer between the repeller and extractor plate, on which high voltages ($U_r = 14\,\text{kV}$ and $U_e = 11\,\text{kV}$) are applied. The laser beam enters the reaction chamber perpendicular to the neutral gas jet. It is focused on the gas jet by a focusing mirror (focal length $f = 75\,\text{mm}$), placed inside the vacuum. All resulting ions from the interaction with the laser are accelerated out of the VMI electrodes into a 30 cm long field-free flight tube. At the end of the flight tube the combined detector, a double-stack MCP in chevron configuration and the Timepix detector at a distance of 1.2 mm behind the MCPs, is located. The reaction and detection chamber are separated by a small tube of 14 cm length and a diameter of 20 mm. This prevents an increase of the pressure in the reaction chamber due to outgassing of the Timepix detector printed circuit board. The vacuum requirements are most strict in the reaction chamber since here the strongly focused laser interacts with the molecular beam. Impinging fragments on the detector from background gas ionization lead to an additional disturbing signal.

The used laser system is home-built, based on an Optical Parametric Chirped Pulse Amplifier (OPCPA) [135]. OPCPAs have the advantage of amplifying a broad range of wavelengths, the possibility of achieving high gains already within a single pass through a nonlinear crystal, and small thermal effects in the gain material. These properties allow for the production of ultra-short pulses with high pulse energy at a large repetition rate. In coincidence experiments, as performed in chapter 3, there is the requirement of having less than one ionization event per laser-pulse and at the same time a high amount of measured data is needed to gain good statistics even for rarely occurring events. Hence, a laser system delivering pulses at a high repetition rate is of high advantage for coincidence pump-probe experiments[1]. Our system uses a non-collinear phase-matching mechanism (NOPA) allowing the phase-matching to work for a large wavelength range. The details of the OPCPA system can be found in Ref. [135]. It produces few-cycle pulses with a pulse length of 7 fs and a pulse energy of 12 µJ at a repetition rate of 400 kHz.

[1] The combined system of the imaging spectrometer and the laser system was designed for coincidence experiments. However, the performed measurement is not a coincidence experiment.

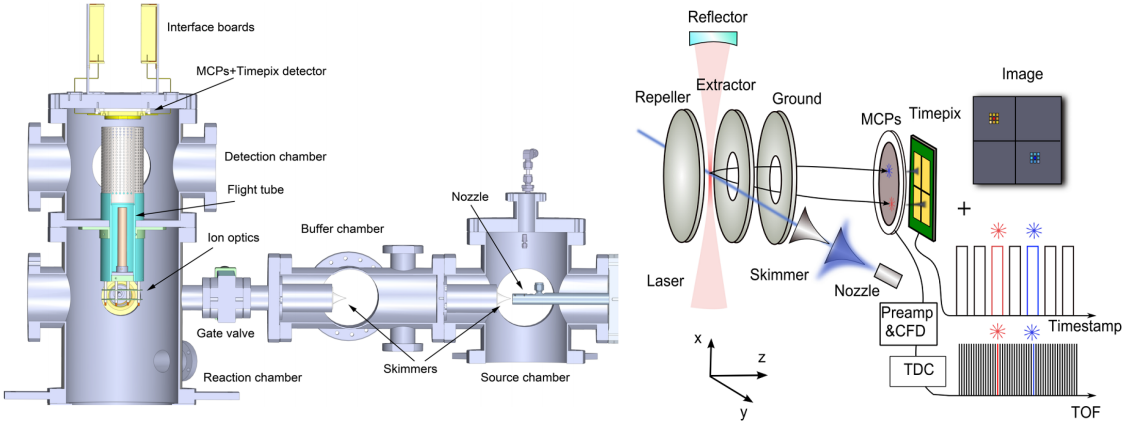

Figure 4.3.: Left: CAD drawing of the experimental setup. A neutral gas jet is expanded through the nozzle in the source chamber. After passing two skimmers it reaches the reaction chamber where it is overlapped with the laser beam inside a VMI (ion optics). Created ions from the laser-molecule interaction are accelerated upwards to the detection system. Right: Schematic drawing of the detection system with the combined MCP and Timepix detector. The recording of the time-of-flight by a timestamp of the Timepix detector in respect to a time-of-flight (TOF) measurement is illustrated. Both illustrations are taken from Ref. [25].

The part of the laser beam-path which includes the delay-stage is shown in Fig. 4.4. We split the output of the NOPA with a 60/40 beam splitter to generate the pump- and the probe-pulse. The weaker pulse (pump-pulse) is sent over a retroreflector, mounted on a motorized delay-stage (standa, 8SMC1-USBhF) and is combined afterwards again with the stronger pulse (probe-pulse). We control the stage by a home-written LabView program. The minimum step size of the stage is 0.5 µm leading to a total delay of 3.3 fs (the beam has to travel back and forth, hence the distance is doubled). A second manual delay stage is included in the beam-path of the stronger arm (probe), enabling a coarse adjustment of the time zero before the experiment.

4.3.2. Timepix detector

The Timepix detector is a CMOS technology-based chip detector developed at CERN [26]. The specific detector we use in this setup consists of four single chips. Each chip has 256 x 256 pixels with a pixel size of 55 µm x 55 µm leading to an active area of 28 mm x 28 mm. Each of the 262144 pixels can be read out individually in three different type of modes. Here, we use the Time-of-Arrival mode, enabling the use of an external trigger signal as a reference for the arrival time of a particle on the detector[2]. The detector works with a frame-based readout. Following an external trigger signal from the laser a shutter is opened and the detector starts recording

[2]The other two modes are the single particle counting and the Time-over-Threshold mode, see Ref. [25] or Ref. [26].

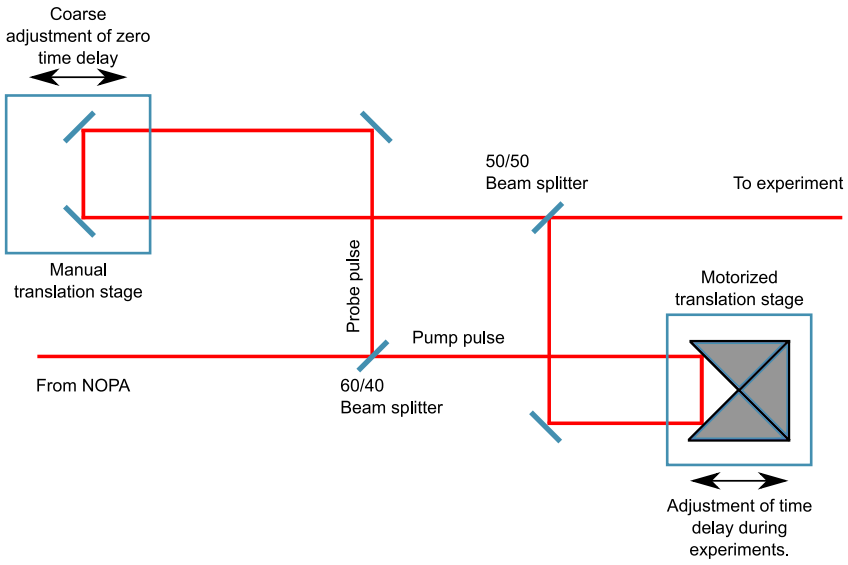

Figure 4.4.: The output beam of the NOPA is split into the pump- and probe-beam via a 60/40 beam splitter. The weaker beam (pump) is sent over a retroreflector mounted on a motorized delay stage, which is used in the experiment to adjust the delay. A second manual delay stage is included in the beam-path of the stronger beam (probe), enabling a coarse adjustment of time zero before the experiment.

incoming particles. These particles have to be recorded first by the MCP detector in front of the Timepix detector which leads to an electron cloud impinging on the chip. Each pixel where the electron signal reaches a certain threshold is regarded as active and the time of activation and the pixel position is stored. This leads to an inherent spatial resolution of 55 µm and a temporal resolution of 10 ns. All impinged pixels stay in the active mode until the shutter closes again and the data is read out. Everything recorded in this time span is called a frame. The shutter opening time is chosen to be 50 µs, leading to 20 laser pulses during one frame at a laser repetition rate of 400 kHz. During the closing time of the shutter, the frames are read out and all data are transferred to two interface boards and further to an acquisition computer. Between the recording of two frames there is a dead time of 286 µs of the detector. In addition to the time of activation of a single pixel, a so-called global time is stored, marking the specific recorded frame. In parallel to the position and time information collected by the Timepix detector, the time-of-flight of the created ions is directly gained from the back plate of the MCP stack. A high-pass filter is used to couple out the fast electric AC signal from an incoming particle but ignoring the DC voltage applied constantly on the back plate. This signal is amplified and passes a constant fraction discriminator first, followed by a fast time-to-digital converter (TDC). Further, the global time is stored at one TDC channel, too. In the following sections in this chapter, we refer to the data gained from the Timepix detector itself as TPX data while we refer to the time-of-flight information from the time-to-digital converter as TDC data.

4.3.3. Data processing

Off-line analysis: centroiding and correlation We process the recorded TPX and TDC data further in an off-line analysis to increase the spatial resolution to a sub-pixel range as well as the temporal resolution of the TPX data. First, a method called centroiding is applied to increase the spatial resolution. As mentioned before, a single pixel is recorded as active if the current of the electron cloud exceeds a certain threshold value. A single particle impact on the MCP results in not only one active pixel but an area of typically 8 x 8 active pixels. The center pixel experiences the highest signal, hence it is the first switched to the active mode. Due to that fact, there is a temporal distribution over the whole area of pixels activated from one single impinging particle. This time distribution can be used to find the impact position on the detector with a sub-pixel resolution. The centroided position is calculated as follows Ref. [25]:

$$x_c = \frac{\sum_{i=1}^{N} x_i \Delta T_i}{\sum_{i=1}^{N} \Delta T_i} \tag{4.2}$$

$$y_c = \frac{\sum_{i=1}^{N} y_i \Delta T_i}{\sum_{i=1}^{N} \Delta T_i}, \tag{4.3}$$

$$\tag{4.4}$$

where x_c and y_c are the centroided positions, x_i and y_i are the positions of the single active pixels resulting from the ion impact, ΔT_i is the difference of the time recorded at the ith pixel and the time recorded at the first activated pixel, and N is the total number of all active pixels. With this off-line centroiding mechanism a spatial resolution $< 6\,\mu m$ is achieved. In a first test Long *et al.* could even resolve the single channels of the MCP plate in front of the Timepix detector [25].

Besides the centroiding to increase the spatial resolution, we apply another off-line mechanism to increase the temporal resolution: the synchronization of the TPX time information with the TDC time information. The intrinsic temporal resolution of the Timepix detector is 10 ns, which is good enough to assign certain masses to the respective time-of-flight peaks but not to receive detailed information on the momenta of the particles. For that reason, in parallel to the Timepix time recording, the time-of-flight of the particles is read out from the MCP directly and fed into the TDC. The idea is, to use the TPX spatial information, and to replace the TPX timestamp with the information from the TDC. This leads to a much higher resolution in the picosecond range[3]. In contrast to the frame-based TPX data recording, the TDC data are stored continuously. To combine the TDC time information in an off-line data analysis with the spatial information of the TPX detector, we store the former mentioned global time in a second TDC channel. In

[3]The bin size of the TDC input channels is 25 ps. There was no final characterization of the temporal resolution done.

the off-line analysis, we apply a synchronization algorithm which compares a package of frames ($\approx$ 100) recorded with the Timepix detector with the list of recorded time data from the TDC. If the difference between the entries in the frame package and the TDC time list at a certain position is below a pre-set value, all stored TPX times in this package are replaced by the corresponding TDC times. This frame matching can be very critical, depending on the specific measurement and the fine-adjustment of the data recording from the TDC, as well as from the Timepix detector. After a particle is recorded by the MCP and an electron avalanche is set free, there are certain detection probabilities from both detection systems. Long *et al.* showed that for an average of 9-10 detected particles per frame with the Timepix detector around 6-7 particles are recorded with the TDC. This led to an average of 5 correlated (synchronized) events. The TDC threshold is set high, in order to avoid wrong entries from the noise of the MCP read-out circuit. Another detail to consider is that particles with the same flight time leave only one entry in the TDC recording, but can be distinguished by the chip if the two ions impinge at different positions. In this case, both time entries in the TPX data have to be replaced by one entry of the TDC data.

Momentum and kinetic energy calculation After all data are collected, centroided, and correlated for each ion recorded with the detector the momentum in all three dimensions is calculated. The calculation is done in the following way, based on Ref. [137]:

$$p_x = \alpha \frac{m\Delta x}{T} \tag{4.5}$$

$$p_y = \alpha \frac{m\Delta y}{T} \tag{4.6}$$

$$p_z = \beta \frac{(U_r - U_e)\, q}{d}\,(T_0 - T), \tag{4.7}$$

where m and q are the mass and charge of the respective particle, T is the respective flight time, and $\Delta x/\Delta y$ is the difference between the ion impact position and the center of the detector. U_r and U_e are the voltages on the repeller and extractor electrode of the VMI spectrometer and d is the distance between the two electrodes. The two coefficients α and β are introduced as correction factors because of the original spatial distribution of the parent molecules and inhomogeneities in the electric field. The coefficients were determined in Ref. [25] in a calibration measurement to

$$\alpha = 0.78 \pm 0.03 \tag{4.8}$$

$$\beta = 1.12 \pm 0.05. \tag{4.9}$$

From the calculated momenta (4.5), (4.6), and (4.7) we calculated the kinetic energy of the respective fragment via:

$$E_{\text{kin}} = \frac{1}{2}\frac{p^2}{m} \qquad \text{with} \tag{4.10}$$

$$p = \sqrt{p_x^2 + p_y^2 + p_z^2}. \tag{4.11}$$

In the first single pulse experiment performed with the detector by Long *et al.*, the group explored the two-body break-up of CO_2^{2+} in different channels in a coincident experiment [25]. The authors detected two different fragmentation channels into the reaction products $CO^+ + O^+$: (i) a fast Coulomb repulsion like decay, (ii) a slow dissociation channel. Additionally, a rare channel leading to the reaction products $C^+ + O_2^+$ was detected in the coincidence data.

4.3.4. Measurement conditions

In the measurement, we expanded dinitrogen tetroxide with a backing pressure of 0.4 bar - 1.0 bar through the nozzle into the vacuum system. The molecular beam was overlapped with the output of the laser system in the reaction chamber (see Fig. 4.3). The produced ions from the laser-molecule interaction were accelerated by the VMI to the combined detector system.

In Fig. 4.5 the characteristics of the two pulses we used in the experiment are given. Shown are SPIDER (Spectral phase interferometry for direct electric-field reconstruction, FC-SPIDER, APE GmbH.) measurements, where the measured traces were adjusted afterwards by calculating the effect of a passage through a plate of fused silica (thickness 200 µm), simulating the window of the machine. The pulses have a measured pulse length (FWHM) of around 7 fs (probe pulse) and 8 fs (pump pulse) and a bandwidth spanning a range from around 700 nm to 1000 nm. The temporal shapes of the pulses show pedestals on both sides of the peak pulse in a range up to around 60 fs delay with respect to time zero. We could adjust the power of both arms in a combined way using a polarizing attenuator in front of the first beam splitter. To adjust the power of both arms individually we used two irises placed in the two beams.

There are some challenges in estimating the intensity of the laser. For the estimation we took into account the measured average power and the beam size in the focus. The beam size is determined outside the chamber, using optics with the same focal distance as inside the chamber to focus the beam and to record images of the beam in the focal plane. With this, we determined a beam size of around 30 µm $\times$ 25 µm in the focal region. The measurement of the beam size is limited by the spatial resolution of the camera (pixel size 6.45 µm), the quality of the reproduction of the focus outside the chamber, and due to imperfections of the beam focus. To take into account the imperfections of the beam focus we estimated a spatial loss factor from the images of the beam ($l_{\text{spatial}} \approx 0.4$). The accuracy of l_{spatial} is limited by the signal-to-noise ratio of the camera. In addition, we included a temporal loss factor ($l_{\text{temp}} \approx 0.7$) due to the post- and pre-pulses, seen in the SPIDER traces in Fig. 4.5. l_{temp} was estimated from the relative contribution of the integral of the

temporal pulse shape between the two minima adjacent to the absolute maximum around $t = 0$ and the integration of the temporal shape between $-200\,\mathrm{fs}$ and $200\,\mathrm{fs}$. The accuracy of the temporal loss factor is limited by the SPIDER sensitivity at the low energy pedestals and by spatio-temporal couplings. With the two correction factors l_{spatial} and l_{temp}, we estimated that at full power the stronger probe pulse had an intensity $I \approx 2 \times 10^{13}\,\mathrm{W\,cm^{-2}}$ and the weaker pump pulse had an intensity of $I \approx 8 \times 10^{12}\,\mathrm{W\,cm^{-2}}$ in the laser focus. Regarding all limiting factors influencing the intensity estimation it is difficult to quantitatively verify the resulting uncertainties in the estimation.

Both pulses have a carrier wavelength of $\lambda = 790\,\mathrm{nm}$ and a pulse energy (right before entering the reaction chamber) of $0.6\,\mu\mathrm{J}$ (pump)/$1.4\,\mu\mathrm{J}$ (probe) at a repetition rate of $400\,\mathrm{kHz}$.

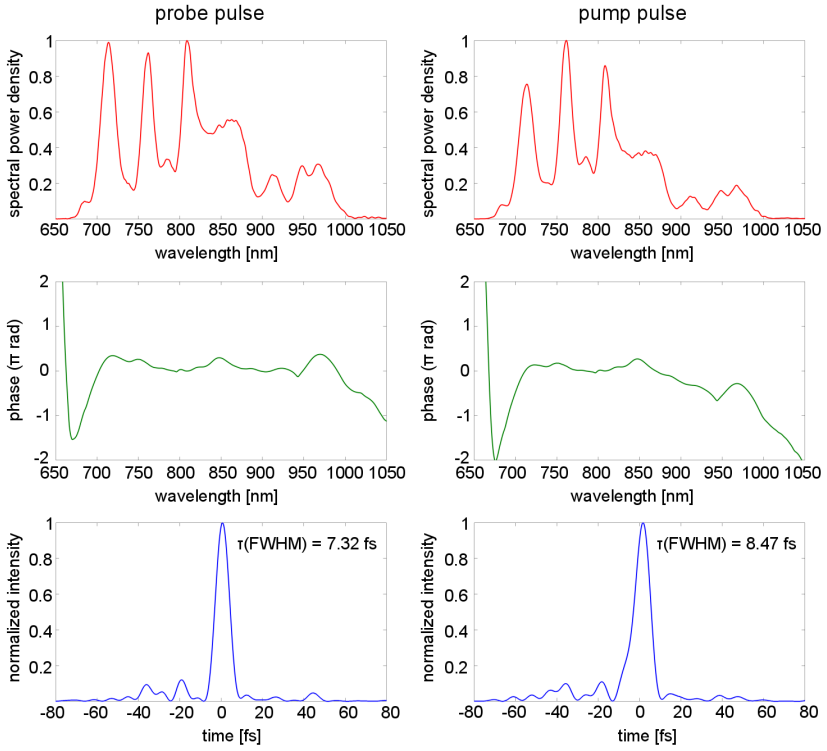

Figure 4.5.: SPIDER measurements of the two pulses. The measured traces have been corrected afterwards by calculating the effect of a passage through a plate of fused silica (thickness $200\,\mu\mathrm{m}$), simulating the window of the machine.

We did two types of experiments. First, we recorded only the TDC time-of-flight data at the full repetition rate of $400\,\mathrm{kHz}$. We recorded a long scan (in two loops), with delay times spanning a range of in total $3600\,\mathrm{fs}$ in 360 steps and a $10\,\mathrm{fs}$ step size. The backing pressure of the $N_2O_4 \rightleftharpoons NO_2$ mixture was $p = 1\,\mathrm{bar}$. In this measurement, we reduced the power of the probe pulse from $\approx 550\,\mathrm{mW}$ (full power) to $\approx 230\,\mathrm{mW}$ by lowering the opening of the iris placed in the respective beam path. The power of the pump pulse stayed the same for both measurements at $\approx 250\,\mathrm{mW}$. Due to the slightly different pulse lengths, the probe pulse kept a higher intensity

although the power was reduced ($\approx 9 \times 10^{12}\,\mathrm{W\,cm^{-2}}$). With a weaker probe pulse, the overall ionization probability decreases and hence, the modulation of the ion yield with the N-N distance becomes more clearly visible.

In the second measurement we recorded both data, the TDC time-of-flight data, and the three-dimensional TPX data. We took a scan spanning a whole delay variation of 1800 fs in 360 steps at a 5 fs step size. The shutter opening time for the Timepix detector was 50 µs, hence per frame the resulting ions of 20 pulses were recorded. With a 1 kHz frame readout this leads to an effective repetition rate of 20 kHz in the experiment. In the measurement recording the TDC data and the TPX data, the laser was running at full power with a backing pressure of the $N_2O_4 \rightleftharpoons NO_2$ mixture of $p = 0.5\,\mathrm{bar}$[4].

4.4. Vibration-dependent ion yield of NO_2^+

Before we start to analyze the time-dependent measurements, the mass spectrum resulting from strong-field ionization of N_2O_4 is introduced. In Fig. 4.6 a mass spectrum recorded with the TDC is shown. We assigned the three main peaks in the spectrum to the ionic fragments NO_2^+, NO^+, and O^+. As expected, the parent molecule does not show up in the spectrum because of the instability of the $N_2O_4^+$ ion in the A_g state. We performed the calibration of the mass axis following the same procedure as described in section 3.2 based on the peaks of NO_2^+ (46 u) and NO^+ (30 u). Based on the mass spectrum we filtered the data in the following analysis for certain species. The chosen time-of-flight range for NO_2^+ fragments is 1300 µs to 1500 µs.

In the first time-resolved measurement, we recorded only time-of-flight data, taken from the TDC, with the full 400 kHz repetition rate. With the measurement we aimed at confirming that vibrations in the ν_3 N-N stretching mode of N_2O_4 are excited with the used broadband laser pulses. In Fig. 4.7 the recorded yield of the ions NO_2^+ (black), NO^+ (red, multiplied by a factor 10), and H_2O^+ (blue, multiplied by a factor 250) is plotted as a function of the pump-probe delay. The delay stage was moved in steps of 10 fs scanning over a long range of 3.6 ps. At the time zero, when both pulses are overlapped temporally, a strong increase in the ion yield of all fragments is recorded. The delay axis was calibrated based on this increase. At approximately ±100 fs around time zero strong modulations in the ion yield appear in the measured signal. A known difficulty of the used laser pulses are pedestals in the pulse shape on both sides of the peak position of the pulse (see Fig. 4.5). Due to the same color of the pump- and the probe-pulse in the overlap region interference effects occur, leading to artifacts in the measurement. The width and shape of these artifactual modulations varied from measurement to measurement, and could not be

[4] We took a second scan under optimized conditions later, but the data recording broke down before the end of the measurement. This was resulting in too few statistics to draw physical conclusions, although the same features are indicated in this data set. Hence, here the results of a measurement are shown, which was not taken under optimized conditions but with more statistics. In addition to the higher laser power, the pressure of the $N_2O_4 \rightleftharpoons NO_2$ mixture was lowered in this measurement, shifting the equilibrium to the NO_2 side.

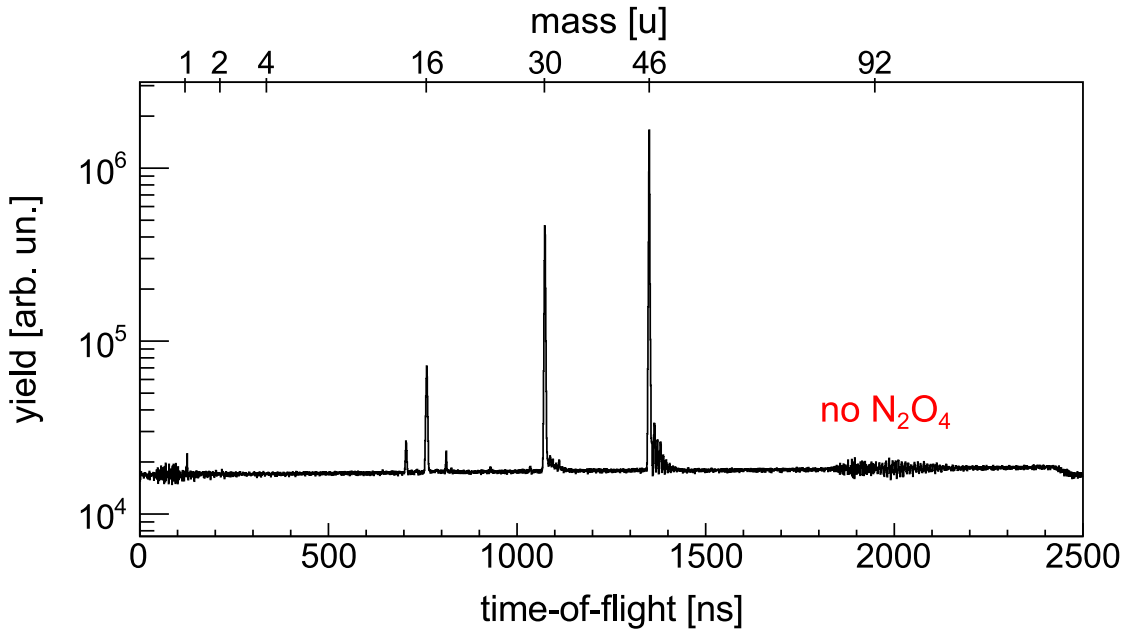

Figure 4.6.: The time-of-flight spectrum of N_2O_4 (TDC data). The three main peaks are assigned to the fragments NO_2^+, NO^+, and O^+. The parent molecular ion $N_2O_4^+$ is not detected in the spectrum.

reproduced on a regular basis. Hence, with the current setup it is crucial to explore a dynamic which is lasting for a longer time than the interference effects from the two laser pulses. Following the modulations from the time zero overlap, the yields of the fragments NO_2^+ and NO^+ are modulated with a clear oscillation at a period on the order of the expected N-N stretching vibration (130 fs). The inset of Fig. 4.7 shows an enlarged area of the histogram where the oscillations are most pronounced. In blue the yield of the water ions is shown, to compare the effect of molecules from the molecular beam, with molecules from the background gas. Effects of a variation of the measurement conditions (e.g. an unstable laser intensity) would show up in all ion yields, independent of whether the ions are originating from the molecular beam or from the background gas. The oscillation is only detected in the NO_2^+ and the NO^+ yield, the blue curve is flat. Hence, we exclude effects from the laser itself or from other variations of the measurement conditions. There is a dropout of the oscillation for longer times and also a decrease in the overall ion signal. At around 3200 fs delay time a sudden step-shaped increase in the signal occurs. The step is present for all observed ion signals, independent of whether they originate from the molecular beam or the background gas. Therefore we conclude that here external effects influenced the data recording. We did not further explore the increase.

For a quantitative analysis of the oscillations, we determined a Fourier transform (FFT) of the recorded signal from the ion yield. The result is plotted in Fig. 4.8 in black (NO_2^+) and red (NO^+). A clear peak centered at (7.75 ± 0.20) THz is detected, which corresponds to a time period of (129.0 ± 3.3) fs and level spacing of $(259.2 \pm 6.7)\,\mathrm{cm}^{-1}$. In the literature, the measured wave number of the anharmonic N-N stretching vibration of N_2O_4 varies from $254\,\mathrm{cm}^{-1}$ [138] to $265\,\mathrm{cm}^{-1}$ [130] in

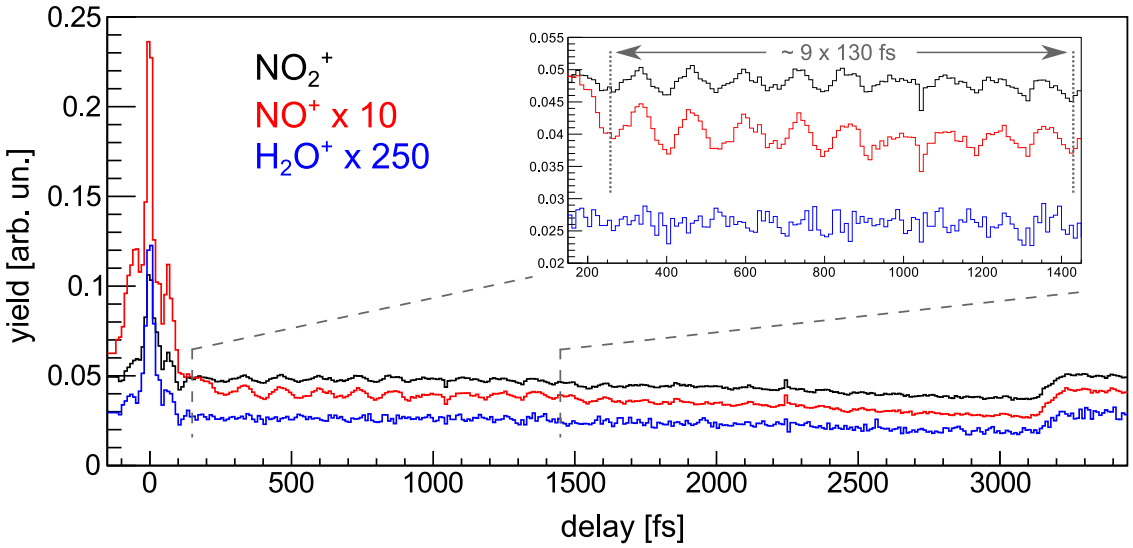

Figure 4.7.: Delay-dependent ion yield of NO_2^+, NO^+, and H_2O^+ from a measurement of the TDC data at the full repetition rate. At time zero when both laser pulses are overlapped, there is a strong increase in the ion yield. At greater time delays a clear oscillation in the range of the N-N stretching vibration period of N_2O_4 is detected in the ion yields of NO_2^+ and NO^+ but not in the ion yield of H_2O^+. The inset shows an enlarged area of the oscillation.

good agreement with the value detected here. From the detected oscillation in the ion yield we conclude that we excite the ν_3 N-N vibration in the current pump-probe experiment. In the next step, we analyze the three-dimensional TPX data gained in the second measurement to extract unknown information on the momenta and kinetic energy distribution of the fragments.

4.5. Time-dependent kinetic energy release of NO_2^+

In the combined TPX/TDC measurement we moved the delay stage in steps of 5 fs scanning a total range of 1.8 ps. We processed the data as described earlier in subsection 4.3.3: we synchronized the time information of the TPX data with the TDC data to increase the temporal resolution, and applied the centroiding algorithm to increase the spatial resolution.

Count rates During the process of data synchronization, there is a certain loss of accessible events. Not all events are detected with both the TDC and the TPX, and in addition, not all doubly detected events are recognized as a matched pair in the synchronization. The number of measured ions (uncorrelated) with the two detection systems is in the same range: we recorded 50736894 ions with the TDC and 62166944 ions with the Timepix detector. We recorded all data in an approximately

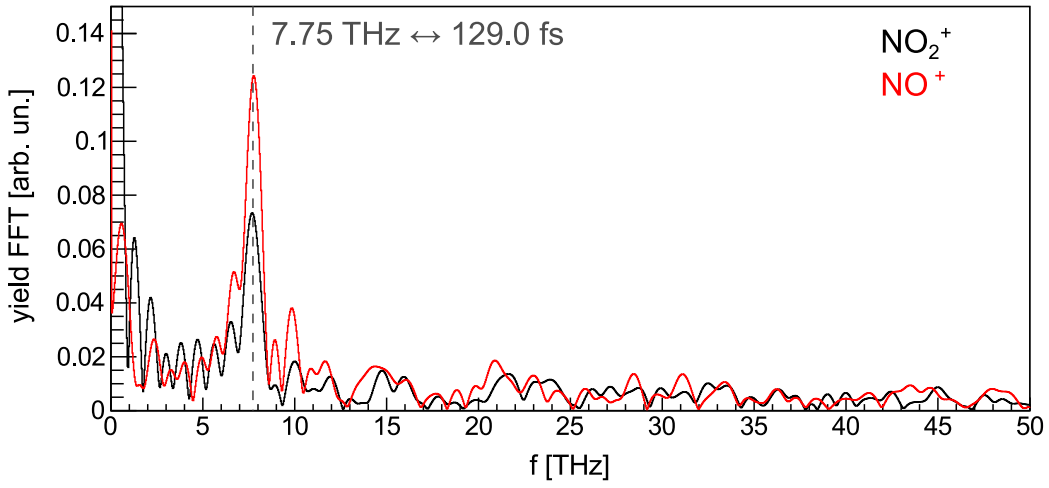

Figure 4.8.: Fourier spectrum of the ion yield signal shown in Fig. 4.7 for NO_2^+ (black) and NO^+ (red). There is a strong peak at 7.75 THz corresponding to an oscillation period of 130 fs.

640 minutes long measurement, leading to an effective ion count rate of approximately 1.3 kHz (TDC)/1.6 kHz (TPX). After the correlation procedure there are only 1478420 ions left, which we used for the further analysis. Hence, an effective ion count rate of 37 Hz is reached[5]. Considering the high repetition rate of the laser of 400 kHz and the effective repetition rate of 20 kHz of the detector-laser combination in the current configuration illustrates that there exist some serious teething troubles with the new machine, especially regarding the data recording and processing. First, the overall count rate of the uncorrelated data can be increased. For conducting coincidence experiments detection rates of less than one ion per laser pulse are desirable. In the experiment done here, we reach rates of around 0.07 (TDC)/0.08 (TPX) ions per laser pulse. Hence, by increasing the laser intensity it should be possible to increase the overall amount of data gained in the same time by a factor of around ten. Furthermore, we do not apply a coincidence condition in the measurement performed here allowing even higher ionization rates. The more severe loss in the measurement done here comes from the synchronization procedure. Around 97 % of the uncorrelated TDC and TPX data are discarded in this process. In the first measurement of Long *et al.* on CO_2 a lower loss of around 50 % (30 %) from the uncorrelated TPX (TDC) data to the correlated data has been reported [25]. In the experiment described here we did not identify the reason for the low efficiency in the correlation process so far. Further investigation has to be done.

[5]In our measurement, it is expected that the prevailing break-up process leads to one singly-charged NO_2^+ ion. Hence, the ion count rate and the event rate are in a similar range.

4.5.1. The integrated kinetic energy release

We calculated the momenta and the kinetic energy release of the NO_2^+ fragments from the correlated data set, based on the procedure described in 4.3.3. In Fig. 4.9 the resulting integrated kinetic energy release of all NO_2^+ fragments is shown. We identify two peaks: a strong peak centered at 0.14 eV and a weaker peak centered at 2.65 eV. This is consistent with Fig. 4.10 where the ion impact position on the detector is plotted. The low kinetic energy peak in Fig. 4.9 corresponds to the two structures in the middle of the histogram in Fig. 4.10 with the highest density of recorded data. The high energy peak in Fig. 4.9 corresponds to the ring-structures in the outer part of Fig. 4.10. The laser polarization was nearly parallel to the x-axis of the detector with a small tilt of $\approx 10\,°$. The tilt is originating from the mounting of the detector, which is not exactly parallel to the axis of the machine. The lines crossing the detection-image in Fig. 4.10 at $x \approx 256$ px and $y \approx 256$ px mark the borders between the four chips of the detector. The gap of 180 µm between the chips gets partly filled in the off-line data processing by the centroiding algorithm. The grid-structure visible in Fig. 4.10 is originating from a grounded mesh which is located in front of the MCP detector to reduce the influence of the high-voltage applied to the MCP plates on the field-free drift zone in front of the detector.

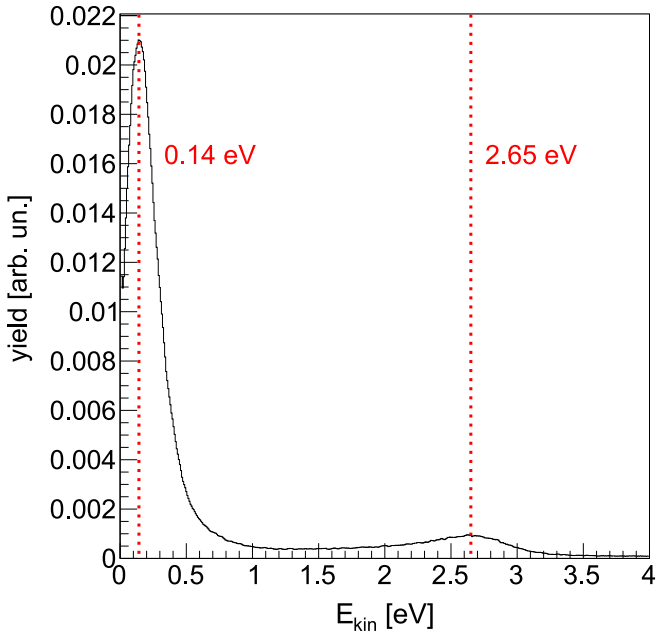

Figure 4.9.: The integrated kinetic energy distribution of NO_2^+ fragments. There are two peaks visible: a strong peak centered at 0.14 eV and a weaker peak centered at 2.65 eV. This points towards two different break-up mechanisms with (i) one charged NO_2^+ ion and (ii) two charged NO_2^+ ions repelling each other.

The two peaks in the kinetic energy release point towards two break-up mechanisms with different final states: (i) two charged NO_2^+ fragments, repelling each other due

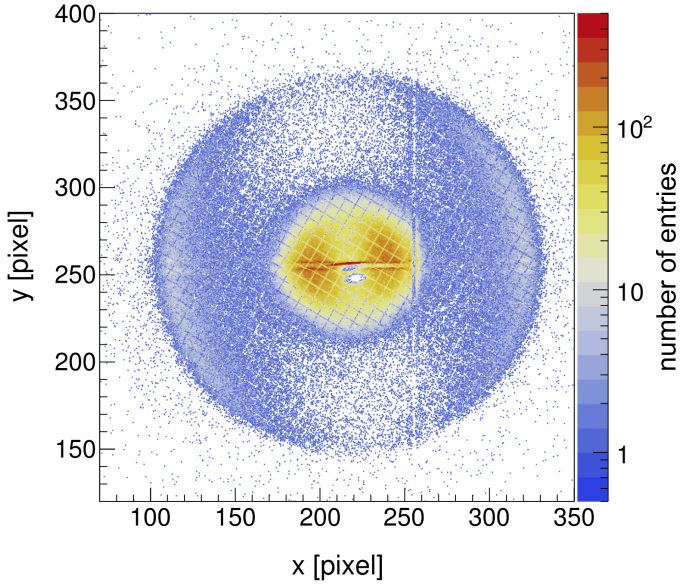

Figure 4.10.: The spatial image of impinging NO_2^+ ions on the detector. The two central spots with the highest density of data points are in accordance with the low energy peak in Fig. 4.9 while the outer ring structure is in accordance with the high energy peak in Fig. 4.9.

to the Coulomb potential and (ii) one charged NO_2^+ fragment and one neutral NO_2 fragment:

$$\text{(i)}\, N_2O_4^{2+} \rightarrow NO_2^+ + NO_2^+ \tag{4.12}$$

$$\text{(ii)}\, N_2O_4^+ \rightarrow NO_2^+ + NO_2. \tag{4.13}$$

4.5.2. Difference-spectrum of the kinetic energy release of NO_2^+ ions

To get insight into the variation of the kinetic energy distribution with the variation of the time delay between the two pulses, we calculated the KER for each time step of $\Delta t = 5\,\text{fs}$ and normalized it to one. We applied a sliding average on each graph. Hence, every bin shows the averaged entry of the original bin and the two neighboring bins. We combined the resulting set of 360 one-dimensional graphs to a two-dimensional graph, showing the normalized KER distribution as a function of the time-step Δt. It is shown in Fig. 4.11.

There are three contributions detected in Fig. 4.11. The strongest feature shows up in the lower energy part, fitting the highest peak in Fig. 4.9. It is a flat band with no detected variation with the time-delay. The second constant feature is a band at high energies, fitting the peak at 2.65 eV in Fig. 4.9. Besides the strong band in the lower energy regions, and the weaker band in the high energy regions, in Fig. 4.11 also a time-dependent decay between both areas is observed. The feature starts

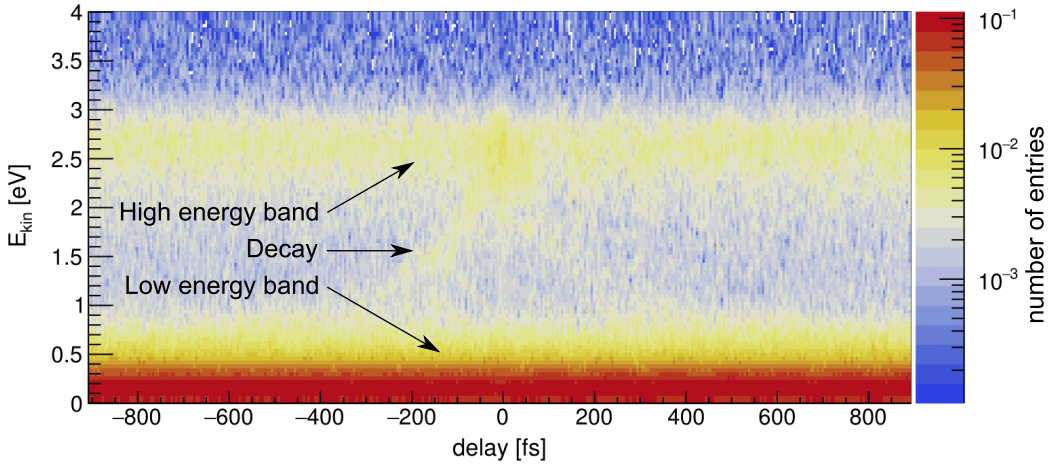

Figure 4.11.: Kinetic energy distribution of NO_2^+ fragments for varying time delays Δt between the two pulses. There is a high energy band and a low energy band which both show no time-dependence in this representation. In addition, there is a time-dependent decay visible between the two bands.

at time zero at the high energy band and decreases with an increasing time-delay (in both directions) to the low energy band. However, no variation in the kinetic energy distribution pointing towards the influence of the N-N stretching vibration can be detected in Fig. 4.11. A common method to make smaller changes in the KER distribution more visible is to analyze the normalized intensity of the KER at a certain time-delay Δt with respect to the overall time-integrated intensity of the KER:

$$I'(E_{\text{kin}}, t) = I(E_{\text{kin}}, t) - \langle I(E_{\text{kin}}, t) \rangle_t \tag{4.14}$$

Hence, we subtracted the integrated and normalized kinetic energy distribution shown in Fig. 4.9 from the data shown in Fig. 4.11. This results in the graph shown in Fig. 4.12.

Comparing the difference-spectrum in Fig. 4.12 with the total KER spectrum in Fig. 4.11 two main differences can be pointed out: (i) the high energy band is not present anymore and (ii) an oscillation in the lower energy band ($E_{\text{kin}}(t) < 0.4\,\text{eV}$) is clearly visible for positive time-delays. The decay detected in Fig. 4.11 is still present in Fig. 4.12. It starts at time zero with a kinetic energy of around 3 eV and merges into the low energy band in the outer parts. Since the high energy band shows no time-dependent behavior it is not further investigated. We analyze the other two features, the decay and the oscillation, separately in the next subsections.

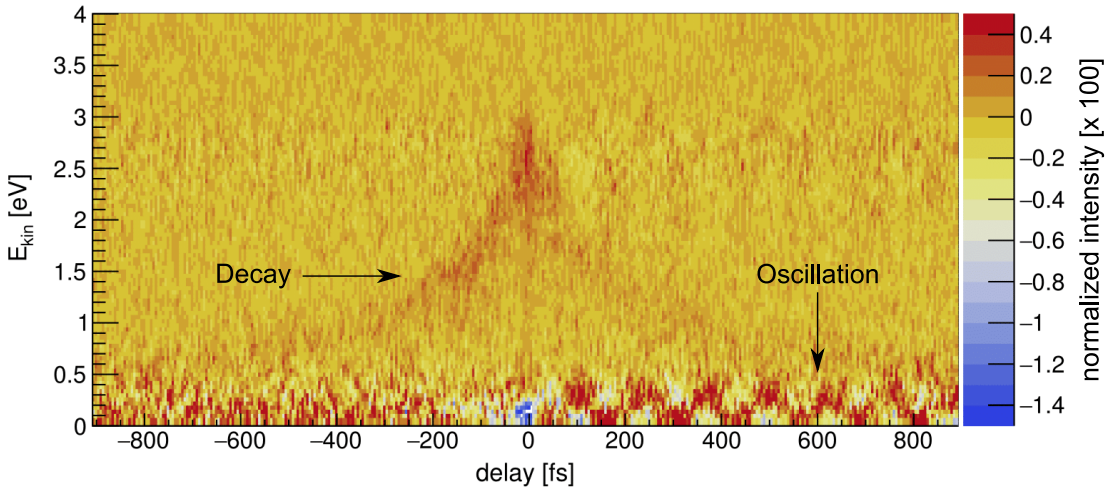

Figure 4.12.: Difference-spectrum of the delay-dependent variation of the KER of NO_2^+ ions. Shown is the normalized intensity $I'(E_{\mathrm{kin}}, t)$ for each time step (see Eq. (4.14)). An oscillating feature at low energies is detected for positive time-delays. In addition, a decay starting at time zero at around 3 eV to the lower energy part is visible.

4.5.3. Time-resolved probing of the 2-body Coulomb repulsion $NO_2^+ + NO_2^+$

Feature one points towards a time-resolved detection of the two-body dissociation of $N_2O_4^{2+}$ into two NO_2^+ fragments that repel each other as a result of their Coulomb interaction. This contribution can arise in the following way: The first laser pulse singly ionizes the parent molecule which starts to dissociate. The second laser pulse ionizes the separating fragments again, leading to two charged fragments:

$$\begin{aligned} N_2O_4 &\rightarrow N_2O_4^+ && \text{first laser pulse} \\ N_2O_4^+ &\rightarrow NO_2^+ + NO_2 && \text{dissociation} \\ NO_2^+ + NO_2 + &\rightarrow NO_2^+ + NO_2^+ && \text{second laser pulse} \end{aligned} \tag{4.15}$$

The two charged fragments repel each other on a $1/r$ Coulomb potential, where r is the distance between the two fragments. Depending on the time delay of the pump and the probe pulse, the system $NO_2^+ + NO_2$ had time to separate in two individual fragments, leading to a reduced KER in the repulsion. In the limit for long time-delays between the two pulses and hence, long distances r between the two fragments the Coulomb repulsion does not influence the break-up anymore. The two NO_2^+ fragments reach a KER which is purely defined by the dissociation due to the ionization by the first laser pulse. From the integrated KER in Fig. 4.9 is was seen that the KER gained by the fragments in the dissociation is 0.14 eV.

In the limit $\Delta t \rightarrow 0$ the kinetic energy of the two charged fragments can be

calculated using the Coulomb potential E_C:

$$E_C = \frac{1}{4\pi\epsilon_0}\frac{q_1 q_2}{r}, \tag{4.16}$$

with the vacuum permittivity ϵ_0, the charge of the two fragments q_i, and the distance between the two fragments r. With $r = 2.42\,\text{Å}$, the distance between the two center-of-masses of the two NO_2 components in the neutral molecule, the Coulomb energy is $E_C = 5.94\,\text{eV}$. Hence, each fragment gains a kinetic energy in the break-up of $E_{\text{kin},NO_2^+} = 2.97\,\text{eV}$. The high energy peak in Fig. 4.9 is centered at 2.65 eV, slightly below the calculated Coulomb energy. Deviations from the expected kinetic energy in a Coulomb explosion have been discussed before (see section 2.2 and section 3.5). Besides the mentioned effects of e.g. moving nuclei during the ionization process or deviations from a purely Coulombic potential, in the case discussed here in addition the localization of the charge within one NO_2^+ fragment has to be considered as a crucial point. In Eq. (4.16) we chose the distance between the two center-of-masses of the two NO_2 components in the neutral molecule for the parameter r, which leads to an overestimation of the Coulomb energy. Regarding the short pulses we use for the ionization, we assume a frozen molecular structure during the ionization process. Hence, a better estimation for the distance r between the two fragments would be the calculation from the measured kinetic energy via:

$$r = \frac{1}{4\pi\epsilon_0}\frac{q_1 q_2}{E_{\text{kin},NO_2^+}}\frac{1}{2} \tag{4.17}$$

$$= 2.72\,\text{Å}, \tag{4.18}$$

where $E_{\text{kin},NO_2^+} = 2.65\,\text{eV}$ is the measured kinetic energy release of one NO_2^+ fragment in the process $N_2O_4^{2+} \rightarrow NO_2^+ + NO_2^+$.

In general, the Timepix setup was built for coincidence experiments, as shown in Ref. [25]. In a coincidence measurement with an event-by-event based analysis, single events fulfilling certain break-up criteria can be filtered from the complete data set. Hence, it should be possible to select directly events with two NO_2^+ ions as reaction products. However, it became apparent in the current measurement that selecting only events containing two fragments leads to a heavily reduced data set. Filtering only events with two ions in the time-of-flight range of NO_2^+ leads to an additional loss of data of around 90 %[6]. In addition, in the filtered data set for events with exactly one ion in the time-of-flight range of NO_2^+ the decaying feature described here is still present. Hence, we concluded that due to the loss of events during the synchronization, we lose also the ability to carry out a coincidence experiment in this specific measurement.

[6] With no filter on the momentum sum applied, as done in the experiment on CH_2BrI, described in the former chapter 3.

4.5.4. Impact of the N-N stretching mode on the kinetic energy release of NO_2^+

The second feature mentioned before is the oscillation in the KER for positive delays in the region $0\,\text{eV} \leq E_{\text{kin}} \leq 0.4\,\text{eV}$. The oscillation period is in the range of the period of the ν_3 N-N stretching vibration of N_2O_4 ($\approx 130\,\text{fs}$). To confirm that we are detecting a variation of the KER due to the ν_3 vibration which was excited in an impulsive stimulated Raman process we analyzed the frequency and the phase of the detected oscillating feature.

To get information on the oscillation period and phase, we calculated the average position in the area $0\,\text{eV} \leq E_{\text{kin}} \leq 0.4\,\text{eV}$ for each time-delay. In a first step, we shifted all entries plotted in Fig. 4.12 by the absolute value of the overall minimum m of the graph to receive only positive values. The respective area of the original graph and of the resulting graph is shown in Fig. 4.13.

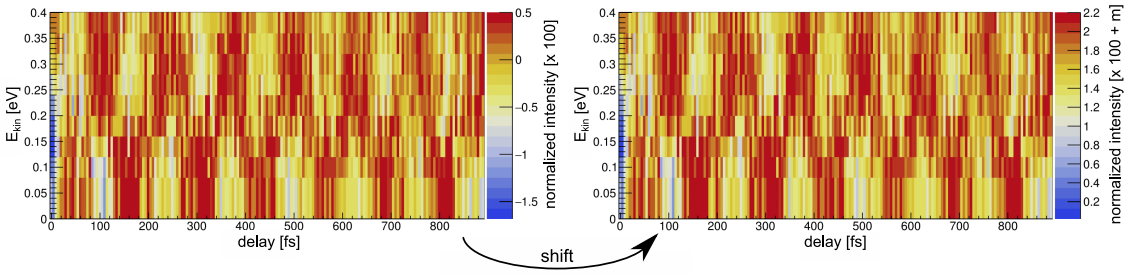

Figure 4.13.: Reproduction of the graph in Fig. 4.12 in the area $\Delta t > 0$ and $E_{\text{kin}} < 0.4\,\text{eV}$ (left) and the same plot with all entries shifted by the number $m = 1.70156$ (right).

In the second step, we calculated the average y-position $A_y(\Delta t)$ as a function of the time-delay Δt in the following way:

$$A_y(\Delta t) = \frac{\Sigma_{i=1}^{N} E_{\text{kin}}(\Delta t, i)\, k(\Delta t, i)}{\Sigma_{i=1}^{N} k(\Delta t, i)}, \tag{4.19}$$

where i denotes the i^{th} bin in the y-direction, N is the total number of bins in the y-direction, and $k(\Delta t, i)$ is the respective bin entry at the position $(\Delta t, i)$. The calculated average position $A_y(\Delta t)$ is plotted in Fig. 4.14. It reproduces the oscillation detected in Fig. 4.12. From this figure, we calculated the fast Fourier transform to get information on the frequency of the oscillation. The output of the FFT is plotted in Fig. 4.15. There is one strong peak located at a frequency of $f = (7.70 \pm 0.20)\,\text{THz}$, which corresponds to an oscillation period of $T = (129.9 \pm 3.4)\,\text{fs}$, and an energy of $(257.5 \pm 6.7)\,\text{cm}^{-1}$. These values are fitting the literature values for the N-N stretching vibration of the neutral N_2O_4 molecule [124, 125, 130, 138] and are in agreement with the values determined in the TDC measurement described in section 4.4 of $f = (7.75 \pm 0.20)\,\text{THz}$, $T = (129.0 \pm 3.3)\,\text{fs}$, and $E = (259.2 \pm 6.7)\,\text{cm}^{-1}$.

There are two processes to excite vibrations in a neutral molecule in the pump

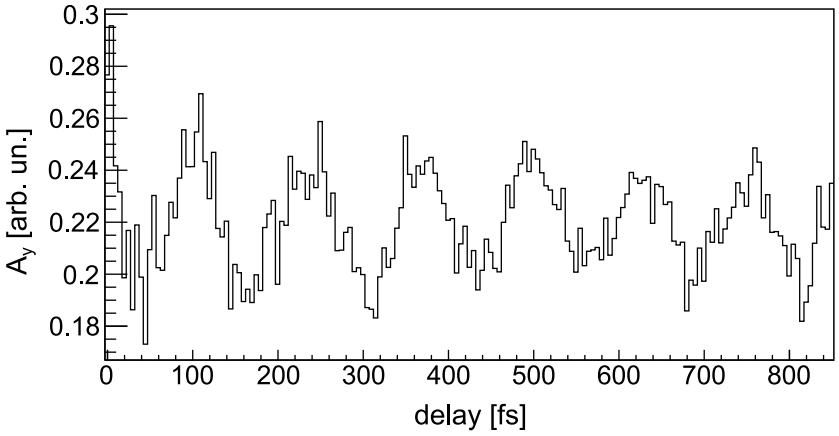

Figure 4.14.: The average position $A_y(\Delta t)$ calculated as function of the time-delay Δt in the selected area in Fig. 4.12 ($E_{\text{kin}} < 0.4\,\text{eV}$.) The graph reproduces the oscillation detected in Fig. 4.12.

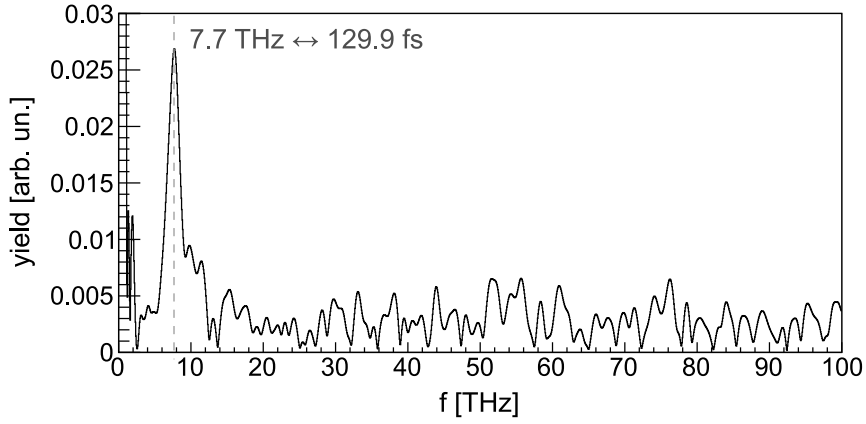

Figure 4.15.: FFT of the oscillation shown in Fig. 4.14. A strong peak at 7.7 THz is detected, which corresponds to an oscillation period of 129.9 fs.

step which can be probed by ionization in probe step[7]. First, via an impulsive stimulated Raman scattering (ISRS) process [79, 139] and second, via a Lochfrass process [140, 141]. Which mechanism is the underlying process in our measurement, can be determined via the phase of the oscillation. The theory of an ISRS process was given before in section 2.4. It is possible to convert the spontaneous (anti-)Stokes Raman process into a stimulated process if two photons with a difference-frequency, matching the needed excitation frequency of the vibration, are present at the same time. Therefore, a broadband laser pulse is needed for the excitation. An ISRS process is a scattering process and the vibration starts at the equilibrium position of the molecule. The momentum transfer due to the scattering and the resulting initial-direction of the excited vibration in an ISRS process can be determined based on the concept of a classical harmonic oscillator with an external impulsive force due to the electric field of the short laser pulse [79]. In Ref. [125] it was calculated that the N-N vibration starts with an outward stretch with an amplitude of the vibration $R_{\mathrm{min}}/R_{\mathrm{max}} = -0.14/0.18\,\text{Å}$. Hence, the maximum distance $R_{\mathrm{max}} = 1.93\,\text{Å}$ of the two NO_2 components is reached after a quarter period $T/4 = 32.5\,\mathrm{fs}$. The maximum in kinetic energy, on the other hand, is gained at the minimum N-N distance. In a vertical excitation scheme the highest kinetic energy release occurs when the molecular ion is created at a point on the A_g potential curve at the inner turning point (see Fig. 4.2). Hence, in an ISRS process, the first maximum in the kinetic energy distribution would be expected to appear at $t_{\mathrm{max}} = t_0 + 97.5\,\mathrm{fs}$.

In molecules with an R-dependent ionization probability also a second process, termed as *Lochfrass* [140, 141], can initiate vibrations. In such a process the neutral wave packet is bleached at the position with the highest ionization probability, leading to the formation of a vibrational wave packet in the neutral state. In a Lochfrass process the phase of the oscillation differs from the phase in an ISRS process. Due to the bleaching of the wave packet at the position R with the highest ionization probability, which is in the case of the N-N vibration of N_2O_4 at the outer turning point, the oscillating wave packet would be created at the inner turning point with an initial velocity directed towards the equilibrium position. The maximum of the kinetic energy release would be expected at $t_{\mathrm{max}} = t_0$ and $t_{\mathrm{max}} = t_0 + 130\,\mathrm{fs}$.

In Fig. 4.16, an additional oscillatory curve is shown (dotted, white), with the frequency that was observed in the FFT, an amplitude of 0.2 eV, and a phase corresponding to an ISRS process. It matches the measured data, hence we conclude that the prevailing excitation process is an ISRS process.

4.5.5. The amplitude of the N-N stretching vibration

In Ref. [125] it was reported that during the anharmonic N-N stretching vibration following an excitation of N_2O_4 in an ISRS process the N-N bond can contract by 0.14 Å and can extend by 0.18 Å. The numbers are a result of calculations of the momentum transfer to the molecule, based on the derivative of the polarizability of

[7] We exclude, that a vibration is excited in the cation by ionization in the pump step since the cationic state in the parent molecule is not stable, as seen from the time-of-flight spectrum in Fig. 4.6.

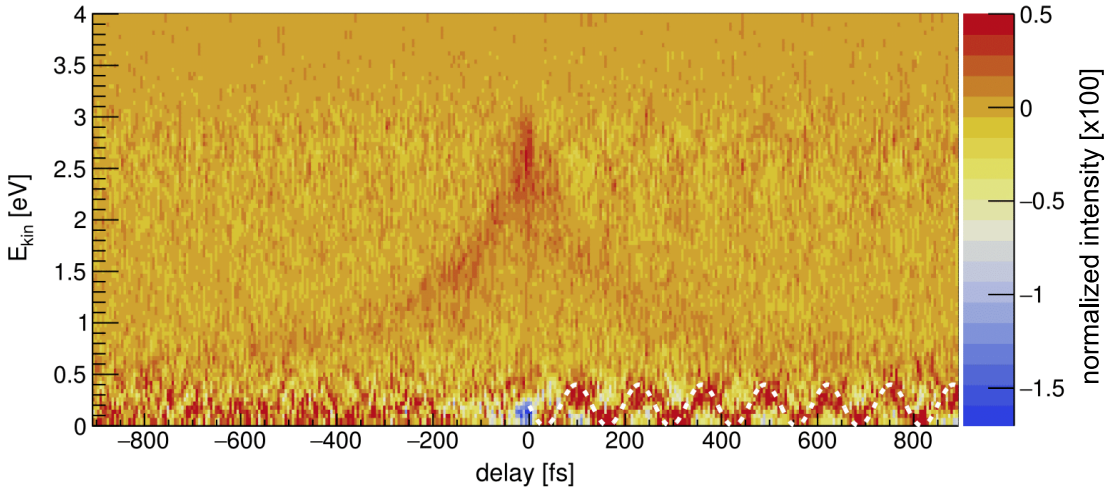

Figure 4.16.: Reproduction of the graph shown in Fig. 4.12. The additional dotted white curve has the oscillation frequency gained from the FFT of the average KER and a phase expected from an ISRS excitation process.

dinitrogen tetroxide. From the kinetic energy release in the pump-probe experiment on the N_2O_4 molecule described here, we can gain an experimental value of the vibrational amplitude at the inner turning point. To extract the amplitude of the oscillation in the kinetic energy we will have a closer look at the original data shown in Fig. 4.11. In Fig. 4.17 an enlarged detail of the kinetic energy release as a function of the time-delay (top) and its three-dimensional representation (bottom) are plotted in the interesting area. In this representation the same oscillation as shown in Fig. 4.12 is detected, although the feature is less distinct. In the three-dimensional representation the oscillations are visible until a maximum kinetic energy release of (0.44 ± 0.08) eV as indicated with the dotted line. The error is estimated from the bin size of the plot. Since the features are not well pronounced, we estimate a large error of $\pm$ four bins (with a bin size of 0.02 eV). The shown energy is the KER of one NO_2^+ fragment. Therefore, both fragments carry a total KER of (0.88 ± 0.11) eV together. In Fig. 4.18 the significant potential curves of N_2O_4 are shown (adapted from Ref. [124]). Marked is the energy that results in a KER of 0.88 eV for a dissociation to R_∞. From the maximum kinetic energy release of (0.88 ± 0.11) eV and the potential curves of N_2O_4 the minimum N-N bond distance of (1.56 ± 0.04) Å and hence, a vibrational amplitude of (0.19 ± 0.04) Å at the inner turning point is gained. We expect that with a repeated measurement with a higher statistical power the oscillations will be clearer visible and hence, a more accurate determination of the vibrational amplitude is possible.

4.6. Summary

We investigated the strong-field ionization of N_2O_4 in a pump-probe experiment with few-cycle laser pulses using a velocity map imaging spectrometer combined

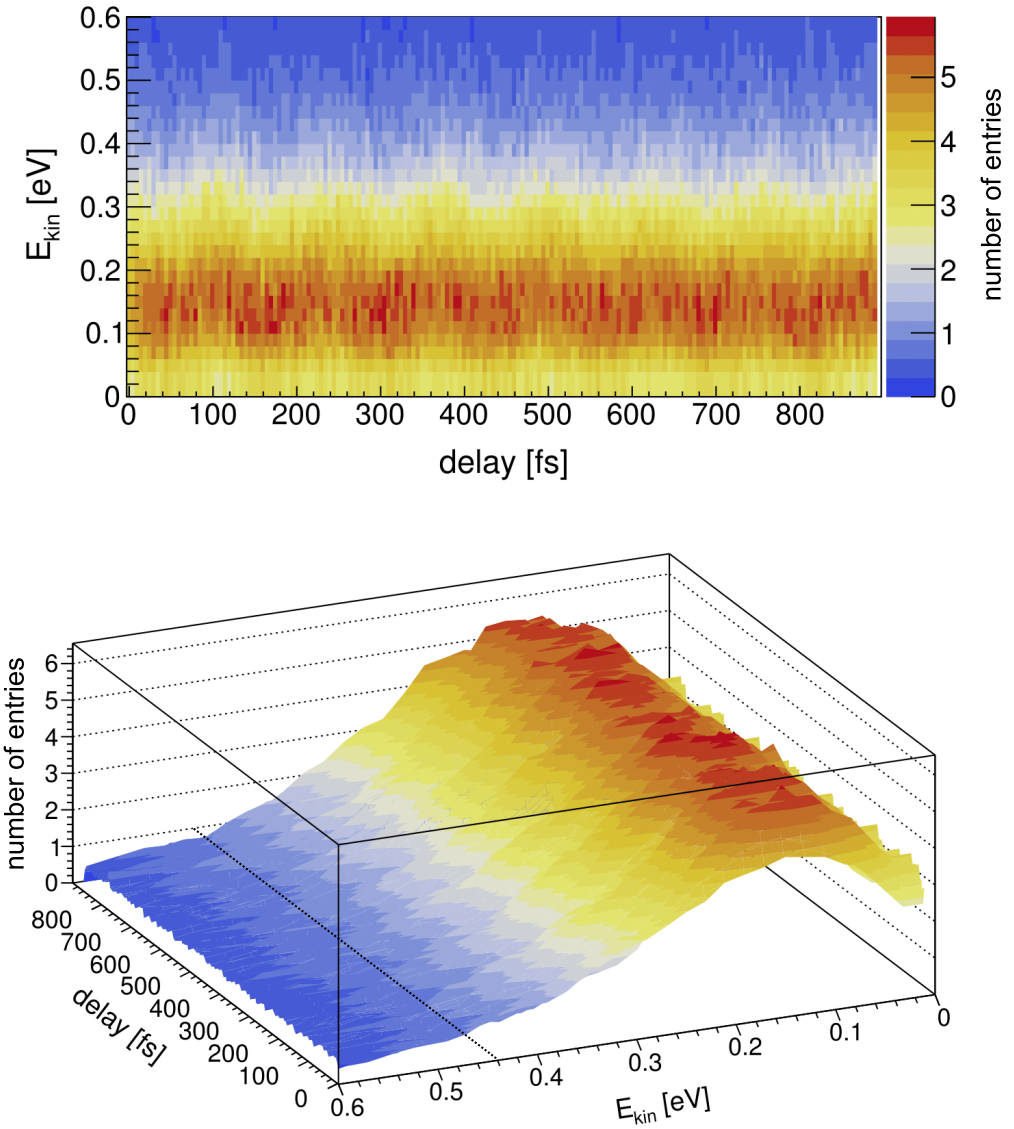

Figure 4.17.: Enlarged detail of the graph shown in Fig. 4.11 (top) and the three-dimensional representation of it (bottom). The dotted curve marks the point 0.44 eV until where oscillations are visible.

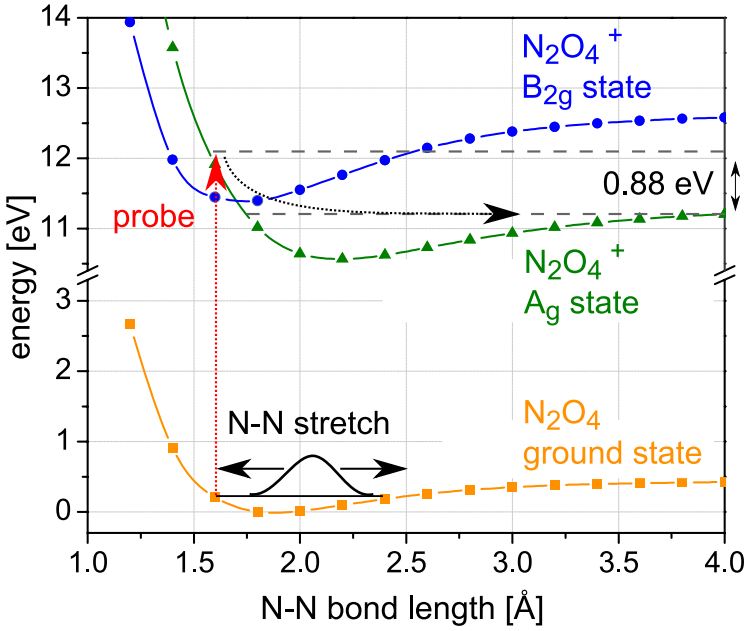

Figure 4.18.: Potential curves N_2O_4, adapted from Ref. [124]. Marked is the maximum kinetic energy release in the detected N-N stretching oscillation which corresponds to a minimum N-N bond distance of 1.57 Å.

with a Timepix detector. We excited the N-N stretching vibration in an impulsive stimulated Raman scattering process with a pump pulse and strong-field ionized the molecule with a probe pulse. We measured the kinetic energy release of the created NO_2^+ fragments. From this we could determine the amplitude and phase of the vibration. It became apparent from the shown results that a huge challenge is to receive sufficient statistical power for the interpretation of an experiment. For future projects it is desirable to investigate the process of data processing within the used setup. To decrease the loss of data during the correlation procedure leads to an higher effective repetition rate of the experiment and hence, to better statistics. At the same time, reducing the data loss enables the possibility to perform experiments under coincidence conditions.

Chapter 5.

5 Towards imaging the structural time-dependent change during molecular dynamics: Design and implementation of a new setup

5.1. Introduction

The ability of Coulomb explosion imaging to image the molecular structure, despite the limitations, was illustrated in chapter 3 of this thesis. Using CEI in a pump-probe experiment opens the potential to map time-dependent structural dynamics in molecules. In the introduction of the thesis (chapter 1) the idea for a novel approach, which combines CEI with established preparation techniques of small ionic molecules and clusters, was presented: *Transition State Coulomb Explosion Imaging (TSCEI)*. During this thesis we constructed and implemented the first parts of a new machine designed for the approach of TSCEI. In the current status there exists an ion source, an time-of-flight mass spectrometer, an imaging spectrometer and a neutral molecular beam source. Further plans are to include a trapping section and a delay-line based imaging detector [115]. The specific design and development is discussed in the next sections. As a last part of the chapter, we report on a first measurement performed with the neutral molecular beam source of the fragmentation of 1-butene upon strong-field ionization.

5.2. New experimental setup

In the frame of this thesis, we built a new setup with the aim to explore bimolecular reaction dynamics with a focus on ionic molecules. In this section, we describe the implemented machine in detail. First, we give an overview of the complete setup and the aim of the different parts. Further, we describe the two spectrometers and the two sources in more detail in the subsections 5.2.1, 5.2.2, and 5.2.3.

A schematic view of the complete setup is shown in Fig. 5.1, a three-dimensional CAD (computer-aided design) drawing can be found at the end of this chapter in Fig. 5.19. There are four main parts: the ion beam source (located in the source chamber

1), the time-of-flight mass spectrometer (located in the spectrometer chamber 1 & 2), the Coulomb explosion imaging spectrometer (located in the spectrometer chamber 2), and the neutral molecular beam source (located in the source chamber 2). The ions are generated in the source chamber 1 and pass through a skimmer into the spectrometer chamber 1 (we define this axis as the y-direction). To increase the vacuum, a cryo shield is implemented in the source chamber 1 to freeze out gas which remains in the chamber. After passing the skimmer, the ions are accelerated by a time-of-flight mass spectrometer, perpendicular to the original flight direction (we define this axis as z-direction). The ions enter the spectrometer chamber 2 through a small tube for differential pumping. On the way to the interaction zone, the ion beam can be controlled by a set of electrostatic lenses and deflectors included in the mass spectrometer. Further, a double MCP (Micro-channel plate) stack with a readout anode behind is included in the mass spectrometer (ToF MCP). This detector can be moved in and out of the beam path and is used as the first stage for measuring a mass spectrum. The interaction zone is located in the CEI spectrometer, which can be operated in a velocity map imaging configuration. Here, the ion beam is crossed with the laser beam. After the interaction with the laser, the fragments generated in the triggered reaction are detected. We intend to use a three-dimensional detector (Imaging MCP), measuring the time-of-flight of the fragments and the respective impinging point on the detector, which enables the correlated measurement of the full momentum vector of the single fragments. Perpendicular to the detection chamber an additional source for neutral molecular beams is located (oriented in the x-direction). The molecular beam enters the interaction zone from the top through two skimmers and serves as first stage to set up a Coulomb explosion imaging experiment. The neutral beam facilitates finding a first overlap with the laser beam. In contrast to the ion beam, it has a well-defined trajectory, independent of electric fields. In addition, in neutral beams a higher molecular density can be reached, increasing the detected signal. Furthermore, with the neutral source experiments on neutral molecules, as done in the former chapters, can be conducted. For better visibility, the neutral source is drawn in the same plane as the rest of the setup.

The machine is designed to produce positive as well as negative ions of several species. With the acceleration in the mass spectrometer, all fragments created in the reaction in the interaction zone can be detected, meaning ionic as well as neutral fragments or molecules. This property in combination with the neutral source enables great flexibility in designing different types of experiments.

5.2.1. Ion source

The first chamber contains the ion source as well as a cryo shield. It is separated from the second chamber by a skimmer (Beam Dynamics, Inc.) which is implemented in a home-built gate valve. The turbomolecular pump in the ion chamber is corrosion resistant to permit the ion source to run with corrosive substances like halogens without complications. Because of the gas inlet, the pressure is highest in this

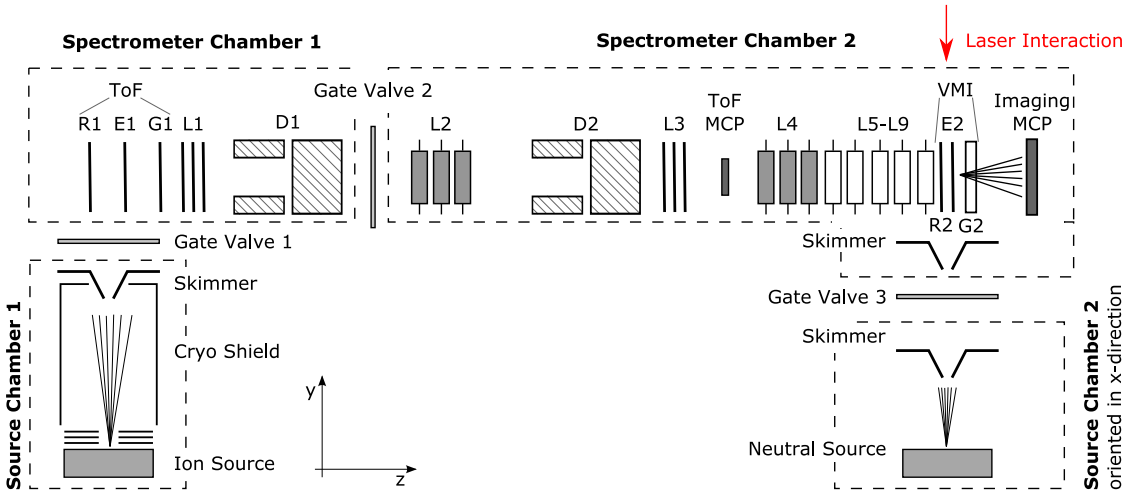

Figure 5.1.: The experimental setup. After the ion source, the beam passes a skimmer and enters a Wiley-McLaren-type [142] time-of-flight mass spectrometer (ToF, R1, E1, G1). The skimmer and ion source are surrounded by a cryo shield. Included in the acceleration-free part of the mass spectrometer is a series of lenses (L1-L9) and deflectors in the x- and y-direction (D1, D2). The CEI/VMI spectrometer consists of the three electrodes, R2, E2, and G2. The interaction zone is located between these electrodes (R2 and E2). A source for neutral molecules is implemented on top of the interaction zone (oriented vertically, but shown in y-direction in the figure for better visibility). The four vacuum systems can be separated by three gate valves, one home-built, and two commercial.

chamber[1]. Most of the gas remains in the source chamber, while only a small fraction passes the skimmer to the spectrometer chamber.

Generating ions We developed the ion source in two stages, referred to as plasma source and electron beam source. The main part of the plasma source is a pulsed Even-Lavie valve [143]. The centerpiece of the valve is a thin plunger, which is moved by a magnetic field to open and close the valve. This fast switching meachnism allows a repetition rate of up to 1 kHz. The valve can produce gas pulses of only 20 µs length and holds a backing pressure up to 100 bar. Gas is led to a small volume inside the valve by a full stainless steel Swagelok connection system. When the plunger is in the open position, the gas can leave the valve through a small ruby expansion nozzle, forming a supersonic expansion. The nozzle has a trumpet shape which ensures the best expansion flow in forward direction and a sub-Kelvin internal molecular temperature [144]. The valve itself can be heated to 250 °C. Due to the heating, the partial pressure of the sample, while using liquid or solid samples filled in the cartridge of the valve instead of a gaseous sample, can be increased and furthermore clogging of the valve can be prevented. The valve is mounted on a manipulator, which can be adjusted by 400 mm in the y-direction, and by 12.5 mm in the x/z-direction (KPM 12-250, VAb Vakuum-Anlagenbau GmbH).

We mounted a home-built discharge unit, to ionize the neutral gas, on top of the Even-Lavie valve following the basic design of Ref. [145]. A schematic drawing of the discharge unit is shown in Fig. 5.2.

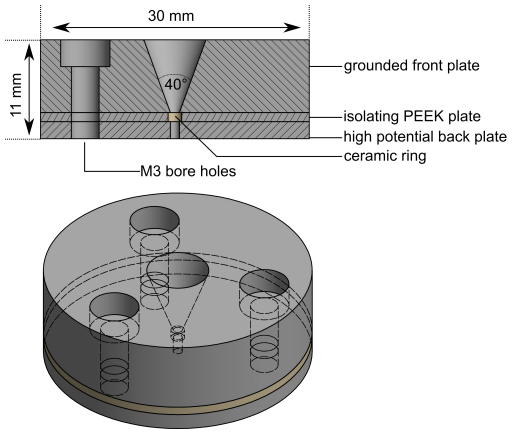

Figure 5.2.: Schematic drawing of the discharge unit which we implemented in the plasma source to ionize the neutral gas. The front plate is grounded while a voltage can be applied to the back plate. Between the two electrodes there is an insulating polyether ether ketone (PEEK) plate and an additional insulating ceramic ring in the inner part of the of the orifice of the plate.

The unit consists of two stainless steel plates which are separated by a thin

[1]The pressure in the source chamber 1 is $\approx 5 \times 10^{-6}$ mbar with the valve running at 1 kHz and 10 bar argon stagnation pressure and $\approx 1 \times 10^{-3}$ mbar with the valve running in continuous mode and 0.6 bar argon stagnation pressure.

polyether ether ketone (PEEK) plate. The thick front plate is grounded and has a conically shaped opening with a full opening angle of 40 °. The thinner back plate, as well as the PEEK plate, have a small aperture with diameter 1.0 mm/1.5 mm for the gas passage. A high voltage can be applied to the back plate, to ionize the neutral gas expanding through the Even-Lavie valve. To prevent the insulating PEEK plate from combustion due to the discharge, we placed a small ceramic ring in the inner part of the orifice of the plate. We applied voltages varying between 1000 V and 2000 V to the back plate to start the discharge. For this, we used a fast MOSFET Push-Pull Switch, to reach voltage rise times < 100 ns (HTS 31-03-GSM, Behlke Power Electronics GmbH). The timing of the voltage switch, as well as the voltage pulse duration, had to be carefully adjusted to the opening time of the Even-Lavie valve, to create a stable plasma. We implemented a 20 kΩ ballast resistor in series between the fast switch and the cathode of the discharge unit. In this way, a high voltage to initialize the first ignition can be used, but the resistor regulates the current during the process of the discharge. By measuring the voltage between the resistor and the discharge unit with a high voltage probe, we could monitor the time of ignition and the stability of the discharge itself. When a plasma was present, a voltage drop to the former high voltage appeared. A picture of the discharge unit mounted on the Even-Lavie valve is shown in Fig. 5.3 as well as a picture of a purple glowing argon plasma produced with it.

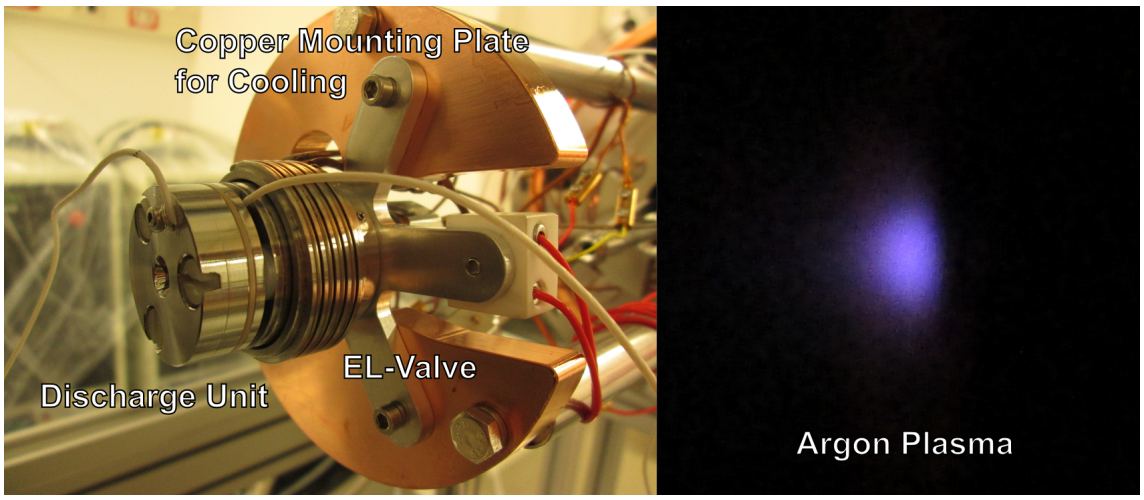

Figure 5.3.: Left: Photograph of the Even-Lavie valve including a home-built discharge unit. Right: Photograph of a purple glowing argon plasma, created with the plasma source.

Although it was possible to create a stable discharge, the discharge unit exhibited some drawbacks in combination with the EL-valve. As described, we had to adjust the parameters for the timing and pulse duration of the discharge very carefully. Moreover, the values were not stable and had to be changed and optimized before each start of the ion source and also while running the source. Furthermore, it was not possible to run the discharge unit continuously over several days. Although the small ceramic ring in the orifice of the PEEK plate provided some protection from the combustion of the PEEK plate, the discharge led to some burned parts

and hence, sediments in the apertures. This led to clogging and the need to open the vacuum system and clean all parts[2]. However, the major issue was that the discharge itself was not only located on the front side of the unit. Part of the plasma was created between the discharge unit back flange and the Even-Lavie valve front flange. This led to a discharge over the Even-Lavie valve and created some serious damage. First, the ruby nozzle got damaged. In Fig. 5.4 the nozzle is shown under a microscope. There is a small black burned spot visible in the lower left part. Since the nozzle itself is part of the sealing system of the valve this leads to leakage. Additionally, over time some damage to the centerpiece of the valve, the plunger, occurred. After careful examination of the plunger, it was detected that the surface sealing the nozzle from the back side showed a small dip instead of a flat or even slightly convex surface, most likely due to ablation. The combination of these two effects resulted in a leakage of the Even-Lavie valve.

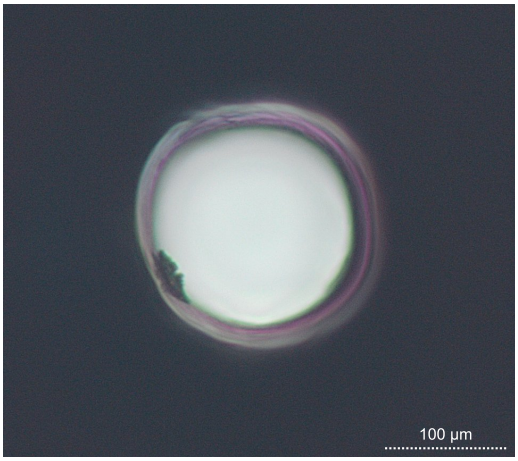

Figure 5.4.: Ruby nozzle under a microscope. A burned spot resulting from the discharge is clearly visible.

As an alternative ion source, we implemented a simpler design combining a continuous valve with an electron gun (electron beam source). We adapted the design for the electron gun from Ref. [146]. A schematic drawing of the electron gun is shown in Fig. 5.5. It consists of a tungsten filament (PLANO A054C, 0.2 mm filament thickness), which is placed inside a repeller electrode. In addition, the gun contains an extractor electrode and a grounded electrode. Applying a current to the filament generates electrons that are emitted from the filament tip. The generated electrons are accelerated and at the same time focused, since the extractor and the grounded electrode work together as a lens. A pair of deflectors placed behind the ground electrode allows to guide and control the generated electron beam. The whole construction is mounted below the continuous valve. Hence, the electron beam is crossed with the neutral gas jet and ionizes the expanding molecules. On the opposite side of the valve, we placed a Faraday cup which captures the electrons.

[2]The contamination of the valve was possibly also the reason for the need to adjust the parameters for the timing and pulse duration of the discharge during the measurement since with the sediments at the inner part of the valve and discharge unit, the material properties and hence, the electric properties change.

Electrons impinging on the cup lead to a current which is measured and serves as a control mechanism. In Fig. 5.6 a picture of the electron gun is shown in the left panel without the shielding. In the right panel, the gun is shown with the shielding and mounted inside the chamber. In this picture, the discharge unit is still attached to the front side of the valve. We removed it at a later stage.

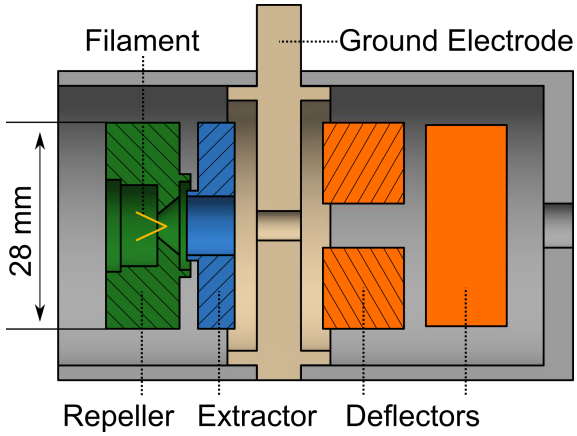

Figure 5.5.: Schematic drawing of the electron gun. The filament is placed inside the repeller. Applying a current to the filament generates electrons that are emitted from the filament tip. The generated electrons are accelerated and at the same time focused, since the extractor and the grounded electrode work together as a lens.

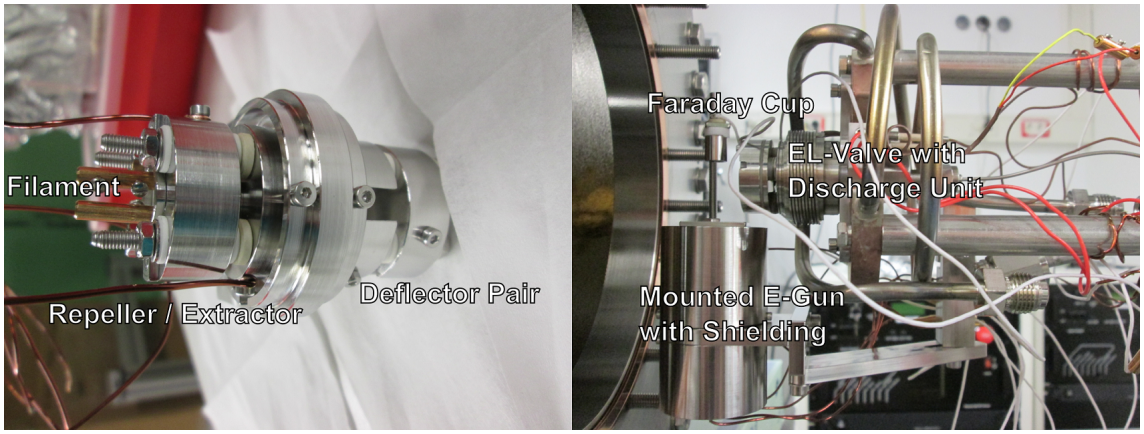

Figure 5.6.: Left: Photograph of the electron gun without the shielding. Right: Electron gun mounted in the chamber including the valve.

The combination of the electron gun with the valve in continuous mode served as a convenient solution for a stable ion source. However, for future projects it is desirable to go back to the pulsed valve mode. There are high requirements for coincidence experiments, regarding the vacuum conditions and there are limitations in the gas pressure inlet of the valve. The gas load of a continuous gas inlet is 20 times higher than that of the pulsed valve at a repetition rate of 1 kHz and with a 50 µs pulse length. We had to controll the stagnation pressure of the valve precisely.

Even with a low argon gas pressure of 0.6 bar, the limitation of the turbomolecular pump was nearly reached ($\approx 1 \times 10^{-3}$ mbar). One alternative proposed solution to ionize the molecules would be to use a dielectric barrier discharge (DBD) unit. Such a solution is commercially available for the Even-Lavie valve [147]. DBD units are known to provide a stable and homogeneous discharge, without arcing and forming hot spots. Luria *et al.* showed that in combination with the Even-Lavie valve positive and negative ions as well as metastable atoms and dissociated neutral radicals are produced with high efficiency [147].

Gate valve A very beneficial feature in a molecular ion beam experimental setup is the possibility to separate the source chamber from the rest of the ultrahigh vacuum system. In the source chamber, modifications have to be performed more frequently, e.g. exchanging the nozzle of the pulsed valve or the skimmer or cleaning the ion source parts. Venting the complete vacuum system means a long pump down and perhaps baking time afterwards. Hence, it is convenient to implement a gate valve in the vacuum system to be able to separate the chambers easily. One important property of gate valves is a low thickness. The flux of the molecular beam decreases with $1/d^2$, where d is the distance to the source [148]. To minimize the ion loss on the way to the interaction zone, it should be possible to place the time-of-flight mass spectrometer, which accelerates the ions, directly behind the skimmer. Unfortunately, commercially available gate valves all have a thickness of several centimeters.

There are several low profile gate valves in elaborated designs which implement the skimmer directly into the valve opening and closing mechanism [148, 149]. Since it is beneficial to have the possibility to change the skimmer from the source chamber side, while the rest of the system is still pumped down to high vacuum we developed a new simple-design gate valve with a low thickness (28 mm) and an exchangeable skimmer. The valve can be operated under full vacuum conditions from the outside with a commercial linear feedthrough and holds a pressure of $p < 2 \times 10^{-8}$ mbar against atmospheric pressure. The skimmer is removable from both sides of the valve, and can be removed from the source chamber side without opening the gate and while isolating the source chamber from the rest of the vacuum system. The gate valve opening and closing mechanism is based on the lateral force generated by pressing two wedges against each other [150, 151].

An exploded view of the valve is shown in Fig. 5.7. The central part is a CF 300 flange (6), which is milled out to contain the valve parts and the skimmer mounting flange (8). On the high-vacuum side, there is a knife edge for a CF 160 flange. An adapted CF 160 flange (1) is mounted, which includes a groove for a Viton O-ring (2) around a 23 mm aperture, ensuring an unrestricted passage of the ion beam. The flange is milled down to a thickness of 10 mm to reduce the overall thickness of the gate valve. A copper beryllium wedge clamp (5) with a 22.5 mm hole is screwed to the CF 160 flange. The wedge has an angle α of 94 °. The counterpart of this wedge clamp is the sealing flange (3) made out of stainless steel, flat on the O-ring side and beveled on the other side, with the same angle as the wedge clamp. This sealing flange can be moved in and out by a commercial linear feedthrough (4) (VAb Vakuum PPL 16-100) which is connected to the 300 CF flange

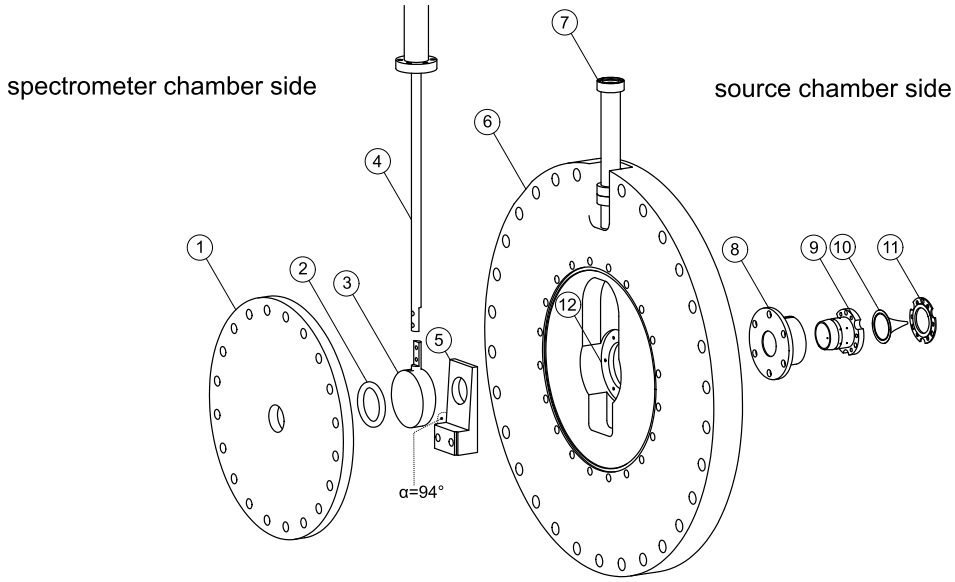

Figure 5.7.: Exploded view of the gate valve. The beveled sealing flange (3) is moved vertically up and down by the linear feedthrough (4) and is pressed against a Viton O-ring (2) by the wedge clamp (5). The skimmer mounting flange (8) is screwed on the 300 CF flange (6) at position (12). It contains the skimmer pedestal (9) with the skimmer (10) mounted on it.

via a CF 16 flange (7), integrated on one side. The skimmer mounting flange (8) is bolted to the inner side of the CF 300 flange at position (12) from the spectrometer chamber side. It contains the skimmer pedestal (9), which can be inserted in the mounting flange from the source chamber side and is secured with three screws. A thin recess ring is incorporated in the pedestal centering the skimmer (10) (Beam Dynamics, Inc.). A thin clamping ring (11) is used to fix the skimmer in place. This design allows to remove the skimmer from the high vacuum side (spectrometer chamber side) by opening the gate valve and taking out the mounting flange or from the source chamber side by removing the pedestal. The latter operation can be accomplished without opening the gate valve, keeping the high vacuum conditions on the spectrometer side.

The gate valve is operated by moving the linear feedthrough in and out. When the sealing flange comes in contact with the fixed wedge clamp while pushing the linear feedthrough vertically down, the sealing flange is experiencing an additional lateral force against the O-ring from the wedge clamp. This principle is schematically depicted in Fig. 5.8 in the right panel. The different materials of the wedge clamp and the flange reduce friction when the flange moves along the wedge clamp. A sectional view of the valve is shown in Fig. 5.8 in the left and the middle panel. On the left-hand side, the valve is in the closed position while in the middle it is in the open position. In the sectional view in Fig. 5.8 the cryo shield is indicated by number (13). When the gate valve is in the closed position both, the source chamber and the spectrometer chamber, can be vented to atmosphere independently, while keeping ultrahigh vacuum conditions in the other side ($p < 2 \times 10^{-8}$ mbar). The

thickness of the gate valve (from the left outer face to the position of the skimmer pedestal) is 28 mm and thereby around 1/3 thinner as commercial available ultrahigh vacuum gate valves applicable for the same flange size[3].

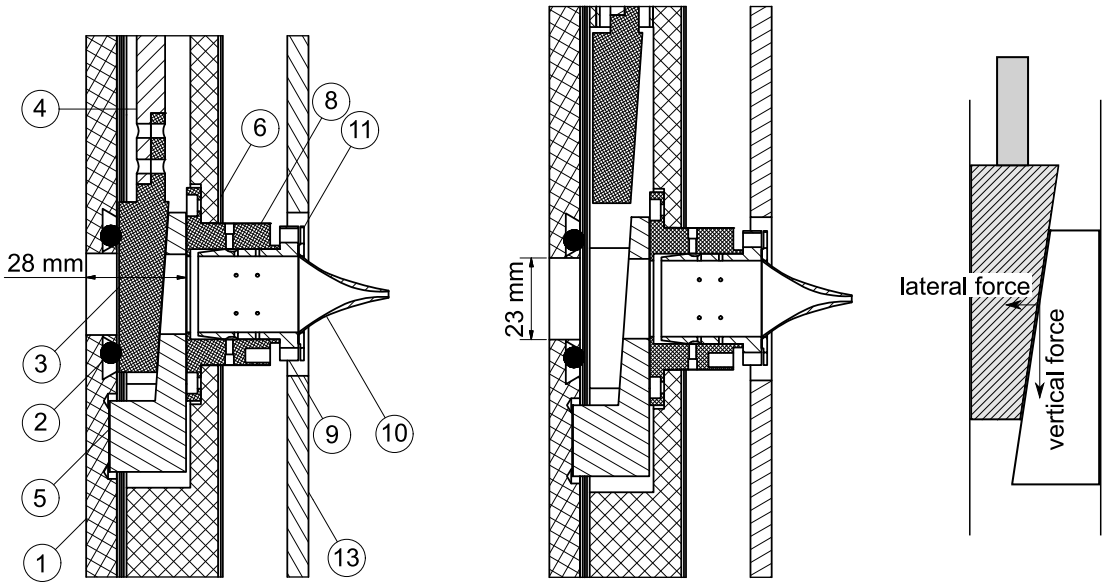

Figure 5.8.: Sectional view of the gate valve. In the left panel the valve is shown with the linear feedthrough (4) in the closed position. The sealing flange (3) is pressed against the O-ring (2) by the wedge clamp (5). The thickness of the valve is 28 mm. In the middle panel the valve is shown with the linear feedthrough in the open position. The open aperture is 23 mm. In the right panel the mechanism of the lateral force when pressing the two wedges against each other is illustrated schematically.

5.2.2. Spectrometer

In this subsection, we describe the two spectrometers which the ion beam traverses after the ion source: a mass spectrometer and a spectrometer for Coulomb explosion imaging. Details on the design of the single ion optic parts (e.g. lenses and deflectors) as well as the designed modular construction system can be found in the appendix B of the thesis.

Mass spectrometer The first spectrometer is a Wiley–McLaren type time-of-flight (ToF) mass spectrometer [142] which the ions enter directly after they passed the skimmer. In a ToF mass spectrometer, ions with different masses are accelerated to different velocities. Hence, depending on their mass the ions arrive at a certain time delay after the acceleration at the interaction zone and can be addressed in the experiment selectively. The main parts of the spectrometer are three electrodes in

[3]For example VAT Vakuumventile AG, 10846-CE08-0008.

the beginning: the repeller, the extractor, and a ground electrode. They constitute the acceleration zone and are labeled R1, E1, and G1, respectively in Fig. 5.1. Each of the three electrodes has an aperture, which is covered by a nickel mesh (Precision Eforming LLC, Nickel-mesh with 70 wires/inch, 90 % transmission). The mesh ensures a homogeneous electric field and minimizes focusing effects. The opening diameters are 10 mm, 20 mm, and 20 mm for the electrodes R1, E1, and G1. The voltage on the electrodes R1 and E1 is switched on with two fast MOSFET Push-Pull Switches (HTS 31-03-GSM, Behlke Power Electronics GmbH). In combination with the pulsed plasma ion source, we had to adjust the timing of switching the voltages carefully to the moment the ion package in located between the two electrodes R1 and E1. When using the continuous source, the voltages were switched at an arbitrary time. To synchronize the leading edges of the applied potentials while triggering the switches with the same logic pulse, we adjusted the length of the trigger cables to compensate for the internal delays. The kinetic energy $E_{\mathrm{kin},i}$ of each ion species i gained in the spectrometer depends only on the applied voltages and the geometry of the spectrometer[4]. Due to the different masses m_i of the ions, this leads to different ion velocities v_i ($v_i = \sqrt{2\,E_{\mathrm{kin},i}/m_i}$).

The advantage of the Wiley-McLaren type time-of-flight mass spectrometer is an adjustable focus position in the flight direction. The ions show a certain initial spatial spread in the area between the electrodes R1 and E1. This leads to different distances the ions have to pass to the interaction zone. However, ions closer to the repeller not only have to travel a longer distance, but also gain more kinetic energy in the acceleration zone. The two effects lead to a specific time (and position in flight direction), where all ions get focused along the axis of the spectrometer. The focus position can be adjusted by the choice of the voltages of the electrodes R1 and E1 with great flexibility [5].

The mass resolution of the spectrometer can be estimated via the expected time spread of one ion package with a certain ion mass due to the initial spatial distribution and the initial kinetic energy distribution of the ions [142]. Following Ref. [142], we calculate for each distribution (spatial/energy) the maximum ion mass for which two neighboring mass peaks are completely separated. The two values are referred to as spatial resolution and energy resolution. Based on the energy and spatial resolution upper and lower limits for the overall mass resolution can be deduced.

The spatial resolution M_s and energy resolution M_E can be calculated via [142]:

$$M_s \;=\; 16\,k_0\,\left(\frac{s_0}{\Delta s}\right)^2 \tag{5.1}$$

$$M_E \;=\; \frac{1}{4}\left(\frac{U_t}{U_0}\right)^{\frac{1}{2}}\left(\frac{k_0+1}{k_0^{\frac{1}{2}}} \;-\; \frac{k_0^{\frac{1}{2}}-1}{k_0+k_0^{\frac{1}{2}}}\frac{d}{s_0},\right), \tag{5.2}$$

[4] An exception is the variation due to the specific initial positions of the ions in the spectrometer and hence, different travel distances.

[5] The beam size in the other dimensions can be controlled via electrostatic lenses, included in the spectrometer. However, the overall phase-space in the ion package is conserved. Hence, the initial spatial distribution limits the final spatial distribution. In the experiment, we reach nevertheless a smaller focus because part of the ions are blocked in the beam path.

with the mean initial distance of the ions from the extractor s_0, the spacing between the repeller and the extractor d, the initial energy distribution U_0 of the ions, and the initial spatial distribution Δs. The energy U_t of the ions is defined by the electric fields between the plates E_s and E_d and the distance the ions travel in the field via

$$U_t \;=\; q\, s_0\, E_s \;+\; q\, d\, E_d. \tag{5.3}$$

The factor k_0 is determined by the distance D between the spectrometer and the end of the flight zone:

$$D \;=\; 2\, s_0\, k_0^{\frac{3}{2}} \left(1 - \frac{1}{k_0 + k_0^{\frac{1}{2}}} \frac{d}{s_0}\right). \tag{5.4}$$

We estimated the initial energy distribution U_0 and spatial distribution Δs from the typical operating parameters of the Even-Lavie valve and the position and size of the skimmer. The geometry parameters s_0, d, and D are given by the actual design of the spectrometer. We extracted the values of the field strengths E_s and E_d, which are used here for the estimation, from an optimized measurement[6]. Typical values for the parameters are given in Tab. 5.1. With these parameters

$$M_s \;\approx\; 8934\,\mathrm{u} \tag{5.5}$$

$$M_E \;\approx\; 417\,\mathrm{u} \tag{5.6}$$

is reached. The overall mass resolution can be estimated from these two values. There are upper and lower limits for the maximum resolvable mass $M_{\max}$. Since M_s and M_E are both limiting values, the maximum resolvable mass is smaller than the minimum of these two numbers. As a lower limit $M_{s,E}$, we assume (according to Ref. [142]) that the total time spread of the ion package (defining the overall mass resolution) is the sum of the time spreads due to the initial spatial and energy distribution. Hence,

$$\frac{1}{M_{s,E}} \;=\; \frac{1}{M_s} + \frac{1}{M_E}. \tag{5.7}$$

The maximum resolvable mass $M_{\max}$ is between the minimum of M_s and M_E (here $M_E \;\approx\; 417\,\mathrm{u}$) and the value $M_{s,E}$:

$$M_{s,E} \;=\; \frac{1}{\frac{1}{M_s} + \frac{1}{M_E}} \;=\; 398\,\mathrm{u}. \tag{5.8}$$

Hence, for the here described setup and chosen voltages, the value of the maximum resolvable mass $M_{\max}$ is between 398 u and 417 u. This corresponds to a mass resolution $\Delta M/M \approx 0.0025\,\mathrm{u}$.

[6] We varied the potentials on the extractor and repeller electrodes while recording a mass spectrum of benzene seeded in argon, ionized with the electron beam source (see Fig. 5.15). For optimized values of the field strengths the single mass peaks are sharp and a maximum peak height is reached.

Following the acceleration zone, a set of electrostatic Einzel lenses (L1-L9) and deflectors (D1-D2) is included in the mass spectrometer to control the position and the spread of the ion packet. Further included in the mass spectrometer is a double MCP stack with a readout anode behind (diameter 25 mm, PHOTONIS USA, Inc). This detector can be used as the first stage for measuring the mass spectra. It can be moved in and out the ion beam path using a linear feedthrough (VAb Vakuum PPL 16-50).

Coulomb explosion imaging spectrometer In the interaction zone, the selected ion packet is overlapped with a femtosecond laser pulse which induces a Coulomb explosion. The interaction zone itself is located in the second spectrometer, which is referred to as CEI spectrometer or velocity map imaging (VMI) spectrometer. The CEI spectrometer is used to study the gained kinetic energies/momenta of ionic fragments resulting from the Coulomb explosion. We use a VMI configuration for the design and the applied voltages. In a VMI spectrometer [136], ions with a certain initial velocity in the interaction zone are projected on a certain position on a detector, independent of their original position in the interaction zone. Our VMI spectrometer is based on the original design of Eppink and Parker [136] and includes three electrodes, the repeller (R2), the extractor (R2), and one grounded electrode (G2). The opening diameters of the apertures in the electrodes are 5 mm, 20 mm, and 26 mm, respectively. In a VMI spectrometer the three-dimensional velocity distribution is projected onto a two-dimensional plane. To gain the full three-dimensional information, we want to implement a delay-line detector which measures the time-of-flight of the particles in addition to the impact position on the detector, similar to the detection system in the former chapter 3. In the current stage the combination of a double stack MCP plate (F2226-24P, Hamamatsu, 77 mm diameter), a phosphor screen, and a digitizer (Agilent Acqiris High-Speed Digitizers) are implemented. The phosphor screen in combination with a CCD camera enables the recording of the impact position on the detector. At the same time, fast changes in the electric potential of the phosphor screen due to impinging charged particles are recorded to measure the time-of-flight of the ions. The phosphor screen is connected via a high-pass filter and a preamplifier with the digitizer. The digitizer

dimensions [cm]	electric fields [V/cm]	energies [eV]
$D = 195.5$	$E_s = 33.5$	$U_t = 3899.56$
$d = 2.0$	$E_d = 1933$	$s_0\,E_s = 33.5$
$s_0 = 1.0$		$d\,E_d = 3866$
$\Delta s = 0.2$		$U_0 = 0.03$

Table 5.1.: Values for the estimation of the mass resolution of the built spectrometer. The parameters are explained in the text. The values of the electric fields are extracted from an optimized measurement of an mass spectrum of benzene, which is shown later in Fig. 5.15. The dimensions are extracted from the actual design of the spectrometer.

is connected to a desktop PC via a high speed connection. It is triggered by the signal from the laser pulses, recorded with a photodiode which is located behind a mirror in front of the interaction zone. The data acquisition is triggered to allow an assignment of single ion signals to a certain laser pulse and hence, an event-by-event based data analysis afterwards.

Simulation To decide on the final design and arrangement of the ion optics in the time-of-flight mass spectrometer and the Coulomb explosion imaging spectrometer we simulated the beam path using the software SIMION [152]. With SIMION, electric fields are calculated as well as the trajectories of charged particles in these fields. The geometries of electrodes in custom designs can be included in the program and used for the calculation. We used the simulations to find the optimum arrangement of electrodes in the new setup. We ignored possible effects of the Coulomb repulsion between the ions in all simulations.

We performed the simulation of the beam path for the I_2^- molecule. Start parameters for simulating the beam path are listed in Tab. 5.2 in the columns 1 and 2. We chose the parameters to fit the supersonic expansion conditions of the Even-Lavie valve with initial gaussian velocity and spatial distributions. The initial position of the ions in the simulation was behind the skimmer in the spectrometer chamber 1. We define a coordinate system, with the y-axis parallel to the initial straight ion trajectory from the nozzle of the Even-Lavie valve to the center of the acceleration region of the mass spectrometer and the z-axis oriented along a line connecting the center of the acceleration region with the center of the interaction region. In the simulations, we optimized the voltages and the respective switching time of the voltages for the electrodes of the mass spectrometer, the deflectors, and the lenses, to achieve a small ion beam focus in the interaction region. Additionally, we optimized the arrangement and geometry of lenses and deflectors. The electrodes R2 and E2 are grounded in the beginning (ToF mode). When the ions reach the interaction region, the potential on the electrodes R2 and E2 is switched on (VMI mode).

Simulated ion trajectories for an optimized electrode configuration are shown in Fig. 5.9. The upper panel A shows the beam path from the skimmer to the interaction zone in the ToF mode in the yz-plane and the xz-plane. The lower panel B shows a detailed view of the ion beam path from the interaction zone to the detector in the VMI mode. In the ToF mode, we terminated the trajectories a short time after the ions passed the interaction zone. The interaction zone was reached around 100 µs after the switching of the potentials of the accelerating electrodes R1 and E1. The thin tube (with diameter 7 mm) which separates the two vacuum chambers that contain the mass spectrometer, is not included as an electrode in the simulation, but via the termination of all ion trajectories which do not clearly pass the open area inside the tube. In Tab. 5.2 the optimized voltages are denoted (excluding lenses and deflectors), as well as the resulting spatial spread of the ion beam in the focus. The last set of lenses (L5-L9) was not needed in the simulation, but included in the beam path, because there was some additional space. In the experiment, a potential can be applied on each of these electrodes. This can be used for additional focusing or for decelerating the ions.

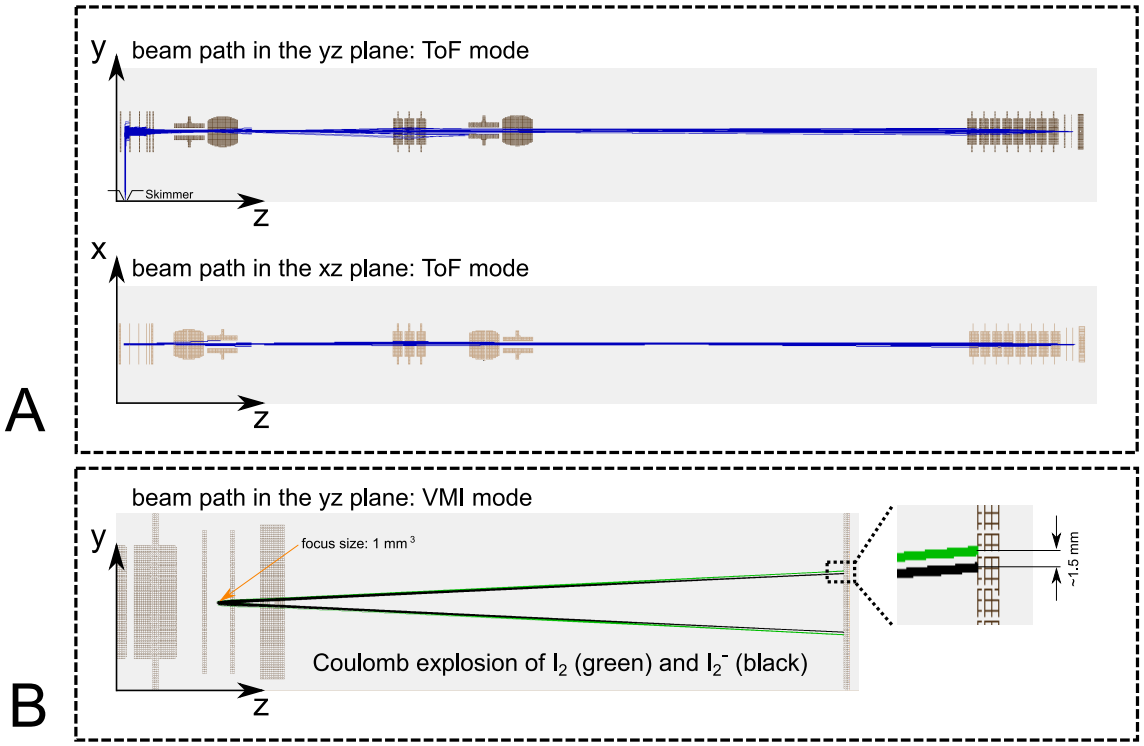

Figure 5.9.: Simulation of the ion trajectories for I_2^- molecules. The upper panel shows the trajectories of 500 ions of the spectrometer with the initial position behind the skimmer (see Fig. 5.1) in the yz-plane and the xz-plane in the ToF mode. The lower panel B shows a detailed view of the ion beam path for two Coulomb exploding molecules (I_2 & I_2^-) from the interaction zone to the detector in the VMI mode. The resulting impact positions of I^+ ions on the detector, originating from the neutral and the anion, have a distance of $\approx$ 1.5 mm and can be clearly distinguished, although the initial spatial distribution of 1 mm^3.

In the experiment it is of importance to receive (i) conditions for a stable ion beam focus, and (ii) to reach a small focus size. The stable focus is needed to ensure a stable overlap with the laser beam. Large ion optics, stable power supplies and the avoidance of electrostatic charging of insulating materials in the chamber can improve the stability of the focus. A large ion beam focus leads to a large spread of the initial spatial position in the CEI spectrometer and hence, to uncertainties in the measurement. Hence, a small focus is desirable. Since the overall phase-space in the ion package is conserved, the focus size is mostly defined by the initial spatial distribution. This is determined by the supersonic expansion conditions and the skimmer. However, we reach a smaller focus in the interaction zone than initially in the accelerating zone of the mass spectrometer, because part of the ions are blocked in the beam path. In addition, we use the CEI spectrometer in a VMI configuration, to reduce the problem of a large initial spatial spread. Anyhow, we want to estimate the number of ions in the overlap region with the laser and hence, the focus size. In a coincidence CEI experiment less than one molecular ion is needed in the laser focus (e.g. in chapter 3 we worked with a rate of in average 0.3 molecules in the focus). However, an ion beam focus is reasonably larger than the laser focus. Depending on the actual ion beam focus size, a certain amount of ions is needed in each ion package.

To estimate the ion beam focus size, we performed a simulation with 10000 ions and recorded the x-, y-, and z-position at time the ions are in the interaction region. In Fig. 5.10 histograms of the data of this measurement are shown. In the x- and

start parameter	value	electrode	potential [V]	focus parameter	spread [mm]
# ions	500	R1	$-850\,\mathrm{V}$	Δx	0.7 mm
mass	254 u	E1	$-790\,\mathrm{V}$	Δy	1.1 mm
charge	-1 a.u.	$\mathrm{R2_{VMI}}$	4000 V	Δz	1.8 mm
FWHM in x/z	1 mm	$\mathrm{E2_{VMI}}$	2840 V		
FWHM in y	15 mm				
v	$290\,\mathrm{m\,s^{-1}}$				
FWHM v	$40\,\mathrm{m\,s^{-1}}$				
speed direction	y				
half angle v	0.6 °				
Δt ToF-VMI	96 µs				

Table 5.2.: Columns 1 and 2: Start parameters for simulating the beam path of $\mathrm{I_2^-}$. Columns 3 and 4: Optimized values from simulations. The electrodes R2 and E2 are grounded in the ToF mode and on potential in the VMI mode ($\mathrm{R2_{VMI}}$ and $\mathrm{E2_{VMI}}$). Δt ToF-VMI is the time delay between switching on the potentials of the electrodes of the time-of-flight mass spectrometer and switching on the potentials of the electrodes R2 and E2 to the VMI mode. Columns 5 and 6: Ion beam parameters in the focus from the SIMION simulations. An ion beam focus of $1.4\,\mathrm{mm^3}$ is achieved.

z-direction, a gaussian-shaped profile is obtained. The focus size in the x and z-direction, which is listed in Tab. 5.2, was determined from a gaussian fit of the respective histogram. We defined the focus size Δx and Δz by the variances σ_x/σ_z of the curves via $\Delta x = \pm 2 \cdot \sigma_x/\Delta z = \pm 2 \cdot \sigma_z$, to keep around 95 % of all ions in the focus in the estimation. In the y-direction the distribution has a square-top shape. Due to the initial velocity distribution within one ion package, the package is spatially spread when it reaches the area between the two initial electrodes of the mass spectrometer R1 and E1. In the y-direction this spread is larger than the aperture of the two electrodes E1 and G1. Hence, part of the package is blocked by the electrodes which changes the overall spatial distribution in the package[7]. The focus size Δy in y-direction was defined as the width of the rectangular red distribution, plotted in the second panel of Fig. 5.10. We achieved an overall ion beam focus of $f_{\mathrm{IB}} = 1.4\,\mathrm{mm}^3$ in the simulation. Focusing a laser beam with a diameter of 5 mm ($\lambda = 800\,\mathrm{nm}$) via a mirror with a focal length of 50 cm leads to a spot size of 100 µm in the focus and a Rayleigh range of 10 mm. Hence, the overlap between the ion beam and the laser focus is defined by the diameter of the laser focus (xz-plane) and the ion beam spread in the y-direction. With these parameters, an interaction region of 0.01 mm^3 is reached (assuming a stable ion beam focus). Hence, for one ion in the interaction region, $\approx$150 ions in the ion focus are needed. On the way from the source to the interaction region, there is a loss of ions of around 70 % because of the initial spatial and velocity distribution[8]. Hence, in the initial ion beam packet around 500 ions should be generated. This number is an upper-limit estimation. In a CEI coincidence experiment a lower number than one ion in the laser focus is intended. One additional challenge in a CEI experiment is intensity averaging. The intensity of the laser decreases with the distance to the center of the laser focus. Since high laser intensities are needed in a CEI experiment to induce a full fragmentation, the intensity in the outer parts of the laser focus will be still high enough to induce an ionization but is already too low to induce the full fragmentation. In the direction of the laser beam propagation this is not problematic since the Rayleigh range of the laser is larger than the spatial spread of the ion beam. In the other directions the effect of intensity averaging will lead to additional detected events, which can not be used in the analysis afterwards. One solution would be to implement a laser system with a flat-top focus [153].

We tested the CEI spectrometer in the VMI configuration numerically by distinguishing the Coulomb explosion of neutral and anionic I_2 molecules, which have a different I-I bond length. In the ground state, the neutral I-I bond length is 2.67 Å [154] leading to a terminal kinetic energy of 2.70 eV per fragment in a purely Coulombic repulsion of two singly positively charged fragments. The anion has an I-I bond distance of 3.23 Å in the ground state [154], leading to 2.23 eV per fragment. In the lower panel B of Fig. 5.9 the velocity mapping of a Coulomb explosion of the neutral iodine molecule I_2 (green) and the anionic iodine molecule I_2^- is plotted.

[7] In addition, there are other parts in the mass spectrometer, where part of the ion package is blocked, e.g. due to the small tube implemented after the first deflector pair, or at the first thin lens.

[8] The main losses are happening at the electrodes E2 and G2, the first lens L1 and the small tube after the first deflector D1.

We adjusted the potentials of the electrodes R2 and E2 to the VMI mode. Further, we choose the initial spatial distribution of the ion target based on the outcome of the first simulation on the ion trajectory from the source to the interaction region. The resulting impact positions of I^+ ions on the detector, originating from the neutral and the anion, have a distance of $\approx$ 1.5 mm and can be clearly distinguished, although the initial spatial distribution of 1 mm^3.

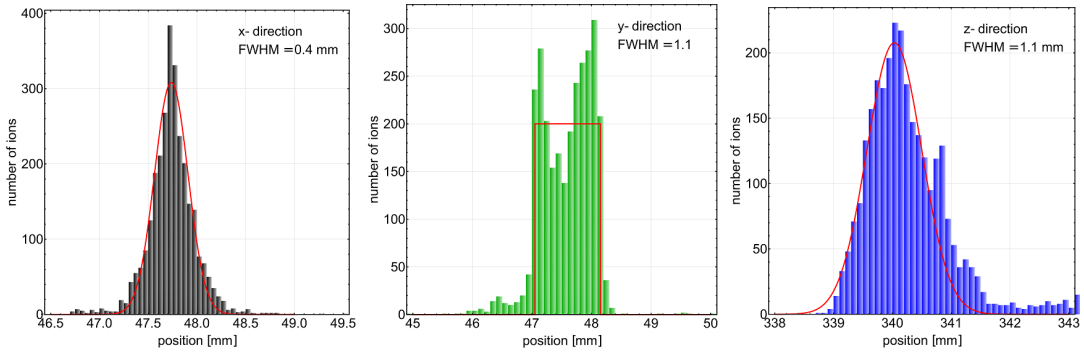

Figure 5.10.: Histograms of the ion beam focus in the x-, y-, and z-direction from a simulation with 10000 ions starting at the skimmer of the ion source. In the x- and z-direction the focus has a gaussian-shaped profile, in the y-direction the focus has a square-top-shaped profile.

The constructed ion optics We built the ion optics in three stacks which are shown in Fig. 5.11-5.13. The first part (Fig. 5.11) contains the electrodes of the acceleration zone of the time-of-flight mass spectrometer (R1, E1, G1), as well as a thin Einzel lens (L1) and a deflector pair (D1). To compensate for the initial ion beam velocity in the y-direction resulting from the supersonic expansion, it is important to locate the first deflector pair as close as possible to the spectrometer. At the same time, a lens is required to compensate for the expansion of the beam which originates from the initial velocity distribution in the ion package. Since a certain distance is needed from the lens to the deflectors, to not disturb the homogeneous field inside the deflectors, we choose a thin lens (length 2 mm, inner diameter 15 mm) at this position instead of longer lens with better focusing conditions.

The second stack of ion optics is shown in Fig. 5.12. Here, we included a second deflector pair (D2) and two lenses (L2 (long) and L3 (thin)). At least two deflector pairs are needed in the complete flight path to ensure full controllability of the final focusing spot, as well as keeping the ions close to the center of the flight tube. Lens L3 was not included in the simulation, but added in the second ion optics stack, because there was additional space. The vacuum chamber housing the first ion optics stack is separated from the vacuum chamber housing the second and third ion optics stack via a 7 mm diameter tube and an electro-pneumatic commercial gate valve (Gate Valve 2, VAT). Hence, an additional differential pumping stage and the possibility to separate the vacuum chamber, where both MCP detectors are included is achieved.

The third and final stack of ion optics is shown in Fig. 5.13. Here, one Einzel

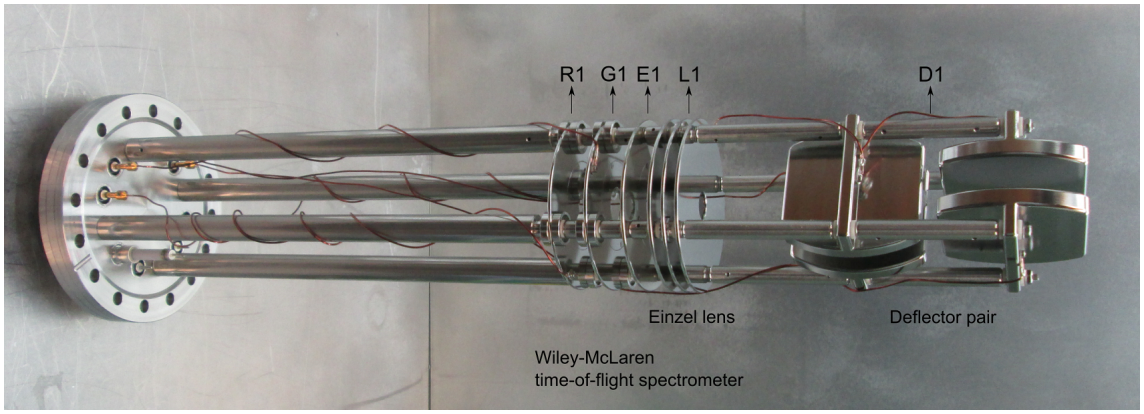

Figure 5.11.: Photograph of the first part of the ion optics. This part includes the acceleration electrodes of the Wiley-McLaren type time-of-flight spectrometer (R1, E1, and, G1), one Einzel lens (L1), and one pair of deflectors (D1).

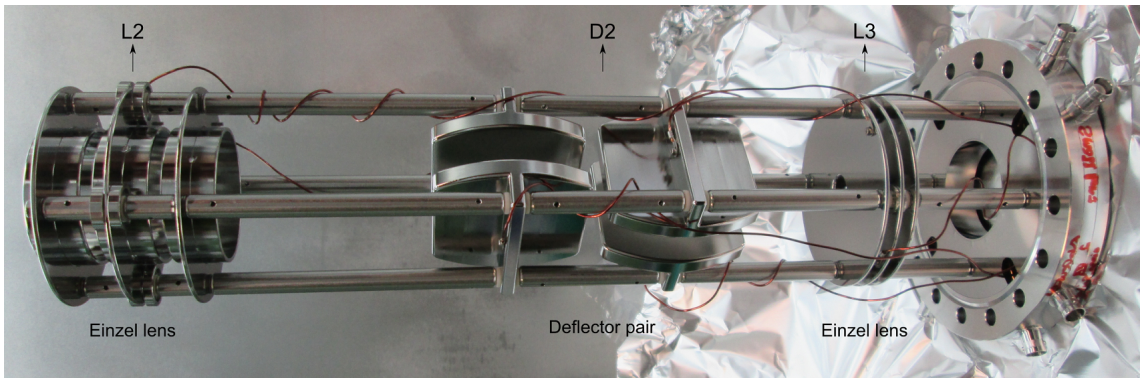

Figure 5.12.: Photograph of the second part of the ion optics. This stack includes a long and a thin Einzel lens (L2 & L3) and one pair of deflectors (D2).

lens (L4) is followed by five cylindrical electrodes (L5-L9). These electrodes can be used as additional lenses or to decelerate the ion beam. As final parts, the three electrodes R2, E2, and G2 constitute the CEI spectrometer. The electrodes R2 and E2 are grounded in the ToF mode and subsequently switched to the VMI mode after the laser interaction. The focus of the mass spectrometer is overlapped with the laser focus in the interaction region between the electrodes R2 and E2.

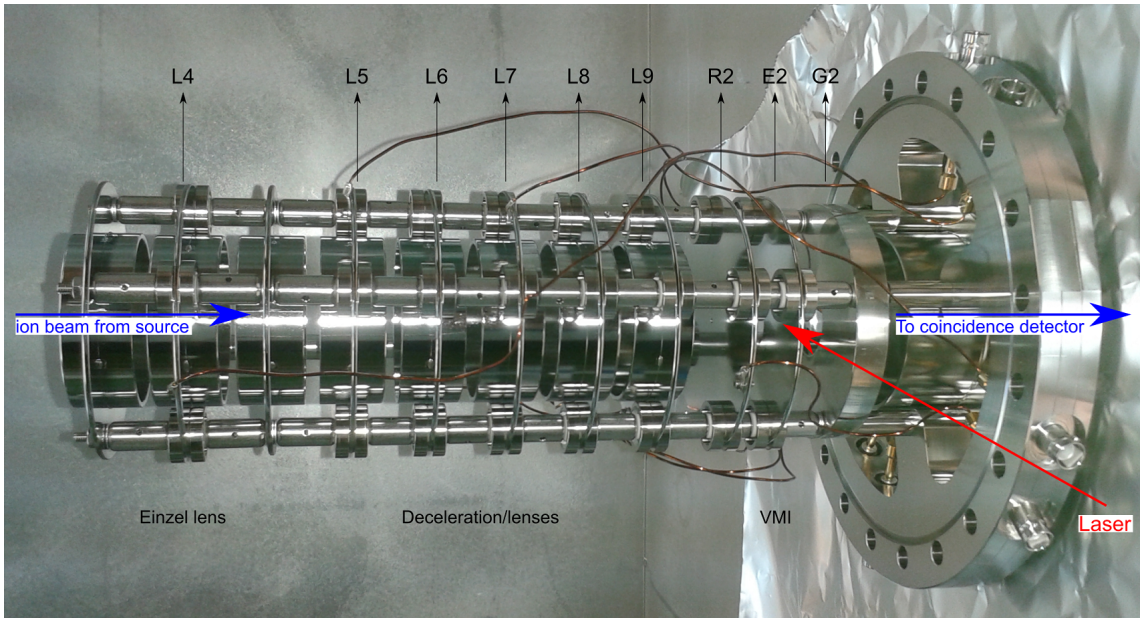

Figure 5.13.: Photograph of the third part of the ion optics. This stack includes one Einzel lens (L4), followed by a set of five electrodes (L5-L9) which can be used as additional lenses or to decelerate the ion beam. In the end the three CEI spectrometer electrodes (R2, E2, and G2) are located.

Testing the ion source and the mass spectrometer We tested both configurations of the ion source. In Fig. 5.14 the mass spectra for positive and negative ions, derived from the application of methanol (CH_3OH), seeded in argon, to the ion source are shown. These were produced with the plasma source. We used the first small diameter ToF MCP, located before the last stack of ion optics, for the test. The anode of the MCP was connected via a high-pass filter and a pre-amplifier to an oscilloscope for the measurement. Negative as well as positive ions assigned to several methanol fragments are produced. We calibrated the mass spectrum for positive ions on the basis of the Ar^+ peak (absolute flight time $\approx 16.6\,\mu s$) and the CH_3O^+ peak (absolute flight time $\approx 14.5\,\mu s$), which is the strongest of the methanol fragments. The mass spectrum for negative ions was calibrated on the basis of the C_2H^- peak (absolute flight time $\approx 9.4\,\mu s$) and the OH^- peak (absolute flight time $\approx 7.8\,\mu s$). It has to be noted, that for the mass spectrum of the negative ions, we applied a sliding average. Each shown data point is the average over three measured data points located next to each other. As expected, the positive ion production is to a considerable degree more effective. The inset in the left panel shows a detailed view of the peaks assigned to fragments of methanol without the dominating

argon peak. The respective values for voltages and timings applied during this measurement can be found in Tab. 5.3. The time delay is given with respect to the leading edge of the pulse which triggers the Even-Lavie valve (starting point of the measurement).

electrode	voltage [V]	time delay [µs]
pulsed valve	5	0
discharge unit	798	180
repeller	850	213
extractor	752	213
lens 1	444	
lens 2	0	
lens 3	0	
lens 4	0	
deflector 1, x	0	
deflector 1, y	19.4	
deflector 2, x	0	
deflector 2, y	5.3	

Table 5.3.: Values for voltages and the pulse timing while recording the mass spectrum for positive ions resulting from plasma ionization of methanol, plotted in Fig. 5.14. The time delay is given with respect to the leading edge of the pulse which triggers the Even-Lavie valve. For electrodes with no given delay time the potential was permanently applied.

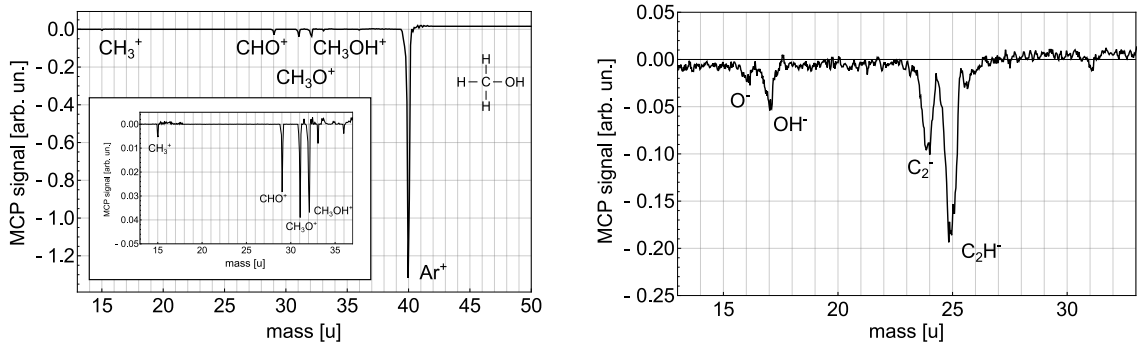

Figure 5.14.: Spectrum of positively (left) and negatively (right) charged ions originating from the ionization of methanol seeded in argon. The ion source was operated in pulsed mode with the discharge unit employed. The inset in the left panel shows a detailed view on the peaks assigned to fragments of methanol without the dominating argon peak.

In Fig. 5.15 a spectrum of positively charged ions originating from the electron impact ionization of benzene (C_6H_6), picked up by argon carrier gas, is shown.

We produced this spectrum with the electron beam ion source. Here, we used the detector located at the end of the flight path. The phosphor screen was connected via a high-pass filter and a pre-amplifier to an oscilloscope for the measurement. The respective values for voltages applied during this measurement can be found in Tab. 5.4. We calibrated the mass spectrum on the basis of the Ar^+ peak (absolute flight time $\approx 37.2\,\mu s$) and the $C_6H_6^+$ peak (absolute flight time $\approx 51.8\,\mu s$). We assigned the strongest peak in the spectrum to argon ions. Smaller peaks are assigned to an intact benzene ring ($C_6H_6^+$) as well as to fragments of it. With the electron beam source also doubly-charged argon ions are produced. To estimate the number of detected benzene ions, we divided the area of the benzene peak by the peak area corresponding to a single ion. The highest yield obtained from the ion source in the present mode were around 60 singly-charged benzene ions (Mass 78 u) and 870 singly-charged argon ions. For a simulated ion focus of $1.4\,mm^3$ we estimated that approximately 150 ions are needed in the ion package to obtain one ion in the laser focus. Hence, depending on the explored ion species, the estimated ion number is sufficient for a coincidence CEI experiment with an intended number of less than one ion in the focus. However, to explore rare ion species an increase of the produced ion number would be desirable.

An additional point to consider is the mass resolution of the spectrometer. We estimated before that the maximum resolvable mass (which is completely separated from the neighboring mass with $\Delta M = 1$) is $M_{max} > 398\,u$. In the mass spectrum shown in Fig. 5.15 it can be seen that already the peaks assigned to the masses 77 u and 78 u start to overlap. We recorded the mass spectrum with the same conditions as we chose for the estimation. Since the mass resolution in the measurement is worse than in the estimation, we conclude that the start parameters for the ion beam spatial and energy distribution are broader than expected.

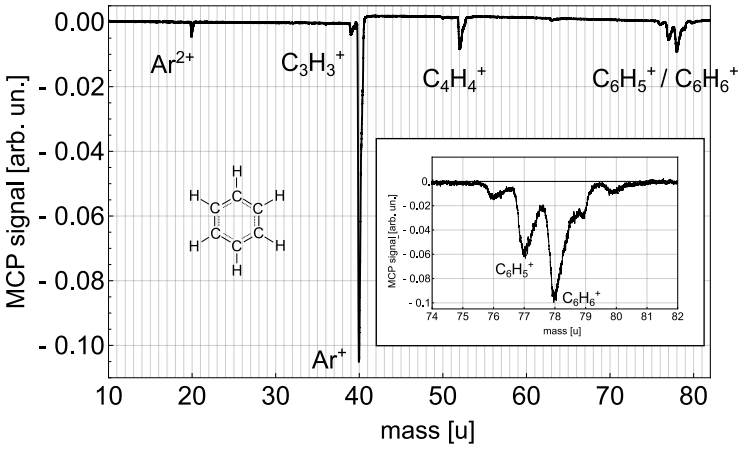

Figure 5.15.: Mass spectrum of argon bubbled through benzene. The ion source was running in continuous mode with the electron gun.

electrode	voltage [V]	electrode e-gun	voltage [V]
repeller	2000	repeller	-723
extractor	1933	extractor	-600
lens 1	-4	deflector 1	0
lens 2	0	deflector 2	35
lens 3	0	filament	4.4 A (13.2 W)
lens 4	-5180		
deflector 1, x	0		
deflector 1, y	17.1		
deflector 2, x	-3.4		
deflector 2, y	-9.0		

Table 5.4.: Values for voltages while recording the mass spectrum for benzene ions, plotted in Fig. 5.15. Since the valve in the electron beam ion source is running in continuous mode, no timing is needed (arbitrary switching of the repeller and extractor electrodes). The value for the filament is a current given in Ampere.

5.2.3. Neutral gas source

For the last part of the setup, we designed an additional supersonic gas source, directly attached to the VMI spectrometer. One challenge anticipated when working with ionic targets is to provide a stable overlap of the ion package and the tightly focused laser beam with a sufficient number of ions in the focus. The second source provides a robust neutral target for setting up the Coulomb explosion. Furthermore, it allows to perform less technically challenging CEI imaging experiments on dynamics in neutral molecules, similar to the experiments described in chapter 3 and 4, or van der Waals clusters. Finally, crossed-beam experiments of neutrals and ions are an alternative mode of operating the experimental setup.

A schematic drawing of the source is shown in Fig. 5.16. The neutral gas source was included in the setup in a separate vacuum chamber located above the interaction zone. The gas is expanded through a nozzle of 20 µm in a supersonic expansion and passes two skimmers (Beam Dynamics, Inc., 1 mm orifice) before it enters the interaction zone centered between the electrodes R2 and E2 of the CEI spectrometer.

5.3. Strong-field induced molecular break-up of 1-butene

We performed a first experiment on the correlation of fragments originating from strong-field ionization of 1-butene molecules using the neutral molecular beam source. By exploring the detailed break-up dynamics, information on (i) the different frag-

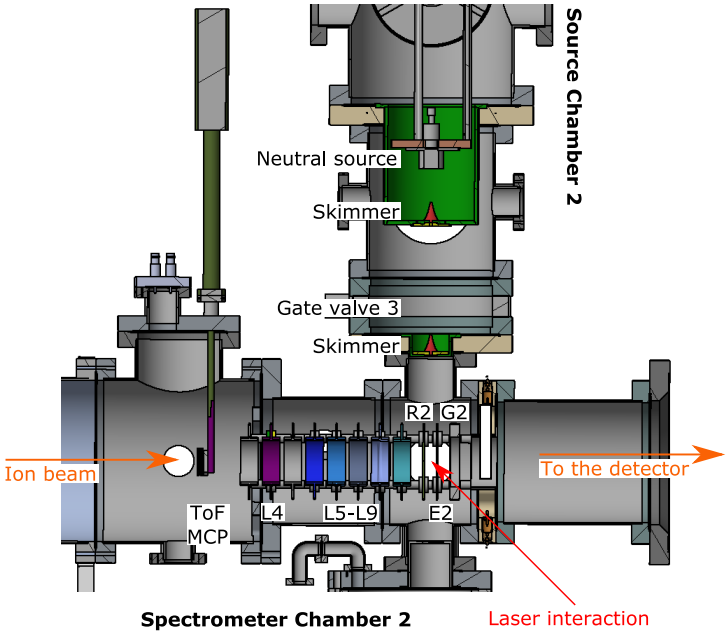

Figure 5.16.: Schematic drawing of the neutral molecular beam source. The neutral source is directly attached to the VMI spectrometer. The source is separated from the interaction zone via two skimmers. In the interaction zone, the molecular beam is overlapped with the laser beam.

mentation channels, (ii) potential rearrangements in the molecule due to the influence of the strong field, and (iii) potential metastable intermediate states can be identified. The following results are explored within the master thesis of Friedrich Freyse [155]. Here, an overview over the results is given, for further details see Ref. [155].

1-butene ($CH_3CH_2CH{=}CH_2$) is an isomer of butene. The singly-charged cation is stable in its ground state, but fragments when it is excited to higher electronic states. The molecular structure of 1-butene is shown in Fig. 5.17.

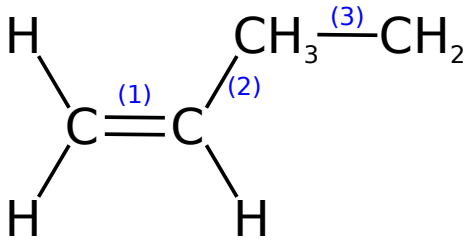

Figure 5.17.: Structural formula of 1-butene. The three C-C bonds are labeled with the numbers (1), (2), and (3).

We used a 1 kHz Ti:Sa-laser system based on a regenerative amplifier (Spitfire, Spectra Physics) to ionize 1-butene. In the experiment, we expanded 2 % of 1-butene seeded in helium with the neutral beam source in a supersonic expansion (2 bar stagnation pressure). In the interaction zone the molecular beam was overlapped with the laser beam. We measured the time-of-flight of the single fragments

per laser pulse, without measuring the two-dimensional spatial distribution on the detector. Hence, in this measurement we operated the CEI spectrometer in the time-of-flight mode. The measurement was done under covariance conditions [156]. In a covariance measurement, the ionization rate can be higher compared to a coincidence measurement. There is no need to have less than one molecule in the laser focus. For a possible set of flight times t_1, t_2 .... t_n the elements in the covariance matrix are calculated via:

$$C_{i,j} = \mathrm{Cov}(t_i, t_j) = \langle (t_i - \langle t_i \rangle)(t_j - \langle t_j \rangle) \rangle = \langle t_i t_j \rangle - \langle t_i \rangle \langle t_j \rangle \tag{5.9}$$

$$= \frac{1}{N} \sum_{k=1}^{N} t_i(k) t_j(k) - \left[\frac{1}{N} \sum_{k=1}^{N} N t_i(k) \right] \left[\frac{1}{N} \sum_{k=1}^{N} t_j(k) \right]. \tag{5.10}$$

Here, $t_{i,j}$ are the flight times of certain fragments and k is the number of measurements from N laser pulses. If there is a higher probability of detecting an ion with the flight time t_i when at the same time an ion with flight the time t_j is detected, the corresponding area in the covariance map has a positive value. Hence, correlations between the fragments get visible.

We varied the pulse length and the pulse energy of the laser in four covariance measurements. In Fig. 5.18 the recorded covariance map (taken from Ref. [155]) for 220 fs laser pulse length and 62 µJ laser pulse energy is shown. In the shown map we converted the flight times into ion masses. The other recorded covariance maps can be found in Ref. [155].

The covariance maps can be analyzed in the same way as the coincidence maps discussed in chapter 3. A diagonal line indicates a correlation between two fragments. In the covariance map in Fig. 5.18 a variety of correlations can be seen. Here, we discuss only a selection (a full list of all detected correlations can be found in Ref. [155]). The map is structured in bands, where each band corresponds to the break-up of one of the three C-C bonds in C_4H_8 (see Fig. 5.17) with an additional loss of a certain number of hydrogen atoms. We assigned the strongest channel to the correlation between the two fragments CH_3^+ (15 u) + $C_3H_3^+$ (39 u). This corresponds to a cleavage of the carbon bond (3) and an additional loss of two hydrogen atoms in the $C_3H_5^+$ fragment. Similar strong is the correlation between the fragments $C_2H_3^+$ (27 u) + $C_2H_2^+$ (26 u). Here, the C-C bond (2) is broken and in addition there is a loss of all three hydrogen atoms of the methyl group. In the same band the symmetric channels $C_2H_2^+$ (26 u) + $C_2H_2^+$ (26 u) and $C_2H_3^+$ (27 u) + $C_2H_3^+$ (27 u) are clearly pronounced as well. Interestingly, a small but visible correlation between two fragments with mass 28 u can be seen in this band. To create these two ethylene fragments in a break-up process of 1-butene, a hydrogen migration has to occur. Another break-up we detected, is the correlation between the two fragments CH_3^+ (15 u) + C_3H^+ (37 u). Besides the short diagonal line, indicating a fast break-up into the two fragments, a long sharp line which approaches the flight time of the doubly-charged parent molecule $C_4H_4^{2+}$ is detected. The long line stems from a slow dissociation of $C_4H_4^{2+}$. The flight times of the two fragments change, depending on at what time delay after switching on the potential on the accelerating electrodes the break-up into the final fragments occurs. If the bond cleavage takes place when the molecule has reached already the end of the accelerating zone, or is

even outside the three spectrometer electrodes, both fragments have the flight time of the doubly-charged parent molecule $C_4H_4^{2+}$.

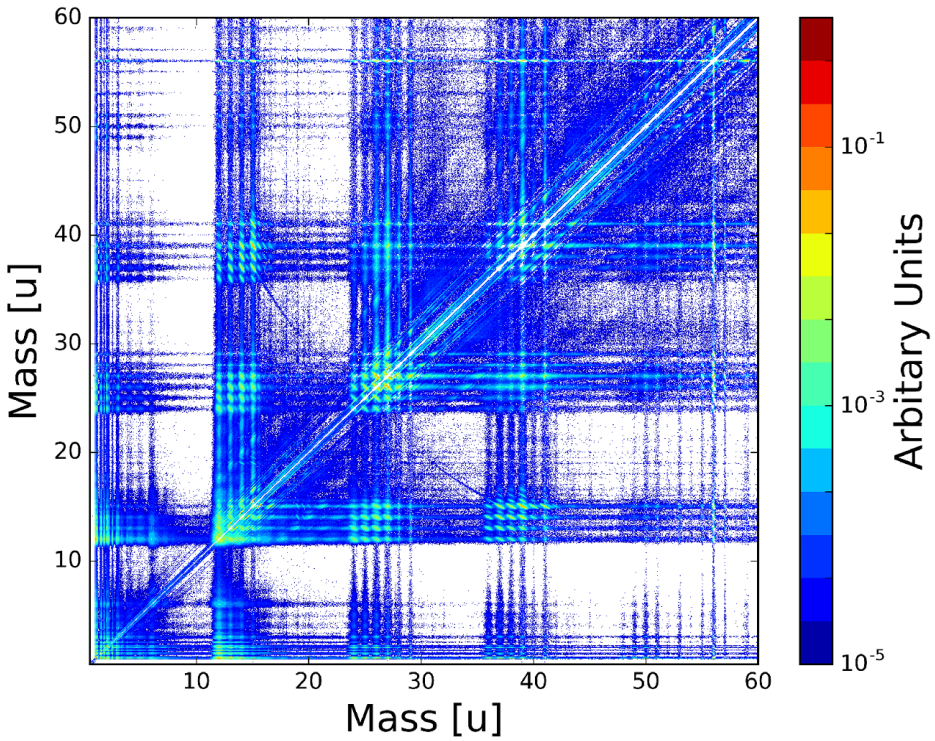

Figure 5.18.: Covariance map taken from Ref. [155]. The map is structured in bands, where each band corresponds to the break-up of one of the three C-C bonds in the parent molecule C_4H_8 with an additional loss of a certain number of hydrogen atoms. See the text for further details.

5.4. Summary

In the introduction of the thesis (chaper 1) we presented the idea for a new approach to explore the time-dependent change of the molecular configuration during bimolecular ion-molecule reactions. For this, we want to combine Coulomb explosion imaging with established precursor preparation techniques. In this chapter the design and implementation of the first stages of a new machine, including an ion source, a time-of-flight mass spectrometer, a Coulomb explosion imaging spectrometer, and a neutral molecular beam source is presented. A three-dimensional drawing of the new setup in the current stage is shown in Fig. 5.19. We performed a first experiment to explore the fragmentation of 1-butene upon strong-field ionization and the correlation between the ionic fragments.

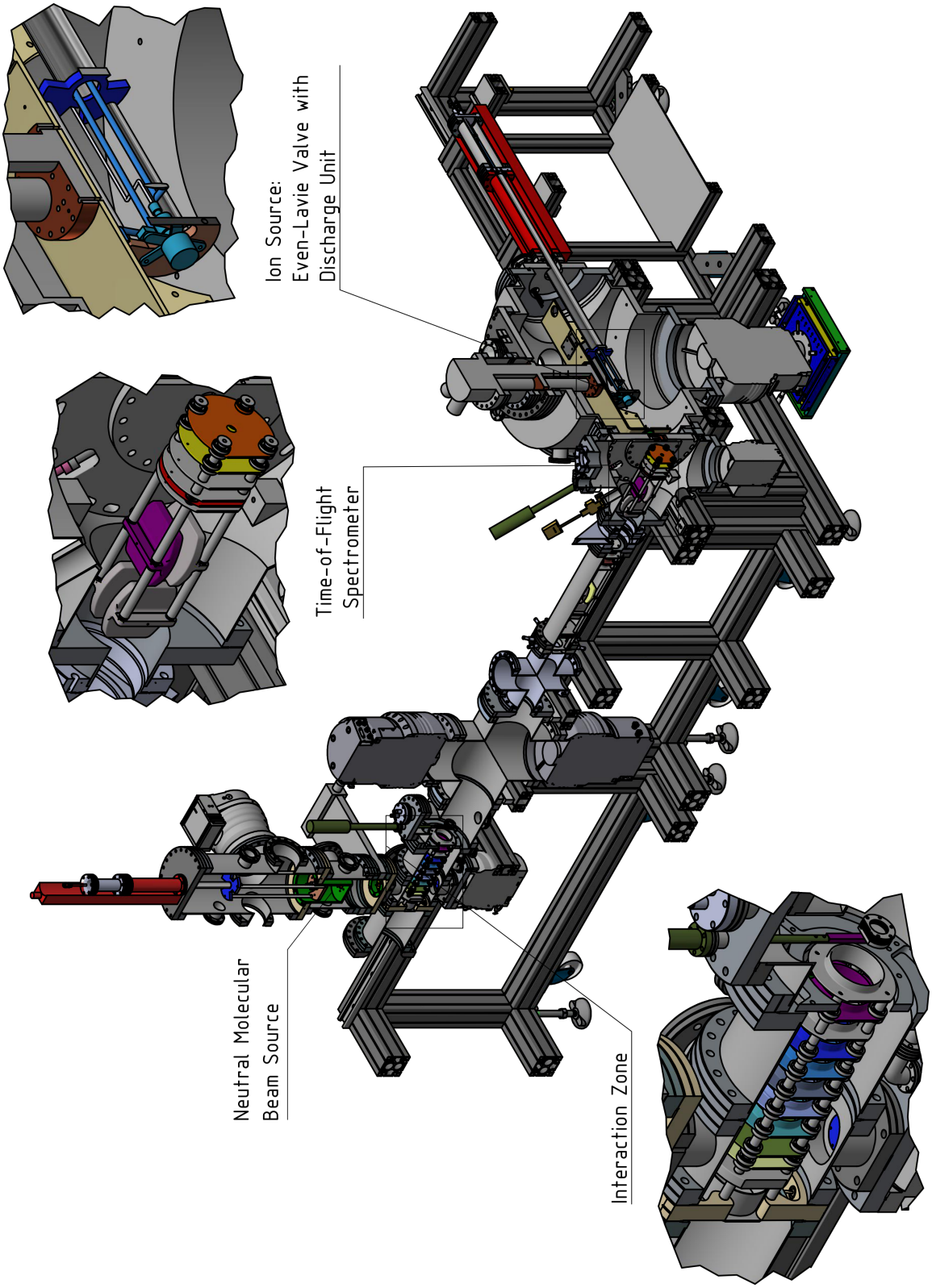

Figure 5.19.: CAD drawing of the complete setup in the final stage. The single parts are described in detail in the text.

6 Chapter 6. Summary and outlook

In this thesis, we studied the two different molecules CH_2BrI and N_2O_4 by measuring the three-dimensional momentum distribution of ionic fragments, created during the strong-field ionization of the molecules in a femtosecond laser pulse. From the gained momentum information we were able to draw conclusions on the distinct molecular dynamics. Additionally, we designed and implemented a new setup in the frame of the thesis, with the aim to image time-dependent bimolecular ion-molecule reactions.

In the first part of the thesis, we studied the fragmentation pathways of CH_2BrI^{3+} following strong-field ionization with a reaction microscope and the technique of coincidence Coulomb explosion imaging. We detected five different fragmentation channels that lead to the three reaction products $CH_2^+ + Br^+ + I^+$. Around 20 % of all fragmentation processes occurred via a direct non-sequential Coulomb explosion channel where both the C-Br and C-I bond break simultaneously. The momentum distribution of fragments in this channel reflects the geometry of the neutral molecule.

Furthermore, we detected two sequential channels with long-lived intermediate states and two sequential channels with short-lived intermediate states. In the two sequential channels with long-lived intermediate states the fragmentation path proceeds via an intermediate doubly-charged state (CH_2I^{*2+} or CH_2Br^{*2+}) with a lifetime longer than the rotational period of the fragment. By breaking the first bond, the intermediate molecule gains rotational energy. At the time of the second bond cleavage, the molecular orientation is randomly distributed with respect to the first leaving fragment. We could detect both possible pathways, where either the C-Br bond breaks first or the C-I bond breaks first. The two sequential channels with long-lived intermediate states were clearly separated from other events in the chosen representation of Newton diagrams and Dalitz plots. From the measured momenta of the final fragments in these channels we calculated the internuclear distance and the rotational constant of the intermediate fragments.

Additionally, we found evidence for two sequential processes, where the intermediate fragments have a lifetime shorter than the rotational period. In these pathways, the intermediate CH_2Br^{*2+} (or CH_2I^{*2+}) starts to dissociate directly after the cleavage of the first bond. The first leaving fragment is still in the vicinity of the intermediate fragment at the time of the second bond cleavage. This leads to structures in the momentum representation of the Newton diagram (energy representation of the Dalitz plot) which mark the transition between the non-sequential Coulomb explosion channel structure and the structures originating from the sequential channels with the long-lived intermediate states. We estimated that it takes around 1 ps after the first bond cleavage until the first leaving fragment does not influence the break-

up of the intermediate anymore, which is the estimated upper limit for the lifetime of the short-lived intermediates in the sequential channels.

As a future perspective, it is desirable to carry out further experiments to explore how the fraction of the direct non-sequential Coulomb explosion events could be increased. Since the momentum distribution from fragments of these break-up process carries the information on the geometry of the neutral molecule, separating only these events in a pump-probe experiment allows to better follow the structural change in induced molecular dynamics. By varying the pulse length, wavelength and intensity the optimal experimental conditions to decrease the deviation from the theoretical kinetic energy release value and to suppress the influence of the sequential channels, overlapping with the non-sequential channel, can be identified.

In the second part of the thesis, we explored the N-N stretching vibration of dinitrogen tetroxide (N_2O_4) with a combination of a velocity map imaging spectrometer, an in-vacuum pixel detector and a high-repetition rate few-cycle laser system. We excited the N-N stretching vibration ($t = 130\,fs$) in an impulsive stimulated Raman scattering (ISRS) process with the pump pulse in the neutral molecule. After a certain time-delay, we strong-field ionized the vibrating molecule with the probe pulse and measured the three-dimensional momentum vectors of the created ionic fragments. After the ionization the cation is in an unstable state, leading to a dissociation of the molecule into the two fragments $NO_2^+ + NO_2$. In the time-dependent kinetic energy release of the measured NO_2^+ fragments we detected an oscillation at small kinetic energies, fitting the vibrational period of the N-N stretch.

From the amplitude of the oscillation, detected in the kinetic energy release, we gained information on the amplitude of the N-N vibration. We determined the N-N bond distance of 1.56 Å at the inner turning point from the maximum kinetic energy release of 0.44 eV per NO_2^+ fragment. The determined minimal bond distance corresponds to a vibrational amplitude of 0.19 Å. This is the first experimental determination of the vibrational amplitude.

Furthermore, we detected fragments resulting from the double ionization of the dissociating molecule. In this process, the parent molecule is singly ionized with the first laser pulse and starts to dissociate into the two fragments $NO_2 + NO_2^+$. The second laser pulse ionizes the neutral fragments and the resulting two NO_2^+ fragments repel each other due to the Coulomb force. Depending on the time delay between the two pulses, the final kinetic energy release of the fragments is changing. From the maximum of the kinetic energy release of the fragments we could estimate the distance between the two charge centers of the two NO_2 groups in the parent molecule to be 2.72 Å.

These results illustrate the high potential of strong-field ionization pump-probe experiments to explore molecular dynamics. In future work with the used setup, possible improvements can be achieved by optimizing the data processing. In the current experiment we detected a not-clarified loss of events in the data processing which led to reduced statistics in the data analysis.

During the third part of this thesis, we designed and implemented a new setup with the aim to explore a great variety of molecular dynamics, including the observation of neutral and ionic molecules separately, scattering dynamics between them both, and

in a future stage of development, imaging time-dependent bimolecular ion-molecule reactions with Coulomb explosion imaging. The new system includes an ion source, a time-of-flight mass spectrometer, a Coulomb explosion imaging spectrometer, and an additional neutral molecular beam source. Currently, the setup is in a stage where first experiments with the neutral source have been carried out and the production of ions and the performance of the ion spectrometer have been tested.

In a first experiment using the neutral molecular beam source, we studied the fragmentation of 1-butene molecules upon strong-field ionization. We used covariance maps to visualize the correlations between the created fragments and hence the different break-up channels. In a first test of the ion source, we measured mass spectra for positive and negative ions derived from ionizing methanol and benzene seeded in argon. We successfully established a stable working ion source. However, at the time of this thesis, the overall amount of detected ions was still too low for experiments on rare ion species. Hence, further investigations in the ion source and the ion beam path are desirable. To improve the ion production, we plan to implement a dielectric barrier discharge unit as an alternative ion source, which is known to produces negative and positive ions with high efficiency.

Besides improving the ion production, we plan to implement a new detection system, to measure the three-dimensional momentum vector of created fragments. These improvements would open the way for coincidence experiments which allow for the exploration of even rarely occurring molecular processes. The coincidence experiments will provide insight into geometry rearrangements and kinetic energy distributions in certain molecular dynamics, including transient intermediate molecular configurations around the transition state of bimolecular chemical reactions.

A Appendix A.

Influence of false coincidences

In chapter 3 the three-body fragmentation of CH_2BrI^{3+} into the three charged particles $CH_2^+ + Br^+ + I^+$ was studied using the technique of coincidence detection. We estimated the percentage of false coincidences after a filter on the momentum sum in the z-direction of -5 a.u.$< \Sigma p_z <$ 5 a.u. to be around 10 %. Here, we want to compare the resulting features for changed filter conditions to motivate that our choice is sufficient. We compare the the result of three additional filter conditions on the momentum sum in the z-direction:

$$\begin{aligned} \text{A} \quad & 20\,\text{a.u.} < \Sigma p_z < 50\,\text{a.u.}\ (^{79}\text{Br}) \\ & 50\,\text{a.u.} < \Sigma p_z < 80\,\text{a.u.}\ (^{81}\text{Br}) \end{aligned}$$

$$\begin{aligned} \text{B} \quad & 50\,\text{a.u.} < \Sigma p_z < 90\,\text{a.u.}\ (^{79}\text{Br}) \\ & 80\,\text{a.u.} < \Sigma p_z < 120\,\text{a.u.}\ (^{81}\text{Br}) \end{aligned}$$

$$\begin{aligned} \text{C} \quad -15\,\text{a.u.} < \Sigma p_z < -5\,\text{a.u.}\ (^{79}\text{Br}) \\ 5\,\text{a.u.} < \Sigma p_z < 15\,\text{a.u.}\ (^{81}\text{Br}) \end{aligned}$$

The first two filters A and B select events which lead to the two additional small peaks in the momentum sum Σp_z on the right-hand side of the main peaks. The third filter C selects the area between the two sharp peaks in the momentum sum in Fig. 3.10 which should represent best, the influence of the false coincidences in our analysis. The resulting Newton diagrams from the three filter conditions are plotted in Fig. A.1.

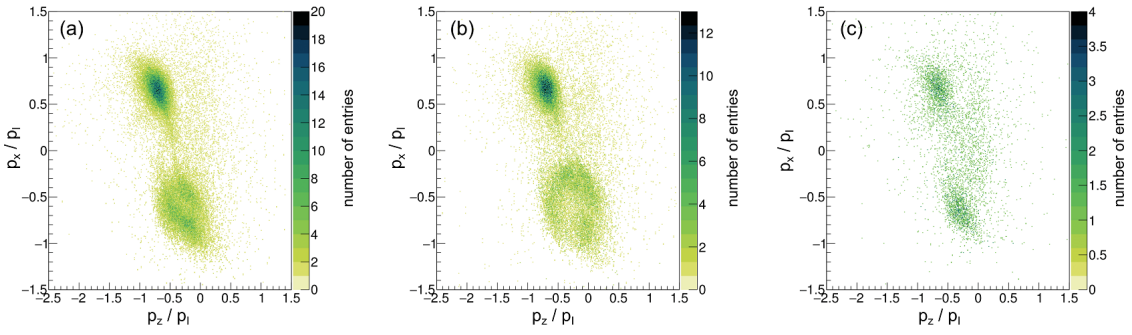

Figure A.1.: The resulting Newton diagrams with the applied filter A, B, and C.

From panel (a) and (b) it can be seen that the smaller side peaks lead to similar structure as analyzed in chapter 3. However, the rings originating from the sequential break-ups are not detected anymore. At the same time, the peak structures are blurred. Especially the momenta of the methylene fragment are bleached in the center of the original peak. We assume, that the side peaks are events of single molecule break-ups, where the CH_2^+ fragment looses one or two hydrogen atoms. Hence, the calculated momenta are wrong, but the resulting structure is similar. Since the Br^+ and the I^+ ion are much heavier than the CH_2^+ ion, the momenta of these two components are less affected.

The plot in panel (c) of Fig. A.1 represents best, which contribution in our selected data is based on false coincidences. The peak structure is still present, but much weaker as for the analyzed data set. It is most likely coming from the tail of the next smaller side peak. However, since the ring structures from the sequential processes are exclusively detected with the applied filter condition -5 a.u.$< \Sigma p_z <$ 5 a.u. and the contribution to the peak structure is to a great extent higher in this range, we conclude that the influence of the 10 % of false coincidences still present in our analyzed data is not severe for the interpretation and are most likely due due single-molecule processes where we detect CH^+ instead of CH_2^+.

B Appendix B.
Ion optics design

In the frame of this thesis we designed our own ion optics and in addition, a flexible modular construction system to assemble the single electrodes. Here, we show drawings of the main parts: the lenses, the deflectors, and the thin circular electrodes used as thin lenses and further as extractor and repeller electrodes of the mass spectrometer and the VMI (see Fig. B.1, B.2, and B.3). We designed the ion optics with a large aperture to ensure a homogeneous field in the middle of the lenses/deflectors, but sufficiently small to be manufactured onto a standard CF 100 flange (circular electrodes: $\varnothing = 95\,\mathrm{mm}$). We choose a reasonably large length of the lenses ($l = 22\,\mathrm{mm}$) at positions where space is available, which improves focusing properties. The single electrodes are connected via stainless steel spacers with tapped holes. Two spacers are attached to each other by a grub screw with the electrode clamped in between. The length of the spacers can be customized to the specific needed arrangement. To isolate the grub screw and the spacers (both grounded) from the electrode which is on potential we used commercial ceramic bushings. Ceramic can charge-up due to impinging ions or electrons. To avoid a distortion of the electric field and increase the stability we placed the isolating ceramic bushings in a small shielding made out of stainless steel.

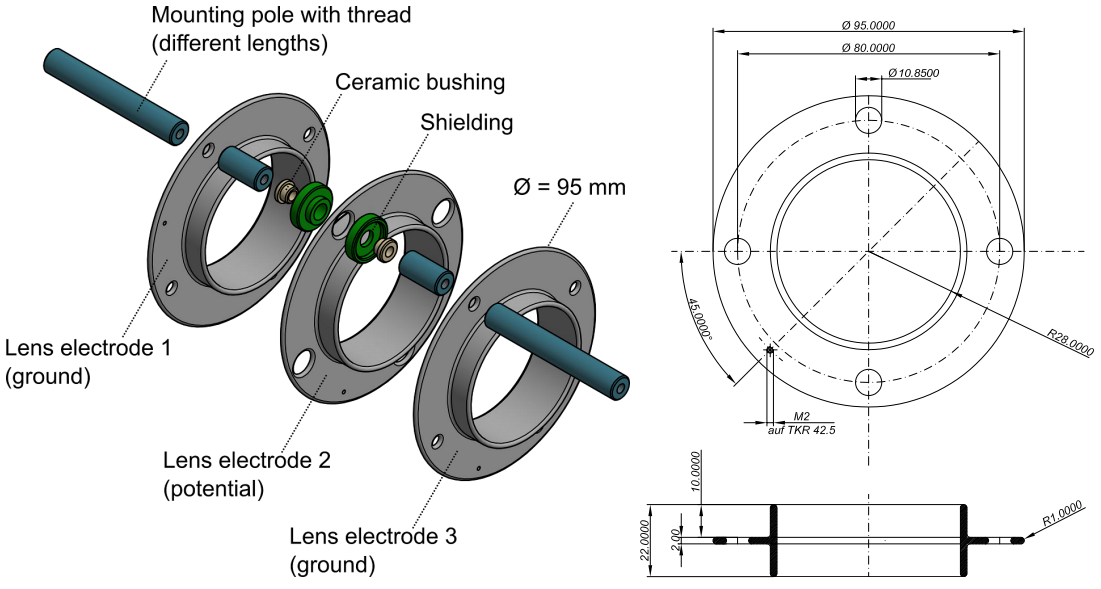

Figure B.1.: Left: Illustration of the modular construction system to assemble the lenses. The middle electrode (on potential) is isolated from the grounded spacers via ceramic bushings. The connecting grub screw is not included in the Figure. Right: Technical drawing of a lens.

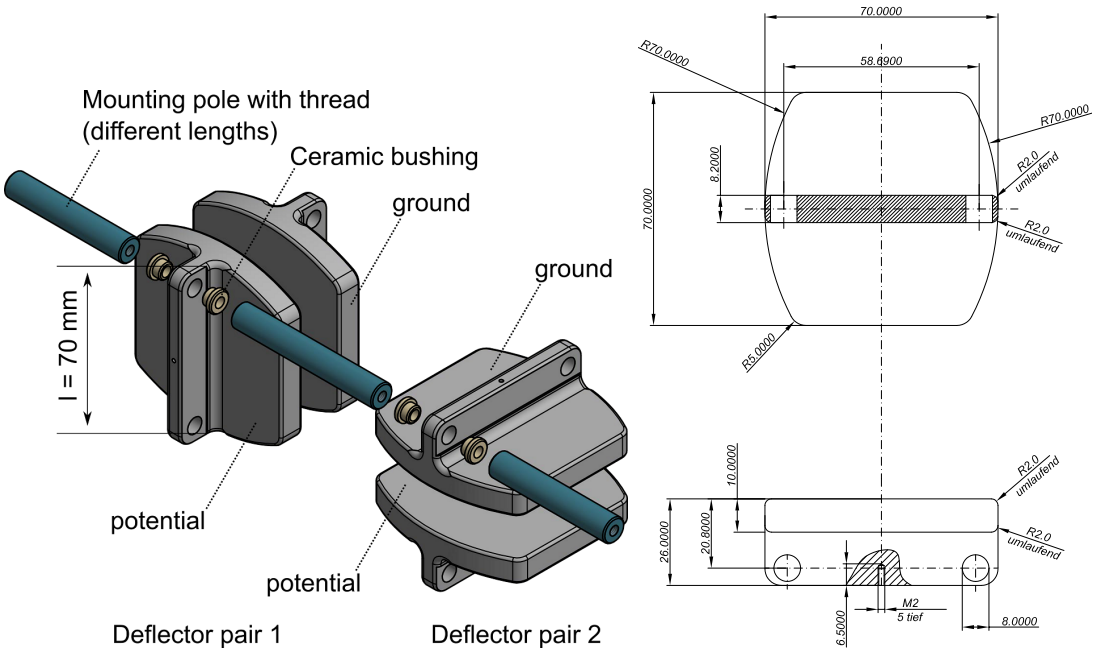

Figure B.2.: Left: Illustration of the modular construction system to assemble the deflectors. One deflector of each pair is on potential while the other one is grounded. To keep the assembling simple, all deflector electrodes are isolated from the spacers with the ceramic bushings and are connected via cable connections to either the applied potential or to the ground. The connecting grub screw is not included in the Figure. Right: Technical drawing of a deflector electrode.

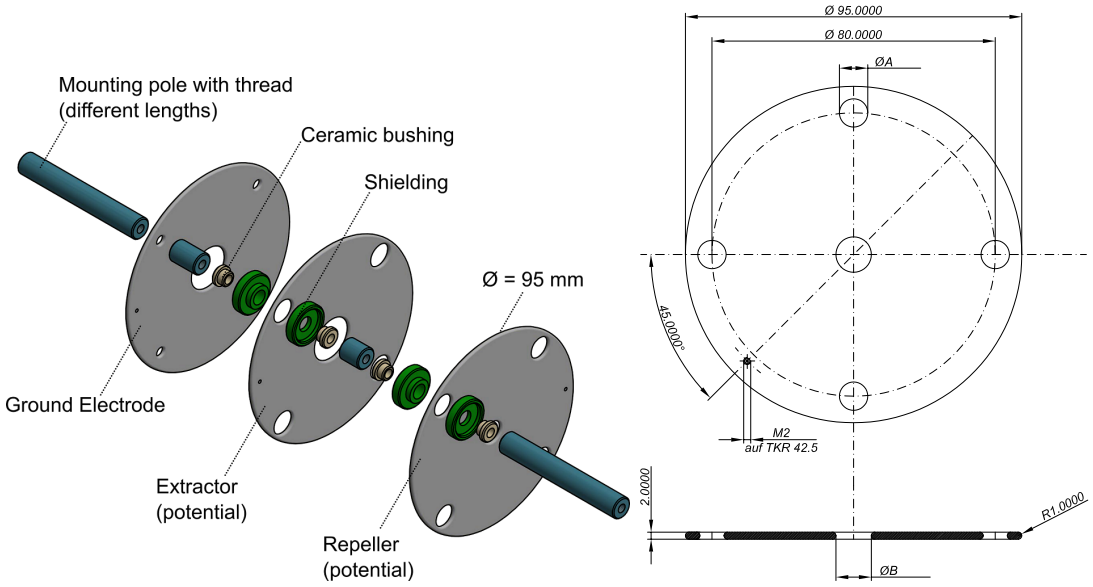

Figure B.3.: Left: Illustration of the modular construction system to assemble the repeller, extractor and grounded electrode of the accelerating zone of the mass spectrometer. The repeller and extractor electrodes (on potential) are isolated from the grounded spacers via ceramic bushings. The connecting grub screw is not included in the Figure. A nickel mesh is attached to the inner open part of these three electrodes with an additional clamping ring. The clamping ring and the mesh are not shown in the drawing. Right: Technical drawing of the thin circular electrodes used for thin lenses and for the extractor and repeller electrodes of the mass spectrometer and the VMI. The opening diameters $øA$ and $øB$ vary, depending on the purpose of the electrode.

Bibliography

[1] J. Xu, C. I. Blaga, P. Agostini, and L. F. DiMauro, "Time-resolved molecular imaging," *Journal of Physics B: Atomic, Molecular and Optical Physics*, vol. 49, no. 11, p. 112001, 2016.

[2] C. Altucci, R. Velotta, and J. Marangos, "Ultra-fast dynamic imaging: an overview of current techniques, their capabilities and future prospects," *Journal of Modern Optics*, vol. 57, no. 11, pp. 916–952, 2010.

[3] A. H. Zewail, "Femtochemistry: Atomic-Scale Dynamics of the Chemical Bond," *The Journal of Physical Chemistry A*, vol. 104, no. 24, pp. 5660–5694, 2000.

[4] M. J. Rosker, M. Dantus, and A. H. Zewail, "Femtosecond Clocking of the Chemical Bond," *Science*, vol. 241, no. 4870, pp. 1200–1202, 1988.

[5] L. Drescher, M. C. E. Galbraith, G. Reitsma, J. Dura, N. Zhavoronkov, S. Patchkovskii, M. J. J. Vrakking, and J. Mikosch, "Communication: XUV transient absorption spectroscopy of iodomethane and iodobenzene photodissociation," *Journal of Chemical Physics*, vol. 145, no. 1, 2016.

[6] F. Ling, S. Li, X. Song, Y. Wang, J. Long, and B. Zhang, "Femtosecond time-resolved observation of butterfly vibration in electronically excited o-fluorophenol," *Scientific Reports*, vol. 7, no. 1, p. 15362, 2017.

[7] J. Yang, M. Guehr, T. Vecchione, M. S. Robinson, R. Li, N. Hartmann, X. Shen, R. Coffee, J. Corbett, A. Fry, K. Gaffney, T. Gorkhover, C. Hast, K. Jobe, I. Makasyuk, A. Reid, J. Robinson, S. Vetter, F. Wang, S. Weathersby, C. Yoneda, M. Centurion, and X. Wang, "Diffractive imaging of a rotational wavepacket in nitrogen molecules with femtosecond megaelectronvolt electron pulses," *Nature Communications*, vol. 7, 2016.

[8] M. P. Minitti, J. M. Budarz, A. Kirrander, J. S. Robinson, D. Ratner, T. J. Lane, D. Zhu, J. M. Glownia, M. Kozina, H. T. Lemke, M. Sikorski, Y. Feng, S. Nelson, K. Saita, B. Stankus, T. Northey, J. B. Hastings, and P. M. Weber, "Imaging Molecular Motion: Femtosecond X-Ray Scattering of an Electrocyclic Chemical Reaction," *Phys. Rev. Lett.*, vol. 114, p. 255501, 2015.

[9] B. Wolter, M. G. Pullen, A.-T. Le, M. Baudisch, K. Doblhoff-Dier, A. Senftleben, M. Hemmer, C. D. Schröter, J. Ullrich, T. Pfeifer, R. Moshammer, S. Gräfe, O. Vendrell, C. D. Lin, and J. Biegert, "Ultrafast electron diffraction imaging of bond breaking in di-ionized acetylene," *Science*, vol. 354, no. 6310, pp. 308–312, 2016.

[10] C. Ellert, H. Stapelfeldt, E. Constant, H. Sakai, J. Wright, D. M. Rayner, and P. B. Corkum, "Observing molecular dynamics with timed Coulomb explosion imaging," *Philosophical Transactions of the Royal Society of London A: Mathematical, Physical and Engineering Sciences*, vol. 356, no. 1736, pp. 329–344, 1998.

[11] H. Stapelfeldt, E. Constant, H. Sakai, and P. B. Corkum, "Time-resolved Coulomb explosion imaging: A method to measure structure and dynamics of molecular nuclear wave packets," *Phys. Rev. A*, vol. 58, pp. 426–433, 1998.

[12] F. Légaré, K. F. Lee, I. V. Litvinyuk, P. W. Dooley, S. S. Wesolowski, P. R. Bunker, P. Dombi, F. Krausz, A. D. Bandrauk, D. M. Villeneuve, and P. B. Corkum, "Laser Coulomb-explosion imaging of small molecules," *Phys. Rev. A*, vol. 71, p. 013415, 2005.

[13] F. Légaré, K. F. Lee, A. D. Bandrauk, D. M. Villeneuve, and P. B. Corkum, "Laser Coulomb explosion imaging for probing ultra-fast molecular dynamics," *Journal of Physics B: Atomic, Molecular and Optical Physics*, vol. 39, no. 13, p. S503, 2006.

[14] J. Gagnon, K. F. Lee, D. M. Rayner, P. B. Corkum, and V. R. Bhardwaj, "Coincidence imaging of polyatomic molecules via laser-induced coulomb explosion," *Journal of Physics B: Atomic, Molecular and Optical Physics*, vol. 41, no. 21, p. 215104, 2008.

[15] A. Matsuda, M. Fushitani, E. J. Takahashi, and A. Hishikawa, "Visualizing hydrogen atoms migrating in acetylene dication by time-resolved three-body and four-body Coulomb explosion imaging," *Phys. Chem. Chem. Phys.*, vol. 13, pp. 8697–8704, 2011.

[16] M. Pitzer, M. Kunitski, A. S. Johnson, T. Jahnke, H. Sann, F. Sturm, L. P. H. Schmidt, H. Schmidt-Böcking, R. Dörner, J. Stohner, J. Kiedrowski, M. Reggelin, S. Marquardt, A. Schießer, R. Berger, and M. S. Schöffler, "Direct Determination of Absolute Molecular Stereochemistry in Gas Phase by Coulomb Explosion Imaging," *Science*, vol. 341, no. 6150, pp. 1096–1100, 2013.

[17] H. Ibrahim, B. Wales, S. Beaulieu, B. E. Schmidt, N. Thiré, E. P. Fowe, r. Bisson, C. T. Hebeisen, V. Wanie, M. Giguére, J.-C. Kieffer, M. Spanner,

A. D. Bandrauk, J. Sanderson, M. S. Schuurman, and F. Légaré, "Tabletop imaging of structural evolutions in chemical reactions demonstrated for the acetylene cation," *Nature Communications*, vol. 5, p. 4422, 2014.

[18] M. Kunitski, S. Zeller, J. Voigtsberger, A. Kalinin, L. P. H. Schmidt, M. Schöffler, A. Czasch, W. Schöllkopf, R. E. Grisenti, T. Jahnke, D. Blume, and R. Dörner, "Observation of the Efimov state of the helium trimer," *Science*, vol. 348, no. 6234, pp. 551–555, 2015.

[19] W. Bothe and H. Geiger, "Über das Wesen des Comptoneffekts; ein experimenteller Beitrag zur Theorie der Strahlung," *Zeitschrift für Physik*, vol. 32, no. 1, pp. 639–663, 1925.

[20] B. Brehm and E. von Puttkamer, "Koinzidenzmessung von Photoionen und Photoelektronen bei Methan," *Zeitschrift Naturforschung Teil A*, vol. 22, pp. 8–10, 1967.

[21] N. F. Scherer, L. R. Khundkar, R. B. Bernstein, and A. H. Zewail, "Real-time picosecond clocking of the collision complex in a bimolecular reaction: The birth of OH from H + CO_2," *The Journal of Chemical Physics*, vol. 87, no. 2, pp. 1451–1453, 1987.

[22] R. Wester, A. E. Bragg, A. V. Davis, and D. M. Neumark, "Time-resolved study of the symmetric SN_2-reaction I^- + CH_3I," *The Journal of Chemical Physics*, vol. 119, no. 19, pp. 10 032–10 039, 2003.

[23] D. Gerlich, *Inhomogeneous RF Fields: A Versatile Tool for the Study of Processes with Slow Ions*, 2007, pp. 1–176.

[24] J. B. Kim, M. L. Weichman, T. F. Sjolander, D. M. Neumark, J. Kłos, M. H. Alexander, and D. E. Manolopoulos, "Spectroscopic observation of resonances in the F + H_2 reaction," *Science*, vol. 349, no. 6247, pp. 510–513, 2015.

[25] J. Long, F. J. Furch, J. Durá, A. S. Tremsin, J. Vallerga, C. P. Schulz, A. Rouzée, and M. J. J. Vrakking, "Ion-ion coincidence imaging at high event rate using an in-vacuum pixel detector," *The Journal of Chemical Physics*, vol. 147, no. 1, p. 013919, 2017.

[26] Medipix collaboration CERN. The Timepix chip. URL: http://medipix.web.cern.ch/technology-chip/timepix-chip Acessed: 2017-10-30.

[27] M. Y. Ivanov, M. Spanner, and O. Smirnova, "Anatomy of strong field ionization," *Journal of Modern Optics*, vol. 52, no. 2-3, pp. 165–184, 2005.

[28] R. Dörner, T. Weber, M. Weckenbrock, A. Staudte, M. Hattass, R. Moshammer, J. Ullrich, and H. Schmidt-Böcking, "Multiple Ionization in Strong Laser

Fields," vol. 48, 2002.

[29] B. Sheehy and L. F. DiMauro, "Atomic and Molecular Dynamics in Intense Optical Fields," *Annual Review of Physical Chemistry*, vol. 47, no. 1, pp. 463–494, 1996.

[30] L. V. Keldysh, "Ionization in the field of a strong electromagnetic wave," *Soviet Physics JETP-USSR*, vol. 20, no. 5, p. 1307, 1965, english translation.

[31] H. B. Bebb and A. Gold, "Multiphoton Ionization of Hydrogen and Rare-Gas Atoms," *Phys. Rev.*, vol. 143, pp. 1–24, 1966.

[32] R. Murray, M. Spanner, S. Patchkovskii, and M. Y. Ivanov, "Tunnel Ionization of Molecules and Orbital Imaging," *Phys. Rev. Lett.*, vol. 106, p. 173001, 2011.

[33] R. Murray, S. Patchkovskii, O. Smirnova, and M. Y. Ivanov, *Strong-Field Ionization of Molecules: Simple Analytical Expressions*. New York, NY: Springer New York, 2011, pp. 135–147.

[34] P. Agostini, F. Fabre, G. Mainfray, G. Petite, and N. K. Rahman, "Free-Free Transitions Following Six-Photon Ionization of Xenon Atoms," *Phys. Rev. Lett.*, vol. 42, pp. 1127–1130, 1979.

[35] P. Kruit, J. Kimman, H. G. Muller, and M. J. van der Wiel, "Electron spectra from multiphoton ionization of xenon at 1064, 532, and 355 nm," *Phys. Rev. A*, vol. 28, pp. 248–255, 1983.

[36] I. V. Hertel and C. P. Schulz, *Atome, Moleküle und optische Physik 1*. Springer, 2008.

[37] A. Saenz. (2014) Atoms and Molecules in Intense Laser Fields (2). URL: https://www.physik.hu-berlin.de/de/amo/teaching/qo_multiphotonenprozesse.pdf Acessed: 2018-04-09.

[38] P. B. Corkum, "Plasma perspective on strong field multiphoton ionization," *Phys. Rev. Lett.*, vol. 71, pp. 1994–1997, 1993.

[39] K. C. Kulander, K. J. Schafer, and J. L. Krause, *Dynamics of Short-Pulse Excitation, Ionization and Harmonic Conversion*. Boston, MA: Springer US, 1993, pp. 95–110.

[40] M. Ferray, A. L'Huillier, X. F. Li, L. A. Lompre, G. Mainfray, and C. Manus, "Multiple-harmonic conversion of 1064 nm radiation in rare gases," *Journal of Physics B: Atomic, Molecular and Optical Physics*, vol. 21, no. 3, p. L31, 1988.

[41] C. I. Blaga, J. Xu, A. D. DiChiara, E. Sistrunk, K. Zhang, P. Agostini, T. A.

Miller, L. F. DiMauro, and C. D. Lin, "Imaging ultrafast molecular dynamics with laser-induced electron diffraction," *Nature*, vol. 483, p. 194, 2012.

[42] M. Meckel, D. Comtois, D. Zeidler, A. Staudte, D. Pavičić, H. C. Bandulet, H. Pépin, J. C. Kieffer, R. Dörner, D. M. Villeneuve, and P. B. Corkum, "Laser-Induced Electron Tunneling and Diffraction," *Science*, vol. 320, no. 5882, pp. 1478–1482, 2008.

[43] M. Spanner, O. Smirnova, P. B. Corkum, and M. Y. Ivanov, "Reading diffraction images in strong field ionization of diatomic molecules," *Journal of Physics B: Atomic, Molecular and Optical Physics*, vol. 37, no. 12, p. L243, 2004.

[44] G. G. Paulus, W. Becker, W. Nicklich, and H. Walther, "Rescattering effects in above-threshold ionization: a classical model," *Journal of Physics B: Atomic, Molecular and Optical Physics*, vol. 27, no. 21, p. L703, 1994.

[45] G. G. Paulus, W. Nicklich, H. Xu, P. Lambropoulos, and H. Walther, "Plateau in above threshold ionization spectra," *Phys. Rev. Lett.*, vol. 72, pp. 2851–2854, 1994.

[46] A. l'Huillier, L. A. Lompre, G. Mainfray, and C. Manus, "Multiply charged ions induced by multiphoton absorption in rare gases at 0.53 μm," *Phys. Rev. A*, vol. 27, pp. 2503–2512, 1983.

[47] D. N. Fittinghoff, P. R. Bolton, B. Chang, and K. C. Kulander, "Observation of nonsequential double ionization of helium with optical tunneling," *Phys. Rev. Lett.*, vol. 69, pp. 2642–2645, 1992.

[48] M. F. Kling and M. J. Vrakking, "Attosecond Electron Dynamics," *Annual Review of Physical Chemistry*, vol. 59, no. 1, pp. 463–492, 2008, pMID: 18031218.

[49] A. Rudenko, V. L. B. de Jesus, T. Ergler, K. Zrost, B. Feuerstein, C. D. Schröter, R. Moshammer, and J. Ullrich, "Correlated Two-Electron Momentum Spectra for Strong-Field Nonsequential Double Ionization of He at 800 nm," *Phys. Rev. Lett.*, vol. 99, p. 263003, 2007.

[50] A. Staudte, C. Ruiz, M. Schöffler, S. Schössler, D. Zeidler, T. Weber, M. Meckel, D. M. Villeneuve, P. B. Corkum, A. Becker, and R. Dörner, "Binary and Recoil Collisions in Strong Field Double Ionization of Helium," *Phys. Rev. Lett.*, vol. 99, p. 263002, 2007.

[51] B. Feuerstein, R. Moshammer, D. Fischer, A. Dorn, C. D. Schröter, J. Deipenwisch, J. R. Crespo Lopez-Urrutia, C. Höhr, P. Neumayer, J. Ullrich, H. Rottke, C. Trump, M. Wittmann, G. Korn, and W. Sandner, "Separation of Recollision Mechanisms in Nonsequential Strong Field Double Ionization of

Ar: The Role of Excitation Tunneling," *Phys. Rev. Lett.*, vol. 87, p. 043003, 2001.

[52] N. Camus, B. Fischer, M. Kremer, V. Sharma, A. Rudenko, B. Bergues, M. Kübel, N. G. Johnson, M. F. Kling, T. Pfeifer, J. Ullrich, and R. Moshammer, "Attosecond Correlated Dynamics of Two Electrons Passing through a Transition State," *Phys. Rev. Lett.*, vol. 108, p. 073003, 2012.

[53] T. Seideman, M. Y. Ivanov, and P. B. Corkum, "Role of Electron Localization in Intense-Field Molecular Ionization," *Phys. Rev. Lett.*, vol. 75, pp. 2819–2822, 1995.

[54] E. Constant, H. Stapelfeldt, and P. B. Corkum, "Observation of Enhanced Ionization of Molecular Ions in Intense Laser Fields," *Phys. Rev. Lett.*, vol. 76, pp. 4140–4143, 1996.

[55] A. D. Bandrauk and F. Légaré, *Enhanced Ionization of Molecules in Intense Laser Fields*, 2012, ch. 2.

[56] E. P. Kanter, P. J. Cooney, D. S. Gemmell, K. O. Groeneveld, W. J. Pietsch, A. J. Ratkowski, Z. Vager, and B. J. Zabransky, "Role of excited electronic states in the interactions of fast (MeV) molecular ions with solids and gases," *Phys. Rev. A*, vol. 20, pp. 834–854, 1979.

[57] D. S. Gemmell, "Determining the stereochemical structures of molecular ions by "Coulomb-explosion" techniques with fast (MeV) molecular ion beams," *Chemical Reviews*, vol. 80, no. 4, pp. 301–311, 1980.

[58] Z. Vager, E. P. Kanter, G. Both, P. J. Cooney, A. Faibis, W. Koenig, B. J. Zabransky, and D. Zajfman, "Direct Determination of the Stereochemical Structure of CH_4^+," *Phys. Rev. Lett.*, vol. 57, pp. 2793–2795, 1986.

[59] Z. Vager, R. Naaman, and E. P. Kanter, "Coulomb Explosion Imaging of Small Molecules," *Science*, vol. 244, no. 4903, pp. 426–431, 1989.

[60] B. Jordon-Thaden, H. Kreckel, R. Golser, D. Schwalm, M. H. Berg, H. Buhr, H. Gnaser, M. Grieser, O. Heber, M. Lange, O. Novotný, S. Novotny, H. B. Pedersen, A. Petrignani, R. Repnow, H. Rubinstein, D. Shafir, A. Wolf, and D. Zajfman, "Structure and Stability of the Negative Hydrogen Molecular Ion," *Phys. Rev. Lett.*, vol. 107, p. 193003, 2011.

[61] H. Jahn and E. Teller, "Stability of Polyatomic Molecules in Degenerate Electronic States - I-Orbital Degeneracy," *Proceedings of the Royal Society of London A: Mathematical, Physical and Engineering Sciences*, vol. 161, no. 905, pp. 220–235, 1937.

[62] P. Herwig, K. Zawatzky, M. Grieser, O. Heber, B. Jordon-Thaden, C. Krantz,

O. Novotný, R. Repnow, V. Schurig, D. Schwalm, Z. Vager, A. Wolf, O. Trapp, and H. Kreckel, "Imaging the Absolute Configuration of a Chiral Epoxide in the Gas Phase," *Science*, vol. 342, no. 6162, pp. 1084–1086, 2013.

[63] V. S. Petrović, M. Siano, J. L. White, N. Berrah, C. Bostedt, J. D. Bozek, D. Broege, M. Chalfin, R. N. Coffee, J. Cryan, L. Fang, J. P. Farrell, L. J. Frasinski, J. M. Glownia, M. Gühr, M. Hoener, D. M. P. Holland, J. Kim, J. P. Marangos, T. Martinez, B. K. McFarland, R. S. Minns, S. Miyabe, S. Schorb, R. J. Sension, L. S. Spector, R. Squibb, H. Tao, J. G. Underwood, and P. H. Bucksbaum, "Transient X-Ray Fragmentation: Probing a Prototypical Photoinduced Ring Opening," *Phys. Rev. Lett.*, vol. 108, p. 253006, 2012.

[64] U. Ablikim, C. Bomme, H. Xiong, E. Savelyev, R. Obaid, B. Kaderiya, S. Augustin, K. Schnorr, I. Dumitriu, T. Osipov, R. Bilodeau, D. Kilcoyne, V. Kumarappan, A. Rudenko, N. Berrah, and D. Rolles, "Identification of absolute geometries of cis and trans molecular isomers by Coulomb Explosion Imaging," vol. 6, p. 38202, 2016.

[65] J. H. D. Eland, R. Singh, J. D. Pickering, C. S. Slater, A. H. Roos, J. Andersson, S. Zagorodskikh, R. J. Squibb, M. Brouard, and R. Feifel, "Dissociation of multiply charged ICN by Coulomb explosion," *The Journal of Chemical Physics*, vol. 145, no. 7, p. 074303, 2016.

[66] H. Tanaka, N. Nakashima, and T. Yatsuhashi, "Anisotropic Coulomb Explosion of CO Ligands in Group 6 Metal Hexacarbonyls: Cr(CO), Mo(CO), W(CO)," *The Journal of Physical Chemistry A*, vol. 120, no. 35, pp. 6917–6928, 2016, pMID: 27529141.

[67] F. J. Furch, T. Witting, A. Giree, C. Luan, F. Schell, G. Arisholm, C. P. Schulz, and M. J. J. Vrakking, "CEP-stable few-cycle pulses with more than 190 µJ of energy at 100 kHz from a noncollinear optical parametric amplifier," *Opt. Lett.*, vol. 42, no. 13, pp. 2495–2498, 2017.

[68] P. B. Corkum, M. Y. Ivanov, and J. S. Wright, "Subfemtosecond Processes in Strong Laser Fields," *Annual Review of Physical Chemistry*, vol. 48, no. 1, pp. 387–406, 1997, pMID: 15012449.

[69] J. L. Hansen, J. H. Nielsen, C. B. Madsen, A. T. Lindhardt, M. P. Johansson, T. Skrydstrup, L. B. Madsen, and H. Stapelfeldt, "Control and femtosecond time-resolved imaging of torsion in a chiral molecule," *The Journal of Chemical Physics*, vol. 136, no. 20, p. 204310, 2012.

[70] H. Stapelfeldt and T. Seideman, "Colloquium," *Rev. Mod. Phys.*, vol. 75, pp. 543–557, 2003.

[71] J. J. Larsen, H. Sakai, C. P. Safvan, I. Wendt-Larsen, and H. Stapelfeldt, "Aligning molecules with intense nonresonant laser fields," *The Journal of Chemical Physics*, vol. 111, no. 17, pp. 7774–7781, 1999.

[72] J. J. Larsen, K. Hald, N. Bjerre, H. Stapelfeldt, and T. Seideman, "Three Dimensional Alignment of Molecules Using Elliptically Polarized Laser Fields," *Phys. Rev. Lett.*, vol. 85, pp. 2470–2473, 2000.

[73] R. Dörner, V. Mergel, O. Jagutzki, L. Spielberger, J. Ullrich, R. Moshammer, and H. Schmidt-Böcking, "Cold Target Recoil Ion Momentum Spectroscopy: a 'momentum microscope' to view atomic collision dynamics," *Physics Reports*, vol. 330, no. 2, pp. 95 – 192, 2000.

[74] J. Ullrich, R. Moshammer, A. Dorn, R. Dörner, L. P. H. Schmidt, and H. Schmidt-Böcking, "Recoil-ion and electron momentum spectroscopy: reaction-microscopes," *Reports on Progress in Physics*, vol. 66, no. 9, p. 1463, 2003.

[75] V. Stert, W. Radloff, C. P. Schulz, and I. V. Hertel, "Ultrafast photoelectron spectroscopy: Femtosecond pump-probe coincidence detection of ammonia cluster ions and electrons," *The European Physical Journal D - Atomic, Molecular, Optical and Plasma Physics*, vol. 5, no. 1, pp. 97–106, 1999.

[76] A. Smekal, "Zur Quantentheorie der Dispersion," *Naturwissenschaften*, vol. 11, no. 43, pp. 873–875, 1923.

[77] C. V. Raman, "A new radiation," *Indian J. Phys.*, vol. 2, p. 387, 1928.

[78] L. M. G. Landsberg, "Eine neue Erscheinung bei der Lichtzerstreuung in Krystallen," *Naturwissenschaften*, vol. 16, no. 28, pp. 557–558, 1928.

[79] Y. Yan, E. B. G. Jr., and K. A. Nelson, "Impulsive stimulated scattering: General importance in femtosecond laser pulse interactions with matter, and spectroscopic applications," *The Journal of Chemical Physics*, vol. 83, no. 11, pp. 5391–5399, 1985.

[80] J. H. Sanderson, A. El-Zein, W. A. Bryan, W. R. Newell, A. J. Langley, and P. F. Taday, "Geometry modifications and alignment of H_2O in an intense femtosecond laser pulse," *Phys. Rev. A*, vol. 59, pp. R2567–R2570, 1999.

[81] C. S. Slater, S. Blake, M. Brouard, A. Lauer, C. Vallance, J. J. John, R. Turchetta, A. Nomerotski, L. Christensen, J. H. Nielsen, M. P. Johansson, and H. Stapelfeldt, "Covariance imaging experiments using a pixel-imaging mass-spectrometry camera," *Phys. Rev. A*, vol. 89, p. 011401, 2014.

[82] H. Stapelfeldt, E. Constant, and P. B. Corkum, "Wave Packet Structure and Dynamics Measured by Coulomb Explosion," *Phys. Rev. Lett.*, vol. 74, pp.

3780–3783, 1995.

[83] T. Ergler, A. Rudenko, B. Feuerstein, K. Zrost, C. D. Schröter, R. Moshammer, and J. Ullrich, "Time-Resolved Imaging and Manipulation of H_2 Fragmentation in Intense Laser Fields," *Phys. Rev. Lett.*, vol. 95, p. 093001, 2005.

[84] L. Christensen, J. H. Nielsen, C. B. Brandt, C. B. Madsen, L. B. Madsen, C. S. Slater, A. Lauer, M. Brouard, M. P. Johansson, B. Shepperson, and H. Stapelfeldt, "Dynamic Stark Control of Torsional Motion by a Pair of Laser Pulses," *Phys. Rev. Lett.*, vol. 113, p. 073005, 2014.

[85] M. Burt, R. Boll, J. W. L. Lee, K. Amini, H. Köckert, C. Vallance, A. S. Gentleman, S. R. Mackenzie, S. Bari, C. Bomme, S. Düsterer, B. Erk, B. Manschwetus, E. Müller, D. Rompotis, E. Savelyev, N. Schirmel, S. Techert, R. Treusch, J. Küpper, S. Trippel, J. Wiese, H. Stapelfeldt, B. C. de Miranda, R. Guillemin, I. Ismail, L. Journel, T. Marchenko, J. Palaudoux, F. Penent, M. N. Piancastelli, M. Simon, O. Travnikova, F. Brausse, G. Goldsztejn, A. Rouzée, M. Géléoc, R. Geneaux, T. Ruchon, J. Underwood, D. M. P. Holland, A. S. Mereshchenko, P. K. Olshin, P. Johnsson, S. Maclot, J. Lahl, A. Rudenko, F. Ziaee, M. Brouard, and D. Rolles, "Coulomb-explosion imaging of concurrent CH_2BrI photodissociation dynamics," *Phys. Rev. A*, vol. 96, p. 043415, 2017.

[86] X. Ding, M. Haertelt, S. Schlauderer, M. S. Schuurman, A. Y. Naumov, D. M. Villeneuve, A. R. W. McKellar, P. B. Corkum, and A. Staudte, "Ultrafast Dissociation of Metastable CO^{2+} in a Dimer," *Phys. Rev. Lett.*, vol. 118, p. 153001, 2017.

[87] A. Khan, L. C. Tribedi, and D. Misra, "Three-body fragmentation of multiply charged nitrous oxide induced by Ar^{8+}- and Xe^{15+}-ion impact," *Phys. Rev. A*, vol. 96, p. 012703, 2017.

[88] U. Ablikim, C. Bomme, E. Savelyev, H. Xiong, R. Kushawaha, R. Boll, K. Amini, T. Osipov, D. Kilcoyne, A. Rudenko, N. Berrah, and D. Rolles, "Isomer-dependent fragmentation dynamics of inner-shell photoionized difluoroiodobenzene," *Physical Chemistry Chemical Physics*, vol. 21, pp. 13 419–13 431, 2017.

[89] A. Ramadhan, B. Wales, R. Karimi, I. Gauthier, M. MacDonald, L. Zuin, and J. Sanderson, "Ultrafast molecular dynamics of dissociative ionization in OCS probed by soft x-ray synchrotron radiation," *Journal of Physics B: Atomic, Molecular and Optical Physics*, vol. 49, no. 21, p. 215602, 2016.

[90] S. Yan, X. L. Zhu, P. Zhang, X. Ma, W. T. Feng, Y. Gao, S. Xu, Q. S.

Zhao, S. F. Zhang, D. L. Guo, D. M. Zhao, R. T. Zhang, Z. K. Huang, H. B. Wang, and X. J. Zhang, "Observation of two sequential pathways of $(CO_2)^{3+}$ dissociation by heavy-ion impact," *Phys. Rev. A*, vol. 94, p. 032708, 2016.

[91] Y. Fan, C. Wu, X. Xie, P. Wang, X. Zhong, Y. Shao, X. Sun, Y. Liu, and Q. Gong, "Three-body fragmentation dynamics of carbon-dioxide dimers induced by intense femtosecond laser pulses," *Chemical Physics Letters*, vol. 653, pp. 108 – 111, 2016.

[92] A. Khan and D. Misra, "Decay dynamics of N_2O under the impact of fast electrons," *Journal of Physics B - Atomic Molecular and Optical Physics*, vol. 49, no. 5, 2016.

[93] Z. Shen, E. Wang, M. Gong, X. Shan, and X. Chen, "Fragmentation dynamics of carbonyl sulfide in collision with 500 eV electron," *Journal of Chemical Physics*, vol. 145, no. 23, 2016.

[94] X. Wang, J. Zhang, S.-A. Zhang, and Z.-R. Sun, "Coulomb explosion of CS_2 molecule under an intense femtosecond laser field," *Chinese Physics B*, vol. 25, no. 5, p. 053301, 2016.

[95] X. Xie, C. Wu, Z. Yuan, D. Ye, P. Wang, Y. Deng, L. Fu, J. Liu, Y. Liu, and Q. Gong, "Dynamical coupling of electrons and nuclei for Coulomb explosion of argon trimers in intense laser fields," *Phys. Rev. A*, vol. 92, p. 023417, 2015.

[96] A. Khan, L. C. Tribedi, and D. Misra, "Observation of a sequential process in charge-asymmetric dissociation of CO_2^{q+}(q= 4, 5) upon the impact of highly charged ions," *Physical Review A*, vol. 92, no. 3, p. 030701, 2015.

[97] L. Hong, L. Min, X. Xi-Guo, W. Cong, D. Yong-Kai, W. Cheng-Yin, G. Qi-Huang, and L. Yun-Quan, "Charge Resonance Enhanced Multiple Ionization of H_2O Molecules in Intense Laser Fields," *Chinese Physics Letters*, vol. 32, no. 6, p. 063301, 2015.

[98] C. Wu, C. Wu, Y. Fan, X. Xie, P. Wang, Y. Deng, Y. Liu, and Q. Gong, "Three-body fragmentation of CO_2 driven by intense laser pulses," *The Journal of Chemical Physics*, vol. 142, no. 12, p. 124303, 2015.

[99] R. Guillemin, P. Decleva, M. Stener, C. Bomme, T. Marin, L. Journel, T. Marchenko, R. K. Kushawaha, K. Jänkälä, N. Trcera, K. P. Bowen, D. W. Lindle, M. N. Piancastelli, and M. Simon, "Selecting core-hole localization or delocalization in CS_2 by photofragmentation dynamics," *Nature Communications*, vol. 6, p. 6166, 2015.

[100] B. Wales, Éric Bisson, R. Karimi, S. Beaulieu, A. Ramadhan, M. Giguère, Z. Long, W.-K. Liu, J.-C. Kieffer, F. Légaré, and J. Sanderson, "Coulomb

imaging of the concerted and stepwise break up processes of OCS ions in intense femtosecond laser radiation," *Journal of Electron Spectroscopy and Related Phenomena*, vol. 195, pp. 332 – 336, 2014.

[101] H. Wu, Y. Yang, S. Sun, J. Zhang, L. Deng, S. Zhang, T. Jia, Z. Wang, and Z. Sun, "Concerted elimination of Br_2^+ resulting from the Coulomb explosion of 1,2-dibromoethane in an intense femtosecond laser field," *Chemical Physics Letters*, vol. 607, pp. 70 – 74, 2014.

[102] C. Wu, C. Wu, D. Song, H. Su, Y. Yang, Z. Wu, X. Liu, H. Liu, M. Li, Y. Deng, Y. Liu, L.-Y. Peng, H. Jiang, and Q. Gong, "Nonsequential and Sequential Fragmentation of $CO_2{}^{3+}$ in Intense Laser Fields," *Phys. Rev. Lett.*, vol. 110, p. 103601, 2013.

[103] X. Gong, M. Kunitski, L. P. H. Schmidt, T. Jahnke, A. Czasch, R. Dörner, and J. Wu, "Simultaneous probing of geometry and electronic orbital of ArCO by Coulomb-explosion imaging and angle-dependent tunneling rates," *Phys. Rev. A*, vol. 88, p. 013422, 2013.

[104] J. Wu and M. Kunitski and L. Ph. H. Schmidt and T. Jahnke and R. Dörner, "Structures of N_2Ar, O_2Ar, and O_2Xe dimers studied by Coulomb explosion imaging," *The Journal of Chemical Physics*, vol. 137, no. 10, p. 104308, 2012.

[105] L. Zhang, S. Roither, X. Xie, D. Kartashov, M. Schöffler, H. Xu, A. Iwasaki, S. Gräfe, T. Okino, K. Yamanouchi, A. Baltuska, and M. Kitzler, "Path-selective investigation of intense laser-pulse-induced fragmentation dynamics in triply charged 1,3-butadiene," *Journal of Physics B: Atomic, Molecular and Optical Physics*, vol. 45, no. 8, p. 085603, 2012.

[106] B. Wales, T. Motojima, J. Matsumoto, Z. Long, W.-K. Liu, H. Shiromaru, and J. Sanderson, "Multiple ionization and complete fragmentation of OCS by impact with highly charged ions Ar^{4+} and Ar^{8+} at $15\,\mathrm{keV\,q^{-1}}$," *Journal of Physics B: Atomic, Molecular and Optical Physics*, vol. 45, no. 4, p. 045205, 2012.

[107] N. Neumann, D. Hant, L. P. H. Schmidt, J. Titze, T. Jahnke, A. Czasch, M. S. Schöffler, K. Kreidi, O. Jagutzki, H. Schmidt-Böcking, and R. Dörner, "Fragmentation Dynamics of CO_2^{3+} Investigated by Multiple Electron Capture in Collisions with Slow Highly Charged Ions," *Phys. Rev. Lett.*, vol. 104, p. 103201, 2010.

[108] E. Wang, X. Shan, Z. Shen, X. Li, M. Gong, Y. Tang, and X. Chen, "Three-body-fragmentation dynamics of $CO_2{}^{4+}$ investigated by electron collisions at an impact energy of 500 eV," *Phys. Rev. A*, vol. 92, p. 062713, 2015.

[109] S. Bailleux, D. Duflot, K. Taniguchi, S. Sakai, H. Ozeki, T. Okabayashi, and W. C. Bailey, "Fourier Transform Microwave and Millimeter-Wave Spectroscopy of Bromoiodomethane, CH_2BrI," *The Journal of Physical Chemistry A*, vol. 118, no. 50, pp. 11 744–11 750, 2014.

[110] S. J. Lee and R. Bersohn, "Photodissociation of a molecule with two chromophores. Bromoiodomethane," *The Journal of Physical Chemistry*, vol. 86, no. 5, pp. 728–730, 1982.

[111] A. F. Lago, J. P. Kercher, A. Bödi, B. Sztáray, B. Miller, D. Wurzelmann, and T. Baer, "Dissociative Photoionization and Thermochemistry of Dihalomethane Compounds Studied by Threshold Photoelectron Photoion Coincidence Spectroscopy," *The Journal of Physical Chemistry A*, vol. 109, no. 9, pp. 1802–1809, 2005, pMID: 16833509.

[112] L. J. Butler, E. J. Hintsa, S. F. Shane, and Y. T. Lee, "The electronic state-selective photodissociation of CH_2BrI at 248, 210, and 193 nm," *The Journal of Chemical Physics*, vol. 86, no. 4, pp. 2051–2074, 1987.

[113] Y.-J. Liu, D. Ajitha, J. W. Krogh, A. N. Tarnovsky, and R. Lindh, "Spin–Orbit Ab Initio Investigation of the Photolysis of Bromoiodomethane," *ChemPhysChem*, vol. 7, no. 4, pp. 955–963, 2006.

[114] S. Birkner, "Strong Field Ionization of Atoms and Molecules: Electron-Ion Coincidence Measurements at High Repetition Rate," Ph.D. dissertation, Freie Universität Berlin, 2015.

[115] RoentDek Handels GmbH, "Software for the RoentDek Hexanode." 2011, Kelkheim, Germany, www.roentdek.com.

[116] W. H. Press, S. A. Teukolsky, W. T. Vetterling, B. P. Flannery, and M. Metcalf, *Numerical Recipes in C: The Art of Scientific Computing, Second Edition.* Cambridge University Press, 1992.

[117] S. Larimian, S. Erattupuzha, S. Mai, P. Marquetand, L. González, A. Baltuška, M. Kitzler, and X. Xie, "Molecular oxygen observed by direct photoproduction from carbon dioxide," *Phys. Rev. A*, vol. 95, p. 011404, 2017.

[118] S. DePaul, D. Pullman, and B. Friedrich, "A pocket model of seeded supersonic beams," *The Journal of Physical Chemistry*, vol. 97, no. 10, pp. 2167–2171, 1993.

[119] J. B. Anderson and P. Davidovits, "Isotope Separation in a "Seeded Beam"," *Science*, vol. 187, no. 4177, pp. 642–644, 1975.

[120] R. Dalitz, "CXII. On the analysis of τ-meson data and the nature of the τ-meson," *The London, Edinburgh, and Dublin Philosophical Magazine and*

Journal of Science, vol. 44, no. 357, pp. 1068–1080, 1953.

[121] L. M. Wiese, O. Yenen, B. Thaden, and D. H. Jaecks, "Measured Correlated Motion of Three Massive Coulomb Interacting Particles," *Phys. Rev. Lett.*, vol. 79, pp. 4982–4985, 1997.

[122] F. Rosca-Pruna, E. Springate, H. L. Offerhaus, M. Krishnamurthy, N. Farid, C. Nicole, and M. J. J. Vrakking, "Spatial alignment of diatomic molecules in intense laser fields: I. Experimental results," *Journal of Physics B: Atomic, Molecular and Optical Physics*, vol. 34, no. 23, p. 4919, 2001.

[123] T. Zuo and A. Bandrauk, "Charge-resonance-enhanced ionization of diatomic molecular ions by intense lasers," vol. 52, pp. R2511–R2514, 1995.

[124] W. Li, X. Zhou, R. Lock, S. Patchkovskii, A. Stolow, H. C. Kapteyn, and M. M. Murnane, "Time-Resolved Dynamics in N_2O_4 Probed Using High Harmonic Generation," *Science*, vol. 322, no. 5905, pp. 1207–1211, 2008.

[125] M. Spanner, J. Mikosch, A. E. Boguslavskiy, M. M. Murnane, A. Stolow, and S. Patchkovskii, "Strong-field ionization and high-order-harmonic generation during polyatomic molecular dynamics of N_2O_4," *Phys. Rev. A*, vol. 85, p. 033426, 2012.

[126] A. Ferré, H. Soifer, O. Pedatzur, C. Bourassin-Bouchet, B. D. Bruner, R. Canonge, F. Catoire, D. Descamps, B. Fabre, E. Mével, S. Petit, N. Dudovich, and Y. Mairesse, "Two-Dimensional Frequency Resolved Optomolecular Gating of High-Order Harmonic Generation," *Phys. Rev. Lett.*, vol. 116, p. 053002, 2016.

[127] P. Atkins and J. de Paula, *Chemical equilibrium: the principles*. Oxford University Press, 2009, pp. 153–171.

[128] Å. Kvick, R. K. McMullan, and M. D. Newton, "The structure of dinitrogen tetroxide N_2O_4: Neutron diffraction study at 100, 60, and 20 K and ab initio theoretical calculations," *The Journal of Chemical Physics*, vol. 76, no. 7, pp. 3754–3761, 1982.

[129] Y. Morino, T. Iijima, and Y. Murata, "An Electron Diffraction Investigation on the Molecular Structure of Hydrazine," *Bulletin of the Chemical Society of Japan*, vol. 33, no. 1, pp. 46–48, 1960.

[130] F. Bolduan and H. Jodl, "Raman spectroscopy on matrix-isolated NO^+, NO_3^- and N_2O_4 in Ne," *Chemical Physics Letters*, vol. 85, no. 3, pp. 283 – 286, 1982.

[131] C. H. Bibart and G. E. Ewing, "Vibrational spectrum, torsional potential, and bonding of gaseous N_2O_4," *The Journal of Chemical Physics*, vol. 61, no. 4, pp. 1284–1292, 1974.

[132] D. Luckhaus and M. Quack, "High-resolution FTIR spectra of NO_2 and N_2O_4 in supersonic jet expansions and their rovibrational analysis," *Chemical Physics Letters*, vol. 199, no. 3, pp. 293 – 301, 1992.

[133] National Institute of Standards and Technology. NIST Chemistry WebBook. URL: https://webbook.nist.gov/cgi/cbook.cgi?ID=C10544726&Units=SI Acessed: 2018-03-13.

[134] J. H. Jungmann and R. M. A. Heeren, "Detection systems for mass spectrometry imaging: A perspective on novel developments with a focus on active pixel detectors," *Rapid Communications in Mass Spectrometry*, vol. 27, no. 1, pp. 1–23, 2013.

[135] F. J. Furch, A. Giree, F. Morales, A. Anderson, Y. Wang, C. P. Schulz, and M. J. J. Vrakking, "Close to transform-limited, few-cycle 12 µJ pulses at 400 kHz for applications in ultrafast spectroscopy," *Opt. Express*, vol. 24, no. 17, pp. 19 293–19 310, 2016.

[136] A. T. J. B. Eppink and D. H. Parker, "Velocity map imaging of ions and electrons using electrostatic lenses: Application in photoelectron and photofragment ion imaging of molecular oxygen," *Review of Scientific Instruments*, vol. 68, no. 9, pp. 3477–3484, 1997.

[137] H. Hasegawa, A. Hishikawa, and K. Yamanouchi, "Coincidence imaging of Coulomb explosion of CS_2 in intense laser fields," *Chemical Physics Letters*, vol. 349, no. 1, pp. 57 – 63, 2001.

[138] C. Dyer and P. J. Hendra, "Raman spectroscopy of NO_2/N_2O_4 in the gas phase using near-infrared excitation," *Chemical Physics Letters*, vol. 233, no. 4, pp. 461 – 465, 1995.

[139] S. D. Silvestri, J. Fujimoto, E. Ippen, E. B. Gamble, L. R. Williams, and K. A. Nelson, "Femtosecond time-resolved measurements of optic phonon dephasing by impulsive stimulated raman scattering in α-perylene crystal from 20 to 300 K," *Chemical Physics Letters*, vol. 116, no. 2, pp. 146 – 152, 1985.

[140] E. Goll, G. Wunner, and A. Saenz, "Formation of Ground-State Vibrational Wave Packets in Intense Ultrashort Laser Pulses," *Phys. Rev. Lett.*, vol. 97, p. 103003, 2006.

[141] T. Ergler, B. Feuerstein, A. Rudenko, K. Zrost, C. D. Schröter, R. Moshammer, and J. Ullrich, "Quantum-Phase Resolved Mapping of Ground-State Vibrational D_2 Wave Packets via Selective Depletion in Intense Laser Pulses," *Phys. Rev. Lett.*, vol. 97, p. 103004, 2006.

[142] W. C. Wiley and I. H. McLaren, "Time-of-Flight Mass Spectrometer with

Improved Resolution," *Review of Scientific Instruments*, vol. 26, no. 12, pp. 1150–1157, 1955.

[143] U. Even, J. Jortner, D. Noy, N. Lavie, and C. Cossart-Magos, "Cooling of large molecules below 1 K and He clusters formation," *The Journal of Chemical Physics*, vol. 112, no. 18, pp. 8068–8071, 2000.

[144] D. Pentlehner, R. Riechers, B. Dick, A. Slenczka, U. Even, N. Lavie, R. Brown, and K. Luria, "Rapidly pulsed helium droplet source," *Review of Scientific Instruments*, vol. 80, no. 4, p. 043302, 2009.

[145] Y.-J. Lu, J. H. Lehman, and W. C. Lineberger, "A versatile, pulsed anion source utilizing plasma-entrainment: Characterization and applications," *The Journal of Chemical Physics*, vol. 142, no. 4, p. 044201, 2015.

[146] S. Trippel, "Aligned Molecules for Reactive Scattering," 2010.

[147] K. Luria, N. Lavie, and U. Even, "Dielectric barrier discharge source for supersonic beams," *Review of Scientific Instruments*, vol. 80, no. 10, p. 104102, 2009.

[148] A. Stolow, "Minimum profile ultrahigh vacuum gate valve based on linear/rotary motion feedthrough," *Journal of Vacuum Science & Technology A*, vol. 14, no. 4, pp. 2669–2670, 1996.

[149] J. Küpper, H. Haak, K. Wohlfart, and G. Meijer, "Compact in-place gate valve for molecular-beam experiments," *Review of Scientific Instruments*, vol. 77, no. 1, 2006.

[150] E. Thain, "A vacuum gate valve for laboratory applications," *Journal of Physics E: Scientific Instruments*, vol. 5, no. 9, p. 853, 1972.

[151] J. C. Sheffield, "Ultrahigh Vacuum Gate Valve," *Review of Scientific Instruments*, vol. 36, no. 8, pp. 1269–1270, 1965.

[152] SIMION, "Ion optics simulation software, Version 8.0.0," 2006, Scientific Instrument Services, Idaho National Labs (USA), www.simion.com.

[153] E. S. Toma, P. Antoine, A. de Bohan, and H. G. Muller, "Resonance-enhanced high-harmonic generation," *Journal of Physics B: Atomic, Molecular and Optical Physics*, vol. 32, no. 24, p. 5843, 1999.

[154] E. C. M. Chen and W. E. Wentworth, "Negative ion states of the halogens," *The Journal of Physical Chemistry*, vol. 89, no. 19, pp. 4099–4105, 1985.

[155] F. K. Freyse, "Dynamics of Reactions of Ions and Molecules and Investigations of an Electrostatic Ion Trap," Master's thesis, 2017.

[156] L. J. Frasinski, K. Codling, and P. A. Hatherly, "Covariance Mapping: A

Correlation Method Applied to Multiphoton Multiple Ionization," *Science*, vol. 246, no. 4933, pp. 1029–1031, 1989.

List of publications

- K. Reininger, F. Schell, F. Freyse, M.J.J. Vrakking, C.P. Schulz, and J. Mikosch, "Sequential and Non-Sequential Pathways in the Coulomb Explosion of CH_2BrI," *(in preparation)*
- K. Reininger, J. Long, F. Furch, M.J.J. Vrakking, C.P. Schulz, and J. Mikosch, "Intramolecular vibration in dinitrogen tetroxide molecules studied with few-cycle laser pulses," *(in preparation)*

Kurzzusammenfassung

Hochintensive Femtosekundenlaser sind wirkungsvolle Instrumente zur Erforschung von sowohl inter- als auch intramolekularen Dynamiken auf Zeitskalen der Kernbewegung und mit einer Ortsauflösung in der Größenordnung der Molekülbindungen. Die vorliegende Dissertation widmet sich der Studie von Moleküldynamiken mithilfe von Starkfeldionisation durch ultrakurze Laserpulse.

Im ersten Teil der Dissertation präsentieren wir eine detaillierte Studie über die verschiedenen Aufbruchkanäle in der durch Starkfeldionisation induzierten Coulomb-Explosion von CH_2BrI^{3+}. Die Impulse der resultierenden Fragmente wurden mithilfe eines Reaktionsmikroskops in Koinzidenz gemessen. Wir haben fünf verschiedene Fragmentationspfade nachgewiesen: eine nicht sequentielle Coulomb-Explosion in welcher die C-I Bindung und die C-Br Bindung gleichzeitig aufbrechen und zusätzlich vier sequentielle Pfade in welchen die Fragmentierung über einen doppelt geladenen Zwischenzustand abläuft und der Bindungsbruch nacheinander erfolgt. Zudem diskutieren wir sowohl die Möglichkeiten als auch die Beschränkungen, die Ergebnisse der Coulomb-Explosion zur Molekülstrukturbestimmung zu verwenden.

Im zweiten Teil der Dissertation stellen wir die Ergebnisse eines zeitaufgelösten Pump-Probe Experiments vor, in welchem die N-N Streckschwingung von N_2O_4 untersucht wurde. Wir haben die Schwingung durch einen impulsiven stimulierten Raman Stoßprozess mit dem Pump-Puls angeregt, um anschließend das oszillierende Molekül mit einem zeitverzögerten Probe-Puls in einem Starkfeldprozess zu ionisieren. Durch die von der Zeitverzögerung abhängige, gemessene kinetische Energie erzeugter NO_2^+ Fragmente, konnten wir den inneren Umkehrpunkt, die Amplitude und die Phase der Schwingen bestimmen. Wir haben für das Experiment eine Kombination aus einem Velocity-Map Imaging Spektrometer, einem im Vakuum integrierten Pixeldetektor und einem Lasersystem, welches 7 fs kurze Impulse erzeugt, verwendet.

Im letzten Teil der Dissertation präsentieren wir eine detaillierte Beschreibung des Designs und der Implementierung eines neuen Messaufbaus. Dieser stellt den ersten Schritt der Entwicklung einer neuen Methode vor, die es ermöglichen soll die zeitabhängige Änderung der Molekülstruktur während einer bimolekularen chemischen Reaktion zu erforschen. Wir wollen dabei zwei etablierte Techniken verbinden: (1) Die Präparation der Ausgangsprodukte einer chemischen Reaktion in kleinen ionischen Clustern und Molekülen und (2) Coulomb-Explosion zur Strukturbestimmung von transienten Molekülkonfigurationen. Der neue Aufbau beinhaltet eine Ionenquelle, ein Flugzeitmassenspektrometer, ein Coulomb-Explosion Imaging Spektrometer und eine zusätzliche neutrale Molekularstrahlquelle.

Short summary

Strong-field femtosecond lasers are powerful tools to explore inter- and intramolecular dynamics on the time scales of the nuclear motion and with a spatial resolution of the molecular bond length. This thesis is dedicated to the investigation of molecular dynamics with strong-field ionization induced by ulta-short laser pulses.

In the first part of this thesis, we present a detailed study on the different fragmentation pathways in the Coulomb explosion of CH_2BrI^{3+} upon strong-field ionization. The momenta of the final fragments were measured in coincidence in a reaction microscope. We detected five different break-up pathways. The non-sequential Coulomb explosion where the C-I and the C-Br bond break at the same time and in addition four sequential channels with a successively bond cleavage and a fragmentation pathway which proceeds via an intermediate doubly-charged state. Furthermore, we discuss the possibilities and limitations of Coulomb explosion imaging as a tool to recover the molecular structure.

In the second part of the thesis we present the results of a time-resolved pump-probe experiment exploring the N-N vibration of N_2O_4. We excited the vibration in an impulsive stimulated Raman scattering process with the pump pulse and strong-field ionized the vibrating molecule with the time-delayed probe pulse. From the time-dependent kinetic energy release of created NO_2^+ fragments we could extract the inner turning point, the amplitude, and the phase of the vibration. In the experiment, we used the combination of a velocity map imaging spectrometer, an in-vacuum pixel detector, and a laser system delivering few-cycle 7 fs long pulses.

In the last part of the thesis, we present the detailed description of the design and implementation of a new setup. The built machine is the first step towards the development of a new approach to study the time-dependent structural change during bimolecular chemical reactions. We want to combine two established methods: (i) the preparation of reaction precursors in small ionic clusters and molecules (ii) Coulomb explosion imaging to determine the transient molecular structure. The new setup includes an ion source, a time-of-flight mass-spectrometer, a Coulomb explosion imaging spectrometer, and an additional neutral molecular beam source.

Acknowledgments

During the last years, I have worked with a lot of people who provided me with their help and guidance. For each project I found individual people who supported me.

First, I would like to mention my supervisor Marc J.J. Vrakking, who gave me the opportunity to work in the fascinating field of femtochemistry and the unique chance of building “my own lab”.

Further, I would like to thank Alexander Dorn for co-refereeing my thesis.

A big thanks goes to my direct supervisor Jochen Mikosch, not only for all discussions about physics and technical details, but also for his incomparable enthusiasm for science and the unique ability to create new ideas for experiments, which helped me always to find a way to reach the next step and stay motivated.

My gratitude goes to C.P. Schulz for his input to the physical discussions and the helping with my writing style. As well his support for dealing with ROOT-scripts was incredibly helpful.

Many thanks to Jingming Long, whose calm and positive nature and patient C++ support guided me through the long nights of the Timepix experiment.

Many thanks also to Friedrich Freyse for giving me a helping hand in building the machine, for conducting the first experiment, and even more for all critical discussions about life. His questioning attitude was always refreshing while troubleshooting in the lab.

I want to thank all people who provided me with their technical support. The entire technical team from the workshop and Arje Katz for all advice on construction issues. A special thanks goes to Roman Peslin, who always helped me even on short notice and who always found a solution to any technical issue. I will probably never again forget to grease screws properly.

I also want to thank Felix Schell, for preparing and conducting the reaction microscope measurement and Federico Furch who always ensured that the laser was running during our (extended) Timepix campaign.

I would like to thank all other present and former colleagues - Johan Hummert, Lorenz Drescher, Felix Braußе, Martin Galbraith, Andrea Lübcke, Oleg Kornilov and many more - for the pleasant working atmosphere, all discussions, the daily joint Mensa visits, for inventing the PhD BBQ and other fun evenings. A special thanks goes to my office colleagues Florian Bach and Peter Jürgens, for always lending me an ear, no matter if it was for discussing physics, upcoming concerts or grumbling about the (always to cold) weather.

Further thanks goes to all I, Scientist ladies - for their incredible drive to change the world and the great energy to realize inspiring projects.

Finally, I want to say my biggest thanks to my family and friends. Thanks, Tini, for being my occasional room-mate and for discussing and chatting the whole night. Thanks to my parents and especially to Steffi for always being there and supporting me. Thanks to Rut for her unique way of idealism - I am sure the Effi team will be reunited one day. And thanks to Julian for always loving and supporting me, also in stressful times - and for exploring the outside physics world together.

Selbstständigkeitserklärung

Hiermit versichere ich, dass ich die vorliegende Dissertation selbstständig und nur unter Verwendung der angegebenen Literatur und Hilfsmittel verfasst habe. Die Arbeit ist weder in einem früheren Promotionsverfahren angenommen noch als ungenügend beurteilt worden.

Berlin, den 17.05.2018 Katrin Reininger